UNIVERSITY OF
LIVERPOOL

Ultra High Speed Optical LADAR

Thesis submitted in accordance with the requirements of the

UNIVERSITY OF LIVERPOOL

for the degree of Doctor in Philosophy

by

Ali Adnan Khalil Al-Temeemy

October 2011

Abstract

A new LADAR prototype system has been designed and implemented to be able to capture the 3D LADAR data from the surfaces of various objects. This system is designed to have a high technical specification and recognition ability through the using of new LADAR image descriptors. These descriptors are arise from the chromatic methodology to extract features from the LADAR images by applying new types of processors called invariant spatial chromatic processors. This represents the first step towards using this methodology for processing LADAR images. The descriptors are developed to have high discrimination ability, robust to the effects that disturb LADAR images, and required less storage space and computational time for recognition.

The performance of the proposed LADAR descriptors were first evaluated using simulated LADAR images, which are generated from special software called LADAR simulator. This software has been written to produce simulated LADAR images under a wide variety of conditions. It models each stage from the laser source to the data generation and using proposed approach to be able to deal with complex models and produces high resolution image with short execution times.

Experimental tests are also being undertaken on the new designed LADAR system in order to asses its ability to provides 3D images and its recognition performance with the proposed descriptors.

The simulation results show high discrimination ability for the new descriptors over the traditional techniques such as Moments descriptor, which is also used to benchmark the results. The results also show the robustness of the proposed descriptors in the presence of noise, low resolution, view change, rotation, translation, and scaling effects.

The experimental results show the effectiveness of the LADAR system and its ability to scan different objects and produce their 3D images with different scanning parameters. The results also show high recognition performance for this systems when using the new LADAR descriptors compared to using Moments descriptor under the same variety of scanning condition.

Acknowledgement

I would like to express my sincere gratitude to my first supervisor *Professor J. W. Spencer* for his guidance and support in all the time of research and writing of this thesis. Besides that, I would like to thank my second supervisor *Dr. J. F. Ralph* for his encouragement and insightful comments.

Also I would like to thank those who have provided the financial support throughout the research, the Iraqi Ministry of Higher Education and Scientific Research.

Finally, I would like to thank my wife and my son *Haydar* for their love and personal support at all times. My parents and my uncle *Dr. Satie* have given me their unequivocal support throughout, as always, for which my mere expression of thanks likewise does not suffice.

Contents

List of Figures

List of Tables

Acronyms

ASCII American Standard Code for Information Interchange.

ATR Automatic target recognition.

CFD Constant Fraction Discrimination.

COTD Continuous Overlapping Triangular Descriptor.

COTP Continuous Overlapping Triangular Processors.

CRT Cathode Ray Tube.

EEPROM Electrically Erasable Programmable Read-Only Memory.

FOV Field of View.

GPS Global Positioning System.

GUI Graphical User Interface.

HHOGD Half Height Overlapping Gaussian Descriptor.

HHOGP Half Height Overlapping Gaussian Processors.

HHOTD Half Height Overlapping Triangular Descriptor.

HHOTP Half Height Overlapping Triangular Processors.

HLS Hue-Lightness-Saturation.

LADAR Laser Detection And Ranging.

LASER Light Amplification by Stimulated Emission of Radiation.

LED Light-Emitting Diode.

LIDAR Light Detection And Ranging.

RADAR Radio Detection And Ranging.

ROI Regions of Interest.

SAR Synthetic Aperture Radar.

STD Standard Deviation.

List of Symbols

A_B Target area seen by the receiver..

A_{tr} Area of target surface im m^2.

C_R, C_G, C_B Centres for the R, G, B processors.

$C_{\mathbf{sv}}$ Image covariance matrix.

D_r Diameter of circular receiver aperture in meters.

$E[N_{dark}]$ Expected number of electrons contributed by dark current.

$E[N_{signal}]$ Average number of the photoelectrons produced by the detector.

E_t Laser pulse energy in unit of joules.

F_c, F_w Filter centre and width.

H_{ls}, V_{ls} Horizontal and vertical cross-range dimensions.

$I(H_{ls}, V_{ls}, R_{ls})$ Proportion of energy contained within a component located at a location of H_{ls}, V_{ls}, R_{ls} dimensions.

K Number of photons.

K_s Number of the vector samples $\mathbf{sv}$.

M Sensing head centre point.

M_{CH} Degrees of freedom number for the laser light.

$N_{\Re}, M_{\Re}$ Numbers of rows and columns in the image $f(x_{\Re}, y_{\Re})$.

N_b Number of photoelectrons contributed by the background.

O Origin of the spherical coordinate system.

P_i^{sample} Reflected sample power.

$P_R(l_o)$ Amplitude of a signal that varies with location parameter l_o.

P_r Received signal power at the LADAR detector in units of watts.

P_t Transmitter pulse power in units of watts.

R_1, R_2 Range limit values for data filtering.

R_c Calculated range from LADAR to object.

R_{ls_o} Rayleigh range.

R_{ls} Range dimension in the direction of the pulse travelling.

$R_{min.}, R_{max.}$ Minimum and maximum measure range values.

S_{IB} Intensity of the background light at the target.

T_a One way atmospheric transmission.

T_o Optical transmission.

$W(R_{ls})$ Beam width (radius) at R_{ls} in unit of metres.

W_{RGB} Widths for the R, G, B processors.

Δ_λ Electromagnetic bandwidth of an optical bandpass filter present in the receiver.

Δs Spatial sampling size.

Δt Sampling period.

Δt_{tot} Round-trip time interval.

Ω_{tr} Solid angle of the dispersed radiation (steradian).

Φ_o Object rotation angles form the $x_{\Re}$-axis.

$\Re(l_{\Re}, \theta_{\Re})$ Projection for image $f(x_{\Re}, y_{\Re})$ at angle $\theta_{\Re}$.

Θ Offset angle, which can take any value to produced different normalized angles.

$\boldsymbol{R}(l_o), \boldsymbol{G}(l_o), \boldsymbol{B}(l_o)$ Responses for the R, G, B processors.

$\boldsymbol{R}_o, \boldsymbol{G}_o, \boldsymbol{B}_o$ Outputs of the R, G, B processors.

η Detector quantum efficiency.

λ Laser wavelength.

$\mu_{p_i q_i}$ Central moments.

ν Frequency of the light.

$\partial_{p_i q_i}$ Normalised central moments of order (p_i, q_i).

$\phi_{M_{min.}}, \phi_{M_{max.}}$ Scanning limits in tilt direction.

ϕ_l Triangle edge angle.

ρ Distance to object surface at specific azimuth and elevation angles.

ρ_{tr} Target surface reflectance.

σ^2_{noise} Variance of the measured photocounts.

$\sigma_s(\lambda)$ Atmospheric coefficient in m^{-1} for the wavelength λ.

σ_w Standard deviation of the Gaussian pulse shape in units of seconds.

τ Full-width at half-max power in unit of seconds.

$\mathbf{N}$ Plane normal.

$\mathbf{P}$ Ray intersects point with the plane.

$\mathbf{P}_0, \mathbf{P}_1, \mathbf{P}_2$ Triangle vertices.

$\mathbf{P}_l$ Any point in the triangle edge.

$\mathbf{P}_{rp}$ Round point in the triangle edge.

$\mathbf{S}$ Ray's starting position.

$\mathbf{V}$ Direction in which the ray points.

$\mathbf{sv}$ Pixels distribution vector for the image.

θ, ϕ Azimuth and elevation angles.

$\theta_{M_{min.}}, \theta_{M_{max.}}$ Scanning limits in pan direction.

θ_M, ϕ_M Pan and tilt motor angles.

$\theta_{\Re}$ Angle between the $x_{\Re}$-axis and x'_{Re}-axis.

θ_o Beam divergance angle after Rayleigh range in radians.

θ_t Angular divergence of the transmitted beam.

a_s Distance between O and the sensing head centre point M.

b_s Distance between M and the start location for the measured value c_s.

c Speed of the light.

c_m Centroid of the (discrete) input signal $P_R(l_o)$.

c_s Measured distance from the sensor lens.

$ed1, ed2$ First and the second editable texts values.

h Planck's constant which is equal to $6.626 \times 10^{-34}\, J\, s$.

h_{tr} Target impulse response.

k Number of nearest neighbours.

$l_{\Re}$ Length of line normal from the origin.

$m_{p_i q_i}$ Moment of order (p_i, q_i).

n Number of the selected border points.

$n_{\Re}$ Numbers of normalised image projections.

$p(t)$ Discrete pulse shape in time domain in unit of watts.

p_i, q_i Moments order.

sf_s Spatial sampling factor.

sf_t Time sampling factor.

slv Slider value.

$slv_{center}, slv_{width}$ Location values for the "**Centre**" and "**Width**" sliding bars.

t_e Propagation time through the electronics.

t_o Period of oscillation.

w_0, w_1, w_2 Barycentric coordinates.

Chapter 1

Introduction

1.1 Research Background

Ultra high speed Laser Detection and Ranging (LADAR) system is a three dimensional spatial measurement tool. The power of this system lies in the inherent 3-D nature of the data that is produced. These data are created by scanning a scene with a laser beam, where the scan time, field-of-view, and angular resolution are dependent upon laser pulse repetition frequency, scanner speed, range of motion, and resolution.

During the scanning process the return time and beam strength are recorded. The return strength produces intensity data and the time of return leads to range data. The intensity data are gray scale values associated with each spatial location in the range. While the format of the range data that obtain by the LADAR is range, azimuth, and elevation angles, which represent the spherical coordinates system whose origin is at the sensor. The LADAR system converts this type of range data into a traditional 3D cartesian format in order to produce the three-dimensional range image, which is represent the spatial location of the laser beam intersection with the scanned scene.

One of the most favoured applications for Ultra high speed LADAR system is the automatic target detection and classification [1]. This is because of the ability for this system to scan at ultra high speed rate [2–7] and providing high resolution 3D images, which allow for more accurate and robust determination of the target type and pose [8]. Several methods have been developed to describe LADAR images for target recognition using different features such as normals, curvature, and regional shape [9, 10], etc. But the complexity, low discrimination ability, noise sensitivity, long computational time, and the large storage requirements associated with these methods are severe limitations. These limitations increase the demand towards the development of new methods.

1.2 Research Objectives

This research aims to design and implement a new LADAR prototype system able to capture the 3D LADAR data from the surfaces of various objects and recognise them

under wide variety of conditions. This system must be design to have a high technical specification (high sampling rate and scanning resolution) and high recognition ability with less execution time.

In order to achieve fast and high recognition ability for the LADAR system, new LADAR image descriptors need to be developed. These descriptors must be robust to noise and other effects (like object rotation, translation, and scaling), have high discrimination ability, and represent the images with small features number in order to decrease the recognition times and the associated required storage.

1.3 Research Methodology

- Utilising the simplicity and high discrimination ability of the spatial chromatic processors for LADAR Data Processing. This is by developing new approaches able to make these spatial processors work as efficient LADAR image descriptors.
- Writing LADAR simulator software able to produces simulated data for a LADAR system under a wide variety of conditions by modeling each stage from the laser source to the data generation.
- Evaluating the performance of the new LADAR descriptors in controlled environments by using simulated LADAR data sets after generating them from the LADAR simulator software. This is to allow decoupling of the different effects that influence the descriptors performance and characterise their impact.
- Defining the technical aspects of the LADAR prototype design which include hardware components and both the mathematical model and the controlling software that are required for reconstructing the resultant LADAR images from the scanning measurements.
- Integrating the new developed LADAR descriptors with this prototype system and evaluating its recognition performance by scanning real models under different conditions.

1.4 Achievements

The main original achievements of this research can be summarised as follows.

- New LADAR image descriptors are proposed, which are Half Height Overlapping Gaussian Descriptor, Half Height Overlapping Triangular Descriptor, and Continuous Overlapping Triangular Descriptor. These descriptors are able to extract invariant features from the LADAR images based on using proposed types of chromatic processors called 'invariant spatial chromatic processors'. These descriptors are simple and able to describe the LADAR data with small number

of robust features, which are relatively unaffected by the noise and other effects that usually disturb the LADAR measurements.

- An efficient LADAR simulator software has been written to simulate the LADAR systems and produce their resultant 3D images under a wide variety of conditions. This software models each stage from the laser source to the data generation and uses proposed approach to be able to deal with complex models and produces high resolution 3D images with short execution times.

- A new LADAR prototype system has been designed and implemented. This new system has high technical specification and recognition ability through combining the high measurements rate for the AccuRange 4000-LV laser distance sensor, high scanning resolution for computer controlled Pan-Tilt Unit D46-17, and the high recognition ability of the new proposed LADAR image descriptors.

1.5 List of Publications

The following publications have arisen as a direct result of the author's research.

- Ali A. Al-Temeemy and J. W. Spencer. Invariant Spatial Chromatic Processors for Region Image Description. *IEEE International Conference on Imaging Systems and Techniques (IST)*, Thessaloniki, Greece, pages 421-425, July 2010.

- Ali A. Al-Temeemy and J. W. Spencer. Simulation of 3D Ladar Imaging System using Fast Target Response Generation Approach. *In Proceeding of SPIE - Optical Design and Engineering IV*, Marseille, France, volume 8167, pages 816720-(1-9), Sep 2011.

- Ali A. Al-Temeemy and J. W. Spencer. Three-Dimensional Ladar Imaging System using AR-4000LV Laser Range-Finder. *In Proceeding of SPIE - Optical Design and Engineering IV*, Marseille, France, volume 8167, pages 816721-(1-10), Sep 2011.

Other publication.

- Ali A. Al-Temeemy, J. W. Spencer, and J.F. Ralph. Levy Flights for Improved Ladar Scanning. *IEEE International Conference on Imaging Systems and Techniques (IST)*, Thessaloniki, Greece, pages 225-228, July 2010.

1.6 Thesis Layout

There are eight chapters in this thesis

Chapter 2 provides the background knowledge to LADAR systems, including the historical background, three dimensional measurement technologies, and some LADAR applications. The field of automatic 3D objects recognition using these systems is described, and the previous work done in this field is presented with identifying the need for new methods.

Chapter 3 introduces detailed information about the LADAR simulator software, that has been written to produce simulated data for a LADAR system under a wide variety of conditions. The theory of propagation of a laser beam and the ray tracing algorithms which are the core of the LADAR simulator are presented. The proposed approach of enabling the simulator to deal with more complex models and produce high resolution image at short execution time is explained. The simulation steps for the LADAR simulator and its graphical user interface are also presented with some selected results that show the effect of changing the scanning parameters on the resultant LADAR images.

Chapter 4 describes the LADAR system and associated software that have been designed and implemented to capture the 3D LADAR data from the surfaces of various objects and recognise them using the chromatic methodologies. The technical aspects of the LADAR design which include hardware components and both the mathematical model and the controlling software that are required for reconstructing the resultant LADAR images from the scanning measurements are described.

Chapter 5 introduces the chromatic methodology for LADAR data processing. An overview about the chromatic methodology and the spatial chromatic processors is presented. The proposed approach of making these processors invariant to the translation and scaling effects and how these invariant processors can be use as region image descriptors is explained. Afterwards the method of processing the LADAR images using the proposed descriptors is presented.

Chapter 6 presents the methodology for evaluating the performance of the new chromatic descriptors with LADAR data processing using simulated LADAR data. The simulation results are presented and are discussed.

Chapter 7 describes the experimental tests that have been undertaken on the new designed LADAR system in order to asses its recognition performance with the proposed chromatic descriptors. The experimental setup and procedure is explained with LADAR recognition program. The experimental results are presented and are discussed.

Chapter 8 draws conclusion about the work done and suggest how this work could be extended in the future.

Chapter 2

Background Knowledge to LADAR Systems

Introduction

This chapter contains information within the scope of the research that will provide a suitable background for the reader. The chapter consists from five sections. The first section gives a historical background about LADAR systems, while the measurement technologies that used with these systems in order to generate the three dimensional data are explained in the second section. The third section presents some applications for the LADAR systems. LADAR's automatic recognition methods and their performance are described in the fourth section. Finally the summary for this chapter is given in the last section.

2.1 LADAR Background

RADAR (RAdio Detection And Ranging) is the process of transmitting, receiving, detecting, and processing an electromagnetic wave reflected from a target [11]. In approximately 1935, RADAR came into being and continued its explosive growth with initial primary application to detection, ranging, and tracking of aircraft [12]. As theoretical and technical developments continued, RADAR techniques and applications expanded into almost every aspect of the modern world. One area of that technical development was in the wavelength of the transmitted signal, where the RADAR techniques are carried to the optical portion of the electromagnetic spectrum [12].

In 1953, the first optical RADAR system was used and called LIDAR, an acronym standing for (LIght Detection And Ranging) [11]. In 1962, the development of high-energy or Q-switched pulsed LASERs (Light Amplification by Stimulated Emission of Radiation) made such sources available for LIDAR applications [11]. Using the laser as an optical transmission source produced, a specific category of LIDAR systems called LADAR. The LADAR acronym stands for (LAser Detection and Ranging), in analogy

to RADAR [12]. LADAR systems are an attractive alternative to the RADAR systems, because using optical wavelengths (which are shorter than the radar wavelengths) provides very high resolution 3D images. In additional to that, the light velocity allow LADAR systems to take numerous amount of measurements per second. By accurately developing LADAR technology and corresponding signal processing techniques required for analyzing the data, a new generation of LADAR systems was developed. These systems are called Ultra High Speed LADAR systems, which are able to scan at ultra high speed rate reached to more than 16 million points per second [2–7].

2.2 LADAR Measurement Technologies

Early LADAR systems were designed with scanning systems to move the beam across a target area in order to collect enough information to build a scene or image of the illuminated area [13]. By 1996, scannerless systems were developed that allowed an area with a larger field of view (FOV) to be illuminated in a single shot [14]. These scannerless systems are now often referred to as flash systems [15–19] . The 3D images for these systems, contain significantly more navigational information than a traditional 2D imager such as: area, volumes, depth, etc.

LADAR systems are operate at wavelengths in the ultraviolet, visible, near, mid and far-infrared regions (i.e. wavelengths between $0.5\,\mu m$ to $10\,\mu m$ or frequencies between $600\,THz$ to $30\,THz$) and usually use one of two techniques when calculating range measurements to an object: *continuous wave LADAR*, which sends out modulated signals and measures the phase difference between transmitted and received signals; or *pulsed LADAR*, which sends out individual laser pulses and measures time-of-flight between transmitted and received signals.

Both techniques have their specific advantages and disadvantages. The most obvious method of operating LADAR systems is in the pulsed light operation, because the time of flight is measured directly [20–22]. The actual time measurement is performed by correlating the start and stop signals with a parallel running counter. The advantage of using pulsed light is the ability of transmitting a high amount of energy in a very short time. Thus the influence of background illumination can be reduced and a high short-term optical signal-to noise (and signal-to-background) ratio is attained while maintaining a low mean value of optical power. This is an important factor for eye safety, which is the limiting criterion for many measurement applications. Furthermore, it reduces the demand on a very high sensitivity and signal-to-noise ratio of the detector, thus enabling long distance measurements. However, at the same time the receiver must offer high dynamic range and a large bandwidth. The basic problem for the receiving path is to detect exactly the arrival time of the back-scattered light pulse. This is because the optical threshold is not a fixed value but changes with background and distance of the object, and atmospheric attenuation leads to dispersion of the light

pulse and flattens the edge of the received pulse. Therefore very short light pulses with fast rise and fall times are necessary, to assure an accurate detection of the incoming light pulse.

In continuous light operation, its possible to use an alternative modulation, demodulation, and detection-mechanisms [23–25]. Generally the phase difference between sent and received signals is measured, rather than directly measuring the pulse time of flight. As the modulation frequency is known, this measured phase directly corresponds to the time of flight. Compared to previous technique, modulation of a larger variety of light sources is possible for this mode of operation because the extremely fast rise and fall times are not required as for pulsed operation. Over the last several decades, the LADAR technologies have been developed so that data could be acquired through a variety of methods. Blais [26] provided a brief review of the past 20 years of development in the field of 3D laser imaging.

2.3 LADAR Applications

LADAR systems have diverse roles in both civilian and military applications. These systems have been used to create 3D models of structures and scenes for quality control, surveying, mapping, reverse engineering, terrain characterization, safety improvement, and disaster reconnaissance [27, 28]. In addition, LADARs have been used for dynamic applications such as ground, aerial, and maritime navigation.

In ground navigation, the LADAR systems are used for obstacle and road-boundary detection [29–35], which represent an important functions in advanced driver-assistance systems and autonomous vehicle navigation systems [36]. The systems are also used for vehicles localization in urban environments, when Global Positioning System (GPS) data is unavailable or has a too poor quality because of bad satellite visibility [37]. In aerial navigation, LADARs are used to provide autonomous navigational capability [38], obstacle warning system [39], and a reliable alternative to GPS [40]. With maritime navigation the LADAR systems are used for both precise manoeuver operation and obstacle avoidance [41].

One of the most favoured applications for LADAR involves target detection and classification [1, 42], anti-ship missile tracking [43], target identification at long range using spectral and vibration measurements [44–46], and identifying military ground vehicles that may be hiding under camouflage or foliage such as tree canopy [47]. There is also an emerging potential to use LADAR systems in space application for orbiter inspection [48], capturing non-cooperative objects on orbit [49], orbital rendezvous [50], and for determining the pose of the satellites [51].

2.4 LADAR Automatic Recognition

Automatic recognition of 3D objects has been an important research topic for many years [52]. The high resolution and the 3D images provided by the LADAR systems allow for more accurate and robust determination of the object type and pose [8]. Where the main advantage of the 3D images lies in the measurement of the third dimension (the range), that enables derivation of robust features. Automatic target recognition (ATR) involves two main tasks: target detection and recognition [53]. The purpose of target detection is to find regions of interest (ROI) where a target may be located. By locating ROIs, a large amount of background can be filtered out from the scene. The ROIs are then passed to a recognition algorithm that identifies the target [53]. The most common approach for target recognition is the view-based approach. View based recognition represents 3D objects as a set of discrete views around the object. Range images are compared to the view database to determine the most probable object. In this approach, database images are typically represented as points in the feature space. The unknown range image is projected into this space and the nearest database point is taken as the closest matching image [54]. The view-based approach historically derives from 2D intensity image recognition techniques.

The 3D object recognition community has developed different methods for computing features which describe LADAR images for classification. Some use the surface properties such as normals, curvature, and regional shape [9, 10]. Surface normals and curvature depend on a reliable extraction of local features such as edges and derivatives, which are sensitive to noise [55]. While the regional shape extraction approach is robust to noise, but the main disadvantages of it are computationally expensive, required large space to store the features, and low discriminating capability [10, 56].

Other methods describe the LADAR images as histograms of point fractions that fall into partitions of the enclosing object space under different partitioning models such as shell and voxels models [57, 58]. The first decomposition model partitions the space into shells concentric to the object's centre of mass [57], while the second model creates distinct voxels of equal size around the object bounded by its extent in the three principal directions [58]. To overcome the shape rotation problem for the later model, specific number of voxels are combined together [59]. Generally the shape histogram methods suffer from the space partitioning in the presence of noise, in additional to that these method use high number of features. This increases the recognition time and requires more memory to store the features.

Furthermore, robust feature descriptors such as moment invariants have been used for LADAR images recognition [60]. These moments are invariant to translation and rotations. A general disadvantage of using these moments is the noise sensitivity. This noise sensitivity limits the use of moments and restricts their applications [61].

Since none of the previously mentioned methods could fully meet the requirements

of LADAR image description, new methods need to be developed. The requirements are: simplicity, high discrimination ability, small features number (which is leads to decrease the recognition time and the storage space), robustness to noise, and invariant to (rotation, translation, and scaling) effects.

2.5 Summary

The background knowledge about the LADAR systems field is introduced in this chapter, which contains information about the LADARs historical background, their three dimensional measurement technologies, and some applications. Furthermore, the chapter describe the previous work done in the field of automatic 3D objects recognition methods and identify the need for a new method that can provide high discrimination ability with small features number , where these features must be robust to noise and invariant to rotation, translation, and scaling effects.

Chapter 3

LADAR Simulator

Introduction

This chapter presents detailed information about the LADAR simulator software, that has been written to produce simulated data for a LADAR system under a wide variety of conditions. This simulator models each stage from the laser source to the data generation and it consists of a simulation software and a graphical user interface (GUI). It represents an efficient simulation tool for developing recognition algorithms for the LADAR systems.

In this chapter, six sections are presented. The first two sections cover the theoretical background for the laser beam propagation and ray tracing algorithms, which represent the core of the simulator. The third section focuses on the main concepts of the simulation implementation. While the fourth section gives a description of the GUI control panels. The fifth section presents the possibilities of the simulator by showing a collection of the selected simulated results. Finally the summary of this chapter is presented in the last section.

3.1 Laser Beam Propagation

The propagation of a laser beam from the transmitter to the target, and back to the receiver, is described in this section. The process of simulating the propagation of a beam has been divided into four parts as shown in Figure 3.1 [62].

The laser range finding principle is reviewed first. Then the laser beam energy distribution is described in both the temporal and the spatial domains [No.1]. Atmospheric effects on the propagating beam [No.2] and the beam interaction with target surface [No.3] are then explained. This is followed by considering the receiver [No.4] and the derivation of the LADAR range equation.

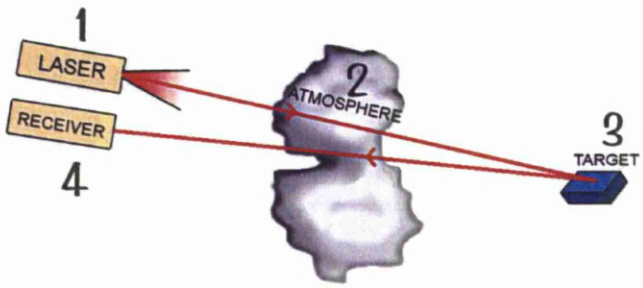

Figure 3.1: The Division of the Process During Simulation (figure adapted from [62]).

3.1.1 Laser Range Finding Principle

The principle of finding range using the laser beam is shown in Figure 3.2. The LADAR transmitter sends a laser pulse and records the time at which it was sent. The pulse travels through the atmosphere to an object and is reflected from its surface. The reflected beam is then collected by the LADAR receiver after travelling through the atmosphere with a distance equal to the transmitted pulse distance. The LADAR receiver then records the receiving time and calculates the round-trip time interval Δt_{tot}, where the laser pulse travels at the speed of light. Finally the LADAR system calculates the range using the following equation [11]:

$$R_c = \frac{\Delta t_{tot}}{2} \times c \tag{3.1}$$

where R_c is the calculated range from the LADAR to the object and c is the speed of the light, which is equal to $3 \times 10^8\ m/s$.

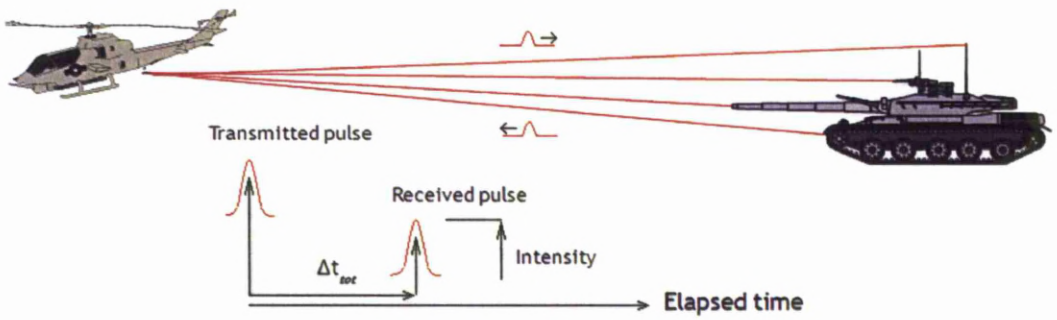

Figure 3.2: Laser Range Finding Principle (figure adapted from [11]).

3.1.2 Laser Beam Energy Distribution

In order to simulate the effects of the target shape, the laser pulse has to be modelled in time (temporal distribution) as well as in space (spatial distribution) which leads to a four dimensional model. So the outgoing pulse intensity is decomposed as [11]:

$$G(t, H_{ls}, V_{ls}, R_{ls}) = p(t) \times I(H_{ls}, V_{ls}, R_{ls}) \tag{3.2}$$

where $p(t)$ is the discrete pulse shape in time domain; $I(H_{ls}, V_{ls}, R_{ls})$ is the proportion of energy contained within a component located at a location of H_{ls}, V_{ls}, R_{ls} dimensions, where $t, H_{ls}, V_{ls}, R_{ls}$ take on discrete values. Figure 3.3 shows these two distributions for the laser pulse travelling from the LADAR system to the target, where H_{ls} and V_{ls} are the horizontal and vertical cross-range dimensions and R_{ls} is range dimension (in the direction of the pulse travelling).

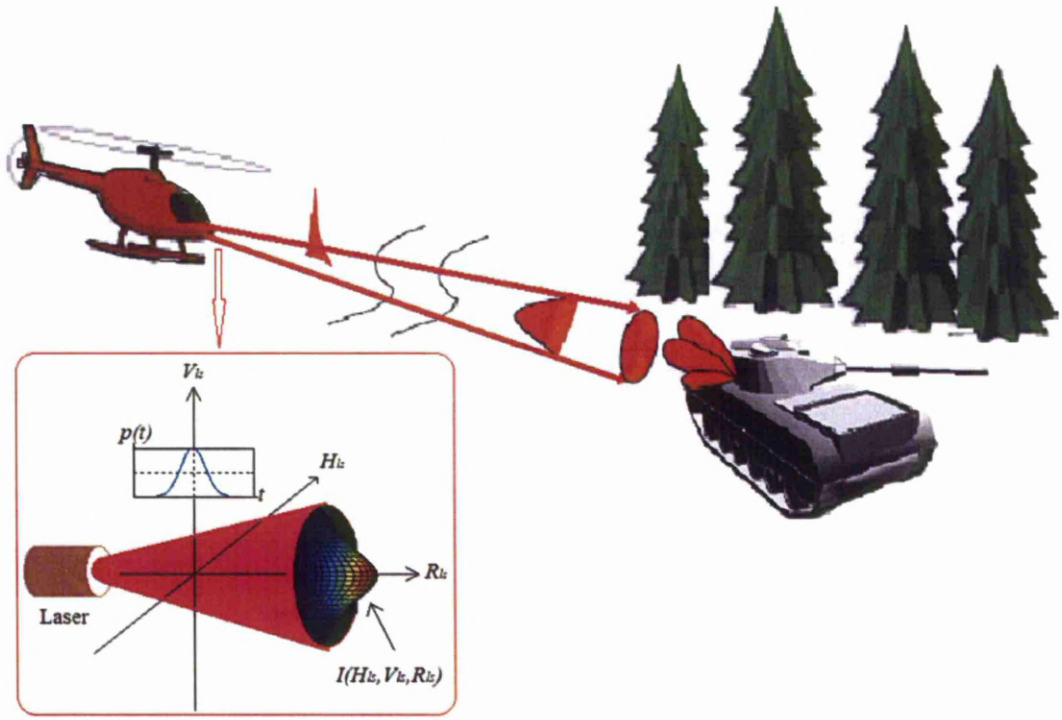

Figure 3.3: Laser Pulse Energy Distribution (figure adapted from [62]).

3.1.2.1 Temporal Distribution

The amount of laser power that is produced by the LADAR source and transmitted toward the target area is assumed to have a Gaussian distribution with time. This distribution is defined by the laser pulse energy E_t in unit of joules and pulse width τ (full-width at half-max power in unit of seconds). The following equation [11, 63] is used to model this distribution as :

$$p(t) = \frac{2E_t}{\tau}\sqrt{\frac{\ln 2}{\pi}} \exp \frac{-t^2}{2\sigma_w^2} \tag{3.3}$$

$$\sigma_w = \frac{\tau}{2\sqrt{2 \ln 2}} \tag{3.4}$$

where $p(t)$ is the laser pulse power in unit of watts at time t and σ_w is the standard deviation of the Gaussian pulse shape in units of seconds. In order to avoid aliasing on the laser pulse waveform, the sampling period Δt is calculated using the following equation [11]:

$$\Delta t = \frac{\sigma_w}{sf_t} \tag{3.5}$$

where sf_t is the time sampling factor and its values must be greater than one for good pulse representation. Figure 3.4 shows the Gaussian distribution for a typical laser pulse of $\tau = 4.7 \times 10^{-9}\, s$, $E_t = 1 \times 10^{-3}\, J$, and $sf_t = 10$.

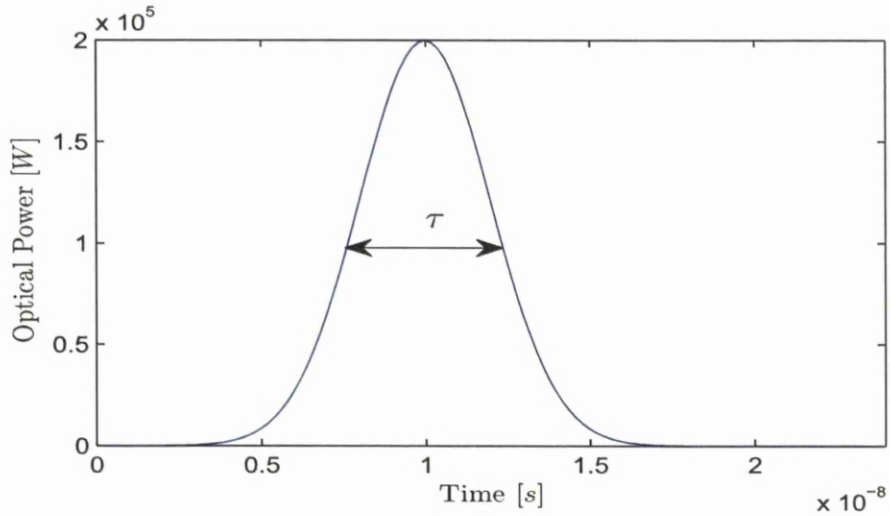

Figure 3.4: The Laser Pulse of $\tau = 4.7\, ns$, $E_t = 1\, mJ$, and $sf_t = 10$.

3.1.2.2 Spatial Distribution

The laser intensity profile produced by a laser source cavity is not constant across the beam diameter at all ranges, and it depends on the technique used to generate the laser beam. Generally this profile or energy distribution is modelled as a spatial Gaussian function in horizontal H_{ls}, vertical V_{ls}, and range R_{ls} dimensions [64, 65]:

$$I(r, R_{ls}) = \frac{2}{\pi W^2(R_{ls})} \exp \frac{-2r^2}{W^2(R_{ls})} \tag{3.6}$$

$$r = \sqrt{H_{ls}^2 + V_{ls}^2}$$

where $W(R_{ls})$ is the beam width (radius) at R_{ls} and it is defined as the radial distance (in unit of metres) at which the profile value is decrease to $1/e^2$ from its peak value as shown in Figure 3.5. The dependence of beam width on the distance R_{ls} is illustrated in Figure 3.6 and governed by [64, 65]:

$$W(R_{ls}) = W_o\sqrt{1+\left(\frac{R_{ls}}{R_{ls_o}}\right)^2} \tag{3.7}$$

where

$$R_{ls_o} = \frac{\pi W_o^2}{\lambda} \tag{3.8}$$

is referred to as the Rayleigh range.

The Rayleigh range is the distance from ($R_{ls} = 0$), for which the beam area has just double $W(R_{ls_o}) = \sqrt{2}W_o$, where W_o is the beam waist at $R_{ls} = 0$ and λ is the laser wavelength. Referring to Figure 3.6 the laser beam starts to diverges as a cone of half-angle after Rayleigh range, this angle (in radians) is given by [64, 65]:

$$\theta_o = \frac{\lambda}{\pi W_o} \tag{3.9}$$

The divergence angle is directly proportional to the wavelength λ, and inversely proportional to beam waist W_o. Therefore, a highly directional laser beam is obtained by using a short wavelength and a thick beam waist.

Referring to [65] and [64], the spatial sampling size Δs that avoids aliasing of the laser intensity profile can be calculated using the following equation:

$$\Delta s = \frac{W(R_{ls})}{sf_s} \tag{3.10}$$

where sf_s is the spatial sampling factor and its values must be greater than one for good intensity representation.

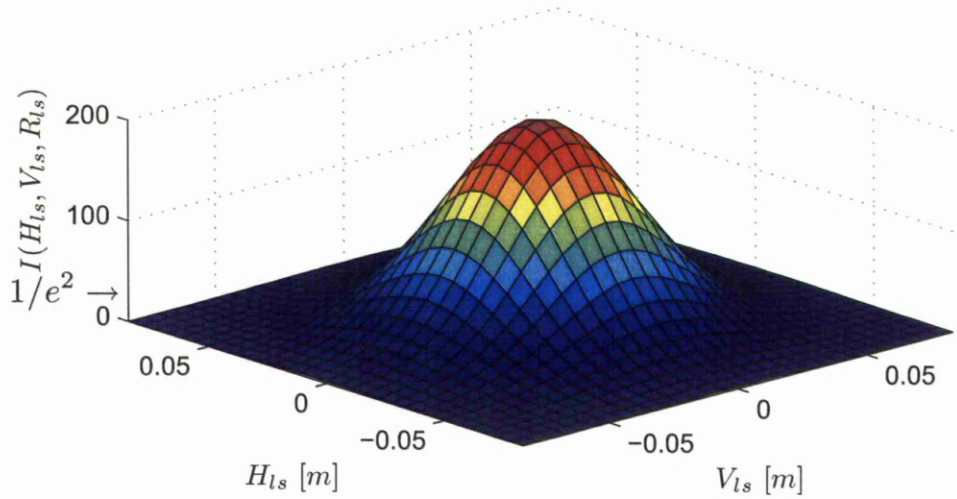

Figure 3.5: Gaussian Profile at $R_{ls} = 1000\,m$ for Laser Beam of $W_o = 9 \times 10^{-3}\,m$, $\lambda = 1.55 \times 10^{-6}\,m$ and $sf_s = 10$.

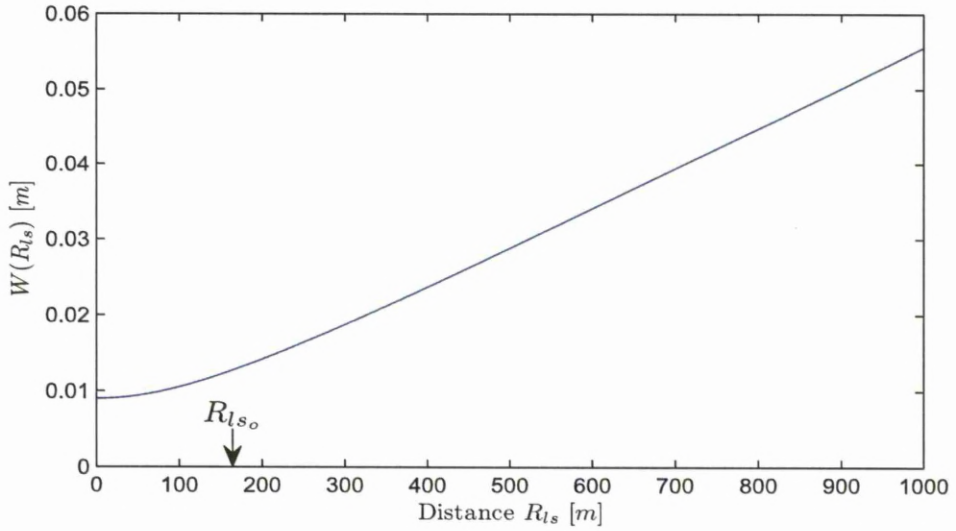

Figure 3.6: Gaussian Beam Width $W(R_{ls})$ Expansion with Increase Distance R_{ls} for Laser Beam of $W_o = 9 \times 10^{-3}\, m$, $\lambda = 1.55\, \mu m$ and $sf_s = 10$.

3.1.3 Atmospheric Effects

When the transmitted laser beam propagates through the atmosphere, some of the energy is absorbed and scattered by atmospheric molecules, dust, and aerosols [11]. This attenuation limits the LADAR system performance and is dependent on the laser's wavelength λ and the propagation length R_{ls}. This can be modelled using Beer's law as shown in Equation 3.11 [11, 66]:

$$T_a = \exp\left(-\sigma_s(\lambda) \times R_{ls}\right) \tag{3.11}$$

where T_a is the one way atmospheric transmission value and $\sigma_s(\lambda)$ is the atmospheric coefficient in m^{-1} for the wavelength λ. Since the laser beam travels twice the distance to reached the receiver, this leads to affected it by $T_a \times T_a = T_a^2$. Figure 3.7 shows a plot of the two way atmospheric transmission T_a^2 against path length for a laser beam of wavelength equal to $1.55\, \mu m$ propagate at clear standard atmosphere in which the atmospheric coefficient $\sigma_s(1.55\, \mu m)$ is equal to $0.1 \times 10^{-3} m^{-1}$[66].

3.1.4 Target Interaction

The interaction between the transmitted laser beam and the target surface produces a reflected signal. The characteristics for this signal depend on the following:

- Surface Reflectance Parameter ρ_{tr}: This depends on the nature of the target and quantifies the percentage of reflected laser radiation. Typical values for this parameter range from as little as 2% to as high as 25%, although some materials have higher reflectance such as polished surface [11].

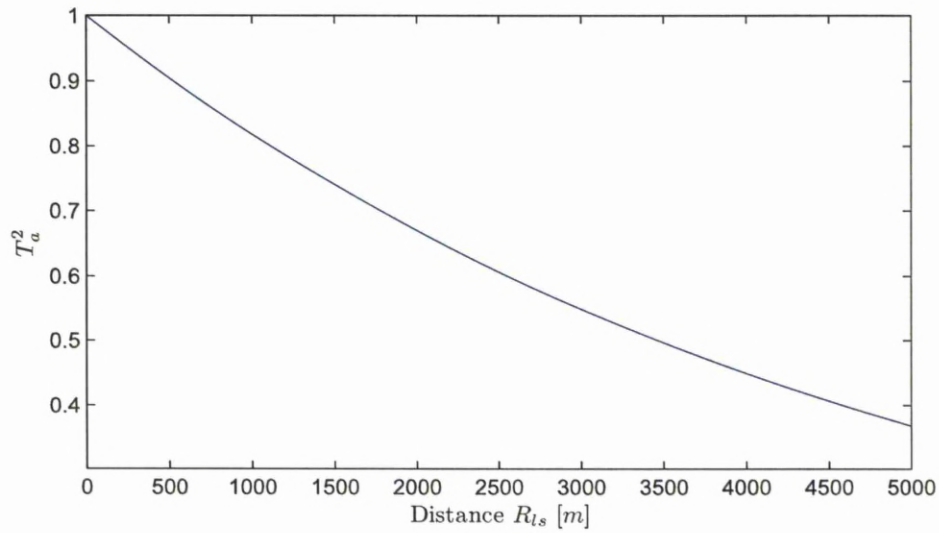

Figure 3.7: Two way Atmospheric Transmission T_a^2 Against Propagation Length R_{ls}.

- Angle of Dispersion Ω_{tr}: The reflected radiation can be reflected back in a variety of ways depending on the reflected surface type (specular, rough). In this simulator, *Lambertian targets* are assumed and the solid angle over which the radiation is dispersed is set to be equal to π steradians [11, 12, 66].

- Surface Area A_{tr}: The area of target surface is also an important factor in determining the amount of radiation that returns to the receiver. This amount is larger for the *extended targets* (target area intercepts the entire beam) than for *point targets* (target area smaller than the transmitted footprint) [66].

- Surface Shape and the Angle of Incidence: The beam-target interaction not only affects the energy in the reflected signal, but it also affects its shape. Both the beam incidence angle and the surface shape (plane, step, etc.) effects, play important roles in changing the transmitted pulse shape. To simulate these effects, the target surface must be sampled at distances relative to the laser source location by using Ray Tracing Algorithms. This process will be explained in more detail in the next sections.

  The simulated shapes for the reflected signals that result from the interaction of the laser beam at different incident angles with the plane and step targets are shown in Figure 3.8. Figure 3.8b presents the shapes of the signal that reflect from a plane target shown in Figure 3.8a, while Figure 3.8d presents the shapes of the signal that reflect from a step target shown in Figure 3.8c.

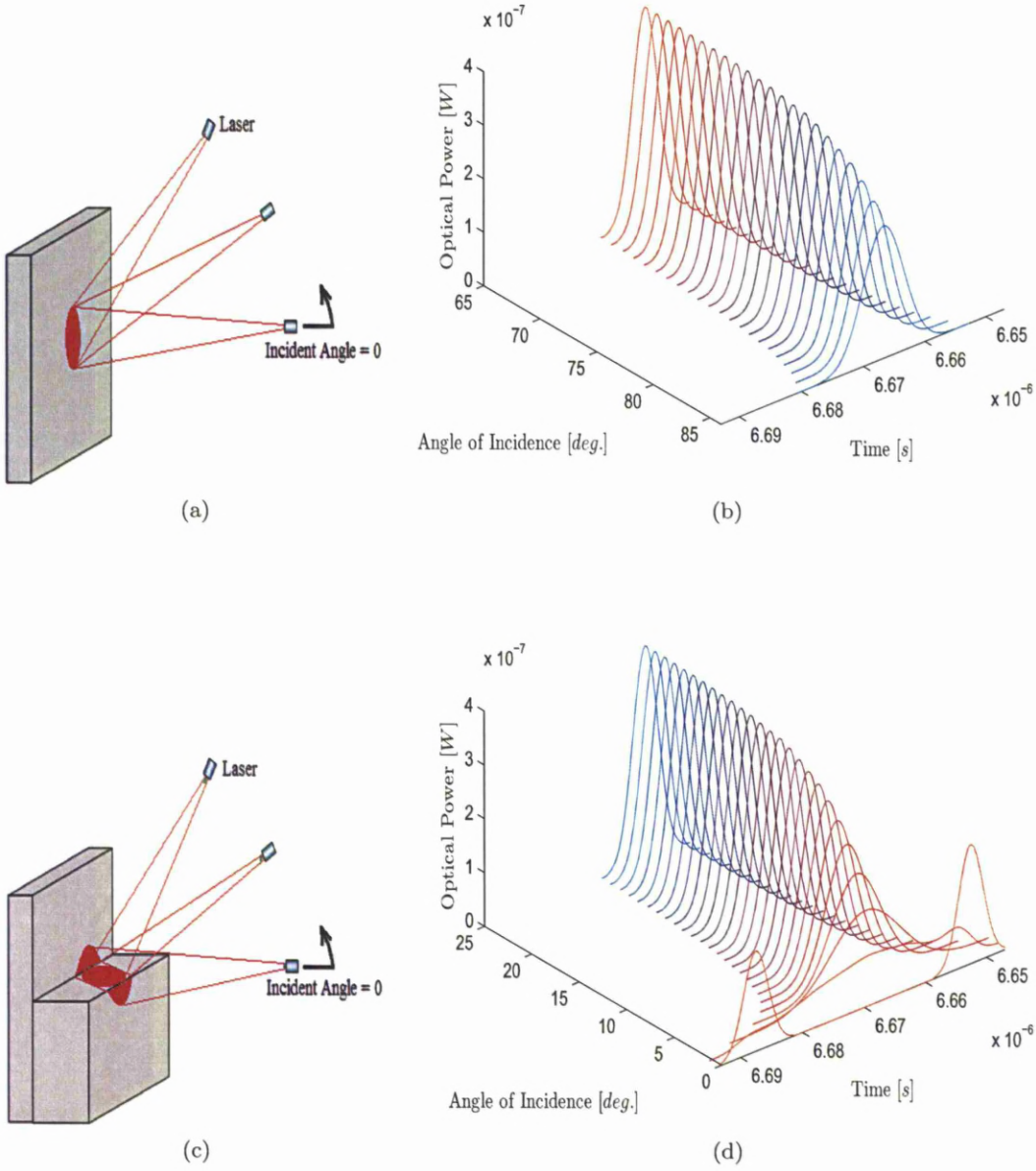

Figure 3.8: Illustration of Return Pulse Shaping by Plane and Step Targets Geometries.

3.1.5 LADAR Receiver

The process of determining the range to the target from the reflected signal is accomplished by the LADAR receiver. This process depends on the following:

3.1.5.1 Detection Technique

Two different detection techniques are used with the LADAR system. These techniques are, direct detection and coherent detection. More details about these techniques are found in [67]. In this simulator the direct detection technique is used, in which the received optical energy is focused onto a photodetector element. This detector generates a current which is directly proportional to the optical power that is incident on it.

3.1.5.2 Receiver Efficiency

The signal power that is measured by the LADAR system is affected by the receiver efficiency. This efficiency is driven by both the optical transmission T_o (the fraction of energy that arrives at the detector from the total energy captured by the receiver aperture) and the quantum efficiency η (the fraction of the signal that is converted into photoelectrons) of the detector. The number of photons K produced by the power falling on the detector P_r is a random variable whose mean is computed by the following equation [11]:

$$E[K] = \frac{P_r \Delta t}{h\nu} \tag{3.12}$$

where $E[\ ]$ is the expectation operation, Δt is the sampling period, h is Planck's constant, and ν is the frequency of the light. Using the detector quantum efficiency η, the average number of the photoelectrons N_{signal} produced by the detector is computed by [11]:

$$E[N_{signal}] = \eta E[K] \tag{3.13}$$

3.1.5.3 Photon Counting and Speckle Noise

The photon counting noise is defined as the random arrival of the reflected photons to detector. This randomness introduces uncertainty in the number of photons measured during a finite time interval Δt. While the laser speckle noise is caused by the electromagnetic field interference occurring at the detector surface from a large collection of independent coherent radiators.

The statistical fluctuations in the measured signal due to speckle and photo counting noise can be simulated in the LADAR measurement by modelling the number of photons detected as a negative binomial random variable with a mean equal to $E[N_{signal}]$ and a variance given by the following equation [11]:

$$\sigma^2_{noise} = E[N_{signal}] \left(1 + \frac{E[N_{signal}]}{M_{CH}}\right) \tag{3.14}$$

where σ^2_{noise} is the variance of the measured photocounts, and M_{CH} is the degrees of freedom number for the laser light. For fully coherent light, $M_{CH} = 1$, and for

fully incoherent light, M_{CH} approaches infinity and the photo counting noise become dominant. Figure 3.9 shows the effect of the photo counting noise on the received signal, while Figure 3.10 shows the effect of both photo counting noise and speckle noise on the received signal.

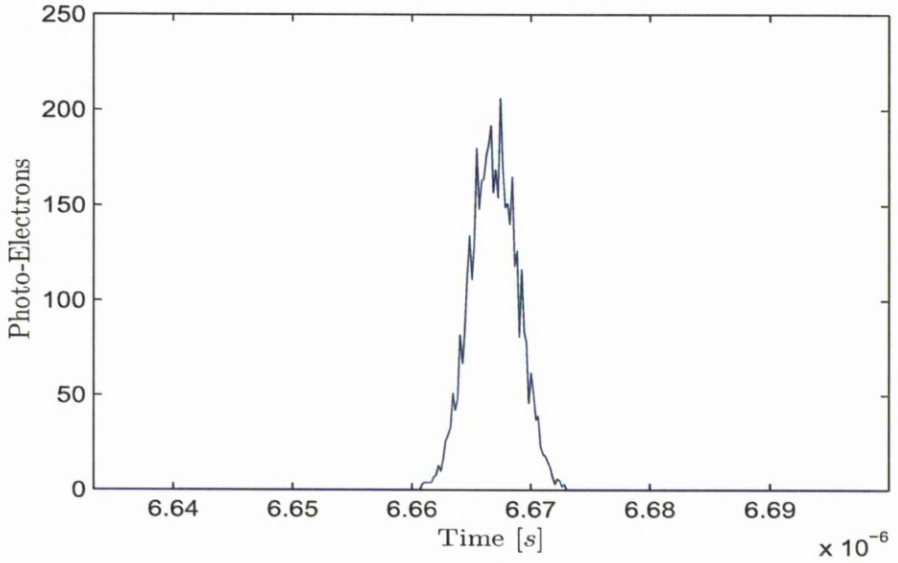

Figure 3.9: Noisy Signal Due to Photo Counting Noise ($M_{CH} = 100$).

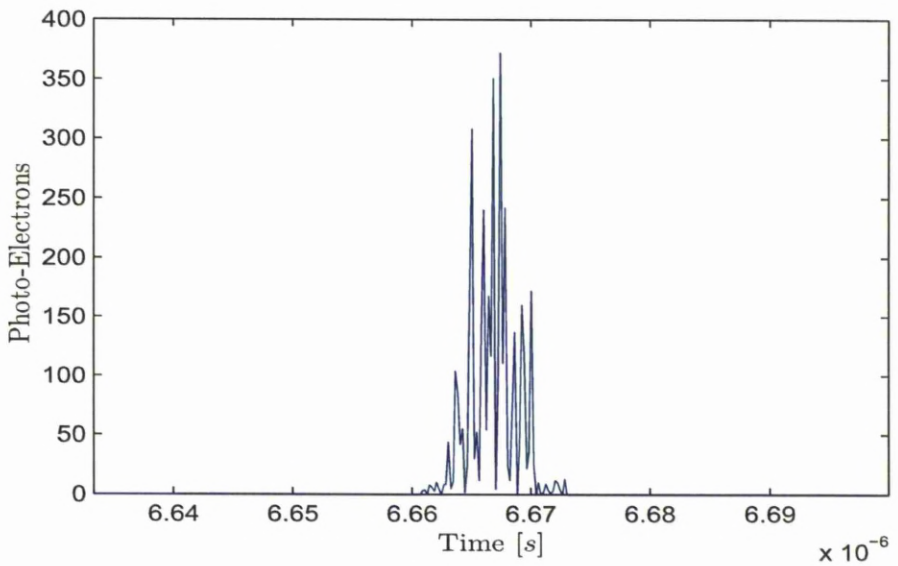

Figure 3.10: Noisy Signal Due to Photo Counting and Speckle Noise ($M_{CH} = 1$).

3.1.5.4 Background Noise

The background photons are the photons that are collected by the sensor which do not originate from the laser transmitter. In most practical scenarios these photons are originated from the sun. The background photons bear no information concerning the range to the target and the random arrival times for these photons contribute noise to the LADAR measurement.

This noise can be simulated during a LADAR measurement by modelling the number of photoelectrons produced by the background as Poisson random variable with a mean $E[N_b]$ given by the following equation [11]:

$$E[N_b] = \frac{S_{IB}\Delta_\lambda A_B \rho_{tr} \eta T_a T_o D_r^2 \Delta t}{4R_{ls}^2 h\nu} + E[N_{dark}] \tag{3.15}$$

where N_b is the number of photoelectrons contributed by the background, including the Poisson noise; S_{IB} is the intensity of the background light at the target in units of W/m^2 per μm of electromagnetic bandwidth; and Δ_λ is the electromagnetic bandwidth in μm of an optical bandpass filter present in the receiver. A_B is the target area seen by the receiver. $E[N_{dark}]$ is the expected number of electrons contributed by dark current. Figure 3.11 shows the signal of Figure 3.10 after adding background noise to it. The figure also shows the selected threshold value that is used to eliminate the effect of this noise. This value is assumed in this simulator to be ten times larger than the maximum noise mean value (which is calculated at a maximum atmospheric transmission, maximum target area seen by the receiver, and minimum target range ($200\,m$) scanned by the LADAR).

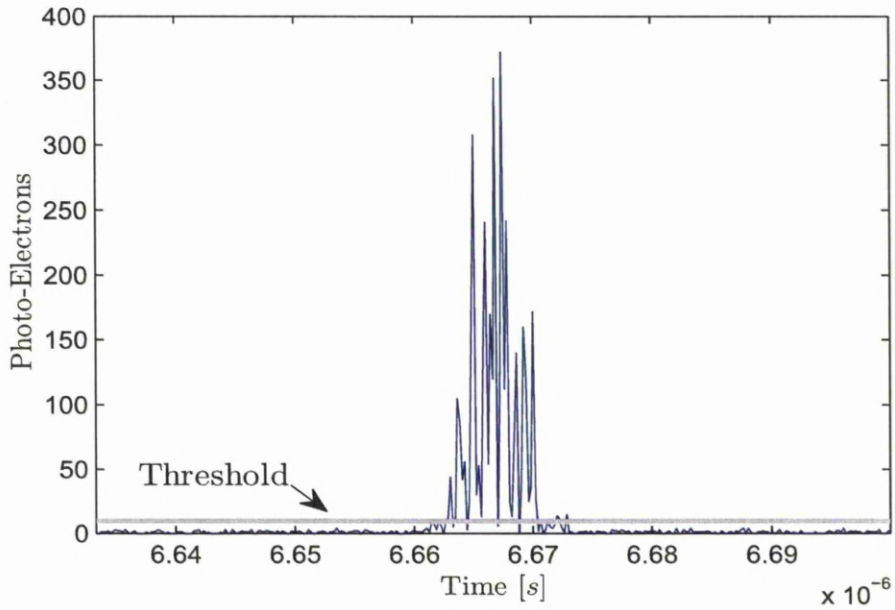

Figure 3.11: Noisy Signal Due to Photo Counting, Speckle Noise and Background Noise.

3.1.5.5 Pulse Detection and Range Measurement

As mentioned in 3.1.1, the idea of computing the target range is done by measuring the time of detecting the laser pulse from the sending time, which represent the round-trip time of flight interval Δt_{tot}.

In this simulator, the Constant Fraction Discrimination *CFD* peak detector is used for pulse detection, as this is insensitive to the amplitude fluctuation that cause jitter in the time of arrival [67]. Referring to Figure 3.12, the *CFD* detector is accomplished by splitting the incoming signal into two channels, delaying one channel by one half of a pulse width, and subtracting the delayed channel from the original. This results in a positive and then negative signal with a characteristic S-shaped profile. The zero crossing of the S-shaped profile is used to stop the timer and the resultant time Δt_{tot} is used to calculate the target range by Equation 3.1.

In order to reduce the effect of the background noise, this discriminator is enabled only when the input signal value is larger than the threshold value shown previously in Figure 3.11.

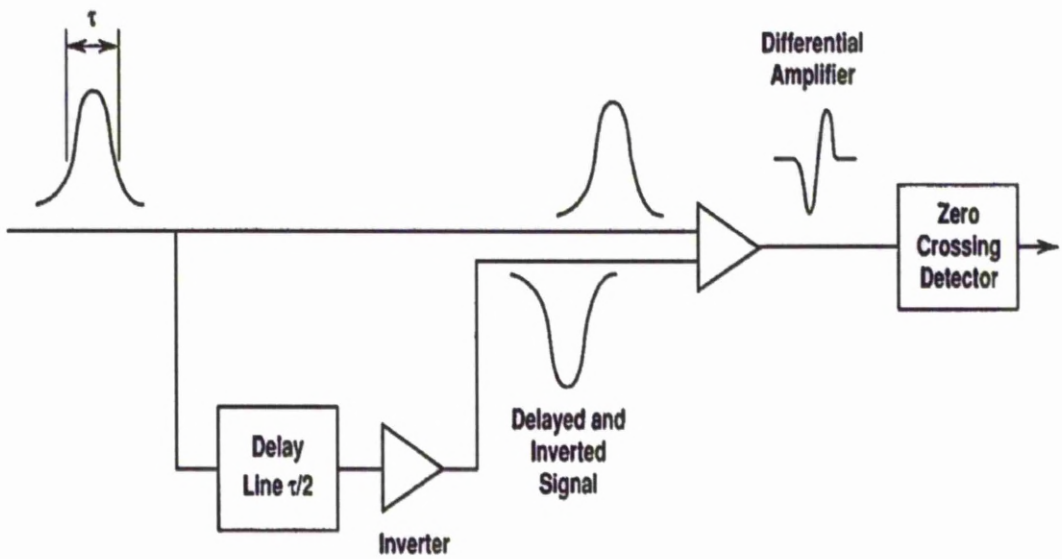

Figure 3.12: CFD Peak Detector (taken from [67]).

3.1.6 LADAR Range Equation

The range equation is widely used as an analytical tool for computing the power received P_r from a target illuminated by a laser pulse containing a given power P_t. The LADAR equation, is directly analogous to the original RADAR equation [12, 66] and can be broken down into several terms that quantify the contribution of the laser propagation elements illustrated previously (transmission, reflection, and reception).

According to [11] the equation is:

$$P_r = \overbrace{\overbrace{\underbrace{\frac{4P_t}{\pi\theta_t^2 R_{ls}^2}}_{1} \times \underbrace{\frac{A_{tr}}{\Omega_{tr} R_{ls}^2}}_{2}}^{3} \times \underbrace{\frac{\pi D_r^2}{4}}_{4}}^{5} \times \underbrace{\rho_{tr} T_a^2 T_o}_{6} \tag{3.16}$$

where

P_r : Received signal power at the LADAR detector(watts).

P_t : Transmitter pulse power (watts).

θ_t : Angular divergence of the transmitted beam (rad).

R_{ls}: Range between LADAR and the target (meters).

ρ_{tr} : Target surface reflectance.

A_{tr}: Target surface area (square meters).

Ω_{tr}: Solid angle of the dispersed radiation (steradian).

D_r : Diameter of circular receiver aperture (meters).

T_a : One way attenuation factor.

T_o : Optical transmission.

1 : Intensity reaching the target area from the transmitter (W/m^2).

2 : Ratio of target area to the reflected beam area.

3 : Intensity at the receiver aperture (W/m^2).

4 : Area for the circular receiver aperture (m^2).

5 : Power captured by the circular receiver aperture (W).

6 : Attenuation by target reflection, atmosphere and optical transmissions.

As mentioned in subsection 3.1.4 on page 15, the simulator assumes *Lambertian targets*. Therefore, Ω_{tr}, is replaced by the value associated with the standard diffuse targets having solid angle of π steradians [11, 12, 66].

In the simulation the laser beam footprint is much smaller than the target extent, which means that the target surface intercepts the entire beam (*extended targets*). This makes the target area A_{tr} equal to the area illuminated by the laser beam, and given by:

$$A_{tr} = \frac{\pi\theta_t^2 R_{ls}^2}{4} \tag{3.17}$$

With the previous assumptions and substituting Equation 3.17 in Equation 3.16, the LADAR range equation become [11, 67, 68]:

$$P_r = \frac{P_t \rho_{tr} T_a^2 T_o D_r^2}{4R_{ls}^2} \tag{3.18}$$

3.2 Ray Tracing Algorithms

The term ray tracing refers to any algorithm that follows a beam of light to determine with which objects they interact in the world [69]. These algorithms are used by the simulation software to obtain the intersection points of the rays vectors that represent the laser beam with the triangular faces (see Figure 3.14) that represent the model surface. These points represent the laser footprint samples on the model surface by which the reflected sample power and the round-trip time for each sample can be calculated.

Referring to Figure 3.13, each laser ray's vector can be defined by the following equation:

$$\mathbf{P} = \mathbf{S} + l\mathbf{V} \tag{3.19}$$

where $\mathbf{S}$ represents the ray's starting position, $\mathbf{V}$ represents the direction in which the ray points, and l corresponding to the point $\mathbf{P}$ where the ray intersects the plane of the triangle. The l value is given by :

$$l = \frac{\mathbf{N} \cdot (\mathbf{P}_0 - \mathbf{S})}{\mathbf{N} \cdot \mathbf{V}} \tag{3.20}$$

$$\mathbf{N} = (\mathbf{P}_1 - \mathbf{P}_0) \times (\mathbf{P}_2 - \mathbf{P}_0)/|(\mathbf{P}_1 - \mathbf{P}_0) \times (\mathbf{P}_2 - \mathbf{P}_0)|$$

where $\mathbf{N}$ is the plane normal and $\mathbf{P}_0$, $\mathbf{P}_1$, and, $\mathbf{P}_2$ are the triangle vertices. If the denominator is equal to zero, then no intersection occurs. Otherwise, plugging this value of l back into Equation 3.19 produces the point $\mathbf{P}$ where the ray intersects the plane of the triangle.

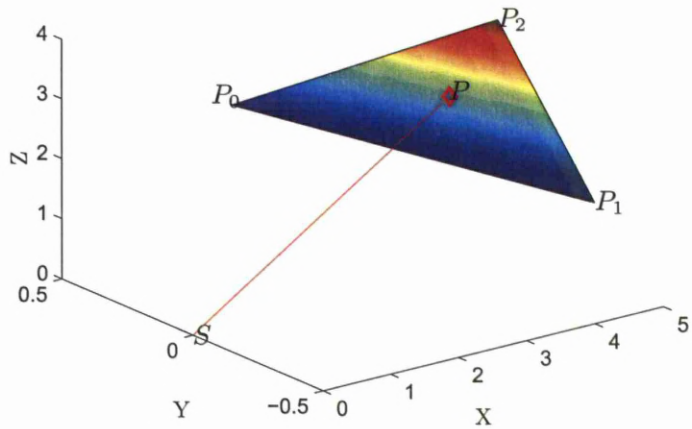

Figure 3.13: Intersection point $\mathbf{P}$ of the laser ray's vector with the triangle face.

To determined whether the point $\mathbf{P}$ lies inside the triangle's edges, *barycentric coordinates* [70] for this point with respect to the triangle's vertices are calculated. These coordinates represent a weighted average of the triangle's vertices and are expressed as the scalars w_0, w_1, and w_2 such that

$$\begin{aligned} \mathbf{P} &= w_0\mathbf{P}_0 + w_1\mathbf{P}_1 + w_2\mathbf{P}_2 \\ \text{where } 1 &= w_0 + w_1 + w_2 \end{aligned} \tag{3.21}$$

In general, a point is inside (or on) the triangle if and only if $0 \leq w_0, w_1, w_2 \leq 1$, or alternatively if and only if $0 \leq w_1 \leq 1, 0 \leq w_2 \leq 1$, and $w_1 + w_2 \leq 1$. To determine the values of these coordinates (w_0, w_1, and w_2), the w_0 in Equation 3.21 was replaced with $1 - w_1 - w_2$ as shown below

$$\begin{aligned} \mathbf{P} &= (1 - w_1 - w_2)\mathbf{P}_0 + w_1\mathbf{P}_1 + w_2\mathbf{P}_2 \\ &= \mathbf{P}_0 + w_1(\mathbf{P}_1 - \mathbf{P}_0) + w_2(\mathbf{P}_2 - \mathbf{P}_0) \end{aligned} \tag{3.22}$$

The calculations were then performed relative to the point P_0 by defining

$$\begin{aligned} \mathbf{v}_0 &= \mathbf{P}_1 - \mathbf{P}_0 \\ \mathbf{v}_1 &= \mathbf{P}_2 - \mathbf{P}_0 \\ \mathbf{v}_2 &= \mathbf{P} - \mathbf{P}_0 \end{aligned}$$

and the Equation 3.22 becomes

$$\mathbf{v}_2 = w_1\mathbf{v}_0 + w_2\mathbf{v}_1 \tag{3.23}$$

A 2×2 system of linear equations can be then formed by taking the dot product of both sides with $\mathbf{v}_0$

$$\begin{aligned} \mathbf{v}_2 \cdot \mathbf{v}_0 &= (w_1\mathbf{v}_0 + w_2\mathbf{v}_1) \cdot \mathbf{v}_0 \\ &= w_1(\mathbf{v}_0 \cdot \mathbf{v}_0) + w_2(\mathbf{v}_1 \cdot \mathbf{v}_0) \end{aligned} \tag{3.24}$$

and with $\mathbf{v}_1$

$$\begin{aligned} \mathbf{v}_2 \cdot \mathbf{v}_1 &= (w_1\mathbf{v}_0 + w_2\mathbf{v}_1) \cdot \mathbf{v}_1 \\ &= w_1(\mathbf{v}_0 \cdot \mathbf{v}_1) + w_2(\mathbf{v}_1 \cdot \mathbf{v}_1) \end{aligned} \tag{3.25}$$

Finally the system is then easily solved with Cramer's rule to obtain the w_1, and w_2 values through the following equations:

$$w_1 = \frac{(\mathbf{v}_2 \cdot \mathbf{v}_0)(\mathbf{v}_1 \cdot \mathbf{v}_1) - (\mathbf{v}_1 \cdot \mathbf{v}_0)(\mathbf{v}_2 \cdot \mathbf{v}_1)}{(\mathbf{v}_0 \cdot \mathbf{v}_0)(\mathbf{v}_1 \cdot \mathbf{v}_1) - (\mathbf{v}_1 \cdot \mathbf{v}_0)(\mathbf{v}_0 \cdot \mathbf{v}_1)} \tag{3.26}$$

$$w_2 = \frac{(\mathbf{v}_0 \cdot \mathbf{v}_0)(\mathbf{v}_2 \cdot \mathbf{v}_1) - (\mathbf{v}_2 \cdot \mathbf{v}_0)(\mathbf{v}_0 \cdot \mathbf{v}_1)}{(\mathbf{v}_0 \cdot \mathbf{v}_0)(\mathbf{v}_1 \cdot \mathbf{v}_1) - (\mathbf{v}_1 \cdot \mathbf{v}_0)(\mathbf{v}_0 \cdot \mathbf{v}_1)} \tag{3.27}$$

Therefore by applying ray tracing algorithms between every laser ray vector and all of the model's triangles, the total laser footprint samples on the target model can be generated [71]. But in spite of the fact that this normal approach is simple and straightforward, extensive calculations are required to do it, making it very slow, especially when the model consists of a large number of triangles, scanning with high resolution, or when a large number of laser footprint samples are required.

To overcome these limitations, another approach is proposed. This approach is to evaluate the intersection points only between the vectors and triangles that lie in the same angular range, which leads to a reduction in the calculations and speeds up the process. Figure 3.14 gives a view of the principles used, where the steps in the procedure are presented in the following:

1. The angular extant in terms of azimuth and elevation angular ranges for each triangle is calculated as follows:

   - Azimuth Angular Range: This angular range can be computed by calculating the azimuth angle for each triangle vertices, and comparing these angles with each other two to find the minimum and the maximum values, these represent the azimuth angular range.
   - Elevation Angular Range: The method for calculating this range is similar to the above method, but the calculated elevation angles for the triangle vertices do not always represent the range. Therefore, additional three edge angles (one per triangle edge) are calculated and added to the comparison. Figure 3.15a shows the calculation principle for the edge angle ϕ_l. It starts by finding the line equation for the triangle edge of points $\mathbf{P}_0$ & $\mathbf{P}_1$ (see red line in Figure 3.15a) by:

$$\begin{aligned} \mathbf{P}_l &= \mathbf{P}_0 + l_l(\mathbf{P}_1 - \mathbf{P}_0) \\ \langle x, y, z \rangle &= \langle x_0, y_0, z_0 \rangle + l_l(\langle x_1, y_1, z_1 \rangle - \langle x_0, y_0, z_0 \rangle) \\ \langle x, y, z \rangle &= \langle x_0 + l_l(x_1 - x_0), y_0 + l_l(y_1 - y_0), z_0 + l_l(z_1 - z_0) \rangle \end{aligned} \tag{3.28}$$

     where $\mathbf{P}_l$ is any point in the line of parameter l_l and its elevation angle ϕ_l can be calculated by:

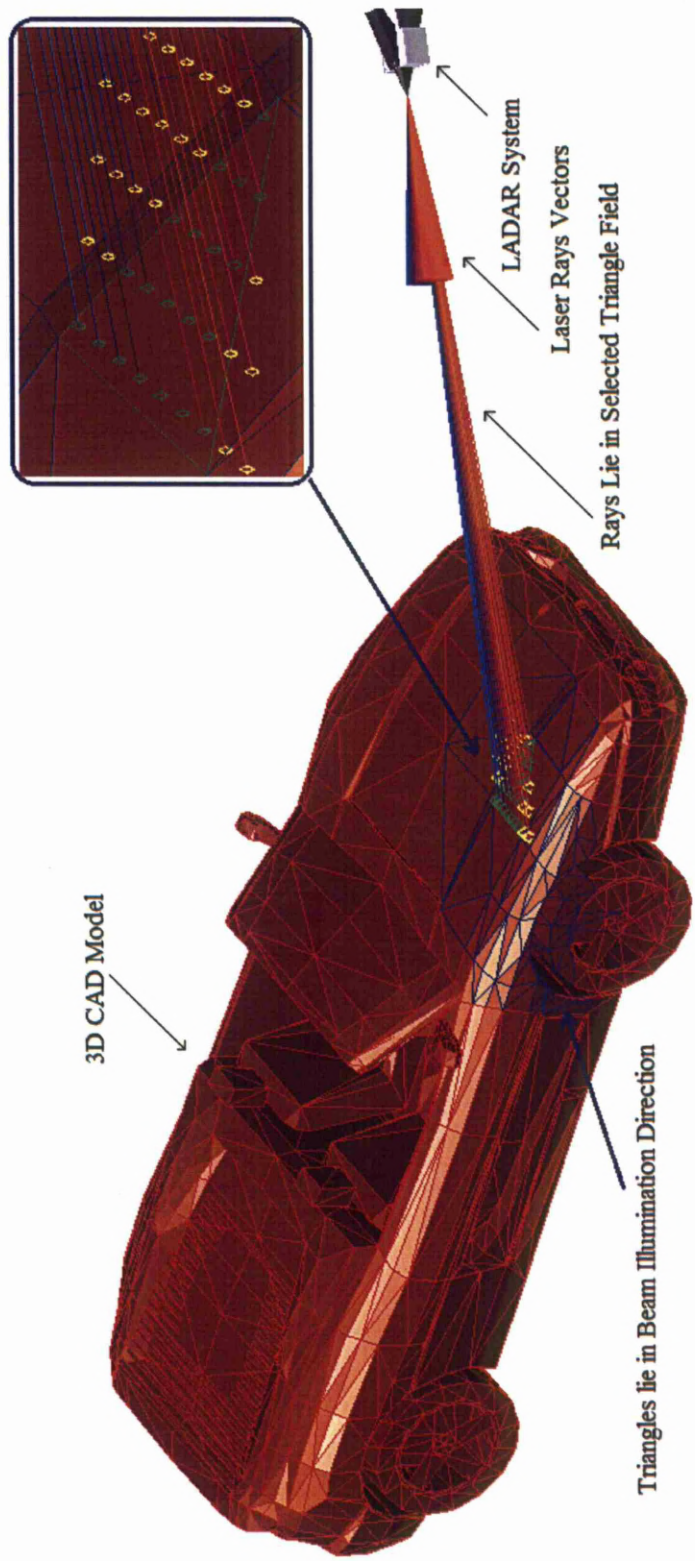

Figure 3.14: LADAR System Scan Car Model with the Proposed Approach.

$$\begin{aligned}\phi_l &= \arctan\frac{z}{\sqrt{x^2+y^2}} \\ &= \arctan\frac{z_0 + l_l(z_1 - z_0)}{\sqrt{(l_l(x_1 - x_0))^2 + (y_0 + l_l(y_1 - y_0))^2}} \end{aligned} \tag{3.29}$$

The first derivative for Equation 3.29 is then taken and solved for zero, in order to find the parameter value l_{rp} at which there is a round point $\mathbf{P}_{rp}$. After the derivation and simplification of the Equation 3.29 it becomes:

$$l_{rp} = \frac{(-z_0 x_0 x_1) - (z_0 y_0 y_1) + (z_1 x_0^2) + (z_1 y_0^2)}{U1 + U2} \tag{3.30}$$

where

$$U1 = (z_0 x_1^2) + (z_0 y_1^2) + (z_1 x_0^2) + (z_1 y_0^2)$$
$$U2 = (z_0 x_0 x_1) - (z_0 y_0 y_1) - (z_1 x_0 x_1) - (z_1 y_0 y_1)$$

If l_{rp} is between 0 and 1 then an additional elevation angle is required and its value can be calculated by substituting l_{rp} value into Equation 3.29. Figure 3.15b shows the vertices elevation angles (at the start and at the end of curve) and the additional edge angle at the round point $\mathbf{P}_{rp}$ (middle red circle).

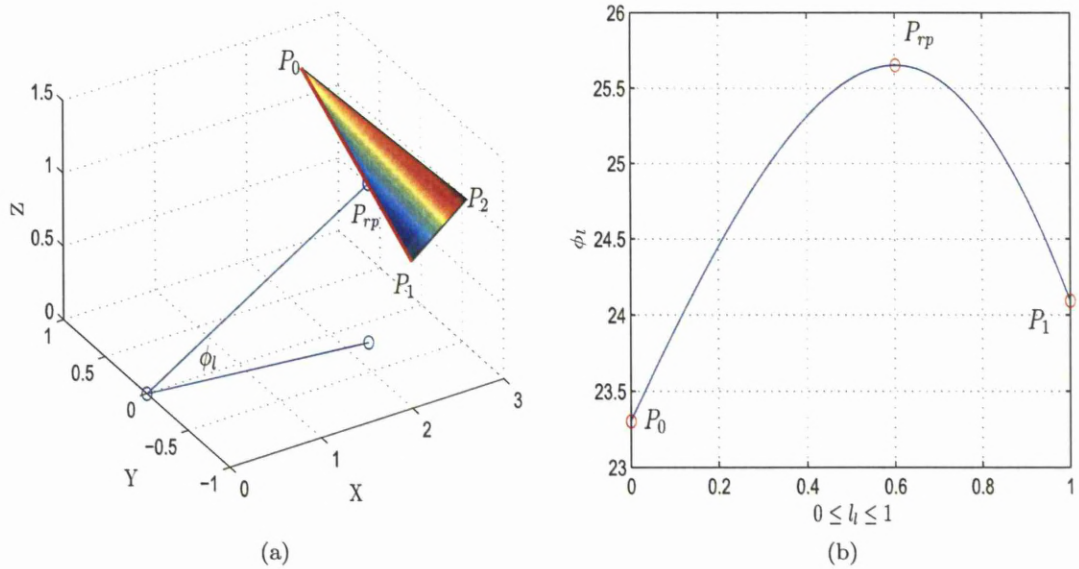

(a) (b)

Figure 3.15: This figure shows: (a) the additional elevation angle ϕ_l for triangle edge (red line) of vertices $\mathbf{P}_0$ & $\mathbf{P}_1$ and (b) the elevation angles values from $\mathbf{P}_0$ to $\mathbf{P}_1$.

2. The laser rays vectors (right side of Figure 3.14) are generated. These vectors are depend on the LADAR viewing direction, laser footprint size, and the number of laser footprint samples.

3. The triangles whose angular extents (calculated in step 1) lie within the laser beam illumination direction, are selected (the blue edges triangles in Figure 3.14).

4. For every selected triangle, the laser rays vectors that lie in the field of that triangle are selected and the intersection points between them are calculated using ray tracing algorithms.

   The up-right side of the Figure 3.14, shows the selected rays that lie in the field of the green edges triangle. It also shows the intersection points on the triangle plane (green & yellow points) and inside the triangle itself (green points).

5. If the laser ray vector lie in the field of more than one triangle, and have intersection point with each one of them, then the point that has the smaller distance to the laser are selected and stored.

The performance of the proposed approach is tested with different triangles and vectors numbers. The testing program starts by scanning a plane target with different laser beams using both approaches (normal and proposed) and calculates the required time to get the intersection points for each individual scan. These laser beams have the same width but they are different with the samples (vectors) number that represent them. The program then increases the number of triangles that represent the target without changing its size and repeats the same procedure again and so on.

The full testing results that represent the effects of changing the triangles and vectors numbers on the execution time for both approaches (normal and proposed) are presented as a 3-D graphs as shown in Figure 3.16. In order to present these effects individually, some selected results are taken from the original 3-D graph and their slopes are also calculated (using a least square method) as shown in Figures 3.17 and 3.18. Figure 3.17 shows the effect of changing the triangles number on the execution time (and its slope) for specific vectors numbers (Vc. No.), and Figure 3.18 shows the effect of changing the vectors number on the execution time (and its slope) for specific triangles numbers (Tr. No.).

The results in 3.16 show that the execution time for the proposed approach is much smaller than the normal approach. The results in Figure 3.17 also show an increment in slopes for both approaches, when the vectors number increases from 49 to 441. The same situation in Figure 3.18 but this time when the triangles number increases from 50 to 800. In general, the normal approach slopes are very large compared to those of the proposed approach, which grows to 55 times larger at Tr. No.=800 in Figure 3.18.

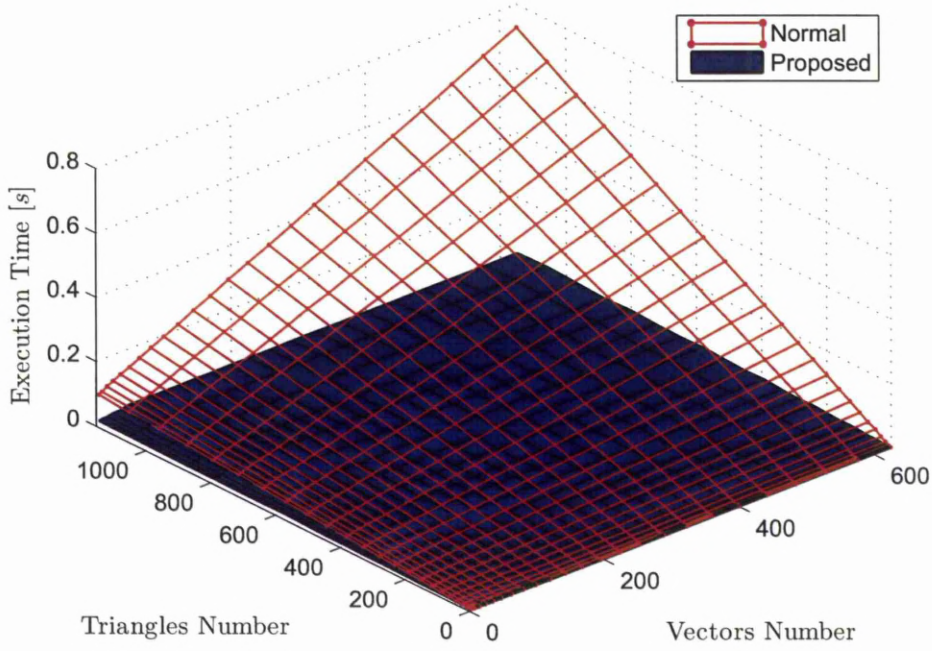

Figure 3.16: Execution Time for Both Approaches Versus the Triangles and Vectors Numbers.

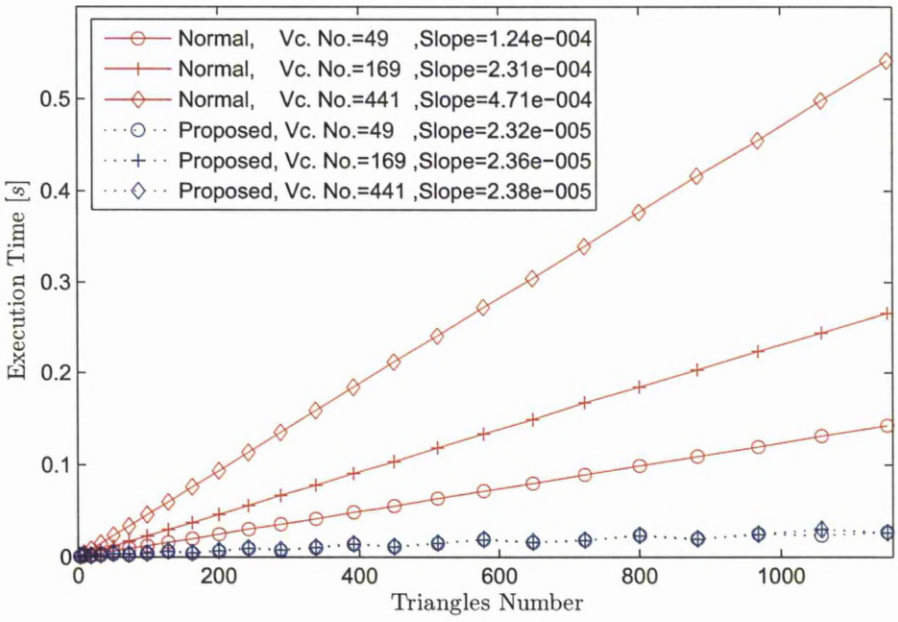

Figure 3.17: Execution Time for Both Approaches Versus the Triangles Number for Specific Vectors Numbers.

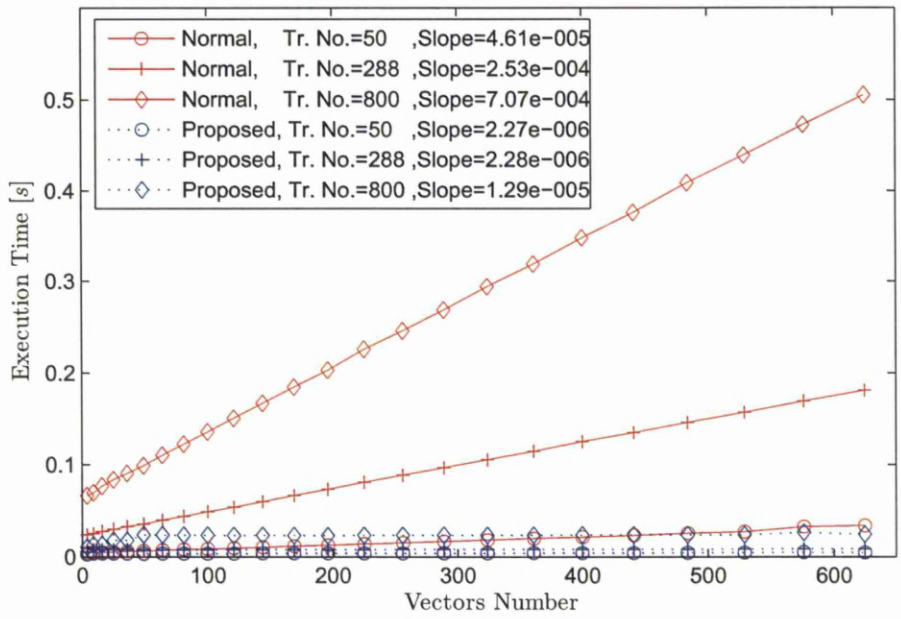

Figure 3.18: Execution Time for Both Approaches Versus the Vectors Number for Specific Triangles Numbers.

3.3 Simulation software

The simulation software is written entirely in Matlab and consists from a tremendous amount of lines of code to produces a simulated LADAR data for the parameters entered through the GUI. The ability of the software to convert the 3D CAD models to matrices of faces and vertices, makes it able to scan different shapes. This types of matrices are compatible with the ray tracing algorithm that previously mentioned (see the triangular faces for the car model shown in Figure 3.14).

In this software the simulated LADAR image is produced by scanning the model with laser pulses, where the main idea is that one laser burst provides one pixel on the LADAR image. The simulation steps for the LADAR simulator are presented as follows:

1. The required simulation parameters are defined, these parameters concerning the: LADAR (viewing direction, field of view, and scanning resolution), laser source (temporal and spatial domains), atmosphere, target, noise and receiver.

2. For every laser burst, the laser pulse in time $p(t)$ and the beam footprint illuminate the target surface $I(H_{ls}, V_{ls}, R_{ls})$ are created using Equations 3.3 and 3.6 respectively.

3. The reflected power reaching the receiver from each sample in the laser footprint

and the corresponding round-trip time i, are calculated to obtained the reflected sample power P_i^{sample}. The round-trip time is calculated from applying the proposed Ray Tracing procedure, while the sample reflected power is calculated from the LADAR range Equation 3.18.

4. The reflected sample powers P_i^{sample} are summed with the same time indices i to create the target impulse response h_{tr}.

$$h_{tr}(i) = \sum_{i=i} P_i^{sample} \tag{3.31}$$

5. The target impulse response is convolved with the temporal laser pulse $p(t)$ to calculate the temporal reflected power signal arriving at the detector.

$$P_r(t) = h_{tr}(i) * p(t) \tag{3.32}$$

6. The resultant power signal is converted to photoelectrons using Equations 3.12 and 3.13. And the background, photon counting, and speckle noise are then applied if they enabled by the user.

7. The target range value is calculated by applying the *CFD* peak detector and the corresponding procedure of range calculation mentioned in subsection 3.1.1 on page 11.

8. Finally the calculated range value is assigned to the corresponding pixel on the LADAR image.

3.4 GUI Control Panels

Two GUI windows are designed for the simulator, the main and the sub windows. They appear directly after running the simulator. The main window shown in Figure 3.19, contains the panels that are required to set the scan parameters and display the results, while the second window shown in Figure 3.20 is used to adjust the position and orientation for both the LADAR and the model (model size also can be adjust in this window).

The simulator panels located in both the main and the sub windows are:

- Visualization Panels
- CAD Model Panel
- Model and LADAR Panels
- LADAR Parameters Panel
- Scanning Panel
- Output Panel
- Multi Views Panel

Figure 3.19: LADAR Simulator Main Window.

Figure 3.20: LADAR Simulator Sub Window.

3.4.1 Visualization Panels

Two visualization panels were designed for this simulator. The first panel is located in the main window and contains one screen to display the results, text box to display the current set value, and push button to enable the user to rotate the graph in three dimensions. The second panel is located in the second window and contains four screens to display the scene (LADAR plus the model) in four different views (top, front, left, and user-selected view). It also has a text box and push button similar to the first panel to perform the same purpose.

3.4.2 CAD Model Panel

This panel deals with the CAD models that are stored in the simulator folder and contains five push buttons, which are:

- Convert CAD to Patches Button: This button is used to convert all the CAD models from the Stereolithography (*.stl) file format to a matrices of faces (patches) and vertices.
- Add and Remove Buttons: After typing the model number in the editable text field. The model can be added to scene or removed from it by pressing add or remove buttons respectively. When the model is added, it is displayed in four different views by the second window visualization panel.
- Save and Load Buttons: These two buttons used to save and load the selected model after adjusting its parameters like size, position, and orientation.

3.4.3 Model and LADAR Panels

These panels are used to adjust the orientations (around x,y,z axis) and the positions (translation in x,y,z directions) for the LADAR system and the selected model before performing the scanning process. Adjusting the orientation or the position is undertaken by moving the sliding bars (which are three one for each axis) to the left or to the right. The output value that results from each bar depends on the bar value (location) and the editable texts values that corresponding to it.

If the first and the second editable texts values are $ed1$ and $ed2$ respectively and the slider value (location) is slv (which is varied between [0 and 1]), then the output value is calculated by the following equation:

$$OutputValue = ed1 + slv \times (ed2 - ed1) \tag{3.33}$$

Another three sliding bars are added to the model panel to enable the size adjustment for the elected model in the x, y, and z dimensions.

3.4.4 LADAR Parameters Panel

This panel is used for adjusting the scanning parameters that related to the LADAR components (scanner, transmitter, and receiver), target, and atmosphere. Setting these parameter is done by typing their values in the corresponding editable texts. Table 3.1 presents these parameters and their default values.

Table 3.1: LADAR Scanning Parameters.

Parameters	Default Values
Scanner	
Pan Angles	
Initial Angle	33.75^o
Final Angle	-33.75^o
Resolution	0.002^o
Tilt Angles	
Initial Angle	33.75^o
Final Angle	-33.75^o
Resolution	0.002^o
Transmitter	
Temporal Domain	
Laser Pulse Energy	$1 \times 10^{-3}\, J$
Laser Pulse Width	$4.7 \times 10^{-9}\, s$
Temporal Sampling Factor	10
Spatial Domain	
Beam Waist at Origin	$9 \times 10^{-3}\, m$
Laser Beam Wavelength	$1.55 \times 10^{-6}\, m$
Spatial Sampling Factor	10
Receiver	
Dark Current	$0.75 \times 10^{-9}\, A$
Aperture Diameter	$0.075\, m$
Detector Quantum Efficiency	0.3
Receiver Optical Transmission	1
Optical Filter Bandwidth	$0.001\, \mu m$
Attenuation	
Target Reflectivity	0.1
Atmospheric Transmission	$0.1 \times 10^{-3}\, m^{-1}$
Background Light Intensity	$1000\, W/(m^2\, \mu m)$

After setting these parameters the simulator calculates the laser beam parameters (Rayleigh range [RY-Range], beam extent at Rayleigh range [RY-Extant], and full divergence angle [DIV-Angle] in *mrad*) and the threshold value, and displays them in the corresponding text boxes.

In this panel the noise type and its parameter can also be adjusted. The pop-up menu shown in Figure 3.21 is used to select the noise type, while the parameter value is set by the corresponding editable text. The default value for the coherent parameter M_{CH} (related to the photon counting and speckle noise) is equal to 100.

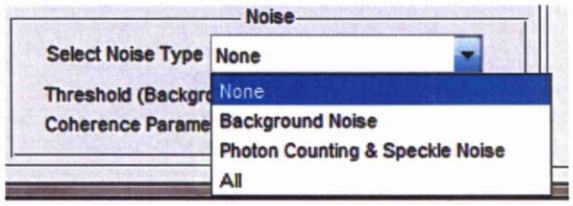

Figure 3.21: Pop-up Menu for the Selecting Noise Type.

3.4.5 Scanning Panel

Pressing the scan button in this panel, make the simulator start to perform the scanning process. This process depends on the panels parameters that were previously adjusted and the scanning modes, which are:

- Current Model - Single View (Default Mode): The simulator will scan the selected model from the view that was previously adjusted by the LADAR and model panels.
- Current Model - Multi Views : Instead of single view the simulator will scan the selected model from multiple view depending on the multi views panel values (The model panel orientation values will be disabled in this mode).
- All Models - Single View : It is the same as the first mode but instead of single, multi models will be scanned from a specified view.
- All Models - Multi Views : It is the same as the second mode but instead of single, multiple models will be scanned from multiple views.

During the scanning process, the simulator creates a folder for each scanned model to save the resultant model view or views (depending on the scanning mode). This will lead to create single folder for the modes that scanned single model and multi folders for the modes that deals with multi models. Figure 3.22 shows the pop-up menu that is used to select these modes, which displayed as a list of choices.

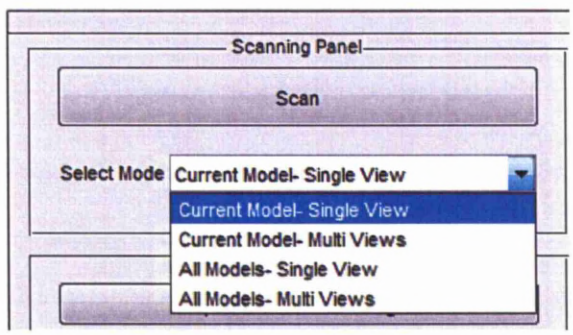

Figure 3.22: Pop-up Menu for the Scanning Panel.

3.4.6 Output Panel

The simulator is designed to be able to display the results after the scanning process in four different formats, one in spherical coordinates (spherical image) and the other three in Cartesian coordinates (point cloud, surfaces, and laser beams intersection spots with the model surface). Selecting these formats can be performed by using the following buttons:

- Spherical LADAR 2D Image Button: This button is used to display the spherical coordinates for the laser spots that reaches the model surface, as a 2D representation called spherical image (see Figure 3.23a). In spherical image the horizontal and vertical pixel locations are represent the location of the laser spot in pan and tilt angles (in radians) respectively, while the pixel color represents the distance from the LADAR system to the laser spot.
- LADAR 3D Image (Point Cloud) Button: Pressing this button will make the simulator display the laser spots as an individual points in the 3D Cartesian coordinates with out connecting them. These points called point cloud and shown in Figure 3.23b.
- LADAR 3D Image (Surfaces) Button: This button performs the same function as the previous one, but instead of displaying the point cloud individually it connects them with triangles surfaces. This leads to an enhanced appearance of the resultant data as shown in Figure 3.23c.
- Collision Laser Spots Button. Pressing this button will make the simulator display both the laser spots and the model surface in one figure, as shown in Figure 3.23d.

The number of the images that are display for each type is depend on the scanning mode. If the selecting mode deals with multi models or views or both, then more than on image will display for each type.

3.4.7 Multi Views Panel

As mentioned before the parameters for this panel will be used only when the multi views modes are selected. It contains three editable texts, two to set the initial and final angles and the third for the angular resolution. After setting these angles the simulator rotates the model around its vertical axis with angle equal to the initial angle value and scans the model.

The same procedure is then repeated with an increment in the angular view equal to the angular resolution value, and so on until reaching final angle value. Figure 3.24 shows the simulation results of scanning car model at different views, where the angular resolution and both the initial and final angles values are equal to 45^o, 0^o, 315^o respectively.

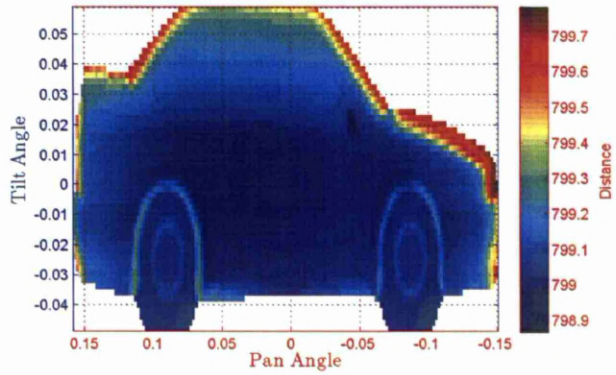

(a)

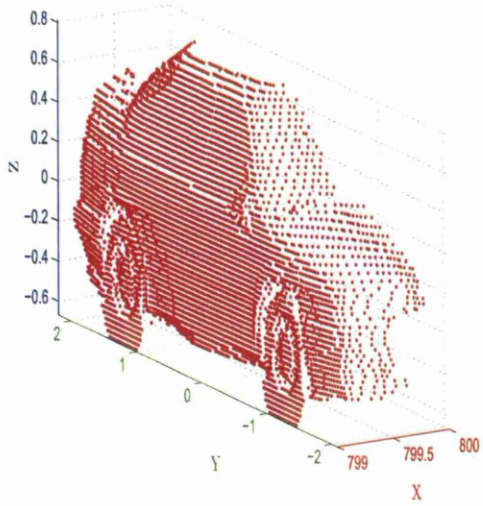

(b)

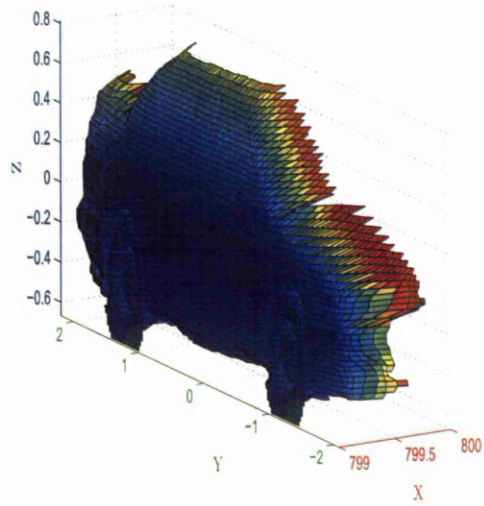

(c)

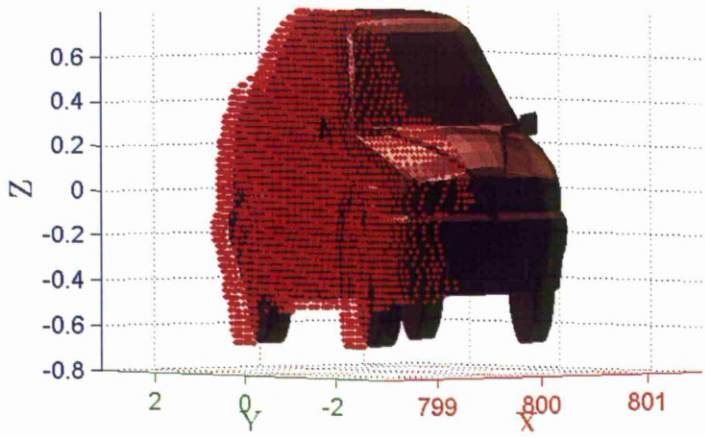

(d)

Figure 3.23: The Simulation Results of Scanning the Car Model (shown in Figure 3.20) with the Scanning Parameters (shown in Figure 3.19) in Four Different Formats: (a) Spherical, (b) Point Cloud, (c) Surfaces, and (d) Collision Laser Spots.

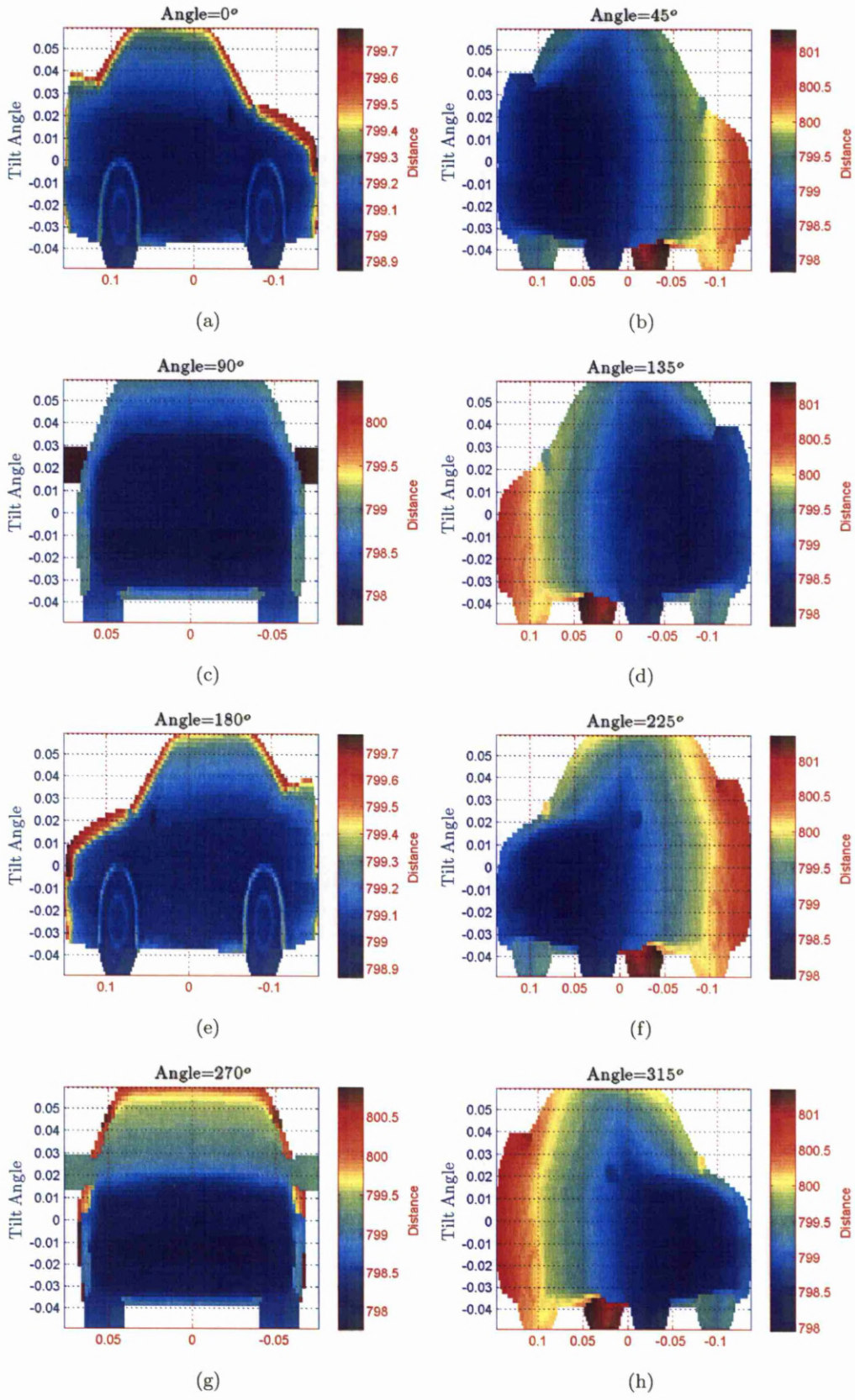

Figure 3.24: Spherical Images for the Model of Figure 3.20 at Different Views.

3.5 Simulation Results

This section presents some selected simulation results that show the effect of changing the scanning parameters on the resultant LADAR image. These parameters are noise type and its strength, scanning resolution, and the laser beam width. To facilitate the interpretations of the parameters effect on the LADAR image, one parameter is changed at a time. Where all the figures that presented in this section are based on the original model and parameters shown in Figures 3.20 and 3.19 respectively. In order to give a clear observation for the effect of changing the scanning parameters, the figures are displayed in surface format.

3.5.1 Noise and its Strength

The resultant LADAR images in the presence of background, photon counting, and speckles noise are presented in the following: Figures 3.25b and 3.26a show the effect of background noise and photo counting noise on the LADAR image respectively, while Figure 3.26b shows the effect of both photo counting and speckle noise. For comparison purpose, the original LADAR image (without noise) is also presented (see Figure 3.25a).

The LADAR images in these figures show, very small distortion effect for the background noise comparing with the other two noise types. Regarding to the photo counting and speckle noise, the figures show a low distortion effect during the dominance of photo counting noise, but in the presence of speckle noise this distortion become larger.

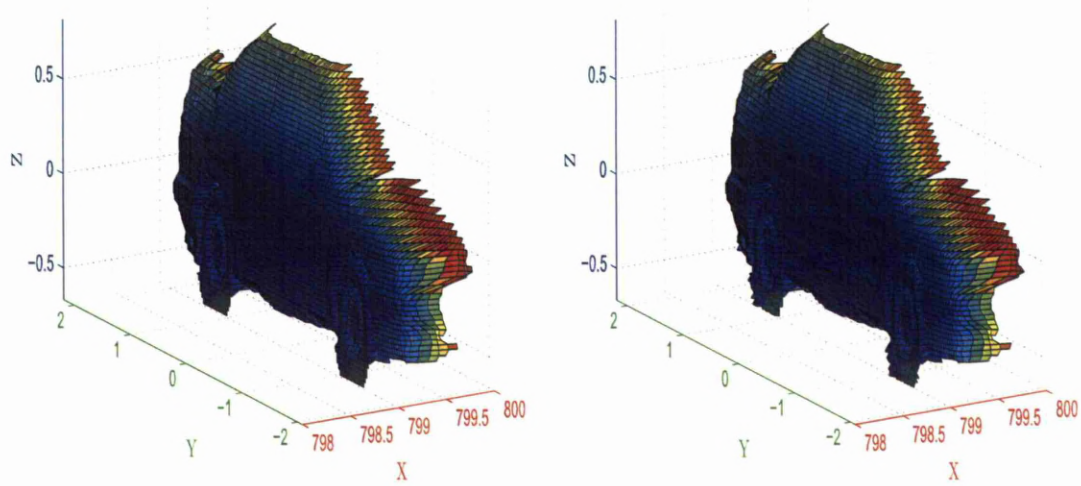

(a) (b)

Figure 3.25: LADAR Image Before (a) and After Applying Background Noise (b).

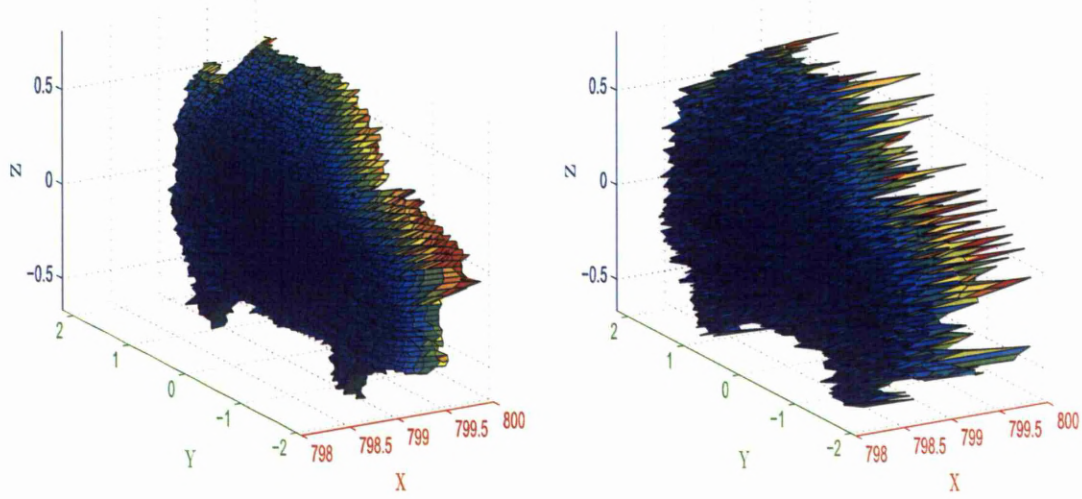

Figure 3.26: Effect of (a) Photon Counting ($M_{CH} = 100$) and (b) Both Photon Counting and Speckle Noise ($M_{CH} = 1$) on the LADAR Image.

3.5.2 Scanning Resolution

One of the most important parameter in the LADAR scanner is the scanning resolution. The effect of decreasing the scanning resolution from 0.002^o to 0.005^o is shown in Figure 3.27a and Figure 3.27b respectively. These figures show that, the separation between the laser pulses that hit the target surface increases when the resolution decrease from 0.002^o to 0.005^o. This separation is represented by the triangles area (in surface image the triangles shapes are used to connect the points that represent the location of the laser pulses intersection with the target surface). Therefore, large separation between these points produces large triangles area and vice versa. The figures also show a details reduction in the low scanning resolution image.

3.5.3 Laser Beam Width

The width of the laser beam can be modified by adjusting the beam waist at the origin and the laser wavelength. Figures 3.28a and 3.28b show the results of scanning the car model with two different beam widths. These widths are larger than the original width, which is equal to $0.0439\,m$.

The results in these figures show a large decay in the edges details with increasing the beam width. The reason behind that is come from the fact that, the laser beam of large width has a large footprint on the target surface, which increase the size of the minimum area that distinguish by the LADAR (i.e. decrease the resolution and lose the details).

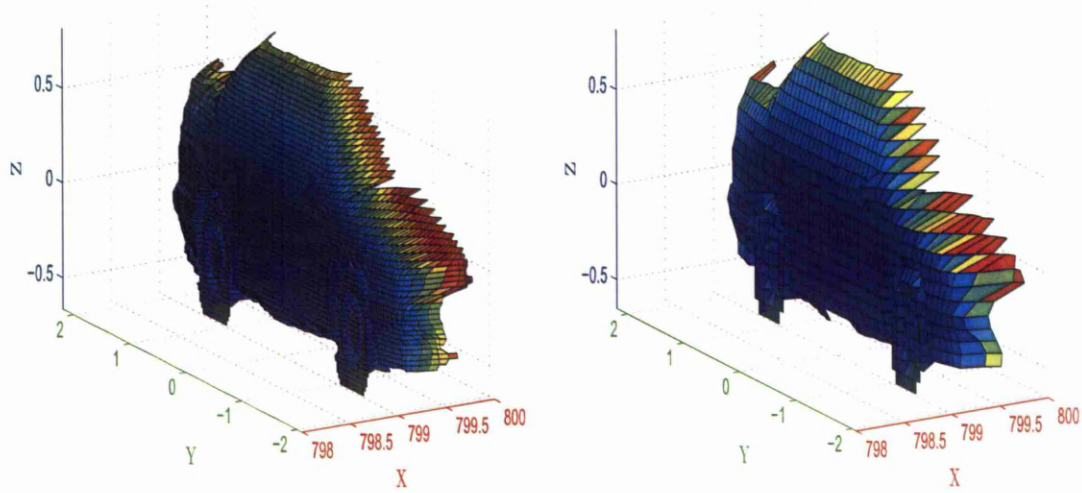

(a) (b)

Figure 3.27: Effect of Scanning Resolution on the LADAR Image: (a) Resolution $= 0.002^o$, (b) Resolution $= 0.005^o$.

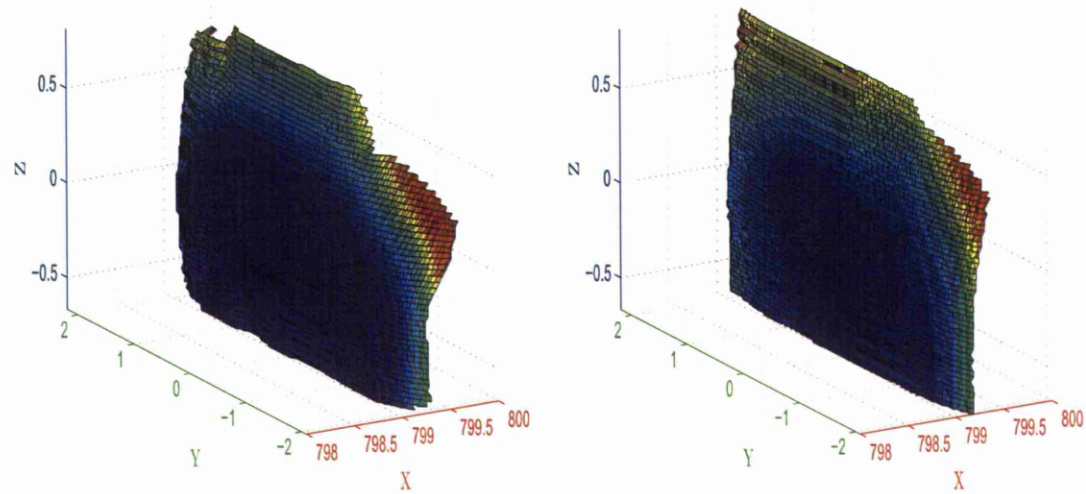

(a) (b)

Figure 3.28: Effect of Beam Width on the LADAR Image: (a) Width $= 0.1974\,m$, (b) Width $= 0.3947\,m$.

3.6 Summary

LADAR simulator software has been written to produce a simulated LADAR data under a wide variety of conditions by modeling each stage from the laser source to the data generation. The theory of propagation the laser beam and the ray tracing algorithms which they represent the core of the LADAR simulator are presented. In order to allow the simulator to deal with more complex models and produces high resolution image at short execution time, another approach for calculating the intersection points of the rays vectors that represent the laser beam is proposed and described. The performance of this proposed approach is tested with different triangles and vectors numbers and the comparison of results shows that the proposed approach produces less execution time than the previous approach especially when the model consists of a large number of triangles, scanning with high resolution, or when a large number of laser footprint samples are required. The simulation steps for the LADAR simulator and its GUI are also presented with some selected results that show the effect of changing the scanning parameters (noise type and its strength, scanning resolution, and the laser beam width) on the resultant LADAR image. The simulation results also show the ability of the simulator to simulate the phenomena that related to the scanning process and produces LADAR images under a wide variety of conditions.

Chapter 4

LADAR System Setup

Introduction

This chapter describes the LADAR system and associated software that have been designed and implemented to capture the 3D LADAR data from the surfaces of various objects and recognise them using the chromatic methodologies. The chapter consists from four sections. The first section presents the system architecture while the hardware and the software implementations will be presented in the second and the third sections respectively. The last section presents the summary for this chapter.

4.1 System Architecture

The LADAR system is designed to have a large field of view. It can reach up to $+/-159^o$ in pan direction and -47^o to $+31^o$ in the tilt direction, and it is able to scan the objects with an angular resolution of 0.0265^o at a scanning speed equal to 714 angular positions per second (in both pan and tilt directions).

The hardware architecture for the LADAR system is shown in Figure 4.1, and it consists of:

- AccuRange 4000-LV Laser Distance Measurement Sensor: This sensor responsible for measures the distance values of the object surface from its location and sends these values to the computer via a serial port. This sensor provides only one dimension for the scanned object, because it measures the distance to a single point on the surface of that object.

- Computer Controlled Pan-Tilt Unit D46-17 with its controller: The pan-tilt unit is responsible for acquiring the other two object dimensions, by positioning the laser sensor in both pan and tilt directions. The controller is used to handle the precise motion control for this unit according to computer commands.

- Two Power Supplies: One for the laser sensor and the other for the pan-tilt unit and its controller, where these power supplies are different in their output power.

- Microsoft LifeCam VX-1000: This colour camera is used to provide the images for the scene on the computer screen
- Computer System **SONY *VAIO*** EB2MOE: The last part of the LADAR system, which provides a platform for the LADAR control software that has been written to generate and recognise the resultant 3D object image.

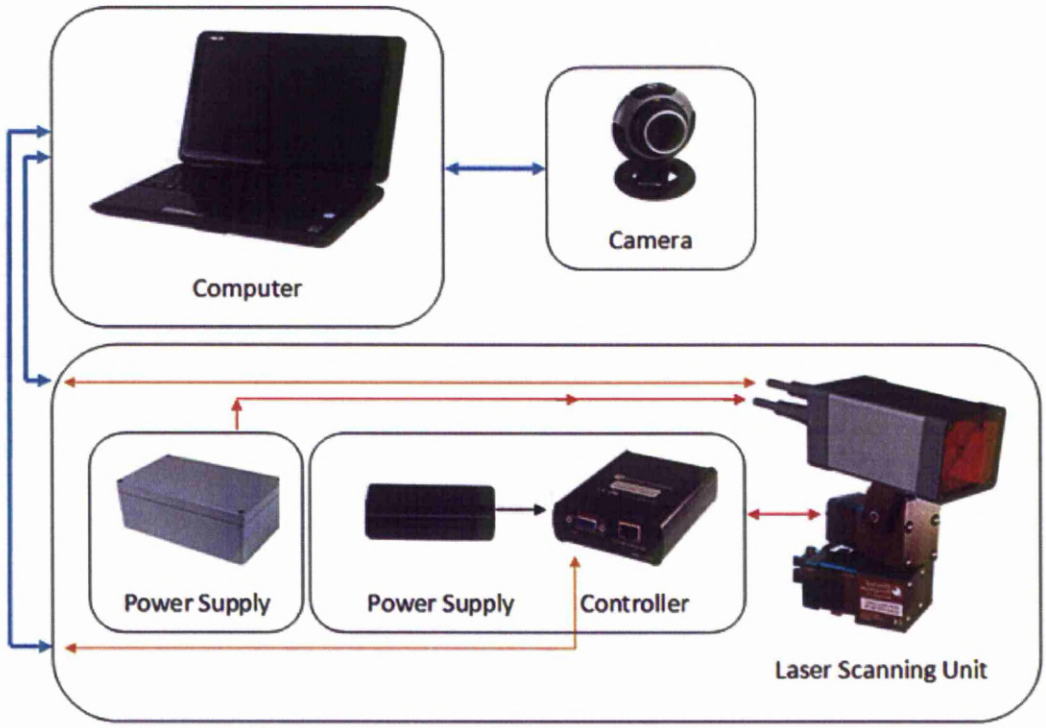

Figure 4.1: Schematic of the LADAR Hardware Architecture.

For the LADAR system construction, the sensing head is mounting with the pan and tilt motors to varies the angular position of the head with pan $\theta_M \in [-159^o, 159^o]$, and tilt $\phi_M \in [-47^o, 31^o]$ angles. This type of mounting required a special LADAR measurement model to reconstruct the LADAR images from the distance measurements that generated by the laser sensor.

The LADAR measurement model starts by defining a spherical coordinate system whose origin is the point O shown in Figure 4.2. It is then models the scene as a spherical range image (ρ, θ, ϕ) with respect to this point, where ρ is the distance to point $\mathbf{P} = \langle x, y, z \rangle$ on the object surface at azimuth angle θ and elevation angle ϕ. For each (θ, ϕ) position, the sensor emits pulses of visible-red laser light that either reflect off a scene surface and generate a range measurement or there is no measurement generated. There are a number of reasons that the measurement could be defected such as absorption of the radiation (dark surfaces), no reflection (out-of-range surfaces), or insufficient energy has been reflected back to the sensor (specular/translucent surfaces).

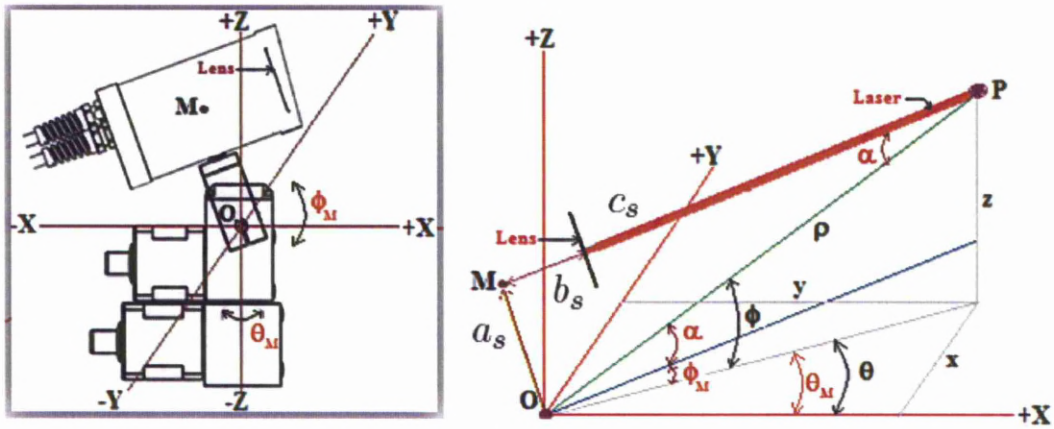

Figure 4.2: Parameters of the LADAR Measurement Model.

The mathematical model then defines a relation between the parameters at which the point **P** is measured (distance from the sensor lens c_s, pan angle θ_M, and tilt ϕ_M) and the spherical coordinates (ρ, θ, ϕ) parameters that represents this point. This is necessary because of the offset introduced by the sensing head mounting. The implication is that the sensing head is no longer at the origin O, which makes the measured distance value c_s and the tilt motor angle ϕ_M not related directly to the ρ and ϕ respectively in spherical coordinate system. Referring to Figure 4.2, the relationships are given by the following equations:

$$\rho = \sqrt[2]{(b_s + c_s)^2 + a_s^2} \tag{4.1}$$

$$\theta = \theta_M \tag{4.2}$$

$$\phi = \phi_M + \alpha \tag{4.3}$$

where

α: is equal to $\arctan[a_s/(b_s + c_s)]$.

a_s: Distance between O and the sensing head centre point M.

b_s: Distance between M and the start location for the measured value c_s.

In this system, a_s and b_s are equal to $90\,mm$ and $95\,mm$ respectively. The conversion from the spherical to Cartesian coordinates is defined by the following equations:

$$x = \rho \cos\phi \cos\theta \tag{4.4}$$

$$y = \rho \cos\phi \sin\theta \tag{4.5}$$

$$z = \rho \sin\phi \tag{4.6}$$

Figure 4.3 shows a photo for LADAR scanning system.

Figure 4.3: LADAR Scanning System.

4.2 Hardware Implementation

This section describes the detail of the hardware used in the LADAR system, including AccuRange 4000-LV laser distance measurement sensor, computer controlled pan-tilt unit D46-17 with its controller, colour camera, and the computer system.

4.2.1 AccuRange 4000-LV Laser Distance Measurement Sensor

4.2.1.1 General Description

The AccuRange 4000-LV is a unique laser distance measurement sensor. It uses a modified time-of-flight measurement principle (patented in 1994 [72]) that leads to ultra fast (up to 200,000 sample/s) and accurate ($7.5\,mm$) distance measurements [73]. The sensor has a working range of zero to $12.2\,m$ on 85% diffuse reflectance surfaces with a resolution equal to $0.32\,mm$ [73], [74]. The figure below shows a photo of an AccuRange laser sensor.

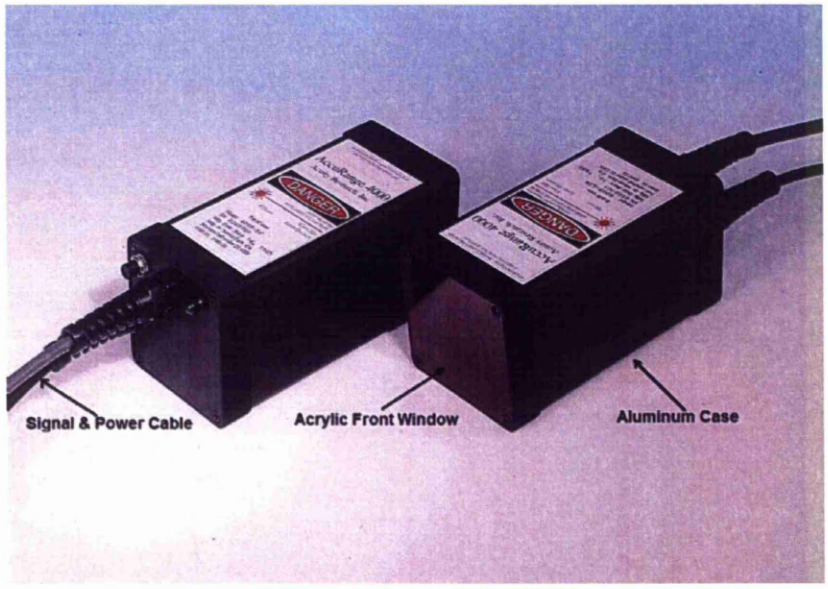

Figure 4.4: AccuRange 4000-LV Laser Distance Measurement Sensor.

The AccuRange 4000-LV is a Class IIIa laser product. It uses a laser diode as an optical source, which emits a visible laser beam at a wavelength equal to $670\,nm$ with $5\,mW$ optical power. The beam leaves the aperture with a spot size of $2.5\,mm$ and a divergence equal to $0.5\,mrad$ [73].

This sensor is differs from other laser distance measurement sensors in that the laser emitter and return signal collection lens are concentric [74], which has the advantage of permitting measurements into narrow opening. Further information about Acuity AR4000 laser sensor is given in Appendix A on page 145 and its technical specifications are summarised in Table 4.1.

Table 4.1: Technical Specifications of AccuRange 4000-LV sensor [73], [75].

Laser Type	$670\,nm$, Visible Laser Diode
Laser Power	$5\,mW$ Maximum, Class IIIa
Range	0 to $12.2\,m$
Resolution	$0.32\,mm$
Standard Deviation Between 22 Calibration Points	$7.5\,mm$
Laser Spot Size	$2.5\,mm$, $0.5\,mrad$ Divergence
Collection Aperture	$63.5\,mm$ Diameter Lens
Weight	$0.625\,kg$
Maximum Sampling rates	$200,000\,Hz$ with optional High Speed Interface Card
Power	Sensor Requires $5-6$ volts DC ($400\,mA$ at $5\,V$) Heater Requires $4.5-7$ volts DC ($4\,A$ max)

4.2.1.2 Principle of Operation

AccuRange 4000-LV sensor uses a patented rangefinding technique to measure the distance to the target [72]. This technique generates a frequency based on range by creating an oscillator with a laser source and the photodetector after the light has traveled to a certain distance. Figure 4.5 shows the schematic diagram of the sensor and the light paths through its optical components and detection and triggering circuits.

Referring to Figure 4.5, the laser diode is controlled by a modulator to produce a laser light at two different intensities. This light is collimated into a beam by collimating optics and emitted from the centre of the front face of the sensor to the target. The reflected light from that target is collected by a Fresnel lens and focused onto an avalanche photodiode. The photodiode signal is amplified up to a limited level by the amplifier and inverted by the inverter.

The resultant signal is a logic level 1 or 0 and is input to the modulator to drives the laser diode. This configuration forms an oscillator, with the laser switching itself on and off using its own signal. The time that the light takes to travel to the target and return plus the propagation time through the electronics t_e from the photodiode to the laser diode determines the period of oscillation t_o (1 / rate at which the laser is switched on and off). This period can be expressed as [72]:

$$t_o = 2t_e + 4c_s/c \tag{4.7}$$

where c_s is the distance from the sensor to the target, and c is the speed of light value. The input and the output optical signals received by and generated by the sensor as a function of time are shown in Figure 4.6.

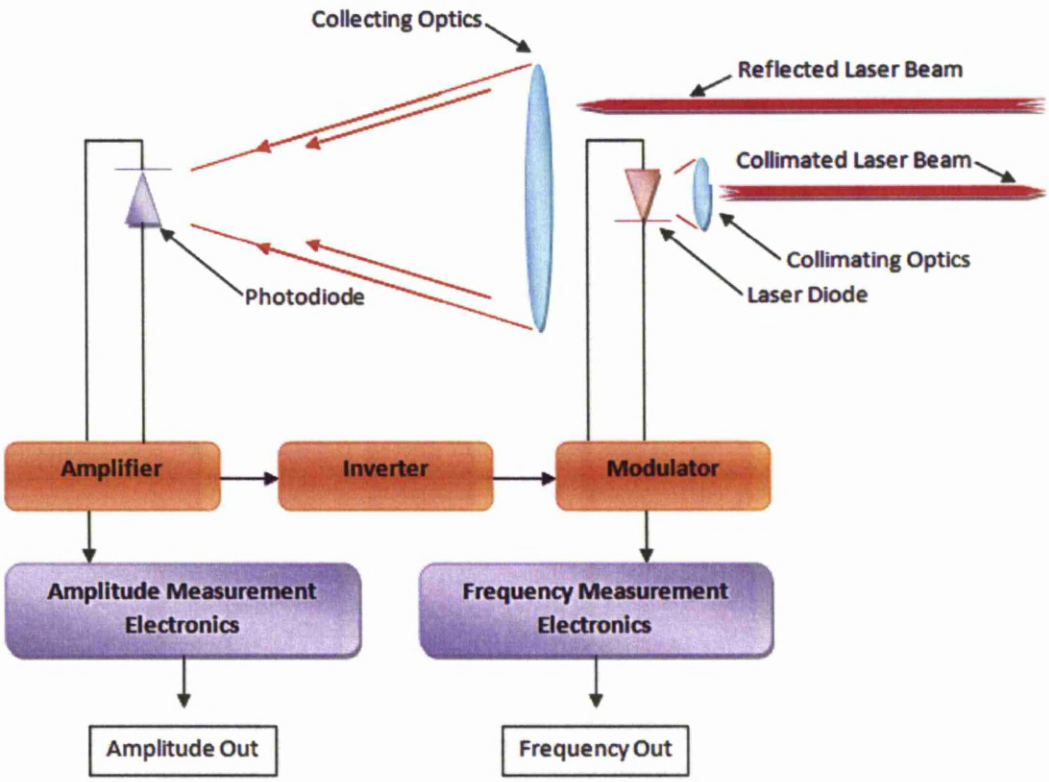

Figure 4.5: The schematic diagram of the Laser Distance Measurement Sensor [72].

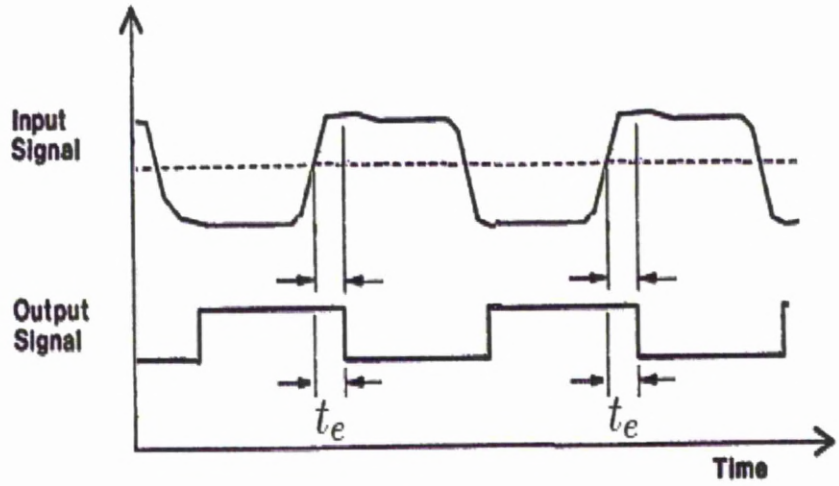

Figure 4.6: Input and Output Optical Signals Received by and Generated by the Sensor.

The oscillation period is measured by frequency measurement circuitry, which counts a fixed number of oscillation cycles and times the interval taken. The measurement is somewhat nonlinear and dependent on signal strength (which is measured by amplitude measurement electronics) and temperature, so a calibration process is performed in the sensor to remove these effects.

The advantages of using this techniques to measure the distance are [72]:

- Higher resolution than the phase measurement method, due to the timers being more accurate than phase detectors.
- Range ambiguity problem that plague phase comparison methods is absent in this technique, where the maximum range is only limited by the power of the light source and the reflectivity of the target.
- By measuring the time required for multiple oscillations the distance can be measured more accurately than if a single pulse of energy is timed.
- The binary switching used in this technique makes it less sensitive to the noise and more immune to errors induced by low intensity return signals from for example dust particles in the beam path. This is due to the small fluctuations in the incoming signal will not cause a transition of the output state.

4.2.1.3 Sensor Output

The AccuRange 4000-LV output can be selected to either calibrated distance readings (readings after removing the nonlinearity, signal strength, and temperature effects by a special calibration process performed in the sensor), un-calibrated sensor data, or both together in each sample. Data is transmitted as 8 data bits with no parity bit and 1 stop bit and sent in American Standard Code for Information Interchange (ASCII) or binary format. The sensor configuration is done via commands sent over the serial port, which are ASCII commands that entered under computer control. The sensor is able to produces calibrated range readings at a sample rate reach to 714 samples per second through the RS-232 serial port [75]. If higher rates is required (up to $200,000\,Hz$) then, the un-calibrated sensor output must be used with the PCI interface card. More details about the sensor data format and commands set are found in Appendix (A.5, A.6) on page 149.

The AccuRange 4000-LV is set to transmit data via the RS-232 serial port as calibrated range measurements and with a sampling rate equal to $714\,sample/s$. This rate is limited by the time required to transmit each sample at the specified baud rate. Therefore, to allow the sensor to transmit the data at this rate, the sensor transmission baud rate is set to the maximum, which is equal to $38400\,bit/s$ and the data format is set to binary. The reason behind selecting the binary instead of ASCII format is, the binary format required only three bytes to represent the measurement (two distance bytes representing the range in mm followed by one byte with a value FF Hex for framing). This makes the time required to transmit each sample at maximum baud rate smaller than the sample time, while the ASCII format required from six to eight bytes and more transmission time (larger than the sample time).

4.2.2 Computer Controlled Pan-Tilt Unit D46-17

This unit is fully computer controlled and has programmable speed, acceleration, power, and other parameters. It is used to position the laser distance measurement sensor in both pan and tilt directions. The load capacity for this unit is reached to $2.72\,kg$ and it's capable of moving in both pan and tilt directions at a speed reached to 300^o/second, with a maximum angular resolution of 0.013^o [76].

The pan-tilt unit is connected to the pan-tilt controller, which handles precise kinematic motion control according to user-set parameters. This controller accepts ASCII and binary command formats via RS-232 from a host computer, and drives the pan-tilt unit to a new position with a certain speed and acceleration. The data is transmitted as an 8 data bit with 1 stop bit and no parity bit at a baud rate equal to $38400\,bit/s$. Figure 4.7 shows a photo for the pan-tilt unit (left) with its controller (right) and the unit structure is shown in Figure 4.8.

Figure 4.7: Pan-Tilt Unit (left side) with its Controller (right side).

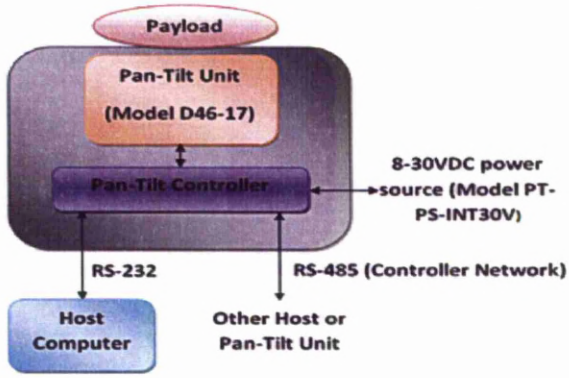

Figure 4.8: Structure of Pan-Tilt Unit [77].

A pan-tilt unit AC/DC power supply is used to supply the unit and its controller with a DC voltage of $30\,V$. This voltage represent the highest motor voltage within the

allowable range (12 – 30 VDC) by which the highest pan / tilt performance can be achieve. The pan-tilt unit calibrates itself automatically on power-up using an internal precision limit detection system. During the calibration process the unit explores the full range of motion in both axes [78]. Figure 4.9 shows the range of motion limits in both pan and tilt directions. Further information about the pan-tilt unit D46-17 is given in Appendix B on page 152 and its technical specifications are summarised in Table 4.2.

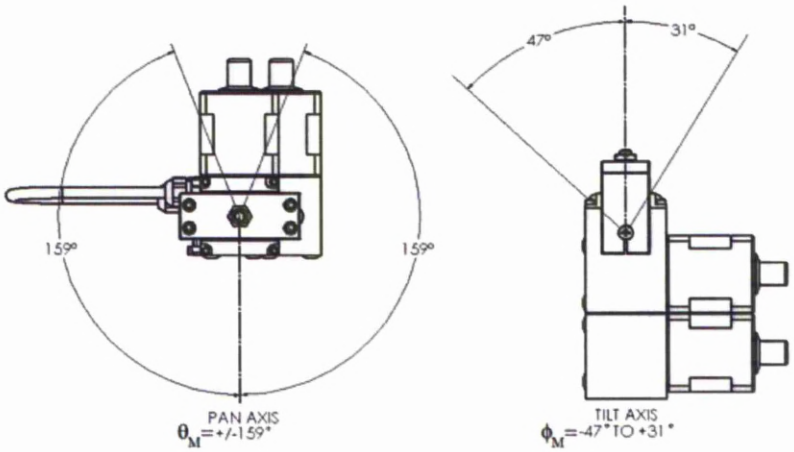

Figure 4.9: Range of Motion Limits for Pan-Tilt Unit [78].

Table 4.2: Technical Specifications of Precision Pan-Tilt Unit D46-17 [76]

Rated Payload	$2.72\,kg$
Maximum Speed	$300^o/s$
Resolution	0.0529^o, 0.0265^o, 0.0132^o
Tilt Range	-47^o to $+31^o$
Pan Range	$+/-159^o$
Input Voltage	12 – 30 VDC
Pan-Tilt Unit Weight	$1.361\,kg$
Controller Weight	$0.23\,kg$

The pan-tilt unit is programmed to position the laser beam over a target surface using a raster scanning pattern (row by row) and with a scanning speed equal to $714\,positions/s$ in both pan and tilt directions. Selecting this value to be the same as the laser sensor sampling rate (714 sample/s), makes the LADAR system capable of producing range measurement for each new position. To guarantee regular (equal) time intervals between each position, the base speeds (in pan and tilt directions) are set to be equal to the scanning speeds.

The motion resolution for the controller is set to 0.0265^o. This available resolution produces fast and smooth positioning for the laser sensor (i.e. moving from one position to another without losing synchronization).

4.2.3 Microsoft LifeCam VX-1000

This camera consists of a CMOS optical array of $640\,(H) \times 480\,(V)$ pixels on which optical signals from distant objects are focused using a lens of 55^o diagonal field of view. The output from this optical array is processed by the embedded electronics before the signal is fed to the computer via the USB (Universal Serial Bus) port.

The camera is used with the LADAR unit to provide the computer with scanned scene images during the step of defining the scanning limits, which will be explained in more detail in the next sections. This step requires the user to direct the laser spot to specific locations in the scene and using the camera instead of looking directly at that spot to prevent the possibility of eye damage.

4.2.4 Computer System SONY VAIO EB2MOE

During the scanning process, the LADAR system performs real-time operation. This operation requires the computer to be able to control the LADAR system and to process data at high speed. For this reason a **SONY** laptop computer is used. This has high processor speed ($2.27\,GHz$) with $3\,MB$ of cache memory and high memory capacity ($4.00\,GB$). More specifications for the computer are given in Table 4.3.

Table 4.3: Technical Specifications of **SONY** Computer

Processor	Intel(R) Core(TM) i3 CPU (Central Processing Unit) $2.27\,GHz$
Installed Memory	$4.00\,GB$ RAM (Random Access Memory)
Graphic Card	Intel(R) Graphics Media Accelerator HD
System Type	64-bit Operating System

4.3 Software Description

This section describes the software that has been written for the LADAR hardware setup in order to control its operation and produce the LADAR data. A Graphical User Interface (GUI) is also designed into this software. This GUI represents an efficient way of working without interacting directly with the software code. The GUI window contains the panels required for setting the scanning parameters and displaying the resultant data. Figure 4.10 shows the GUI window's panels that are used for scanning the train model shown in Figure 4.11, where these panels are:

- Visualization Panels
- LADAR Parameters Panel
- Scanning Panel
- Output Panel
- Data Filtering Panel

Figure 4.10: LADAR GUI Control Window.

Figure 4.11: LADAR Scanning the Train Model.

4.3.1 Visualization Panels

Two visualization panels were designed in the window. The first panel is located on the right-side and contains one screen to display the results, a text box to display the current status or the set value, and a push button to enable the user to rotate the graph in three dimensions. The second panel is located on the left-side of the window and contains one screen to display the scanned scene image and the laser spot marker. This marker is displayed over the scene image as a red shape (see Figure 4.10) and used to guide the user to the location of the laser spot by finding the maximum intensity on the red channel of the scene image.

4.3.2 LADAR Parameters Panel

This panel is used for adjusting the LADAR scanning resolutions and its scanning limits. Estimating the exact LADAR scanning limits for a specific object is not easy task in most cases. Therefore the panel is designed to aid the user to specify these limits easily, by positioning the laser beam directly towards the object border points and then set the pan / tilt values for each point to determine the scanning limits. Figure 4.12 shows three ways of selecting different numbers of train border points in order to specify the scanning limits that are required to scan the train.

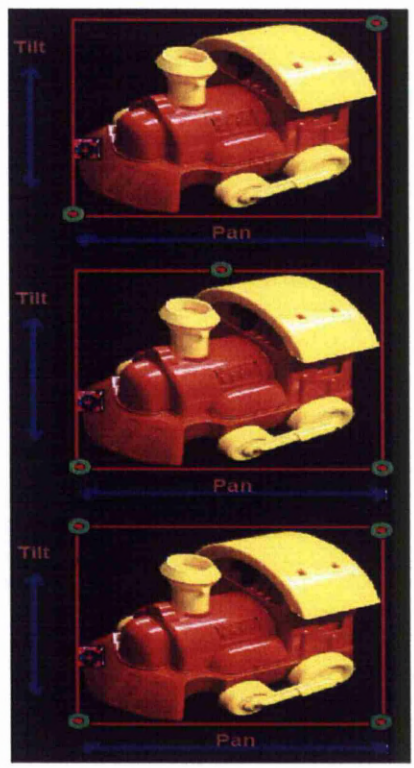

Figure 4.12: Scanning Limits (red rectangle) Defining Using Border Points (green circles).

Moving the laser beam to a specific direction is done by pressing one of the four toggle buttons, which are "**Up**", "**Down**", "**Left**", and "**Right**" buttons, while stopping the movement is done by pressing the selected button again. During the laser movement, the software activates the camera to show the user where the laser spot is on the scanned scene. The marker is also activated to guide the user towards that spot. The "**Select Points**" button is then used to set the pan θ_M and the tilt ϕ_M values for each selected point, while the "**Clear Points**" button is used to delete them.

Calculating the scanning limits from the border points values is then performed by applying the following equations:

$$\theta_{M_{min.}} = min([\theta_M^1, \theta_M^2, ..., \theta_M^n]) \tag{4.8}$$

$$\theta_{M_{max.}} = max([\theta_M^1, \theta_M^2, ..., \theta_M^n]) \tag{4.9}$$

$$\phi_{M_{min.}} = min([\phi_M^1, \phi_M^2, ..., \phi_M^n]) \tag{4.10}$$

$$\phi_{M_{max.}} = max([\phi_M^1, \phi_M^2, ..., \phi_M^n]) \tag{4.11}$$

where $(\theta_{M_{min.}}, \theta_{M_{max.}})$ and $(\phi_{M_{min.}}, \phi_{M_{max.}})$ are the scanning limits in pan and tilt directions respectively and n is the number of the selected border points, which is varied between 2 and 4.

The calculated scanning limits are then set as inputs in the corresponding edit texts. This will allow the user to know these limits and to be able to re-adjust them, where their default values are set to the maximum LADAR field of view.

Adjusting the LADAR scanning resolution in both pan and tilt direction is done by typing their values in the corresponding edit texts, where their default values are set to 0.0265^o. After setting the scanning limits and the angular resolutions, the "**Set Angles**" button is then used to replace the old scanning parameters (scanning resolutions and scanning limits) with these new parameters.

4.3.3 Scanning Panel

Pressing the "**Scan Start/Stop**" button in this panel, starts the LADAR scanning operation, which can be also stopped at any time by pressing this button again. During this operation, the resultant LADAR data are displayed directly on the visual panel screen (row by row) until the end of that operation. In addition to this button the panel has another three buttons, one for laser beam control and the other two for object recognition. The laser controlling button "**Laser On/Off**" is used to switch the laser on and off. This button is designed to be inactive during the scanning and the laser beam positioning operations. The recognition buttons are used to train the classifier with the training set that previously scanned and stored in a specific folder, and to recognise the scanned object with a specific descriptor (which is selected by using the pop-up menu), and finally to display its name in the text box.

4.3.4 Output Panel

The software is designed to be able to display the resultant LADAR data after performing the scanning operation in four different formats, one in spherical coordinates (spherical image) and the other three in Cartesian coordinates (Mesh, Surfaces, and point cloud). The formats can be selecting by using the following buttons:

- Spherical Image
- Cartesian (Surfaces)
- Cartesian (Mesh)
- Cartesian (Point Cloud)

Beside the data format selection, the panel is also used for saving the formats with a specific name by typing it in the corresponding edit text box and pressing the "**Save**" button. Figure 4.13 shows the scanning results for the train model and the scanning parameters shown in Figures 4.11 and 4.10 respectively.

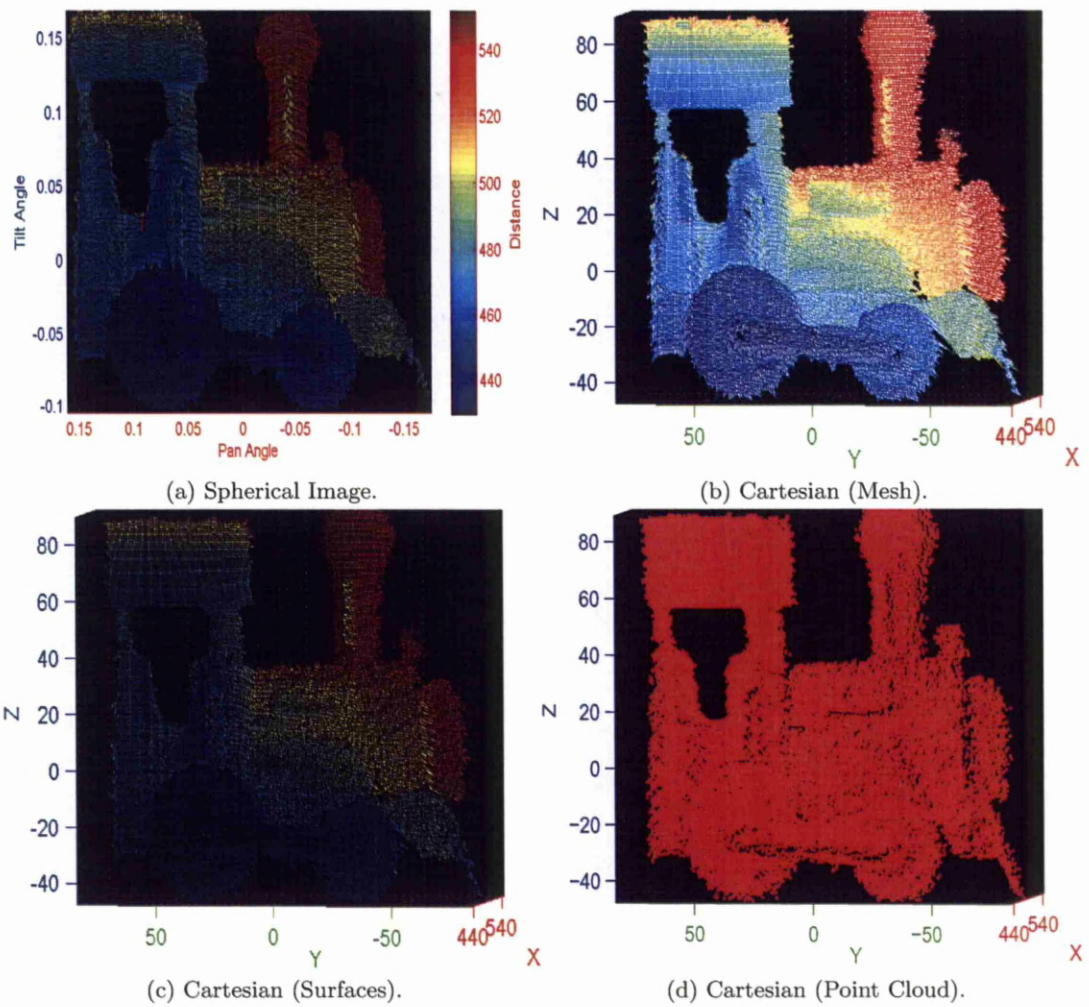

(a) Spherical Image.

(b) Cartesian (Mesh).

(c) Cartesian (Surfaces).

(d) Cartesian (Point Cloud).

Figure 4.13: Four types of Scanning Results for Train Model (Note: in spherical image the pan and tilt angles are the corrected angles which are equal to θ and ϕ respectively)

4.3.5 Data Filtering Panel

This panel consists from two filters, which are the objects and the mixed pixel filters:

4.3.5.1 Objects Filter

This filter works in conjunction with the output panel to remove unwanted objects from the resultant data manually. The filter is designed to be able to filter the data in three dimensions with one of two different coordinates, which are spherical and Cartesian coordinates. The type of coordinates that will be used during the filtering process will depend on which data format has been selected via the output panel. Therefore if the data is displayed as a spherical image the spherical coordinates will be selected, while the Cartesian coordinates will be selected if the data are displayed with one of the other three formats (Mesh, Surfaces, Point Cloud).

The data filtering is performed by defining the range limits of the desired measurement values in each dimension. This will allows the filter to remove all the unwanted values that lay outside this range in that dimension.

In each dimension, the range limit values R_1 and R_2 are calculated by applying the following equation:

$$\begin{aligned} Range &= [R_1, R_2] \\ &= [(F_c - F_w/2), (F_c + F_w/2)] \end{aligned} \tag{4.12}$$

where F_c and F_w are the filter centre and filter width respectively. These can be set either by typing their values directly in the corresponding edit text boxes or by using the corresponding sliding bars. If the sliding bars are used then F_c and F_w values are calculated using the following equations:

$$F_c = R_{min.} + slv_{center} \times (R_{max.} - R_{min.}) \tag{4.13}$$

$$F_w = slv_{width} \times (R_{max.} - R_{min.}) \tag{4.14}$$

where

$R_{min.}$: Minimum measure range value.
$R_{max.}$: Maximum measure range value.
slv_{center}: Location value for the "**Centre**" sliding bar.
slv_{width} : Location value for the "**Width**" sliding bar.

Both slv_{center} and slv_{width} values are adjusted by moving the corresponding slider bars to the left or to the right, where their values are varied between 0 and 1. During the slider bars movement, both the centre and width edit texts values are set to the new calculated F_c and F_w (to allow re-adjustment using edit text boxes) and the filtered

data are directly displayed on the visual panel screen. Figure 4.14 shows the train after filtering the wall that lies behind it using $F_c = 485\,mm$ with $F_w = 120\,mm$ in X-axis and $F_c = 22\,mm$ with $F_w = 140\,mm$ in Z-axis. The "**Save**" button in the output panel is then used to save the resultant filtered data with a specific name.

4.3.5.2 Mixed Pixel Filter

LADAR system measurements are corrupted by noise and artifacts that can undermine the performance of registration, segmentation, surface reconstruction, recognition, and other algorithms operating on the data [79]. Laser data artifacts can be divided into two categories: intrinsic sensor errors (range drift due to temperature variations , systematic errors and random noise, etc), and errors due to the interaction of the laser beam with the environment. Most common spurious range measurements occur when the laser beam hits simultaneously two objects at different distances. Such errors are known in the literature as mixed pixels, or discontinuous points [80–83], and several method have been developed in order to identified, filtered, and restored these mixed pixels [79–82, 84–87]. Figure 4.14a shows the mixed pixels between the train and the wall, while Figure 4.14b shows these pixels on the train edges.

In this software, the edge-length algorithm is used to remove these pixels [79]. Referring to Figure 4.15, this algorithm starts by triangulated the point cloud data shown in Figure 4.15a by organizing these points in a grid with storing their corresponding 3D Cartesian coordinates. The grid is then triangulated by connecting adjacent points in a square and then connecting one of the diagonals as shown in Figure 4.15b.

The edge-length algorithm relies on the observation that triangles spanning a depth discontinuity often have long edge lengths (see Figure 4.15b). Any triangle with an edge longer than a specified threshold is marked as a depth discontinuity triangle, where the summation of the mean and standard deviation values for the triangles edge lengths is used as a threshold value. After eliminating depth discontinuity triangles as shown in Figure 4.15c, any isolated 3D points (i.e., points not connected to any remaining triangles) are considered mixed pixel points.

Once a mixed pixel is identified the general approach is to remove it outright. This deals with the problem of the mixed pixel, but has potential to introduce other errors, such as distorting object edges and creating holes in surfaces [84]. For this reasons, the first and second mixed pixel neighbors points (that are not marked as mixed pixels) are used to restored that pixel. This is by replacing the mixed pixel Cartesian coordinates with the mean values of the neighbors Cartesian coordinates. The procedure then is to checked if the resultant restored pixel is still produces long edge triangle in order to remove it from the point cloud. Figure 4.15d shows the remaining triangles after mixed pixels restoration, while Figure 4.15e shows the resultant filtered point cloud data (which is more clearer than the original point cloud shown in Figure 4.15a).

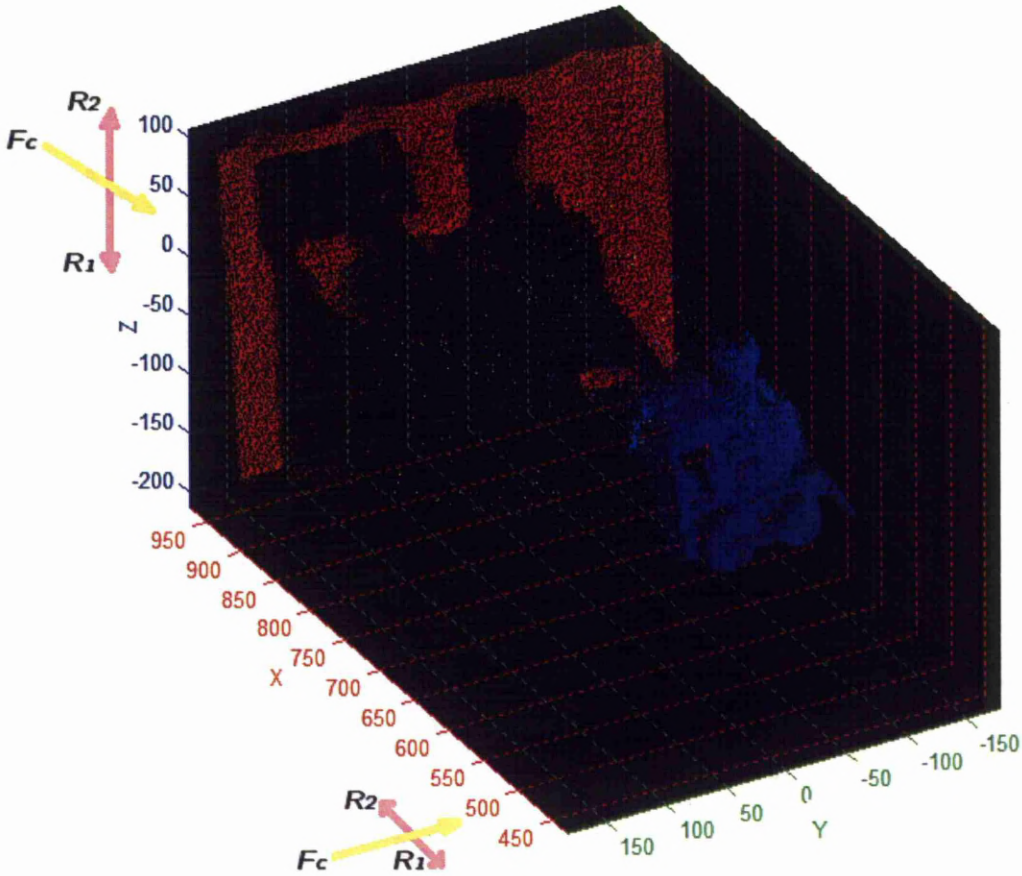

(a)

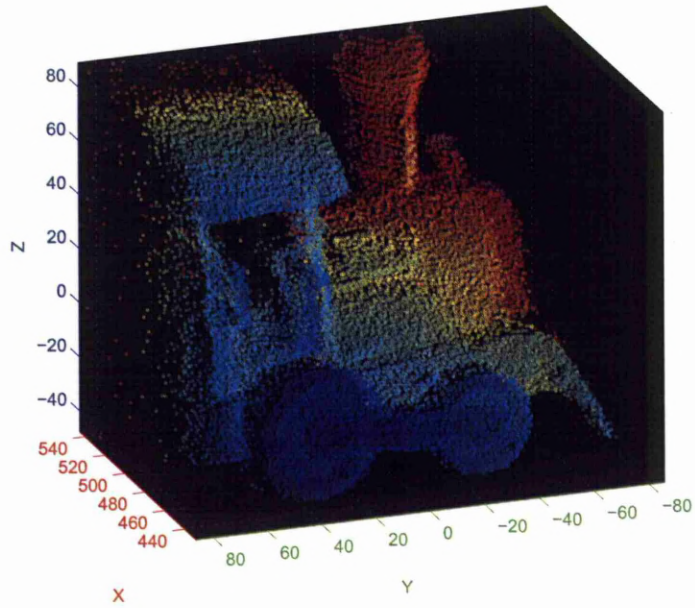

(b)

Figure 4.14: Figure shows the LADAR Data Before (a) and After (b) removing the un-wanted wall measurement.

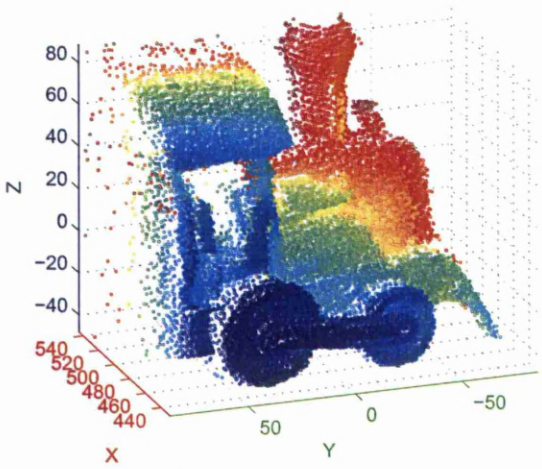

(a) Noisy Point Cloud.

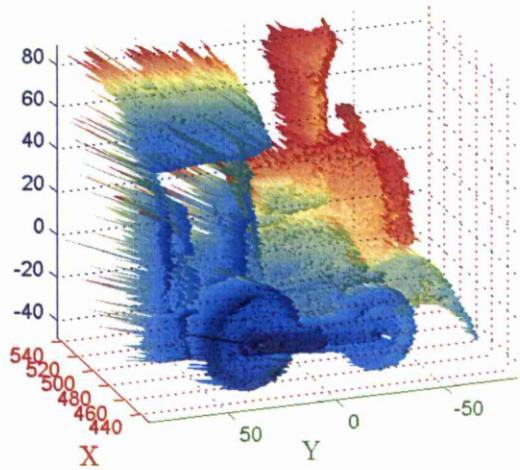

(b) Triangulated Point Cloud.

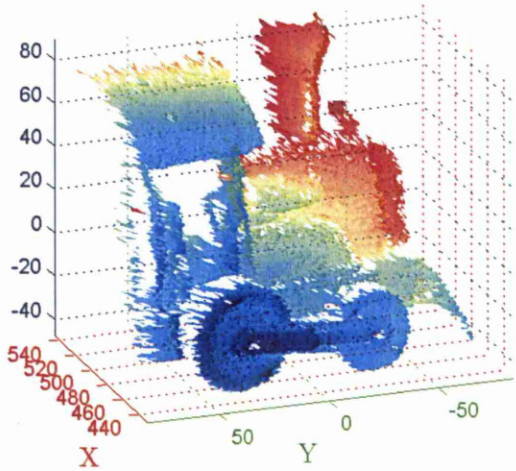

(c) Triangulated Point Cloud after Filtering.

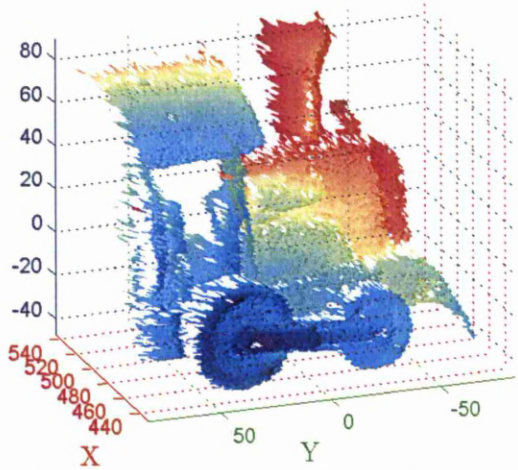

(d) Results of 4.15c after Mixed Pixels Restoration.

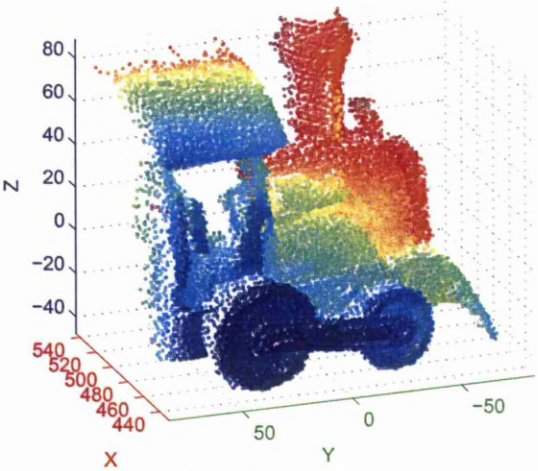

(e) Filtered Point Cloud.

Figure 4.15: Mixed Pixel Filtering using Edge-Length Algorithm.

4.4 Summary

A new LADAR prototype system has been designed and implemented to be able to capture the 3D LADAR data from the surfaces of various objects. This system is designed to have a high technical specification ($714\,sample/s$ and 0.0265^o scanning resolution) at a minimum cost. This opens up the possibility for further research in testing the chromatic descriptors with a real LADAR data, which is currently limited because of the high cost of traditional LADAR systems. The technical aspects of the LADAR design which include hardware components and both the mathematical model and the controlling software that are required for reconstructing the resultant LADAR images from the scanning measurements are described. The resultant LADAR images of scanning the train model show the effectiveness of this system and its ability to produce clear and high resolution images with different formats.

Chapter 5

Chromatic Methodology for LADAR Data Processing

Introduction

In this chapter new LADAR image descriptors are proposed. These descriptors arise from the chromatic methodology to extract the features from the LADAR images by applying new types of processors called 'invariant spatial chromatic processors'. This represents the first step toward using this methodology for processing LADAR images.

In this chapter, five sections are presented. The first section gives an overview about the chromatic methodology and the spatial chromatic processors. The second and the third sections explain the proposed approach of making these processors invariant to the translation and scaling effects and how these invariant processors can be use as region image descriptors. The method of processing the LADAR images using the proposed descriptors is presented in the fourth section. Finally, a summary of this chapter is presented.

5.1 Chromatic Methodology

The chromatic methodology has evolved from a number of origins, some based upon human perceptions and the others on scientific and analytical approaches [88]. It provides a means of processing a signal that avoids some of the difficulties associated with the Fourier approach, at the expense of depressing some minor signal details relative to major ones. These difficulties include complexity of the Fourier transformed signal and the transformation instability in the presence of noise [89]. The chromatic method derived initially from the photic field concepts described by Moon and Spencer [90], but its generic nature has recently enabled it to be extended far beyond the visible part of the spectrum to other domains of information extraction. These domains include ultrasonic domain for tracking systems [91], time domain for processing continuous signals [92], and acoustic domain for rail track monitoring [93] and identifying optoacoustical signals from high voltage circuit breakers [94].

5.1.1 Spatial Chromatic Processors

Chromatic processing often involves three (R, G, B) non-orthogonal (overlapping) processors. The outputs from these processors (R_o, G_o, B_o) are used to form cross correlations between the signal and the different processors responses [88]. Normally each processor response may have a Gaussian shape aligning with the Gabor transform [95], a triangle or other shapes may be preferred for some cases when a special type of responsivity is required. Figure 5.1 shows the $R(l_o)$, $G(l_o)$, $B(l_o)$ processors responses for the R, G, B Gaussian processors respectively, where these responses are a function of the location parameter l_o and $P_R(l_o)$ is the amplitude of a signal that varies with l_o.

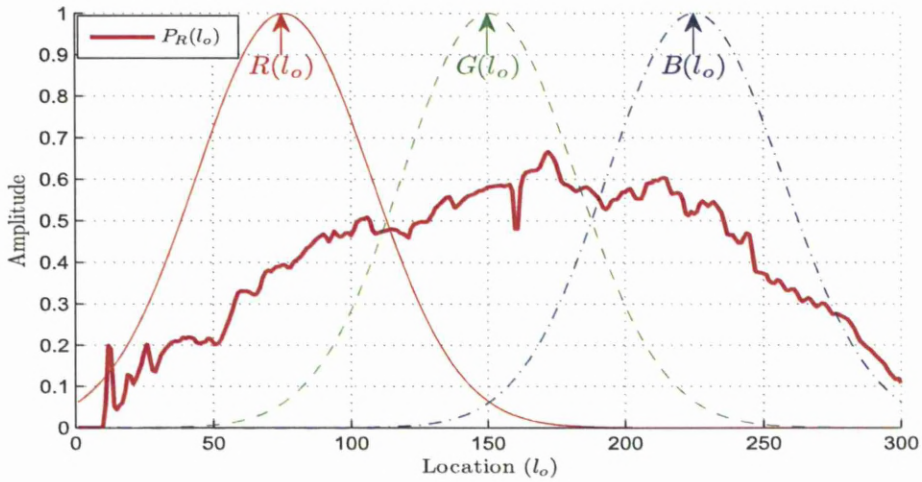

Figure 5.1: Response Profiles for Gaussian Spatial Chromatic Processors.

According to [88] the outputs of the R, G, B processors that address the discrete signal $P_R(l_o)$ are:

$$R_o = \sum_{l_o} R(l_o)P_R(l_o) \tag{5.1}$$

$$G_o = \sum_{l_o} G(l_o)P_R(l_o) \tag{5.2}$$

$$B_o = \sum_{l_o} B(l_o)P_R(l_o) \tag{5.3}$$

Whatever the processor shape, the non-orthogonality is significant in cross correlating the subdivided signal on each channel and in providing a means of selective tuning in the regions of overlap. It has been shown that although three spatial chromatic processors provide a high level of signal discrimination, additional processors could enhance signal discrimination even further but that extending the number beyond six gives little advantage [95], [96]. For this reason and for computing simplicity three spatial chromatic processors were used in this study.

The approach then is to evaluate combinations of these cross correlations to yield coordinates which define the signal in one of several chromatic modes (e.g. x:y, Lab, *HLS*, etc.) depending on the nature of the information sought [88]. The Hue-Lightness-Saturation (*HLS*) scheme is used in this work. The choice of this scheme enables the intuitive methods of colour science to be related to signal defining factors, where L represents the strength of the signal, S its spread in the measured domain and H is the dominant measured value [97].

The transformation of the processors outputs (R_o, G_o, B_o) to *HLS* is performed using the following relationships [88, 97]:

$$\begin{aligned} H &= 0.667 - 0.333\left(\frac{g_o}{g_o + b_o}\right), \quad r_o = 0 \\ &= 1.000 - 0.333\left(\frac{b_o}{b_o + r_o}\right), \quad g_o = 0 \\ &= 0.333 - 0.333\left(\frac{r_o}{r_o + g_o}\right), \quad b_o = 0 \end{aligned} \tag{5.4}$$

$$L = \frac{R_o + G_o + B_o}{3} \tag{5.5}$$

$$S = \frac{max(R_o, G_o, B_o) - min(R_o, G_o, B_o)}{max(R_o, G_o, B_o) + min(R_o, G_o, B_o)} \tag{5.6}$$

where

$$r_o = R_o - min(R_o, G_o, B_o) \tag{5.7}$$

$$g_o = G_o - min(R_o, G_o, B_o) \tag{5.8}$$

$$b_o = B_o - min(R_o, G_o, B_o) \tag{5.9}$$

$max(R_o, G_o, B_o)$ and $min(R_o, G_o, B_o)$ represents the parameter (R_o, G_o, B_o) having the highest and lowest values, respectively. If $R_o \,\&\, G_o \,\&\, B_o = 0$ then $S = 0$ and H is undefined.

5.1.2 Types of Spatial Chromatic Processors

Three different types of spatial chromatic processors are presented with their monochromatic responses. These types have different processors response profiles and arrangements. The monochromatic responses are evaluated by sweeping a monochromatic signal spatially under each type and calculating the resultant Hue values, where the responses can be tracked in terms of Hue. The spatial chromatic processors types are:

- Half Height Overlapping Gaussian Processors (HHOGP).
- Half Height Overlapping Triangular Processors (HHOTP).
- Continuous Overlapping Triangular Processors (COTP).

5.1.2.1 Half Height Overlapping Gaussian Processors (HHOGP)

In this processors type, two Gaussian processors R (left) and B (right) are overlapped at their half-height points with another processor G (middle) as shown in Figure 5.2a. The response profiles for these processors make the Hue value vary between 0 and 0.67 when a monochromatic signal swept under them as shown in Figure 5.2b. This variation is nonlinear with low sensitivity between 0 and 50, and between 250 and 300, because there is no overlap in these regions. The maximum sensitivity occurs between 50 and 250, where the overlap at these locations is substantial.

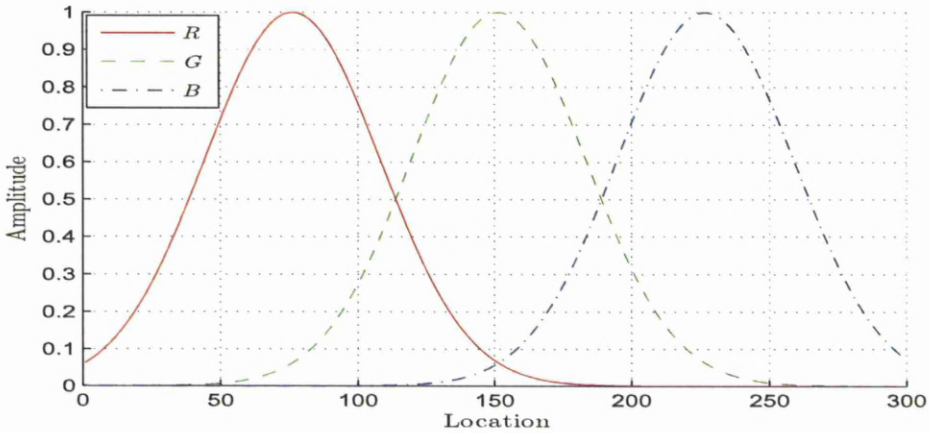

(a) Response Profiles for R, G, B Chromatic Processors.

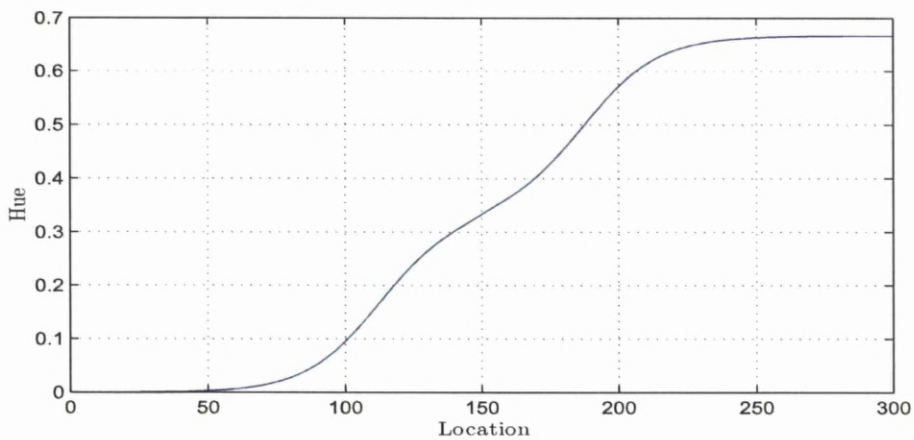

(b) Monochromatic Response.

Figure 5.2: Half Height Overlapping Gaussian Processors and their Monochromatic Response.

5.1.2.2 Half Height Overlapping Triangular Processors (HHOTP)

This type is similar to HHOGP but instead of Gaussian shape response, processors with a triangle shape response are used in this type as shown in Figure 5.3a. Figure 5.3b shows the monochromatic response for this processors arrangement, which is also varied

between 0 and 0.67. This variation is linear and its sensitivity is high at the overlapping locations (between 75 and 225) and zero outside these locations, where there is no overlap between the processors.

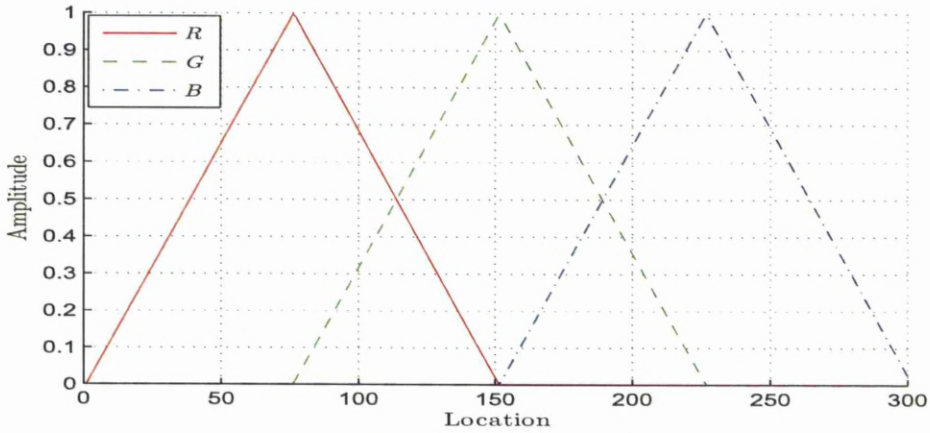

(a) Response Profiles for R, G, B Chromatic Processors.

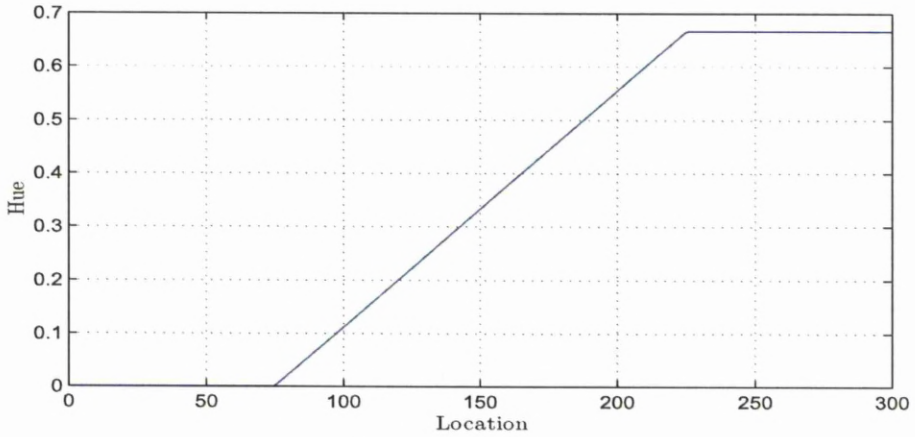

(b) Monochromatic Response.

Figure 5.3: Half Height Overlapping Triangular Processors and their Monochromatic Response.

5.1.2.3 Continuous Overlapping Triangular Processors (COTP)

This type consists of three triangular processors, two processors G (left) and B (right) are overlapped at their half-height points with each other from one side and with the third processor R (shifted) from the opposite sides as shown in Figure 5.4a. This type of processors arrangement makes the triangular processors overlap with each other across the entire locations unlike the previous types in which the overlapping regions cover specific locations. This leads to produce a continuous sensitivity across the entire locations as shown in Figure 5.4b. In Figure 5.4b, the monochromatic response for this arrangement is linear and varied between 0 and 1.

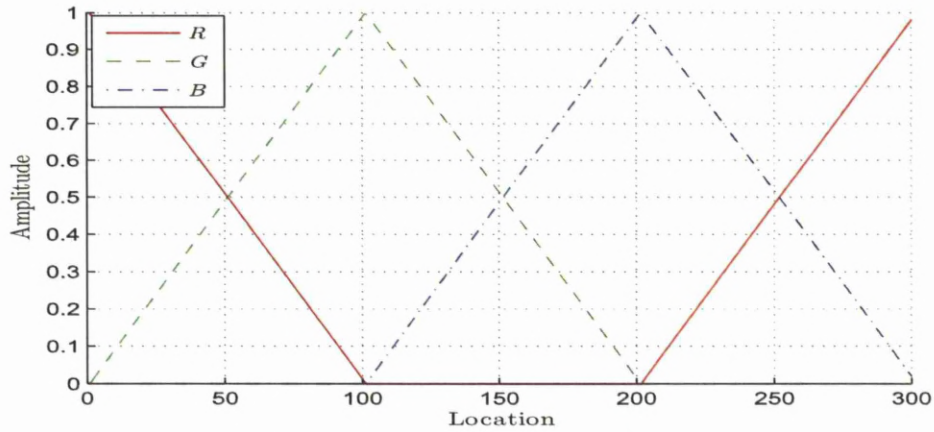

(a) Response Profiles for R, G, B Chromatic Processors.

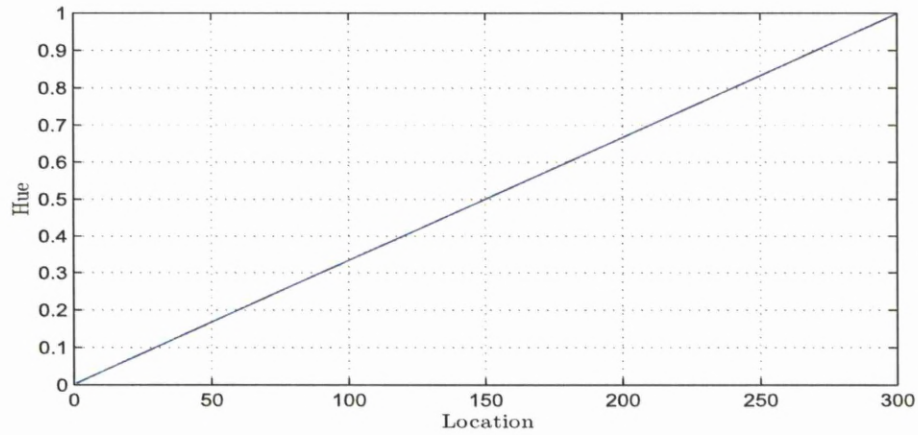

(b) Monochromatic Response.

Figure 5.4: Continuous Overlapping Triangular Processors and their Monochromatic Response.

5.2 Invariant Spatial Chromatic Processors

The spatial distributions of the chromatic processors make them variant to the shift and scale effects. If the signal is moved from its original location, or enlarged the H, L, and S values will change. Figures 5.7 and 5.8 show the change in the processors output values (H, L, S) for three processors types (HHOGP, HHOTP, COTP), when two signal types (symmetrical and asymmetrical) were moved from their original locations to the right and enlarged in the horizontal direction as shown in Figures 5.5 and 5.6 respectively.

To make the chromatic processors invariant, a new approach is proposed. This approach is to make the centres of the processors and widths adaptable to the input signal type. The methods of applying this proposed approach with each processors type to make them invariant, are presented in the following subsections:

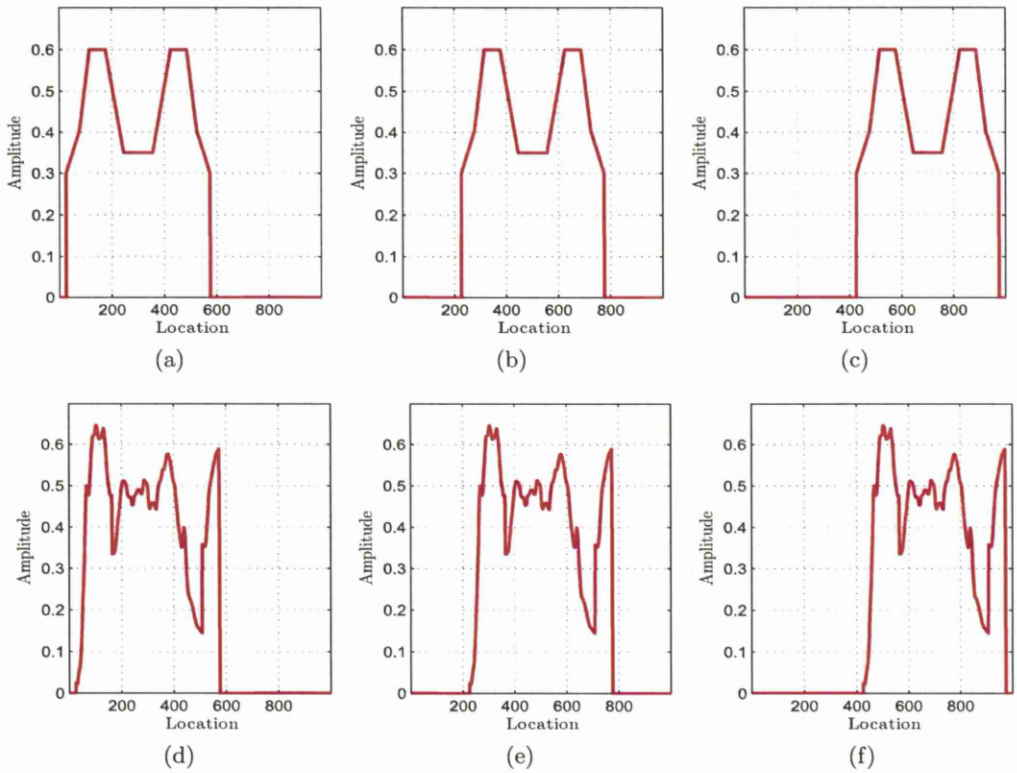

Figure 5.5: Shift Effect on the Symmetrical (a,b,c) and Asymmetrical (d,e,f) Signals.

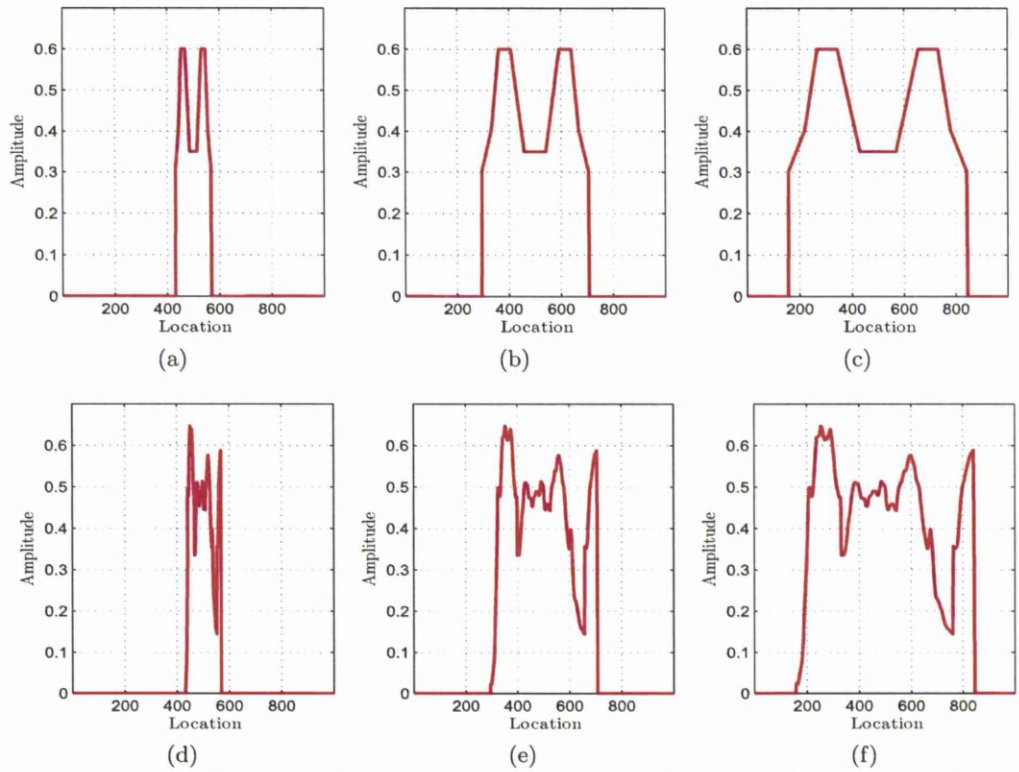

Figure 5.6: Scale Effect on the Symmetrical (a,b,c) and Asymmetrical (d,e,f) Signals.

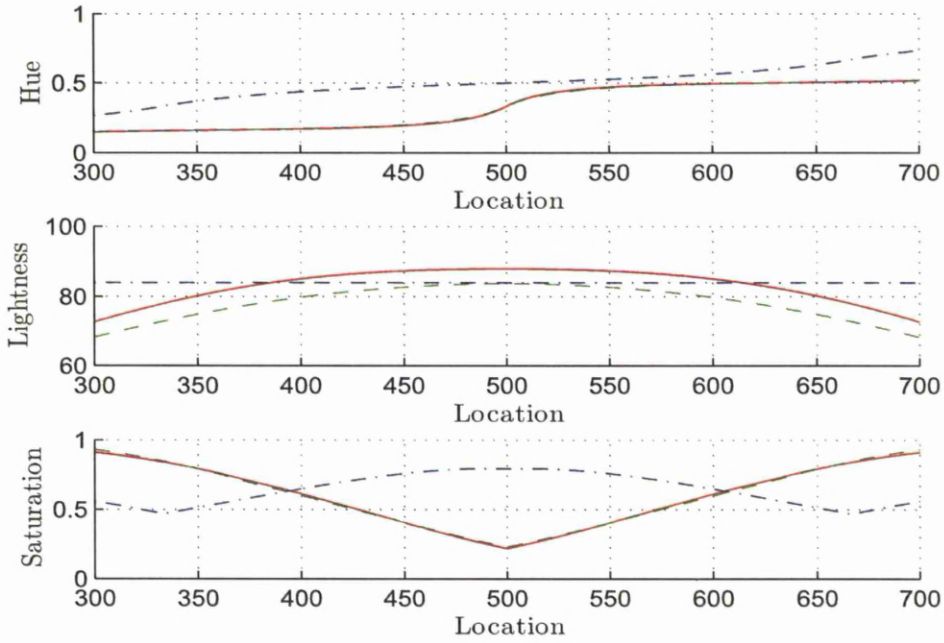

(a) *HLS* Values of Processing Symmetric Signal Moved from Location 300 to 700.

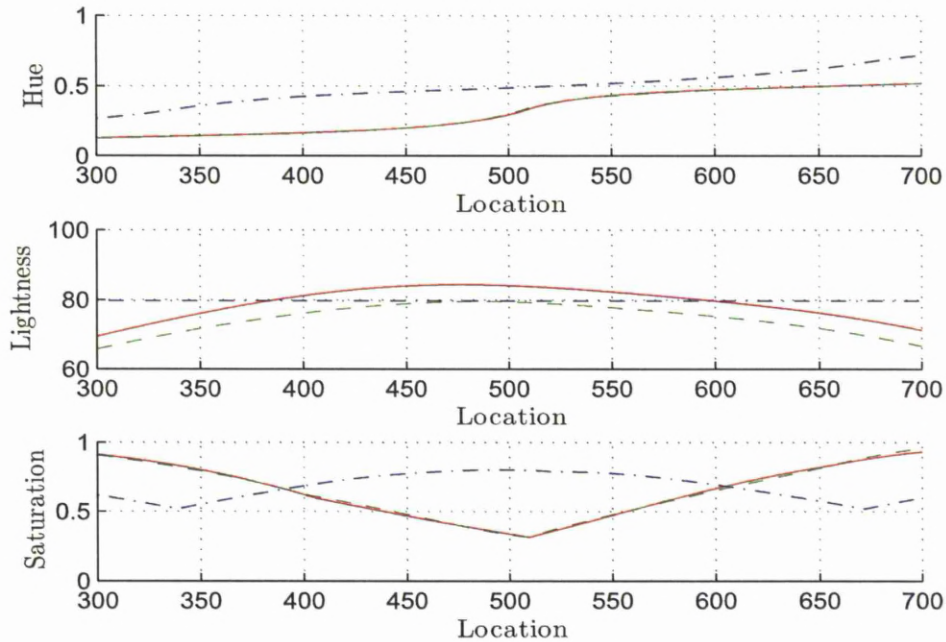

(b) *HLS* Values of Processing Asymmetric Signal Moved from Location 300 to 700.

Figure 5.7: H, L, and S Values During Shift Effect for HHOGP "-", HHOTP "- -", and COTP "-.-".

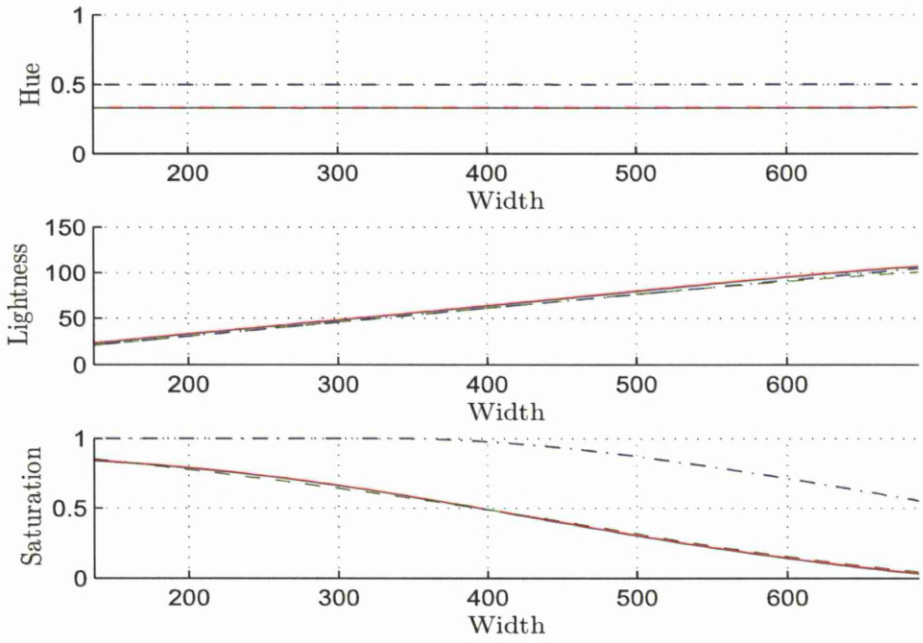

(a) *HLS* Values of Processing Symmetric Signal its Width Enlarged from 137 to 688 unit.

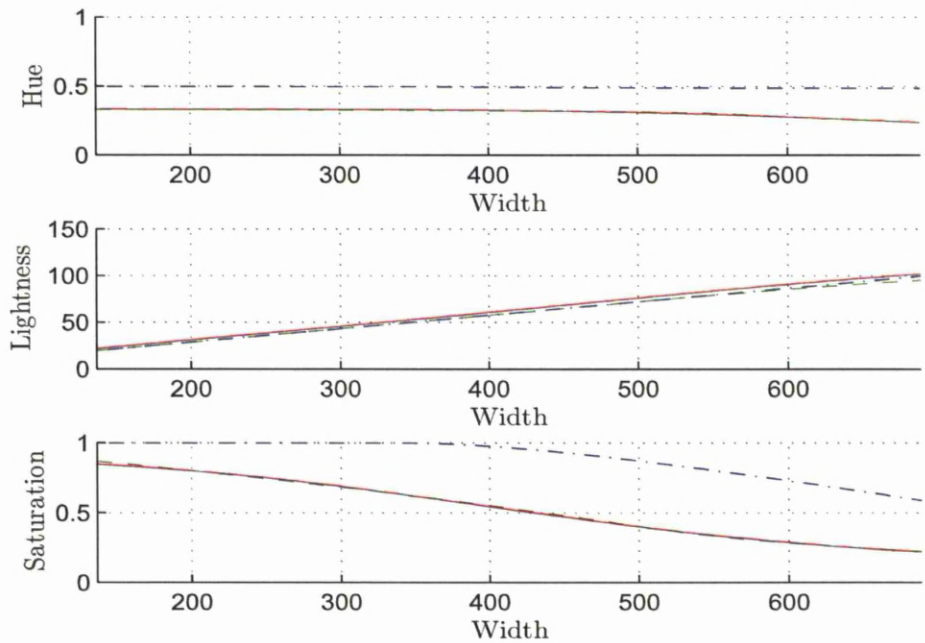

(b) *HLS* Values of Processing Asymmetric Signal its Width Enlarged from 137 to 688 unit.

Figure 5.8: H, L, and S Values During Scale Effect for HHOGP "-", HHOTP "- -", and COTP "-.-".

5.2.1 Invariant Half Height Overlapping Gaussian Processors

Referring to Figure 5.9, the approach of making the HHOGP invariant is started by calculating the centroid c_m of the (discrete) input signal $P_R(l_o)$ of ℓ length by

$$c_m = \sum_{l_o=1}^{\ell} l_o P_R(l_o) / \sum_{l_o=1}^{\ell} P_R(l_o) \tag{5.10}$$

This centroid is then used as a boundary condition for calculating two processors centres C_R and C_B as follow:

$$C_R = \sum_{l_o=1}^{c_m} l_o P_R(l_o) / \sum_{l_o=1}^{c_m} P_R(l_o) \tag{5.11}$$

$$C_B = \sum_{l_o=c_m}^{\ell} l_o P_R(l_o) / \sum_{l_o=c_m}^{\ell} P_R(l_o) \tag{5.12}$$

The third processor centre G_G can be then determined from the following equation:

$$C_G = (C_R + C_B)/2 \tag{5.13}$$

The widths for these three processors W_{RGB} are all equal and they define as

$$W_{RGB} = (C_B - C_R)/2 \tag{5.14}$$

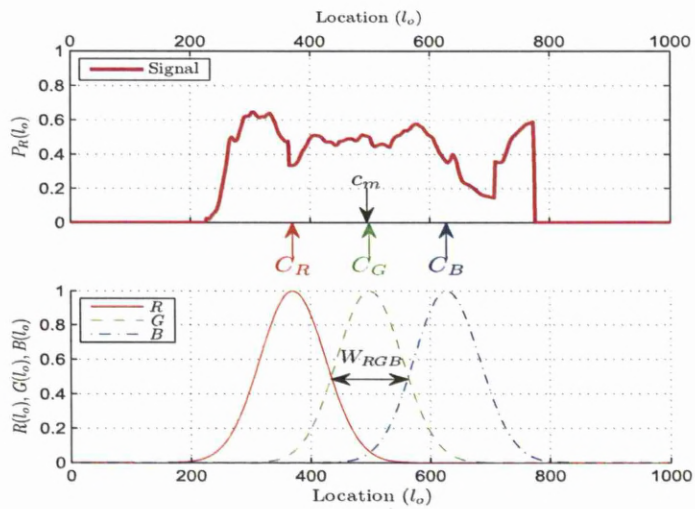

Figure 5.9: Calculated Centres and Widths for HHOGP Using the Proposed Approach.

The calculated centres and widths are then used to determine the response profiles $(R(l_o), G(l_o), B(l_o))$ for these Gaussian processors by using the following equations respectively:

$$R(l_o) = \exp\left(\frac{-4\ln(2)(l_o - C_R)^2}{W_{RGB}^2}\right) \tag{5.15}$$

$$G(l_o) = \exp\left(\frac{-4\ln(2)(l_o - C_G)^2}{W_{RGB}^2}\right) \tag{5.16}$$

$$B(l_o) = \exp\left(\frac{-4\ln(2)(l_o - C_B)^2}{W_{RGB}^2}\right) \tag{5.17}$$

The processors (of adapted centres and widths), are then applied on the input signal $P_R(l_o)$ to extract the features from it. The outputs (R_o, G_o, B_o) of these processors are calculated by applying the following equations respectively:

$$R_o = \sum_{l_o=1}^{\ell} R(l_o)\, P_R(l_o) \tag{5.18}$$

$$G_o = \sum_{l_o=1}^{\ell} G(l_o)\, P_R(l_o) \tag{5.19}$$

$$B_o = \sum_{l_o=1}^{\ell} B(l_o)\, P_R(l_o) \tag{5.20}$$

Applying this approach, makes the processors deployments change their locations and widths with respect to shift and scale effects. In order to show the effectiveness of the proposed approach on the processors performance, two different types of signals (symmetrical and asymmetrical) are processed by these invariant processors. These signals were moved and enlarged gradually and the processors outputs were recorded for each new location and width respectively.

Figure 5.10 shows how these processors change their centres in order to follow the signals (symmetrical and asymmetrical) when they moved from left to right. While Figure 5.11 shows how these processers change their centres and widths when the signals width enlarges horizontally. The processors outputs for both effects (shift and scale) are shown in Figures 5.12a and 5.12b respectively. The results in these figures show that both the Hue and Saturation have constant values during these effects, while the lightness values are changed during the scale effect. The reason behind that is related to the nature of the $RGB - HLS$ conversion scheme. This scheme makes both the H and S values insensitive to the signal strength (which is varied during scalling), while it makes the L value sensitive to it. During scale effect, Figure 5.12b shows small fluctuation in H values at small signals width. This comes from the fact that a reduction in the signals width, reduces the signal details (which is higher in asymmetrical signal type) and this is in turn change the H values.

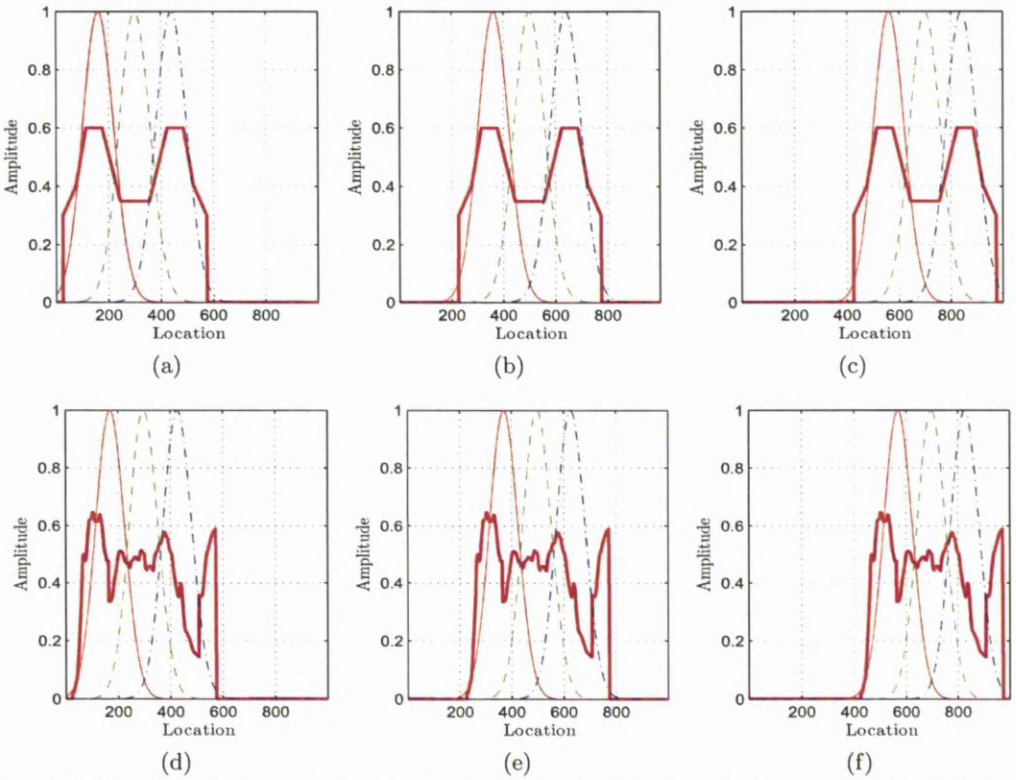

Figure 5.10: Shift Effect on the Symmetrical (a,b,c) and Asymmetrical (d,e,f) Signals.

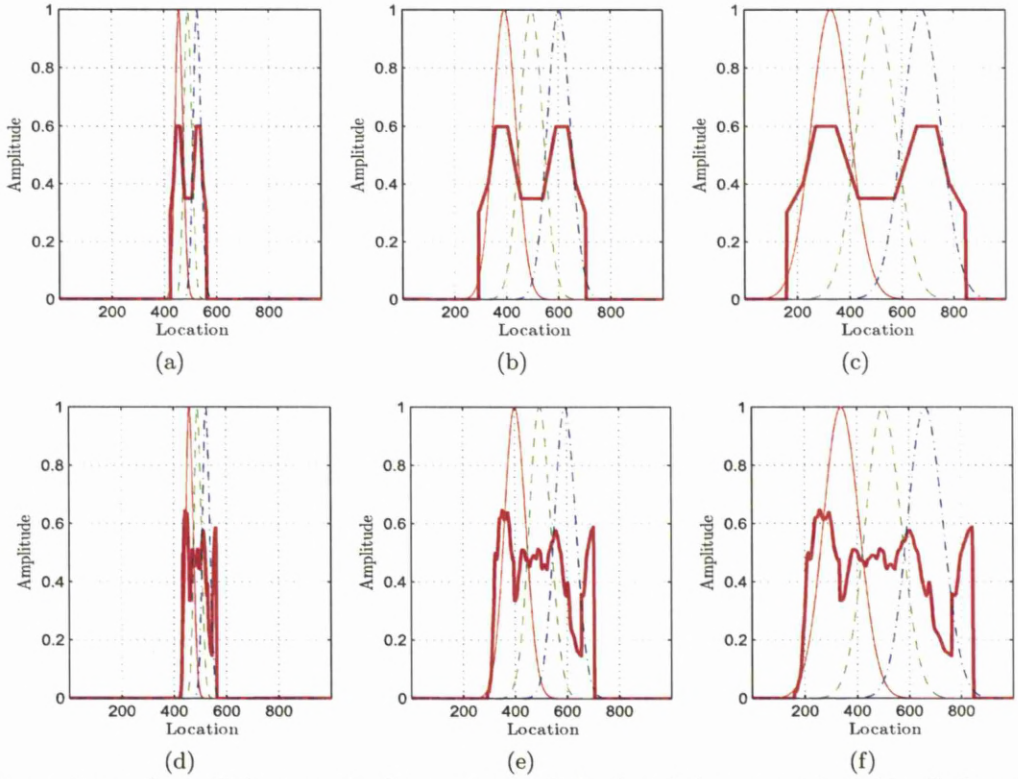

Figure 5.11: Scale Effect on the Symmetrical (a,b,c) and Asymmetrical (d,e,f) Signals.

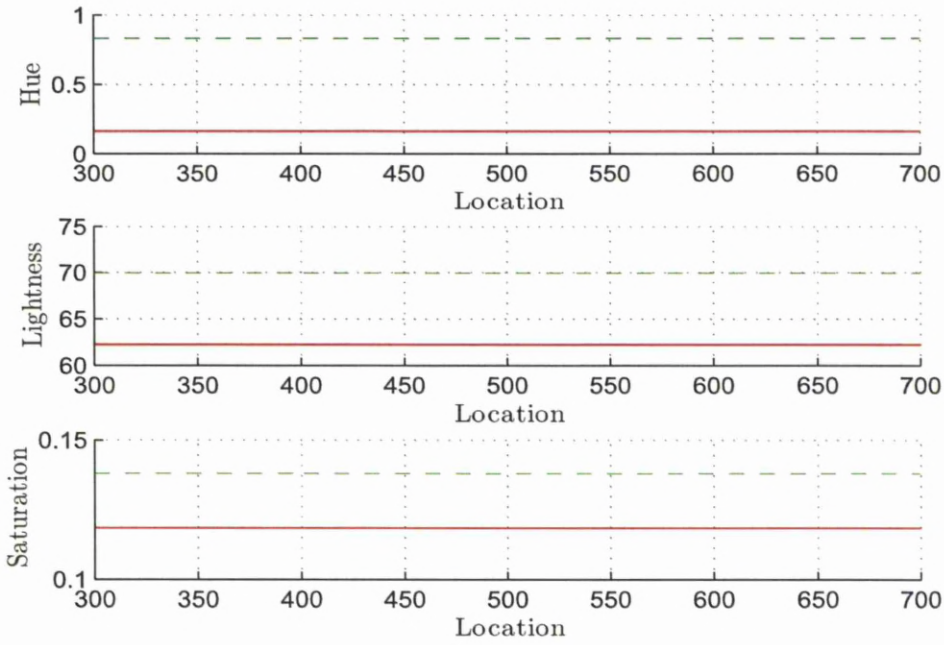

(a) *HLS* Values of Processing Symmetric "- -" and Asymmetrical "-" Signals Moved from Location 300 to 700.

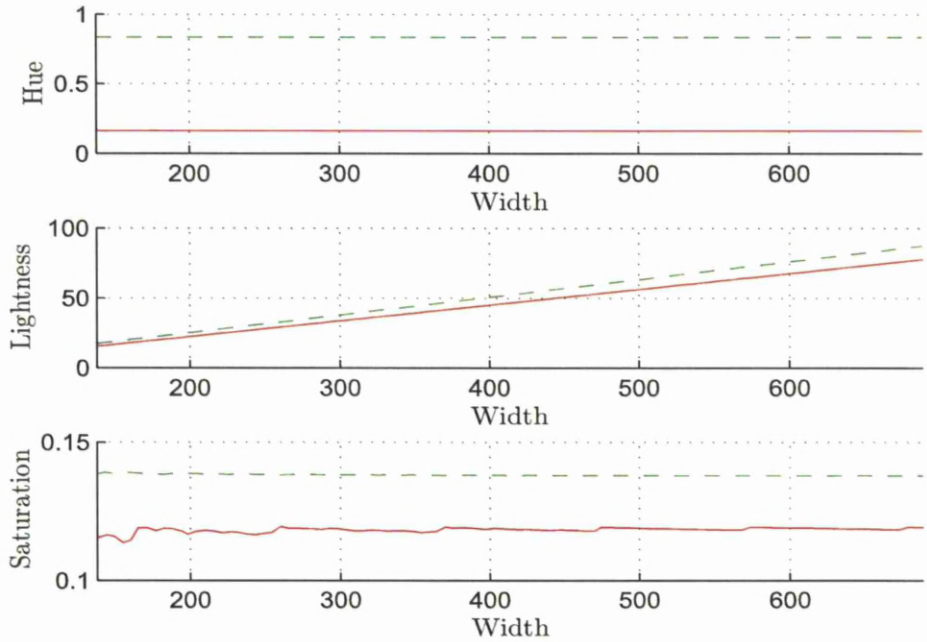

(b) *HLS* Values of Processing Symmetric "- -" and Asymmetrical "-" Signals their Widths Enlarged from 137 to 688 unit.

Figure 5.12: H, L, and S Values for the Invariant HHOGP During Shift (a) and Scale (b) Effects.

5.2.2 Invariant Half Height Overlapping Triangular Processors

The approach of making this type of processors invariant is similar to the previous approach. In Figure 5.13 the processors centres (C_R, C_G, C_B) were calculated by using Equations 5.11, 5.13, and 5.12 respectively, while the widths (W_{RGB}) were calculated by using Equation 5.14.

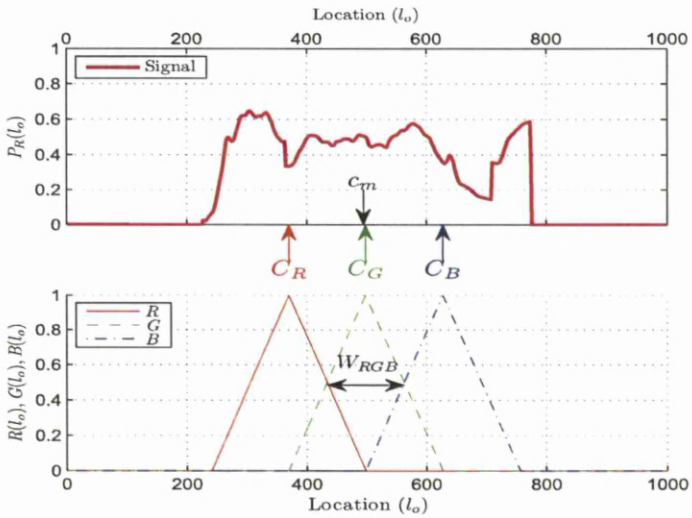

Figure 5.13: Calculated Centres and Widths for HHOTP Using the Proposed Approach.

The calculated centres and widths are then used to determine the response profiles $(R(l_o), G(l_o), B(l_o))$ for these triangular processors by using the following equations respectively:

$$R(l_o) = \begin{cases} \dfrac{l_o - C_R + W_{RGB}}{W_{RGB}} & l_o \in (C_R - W_{RGB}, C_R) \\ \dfrac{-l_o + C_R + W_{RGB}}{W_{RGB}} & l_o \in [C_R, C_R + W_{RGB}) \\ 0 & Otherwise \end{cases} \tag{5.21}$$

$$G(l_o) = \begin{cases} \dfrac{l_o - C_G + W_{RGB}}{W_{RGB}} & l_o \in (C_G - W_{RGB}, C_G) \\ \dfrac{-l_o + C_G + W_{RGB}}{W_{RGB}} & l_o \in [C_G, C_G + W_{RGB}) \\ 0 & Otherwise \end{cases} \tag{5.22}$$

$$B(l_o) = \begin{cases} \dfrac{l_o - C_B + W_{RGB}}{W_{RGB}} & l_o \in (C_B - W_{RGB}, C_B) \\ \dfrac{-l_o + C_B + W_{RGB}}{W_{RGB}} & l_o \in [C_B, C_B + W_{RGB}) \\ 0 & Otherwise \end{cases} \tag{5.23}$$

The outputs (R_o, G_o, B_o) of these processors are then calculated by applying Equations 5.18, 5.19, and 5.20 respectively. The performance of the new processors was also tested with shift and scale effects using two different signals. Figures 5.14 and 5.15 show how these processors adapt their deployments with shift and scale effects respectively to produce robust H and S values as shown in Figures 5.16a and 5.16b.

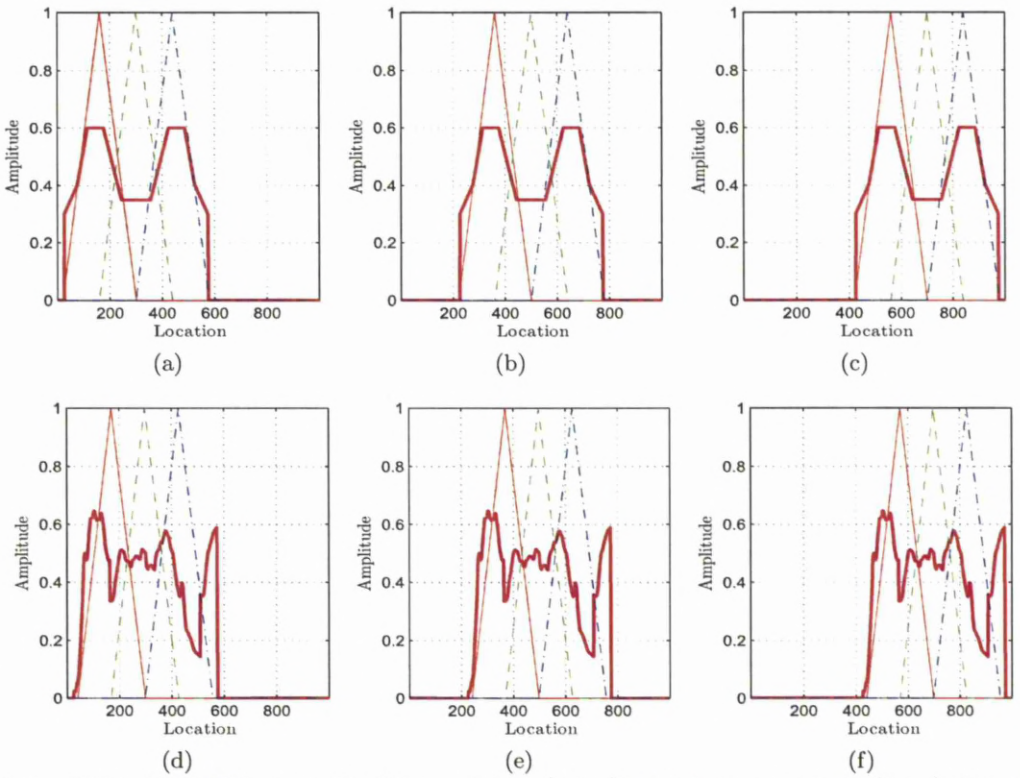

Figure 5.14: Shift Effect on the Symmetrical (a,b,c) and Asymmetrical (d,e,f) Signals.

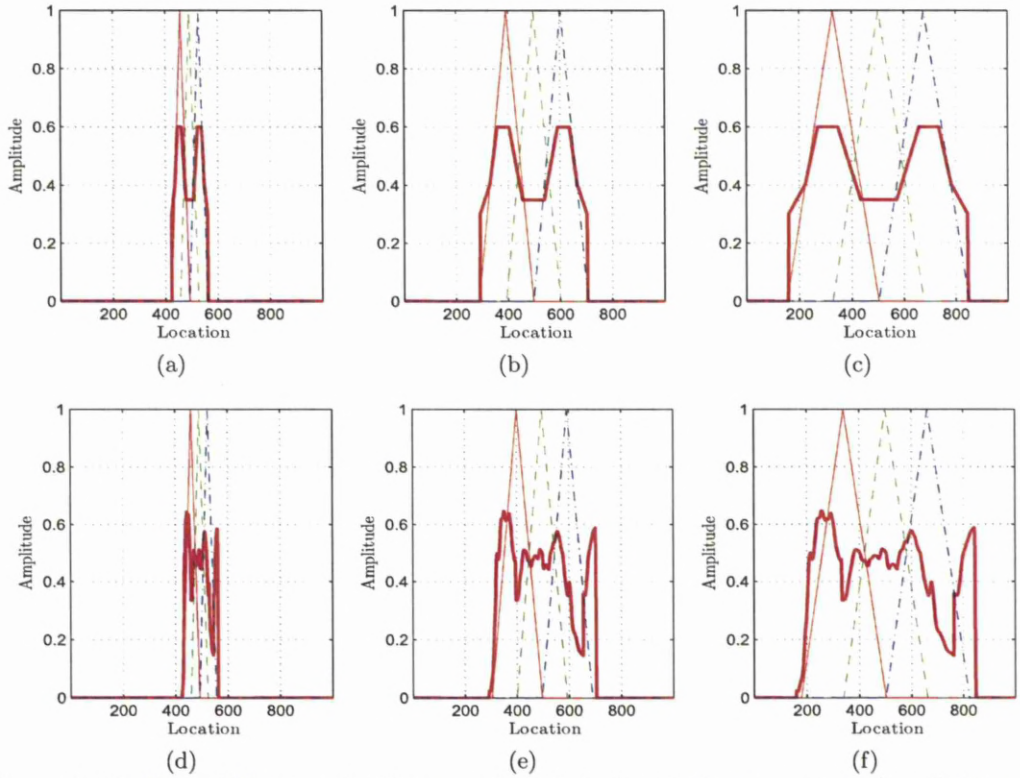

Figure 5.15: Scale Effect on the Symmetrical (a,b,c) and Asymmetrical (d,e,f) Signals.

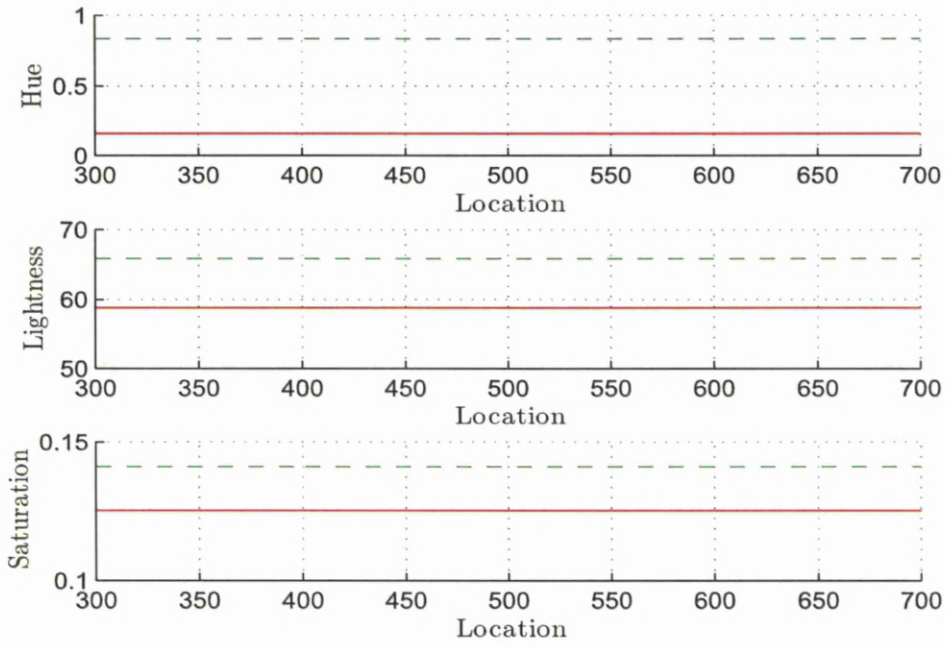

(a) *HLS* Values of Processing Symmetric "- -" and Asymmetrical "-" Signals Moved from Location 300 to 700.

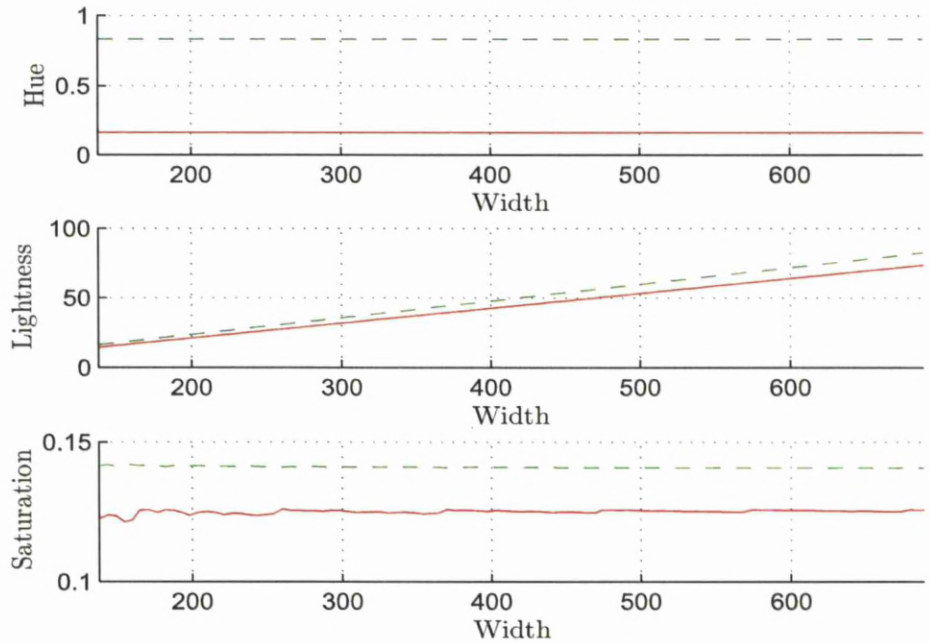

(b) *HLS* Values of Processing Symmetric "- -" and Asymmetrical "-" Signals their Widths Enlarged from 137 to 688 unit.

Figure 5.16: H, L, and S Values for the Invariant HHOTP During Shift (a) and Scale (b) Effects.

5.2.3 Invariant Continuous Overlapping Triangular Processors

The same principle is used with this type in order to make it invariant but with different centre (C_G) and widths equations. Referring to Figure 5.17 the C_G value is equal to $\sum_{l_o=1}^{c_m} l_o P_R(l_o) / \sum_{l_o=1}^{c_m} P_R(l_o)$, where c_m is defined by Equation 5.10. The C_B value is calculated from Equation 5.12, and the processors widths W_{RGB} are equal to $(C_B - C_G)$.

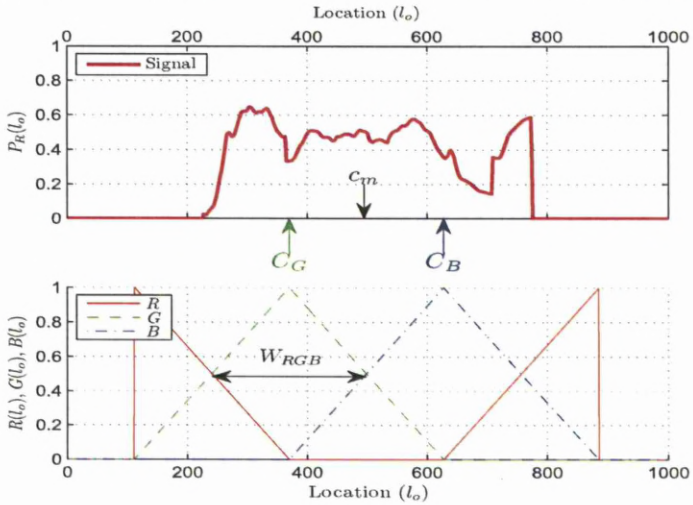

Figure 5.17: Calculated Centres and Widths for COTP Using the Proposed Approach.

The calculated centres and widths are then used to determine the response profiles $(R(l_o), G(l_o), B(l_o))$ for these triangular processors by using the following equations respectively:

$$R(l_o) = \begin{cases} \dfrac{-l_o + C_G}{W_{RGB}} & l_o \in [C_G - W_{RGB}, C_G) \\ \dfrac{l_o - C_B}{W_{RGB}} & l_o \in (C_B, C_B + W_{RGB}] \\ 0 & Otherwise \end{cases} \tag{5.24}$$

$$G(l_o) = \begin{cases} \dfrac{l_o - C_G + W_{RGB}}{W_{RGB}} & l_o \in (C_G - W_{RGB}, C_G) \\ \dfrac{-l_o + C_G + W_{RGB}}{W_{RGB}} & l_o \in [C_G, C_G + W_{RGB}) \\ 0 & Otherwise \end{cases} \tag{5.25}$$

$$B(l_o) = \begin{cases} \dfrac{l_o - C_B + W_{RGB}}{W_{RGB}} & l_o \in (C_B - W_{RGB}, C_B) \\ \dfrac{-l_o + C_B + W_{RGB}}{W_{RGB}} & l_o \in [C_B, C_B + W_{RGB}) \\ 0 & Otherwise \end{cases} \tag{5.26}$$

The outputs (R_o, G_o, B_o) of these processors are then calculated by applying Equations 5.18, 5.19, and 5.20 respectively. The performance of the new processors was also tested with shift and scale effects using two different signals. Figures 5.18 and 5.19 show how these processors adapt their deployments with shift and scale effects respectively to produced robust H and S values as shown in Figures 5.20a and 5.20b.

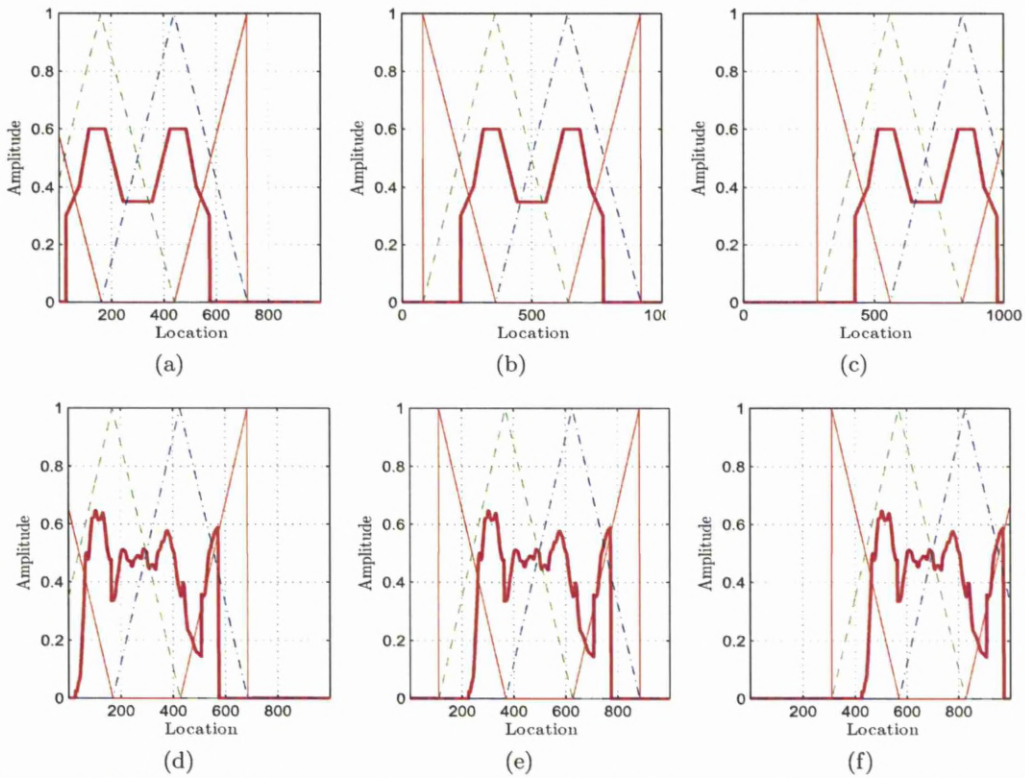

Figure 5.18: Shift Effect on the Symmetrical (a,b,c) and Asymmetrical (d,e,f) Signals.

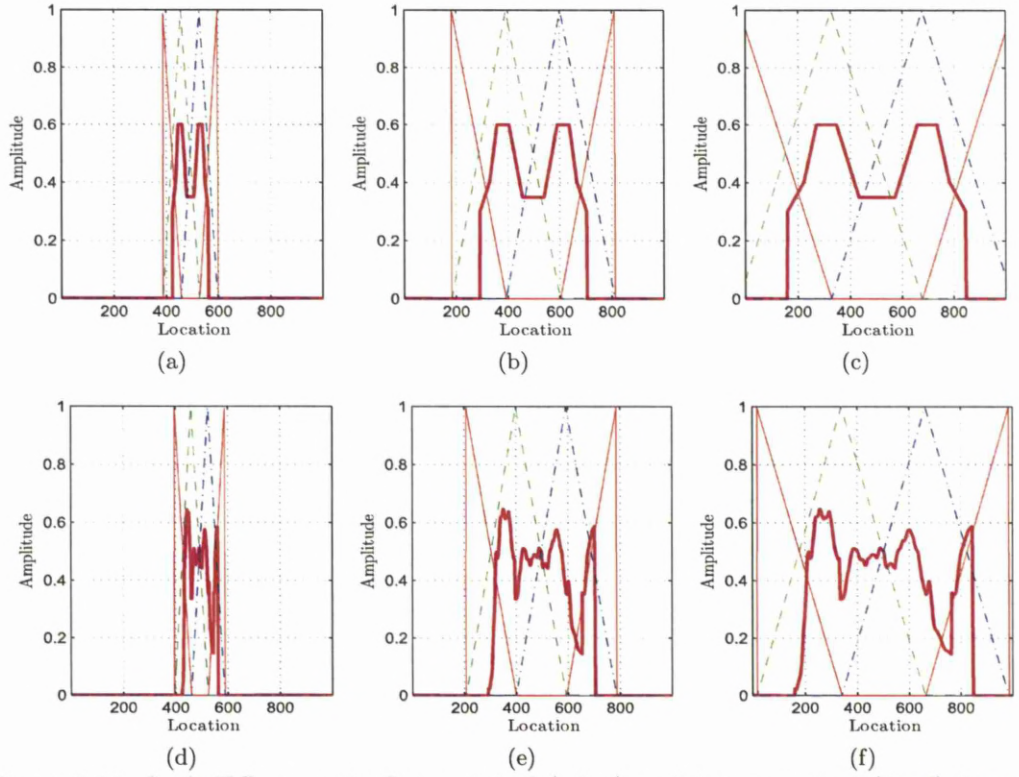

Figure 5.19: Scale Effect on the Symmetrical (a,b,c) and Asymmetrical (d,e,f) Signals.

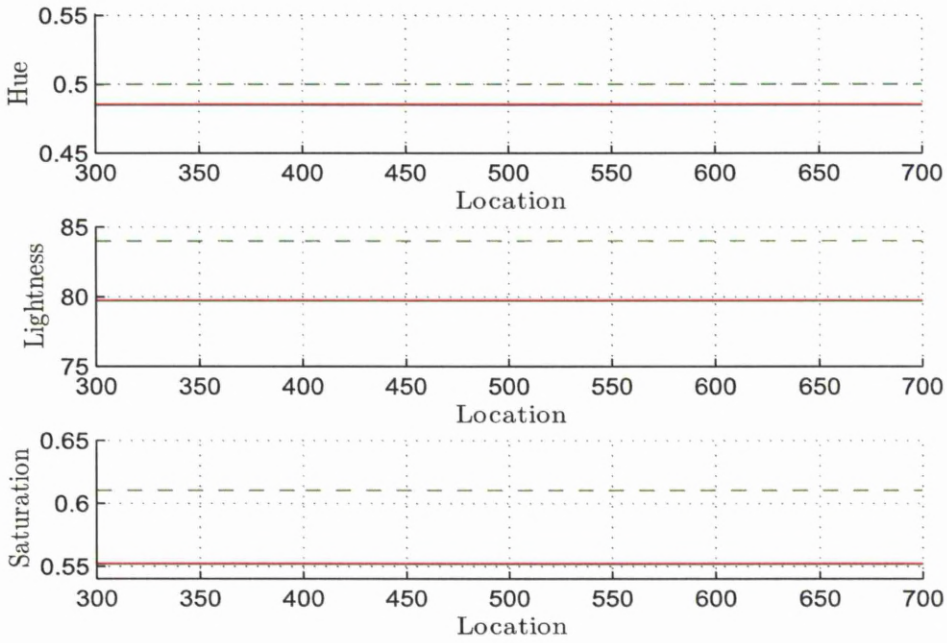

(a) *HLS* Values of Processing Symmetric "- -" and Asymmetrical "-" Signals Moved from Location 300 to 700.

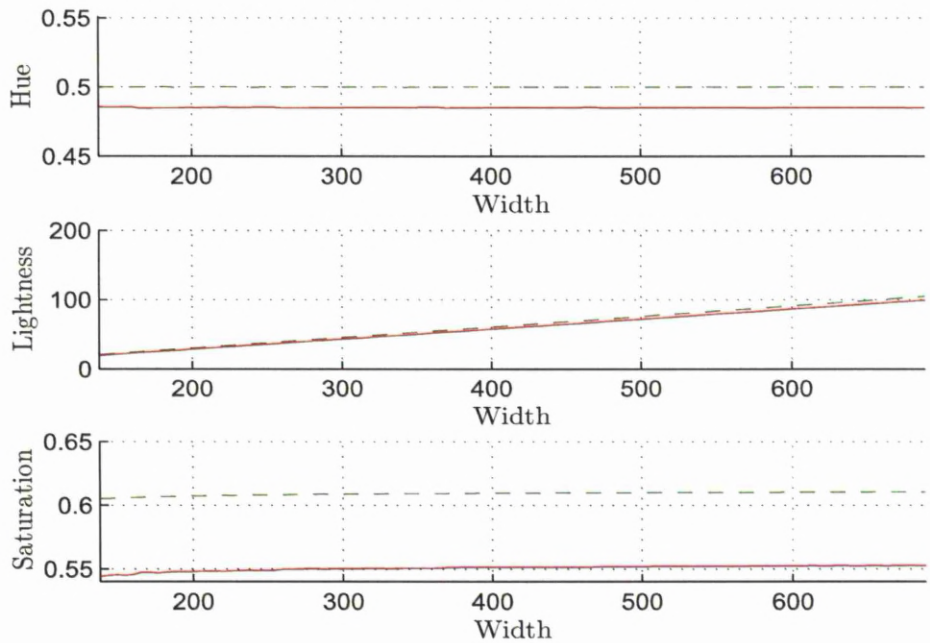

(b) *HLS* Values of Processing Symmetric "- -" and Asymmetrical "-" Signals their Widths Enlarged from 137 to 688 unit.

Figure 5.20: H, L, and S Values for the Invariant COTP During Shift (a) and Scale (b) Effects.

5.3 Invariant Chromatic Descriptors

The proposed descriptors utilise the discrimination ability of the invariant spatial chromatic processors to describe the images with rotational, translational, and scaling invariant features, by applying $n_{\Re}$ sets of these processors on the $n_{\Re}$ numbers of normalised image projections. These projections are calculated by applying Radon transform to the image $f(x_{\Re}, y_{\Re})$ at $n_{\Re}$ number of normalising angles.

Figure 5.21 illustrates the Radon transform geometry for calculating the projection $\Re(l_{\Re}, \theta_{\Re})$ for a an image $f(x_{\Re}, y_{\Re})$ at angle $\theta_{\Re}$.

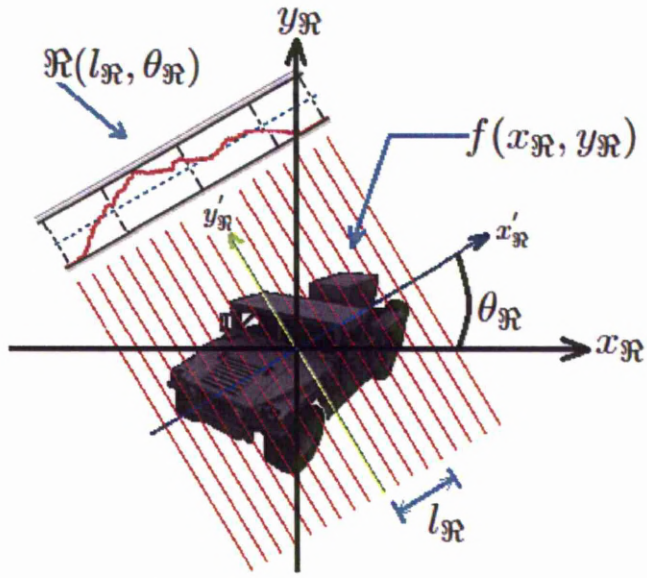

Figure 5.21: Geometry of the Radon Transform.

The Radon transform for this image is the line integral parallel to the $y'_{\Re}$-axis and is defined by the following equation [98]

$$\Re(l_{\Re}, \theta_{\Re}) = \sum_{x_{\Re}=0}^{M_{\Re}-1} \sum_{y_{\Re}=0}^{N_{\Re}-1} f(x_{\Re}, y_{\Re}) \delta(x_{\Re} \cos\theta_{\Re} + y_{\Re} \sin\theta_{\Re} - l_{\Re}) \tag{5.27}$$

where

$l_{\Re}$: is the length of line normal from the origin.

$\theta_{\Re}$: is the angle between the $x_{\Re}$-axis and x'_{Re}-axis.

$N_{\Re}, M_{\Re}$: are the numbers of rows and columns in the image $f(x_{\Re}, y_{\Re})$.

Normalised angles have been widely used in pattern recognition [99–101]. These angles are defined by the following equation:

$$\Phi_{\Theta} = \Phi_o + \Theta \tag{5.28}$$

where

Φ_o: Object rotation angles form the $x_{\Re}$-axis.

Θ: Offset angle, which can take any value to produced different normalized angles.

The object rotation angles Φ_o can be calculated using different methods such as moments [101] and principle component analysis PCA [69, 98]. Further information about the angle calculation procedure is given in Appendix C on page 158.

The calculation of the projections from the normalised angles make them invariant to object rotation. While object translation and scaling effects, make the projections location and size change respectively, without changing the pattern. Therefore applying the translation and scale invariant chromatic processors on these normalised projections make the descriptors features invariant to rotation, translation and scaling effects. In these descriptors the H and S processors outputs are only used without L, because of their robustness to the scale effect and their built-in ability to have a fixed range of values ([0 1]), while L requires normalisation and it is sensitive to scale effect as shown in the previous section.

Figures 5.22 and 5.23 show two projections taken at two normalised angles ($\Phi_0 = \Phi_o+0$ and $\Phi_{90} = \Phi_o+90$) for a car image before 5.22a and after applying rotation 5.22b, translation 5.23a, and scaling 5.23b effects. Comparing with Figure 5.22a, Figure 5.22b shows the similarity between the normalised projections of the rotated image and the original image, while Figures 5.23a and 5.23b show the changed in projections location and size during translation and scaling effects respectively without changing the pattern. These figures also show how the invariant half hight overlapping Gaussian processors changed their centres and widths as the projections change to produced invariant features. Table 5.1 presents the processors output values (H and S) for these normalised projections at angles Φ_0 and Φ_{90}. The output values show the robustness of the chromatic descriptor to produce very similar H, and S values.

Table 5.1: Hue and Saturation Values for the Chromatic Descriptor

Normalized Angle	Φ_0		Φ_{90}	
Processors Outputs	Hue	Saturation	Hue	Saturation
Original Image	0.519	0.087	0.128	0.184
Oriented Image	0.518	0.084	0.129	0.184
Shifted Image	0.518	0.085	0.129	0.183
Enlarged Image	0.518	0.086	0.129	0.184

In order to evaluate the performance of the proposed method of using the invariant processors as image descriptors, more than one thousand grayscale images are used [102]. These images depict one hundred objects of different shapes, each one representing a different class and are subject to different translation, scale, rotation transformations and noise effects (Gaussian and salt pepper noise) to create training and testing sets [103] (See Figure 5.24). The classifier used in all tests was k-nearest neighbour classifier of two k values, which are equal to 1 and 3. This classifier is used with Euclidean distance metric and Majority rule [104].

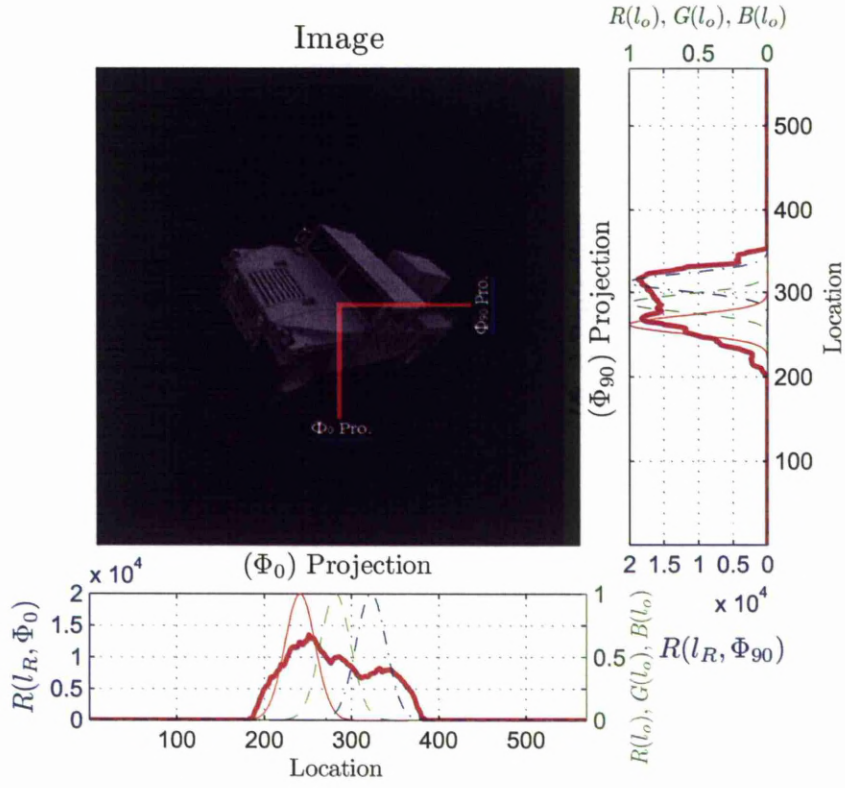

(a) Original Image.

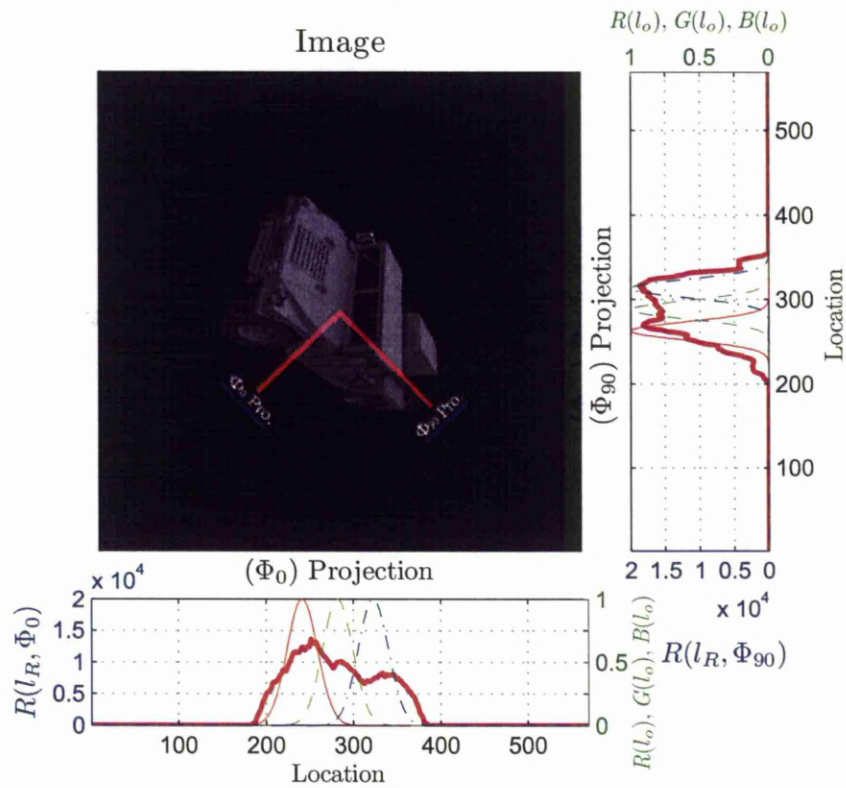

(b) Rotated Image by -46^o.

Figure 5.22: Normalised Projections for Original and Rotated Car Images.

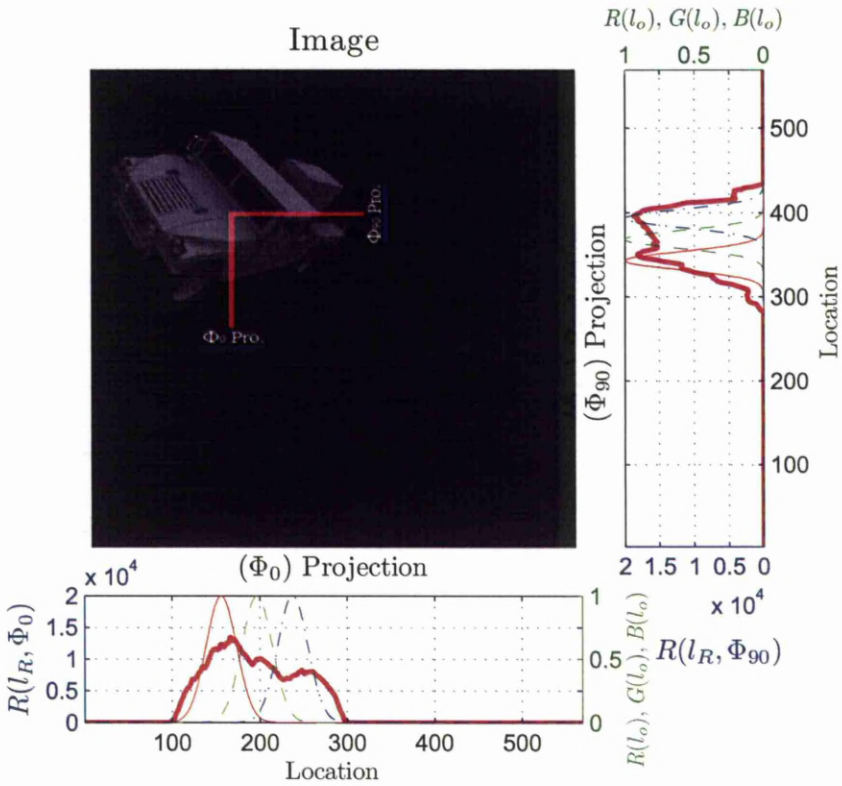

(a) Shifted Image to the Left by 85 location units and to Top by 80 units.

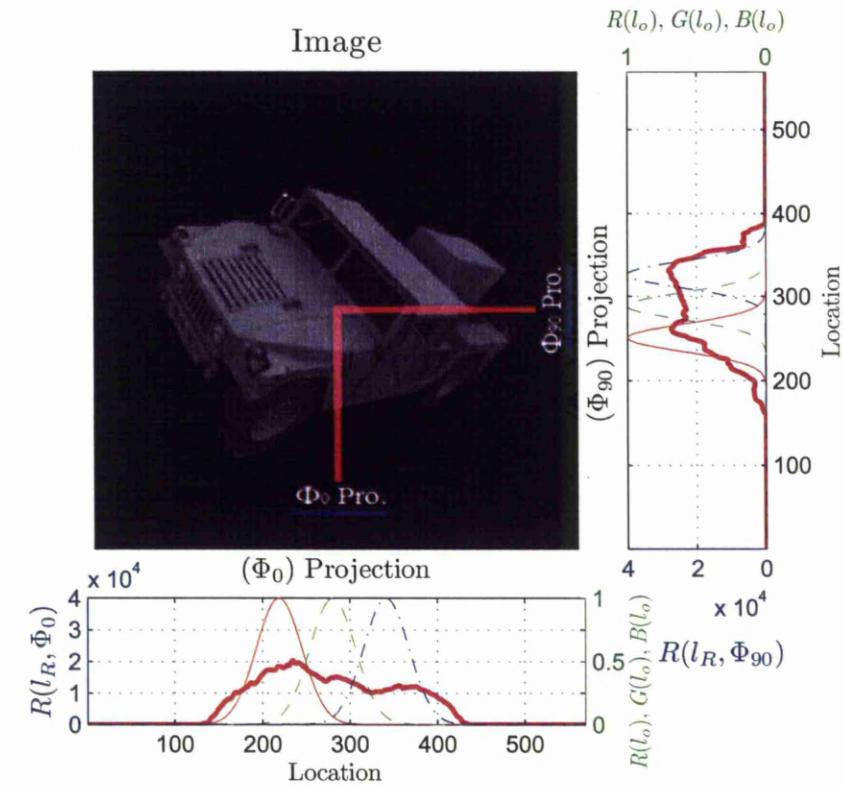

(b) Enlarged Image by One and Half.

Figure 5.23: Normalised Projections of Shifted and Enlarged Car Images.

Figure 5.24: Example of Some Images used for Evaluation the Proposed Method.

In these tests two projections ($\Theta = 0^o$, and 90^o) are processed by invariant HHOGP, where the object rotation angles Φ_o is calculated using the tensors method [101]. The recognition rates for the proposed method and the Moment Invariant descriptor are shown in Table 5.2, where the later is used to benchmark the results [105].

Table 5.2: Recognition Rate for the Proposed Method with the Invariant Moment

Descriptor Type	Chromatic Descriptor		Invariant Moment	
Neighbours Number	k=1	k=3	k=1	k=3
Affine Effects				
Translation by [40, /40]	100%	98%	100%	89%
Scaling by 0.3	92%	89%	91%	83%
Scaling by 1.2	100%	98%	100%	91%
Rotation by 45^o	100%	98%	99%	88%
Rotation by 270^o	100%	98%	100%	89%
Gaussian Noise Effects				
Variance equal to 2%	65%	65%	25%	29%
Variance equal to 6%	34%	31%	9%	11%
Salt Pepper Noise Effects				
Density equal to 2%	94%	94%	79%	71%
Density equal to 6%	78%	75%	39%	42%
Average Performance	84.77%	82.88%	71.33%	65.88%

The simulation results show that for k equal to one, the recognition rate between the Invariant Moments and the proposed method are comparable when subjected to affine effects. When the k value is equal to three, the performance for both are decreased, but with better performance for the proposed method over the Moments.

During noise effect test, two types of noise were applied. Each noise was applied at two different levels. With Gaussian noise, the performances for descriptors decreased with increase variance level for both k values. And for Salt Pepper noise the recognition rate also decreased with increase density level for both k values. For both types of these noises the proposed method shows higher performance than the Invariant Moment.

5.4 Invariant Chromatic Descriptors for LADAR Data Processing

LADAR data processing has been focused on dealing with robust target features that are relatively unaffected by the noise that usually disturb the LADAR measurements. One such unaffected feature is the silhouette image of the 3D LADAR data [54]. Figure 5.25 shows scan data of a tank from the LADAR perspective 5.25b and in a rotated view 5.25a. While the range data shows significant noise (background, photo counting, and speckle with fully coherent laser light) the LADAR view shows a relatively smooth appearing image. This smoothness comes from the high pointing accuracy of the LADAR in comparison to the noise and distortion of the range measurement [54].

However, the silhouette still can suffer from perspective effects. This making it appear different at varying ranges [106, 107]. To overcome this problem, the 3D LADAR neighbour points were connecting with each other using triangular connections. Figures 5.26c and 5.25c show the triangular connection for the distorted (Figure 5.26a) and undistorted (Figure 5.25a) data respectively. The resultant triangles are then projected orthogonally on regular grid of a defined size and resolution in order to generate a regular silhouette image. Figures 5.25d and 5.26d show the resultant silhouette images for the distorted and undistorted LADAR point cloud data respectively. The figures also show the similarity between these two images. More information about the silhouette image generation process is given in Appendix D on page 159.

The silhouette image is then processed by the proposed chromatic descriptors that mentioned in the section 5.3. Figures 5.27 and 5.28 show two projections taken at two normalised angles ($\Phi_0 = \Phi_o + 0$ and $\Phi_{90} = \Phi_o + 90$) for the tank silhouette image shown in Figure 5.25d before 5.27a and after applying rotation 5.27b, translation 5.28a, and scaling 5.28b effects. The changes in the invariant half hight overlapping Gaussian processors response profiles with respect to the projections changes are also shown in these figures.

Table 5.3 presents the processors output values (H and S) for these normalised projections at angles Φ_0 and Φ_{90}. The output values show the ability of the chromatic descriptor to process the LADAR silhouette images and produce robust features values (H, S) with rotation, translation and, scaling effects.

Table 5.3: Hue and Saturation Values for the Chromatic Descriptor

Normalized Angle	Φ_0		Φ_{90}	
Processors Outputs	Hue	Saturation	Hue	Saturation
Original Image	0.200	0.062	0.214	0.087
Oriented Image	0.204	0.061	0.215	0.086
Shifted Image	0.204	0.061	0.213	0.089
Enlarged Image	0.203	0.061	0.214	0.088

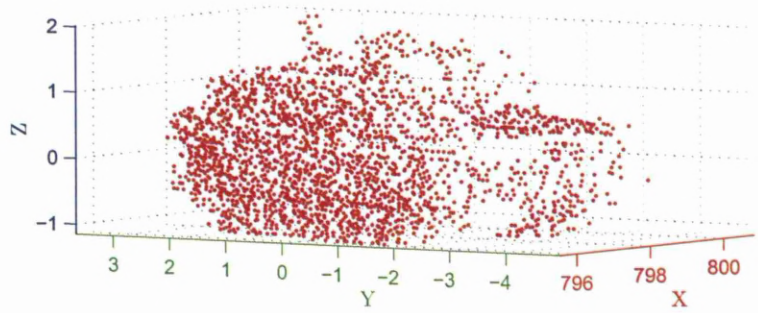

(a) Scan Data of a Tank from Rotated View.

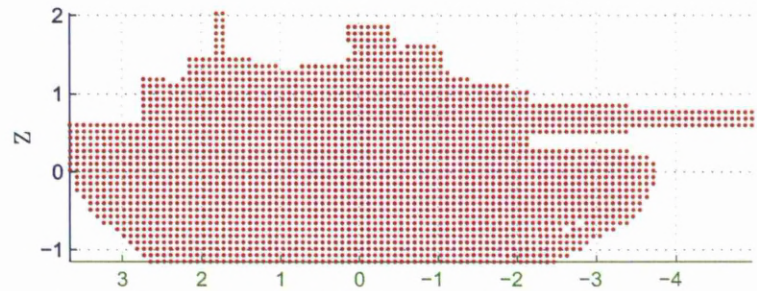

(b) Scan Data of a Tank from the LIDAR Perspective View.

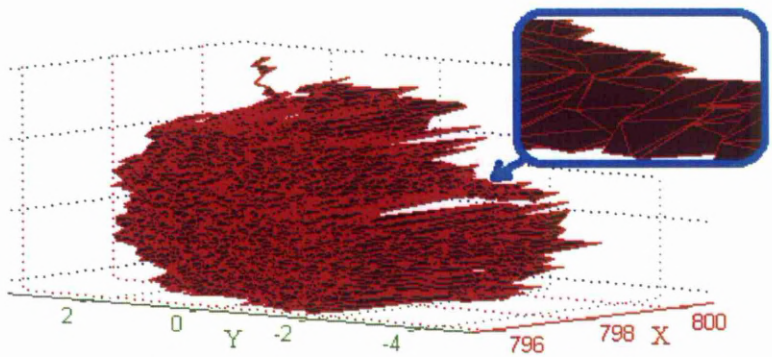

(c) Triangular Connection for the Neighbor Points.

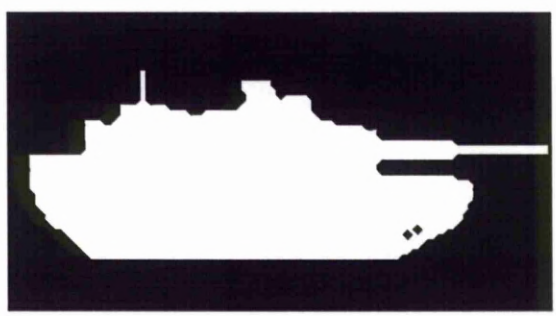

(d) Resultant Silhouette Image.

Figure 5.25: Silhouette Image Generation from Distorted LADAR Data.

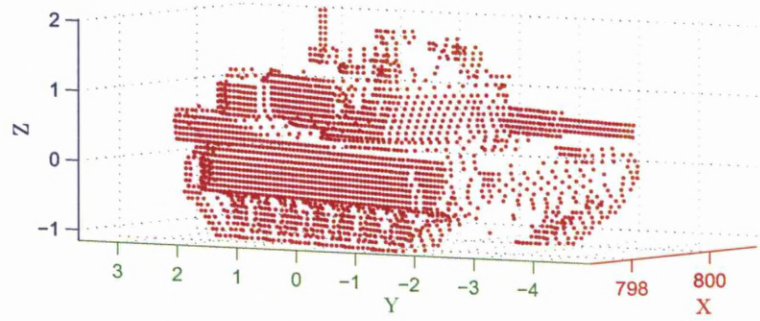

(a) Scan Data of a Tank from Rotated View.

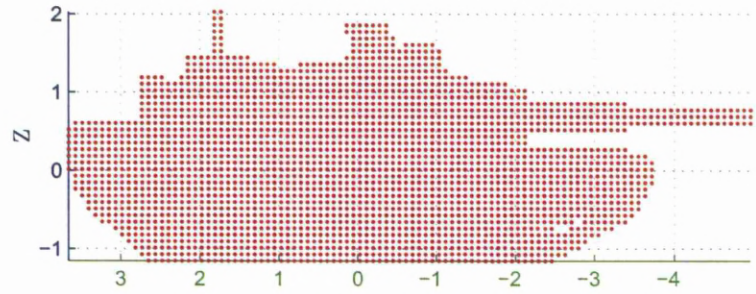

(b) Scan Data of a Tank from the LIDAR Perspective View.

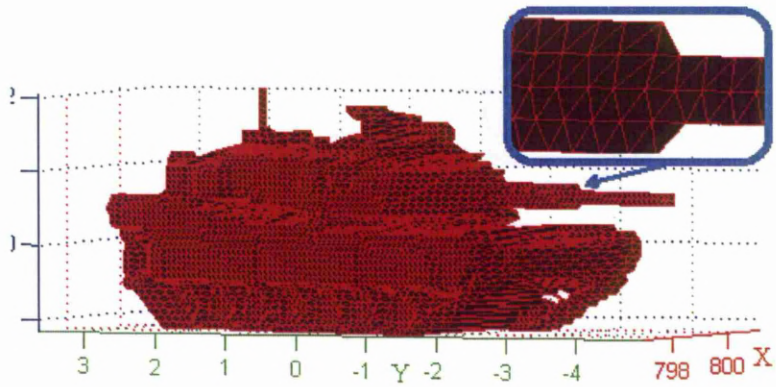

(c) Triangular Connection for the Neighbor Points.

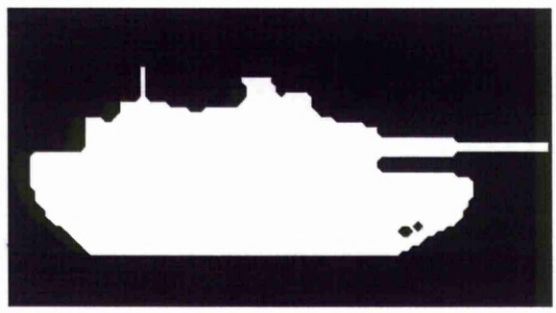

(d) Resultant Silhouette Image.

Figure 5.26: Silhouette Image Generation from Undistorted LADAR Data.

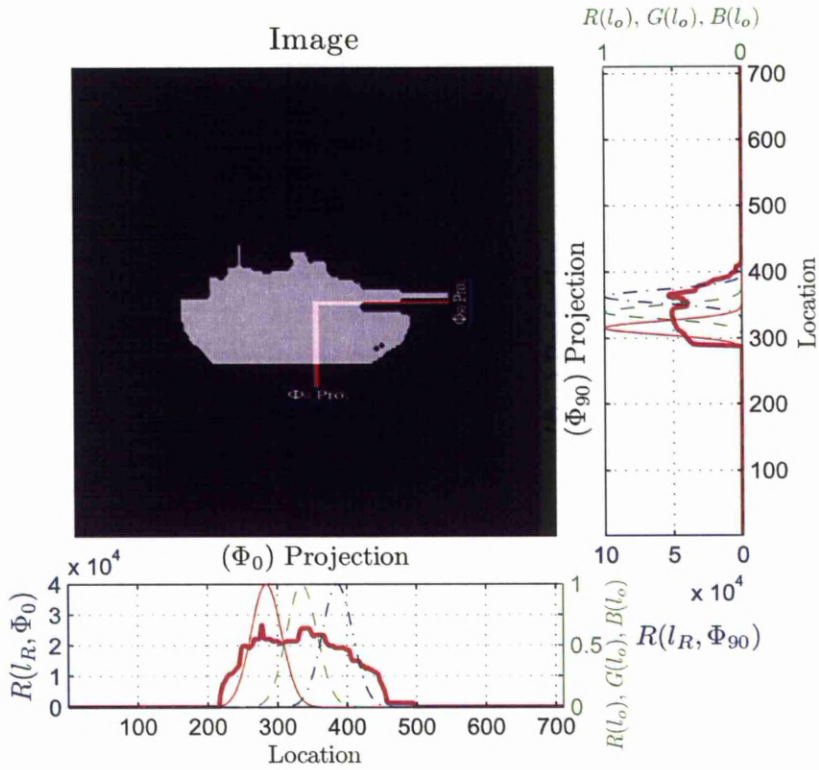

(a) Original Image.

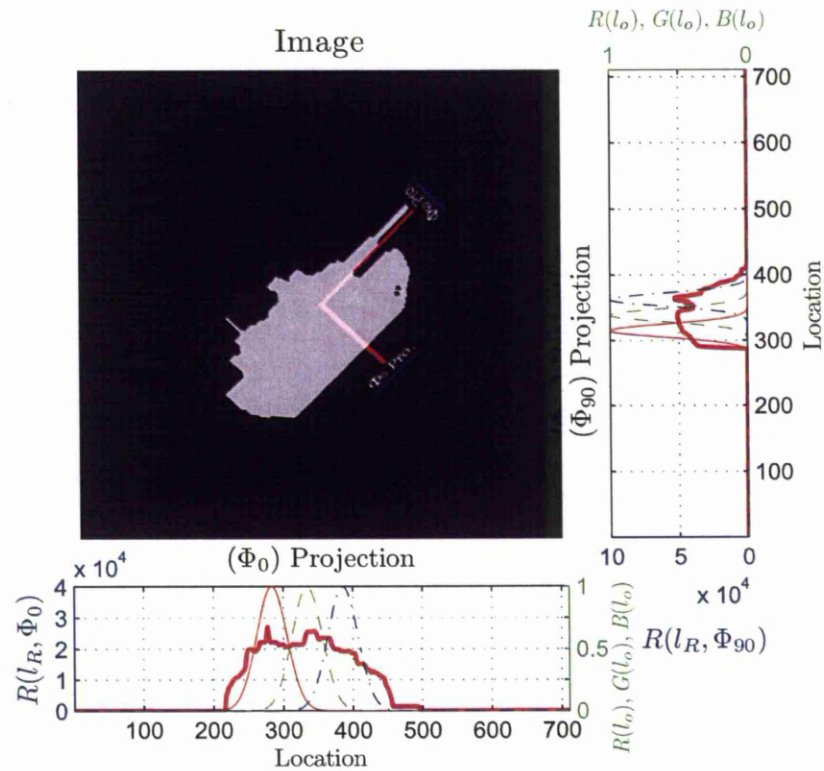

(b) Rotated Image by 46°.

Figure 5.27: Normalised Projections for Original and Rotated Tank Images.

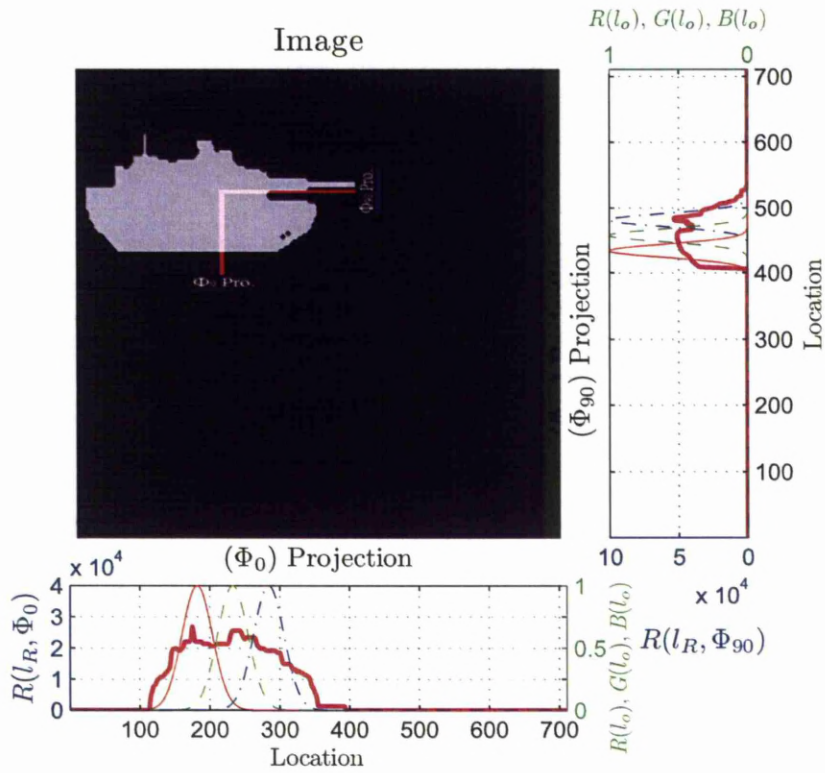

(a) Shifted Image to the Left by 100 location units and to Top by 120 units.

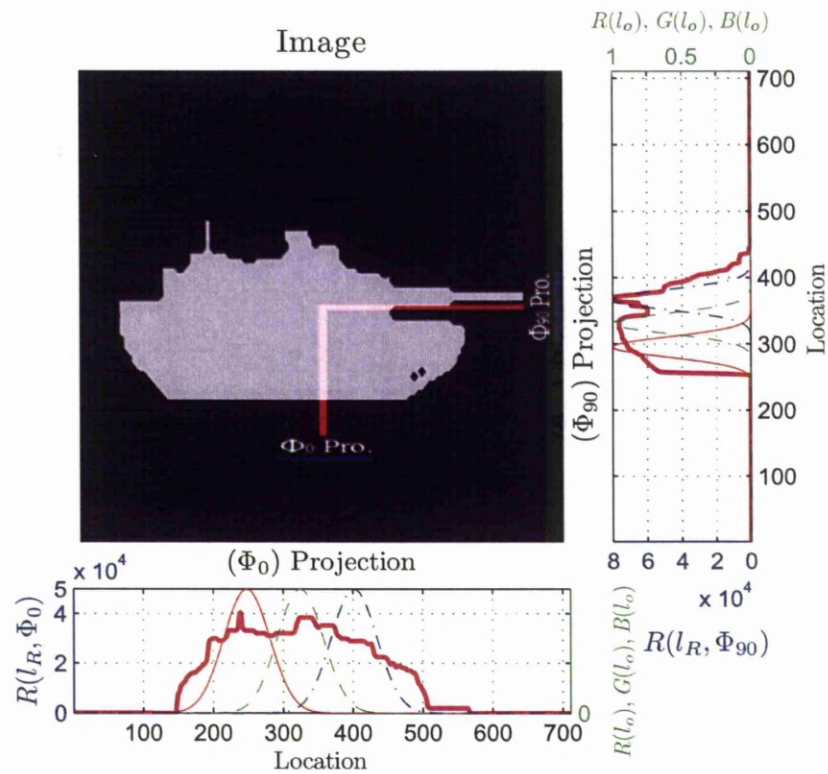

(b) Enlarged Image by One and Half.

Figure 5.28: Normalised Projections of Shifted and Enlarged Tank Images.

5.5 Summary

New LADAR image descriptors are proposed. These descriptors are able to extract invariant features from the LADAR silhouette images based on using proposed types of chromatic processors called 'invariant spatial chromatic processors'.

Three types of these processors are described with the proposed approach to making them invariant. These are Invariant Half Height Overlapping Gaussian Processors, Invariant Half Height Overlapping Triangular Processors, and Invariant Continuous Overlapping Triangular Processors. The methods of using these new types of processors as image descriptors to describe the images with invariant rotation, translation, and scaling features is also presented.

The proposed method is tested with different objects at varies affine transformation (rotation, translation and scaling) and distortion (Gaussian and salt pepper noise) effects and its performance was compared with the Invariant Moment descriptor. The simulation results show, a comparable performance between them during affine effects with better performance for the chromatic descriptor during distortion effect.

Finally the proposed approach of using the new chromatic descriptors with LADAR data processing (starting from generating the silhouette image and ending with extracting the chromatic features from it) is explained by presenting some results that show the robustness of these descriptors.

The proposed descriptors are simple and their discrimination abilities can be easily extended by either increase the processors number or using additional image projections.

Chapter 6

Testing Methodology and Simulation Results

Introduction

This chapter presents the methodology for evaluating the performance of the new chromatic descriptors with LADAR data processing using simulated LADAR data. The purpose of using this kind of data is to evaluate the performance of these descriptors in controlled environments. This allow decoupling of the different effects that influence the descriptors performance and characterise their impact.

In this chapter, four sections are presented. The first section gives an explanation about the method that is used for generating both the training and the testing sets. The second and third sections describe the procedure for testing these descriptors and present the results of these tests. The last section presents the summary for this chapter.

6.1 LADAR Data Sets

The new chromatic descriptors are tested on a set of 60 3D CAD models taken from 3DVIA and ARTIST 3D model libraries [108, 109]. These models are first simplified to have less than 6000 faces using MeshLab (advanced mesh processing software) [110] and rescaled to their actual sizes. The models then splits into ten classes depending on their general shapes. Figures 6.1, 6.2, and 6.3 show the 3D CAD models used in testing the new chromatic descriptors. These figures also show the division of these models into ten classes, where each frame colour represents an individual class type, and the models that have the same frame colour are classified under the same class type. Table 6.1 presets the models labels for each class with the corresponding colour.

The LADAR point clouds are then generated using LADAR Simulator (previously described in chapter 3) that emulates LADAR system with the scanning parameters shown in Table 3.1. Two sets from these point clouds are generated: a training sets of models or reference scans, and several testing sets of scene or query scans.

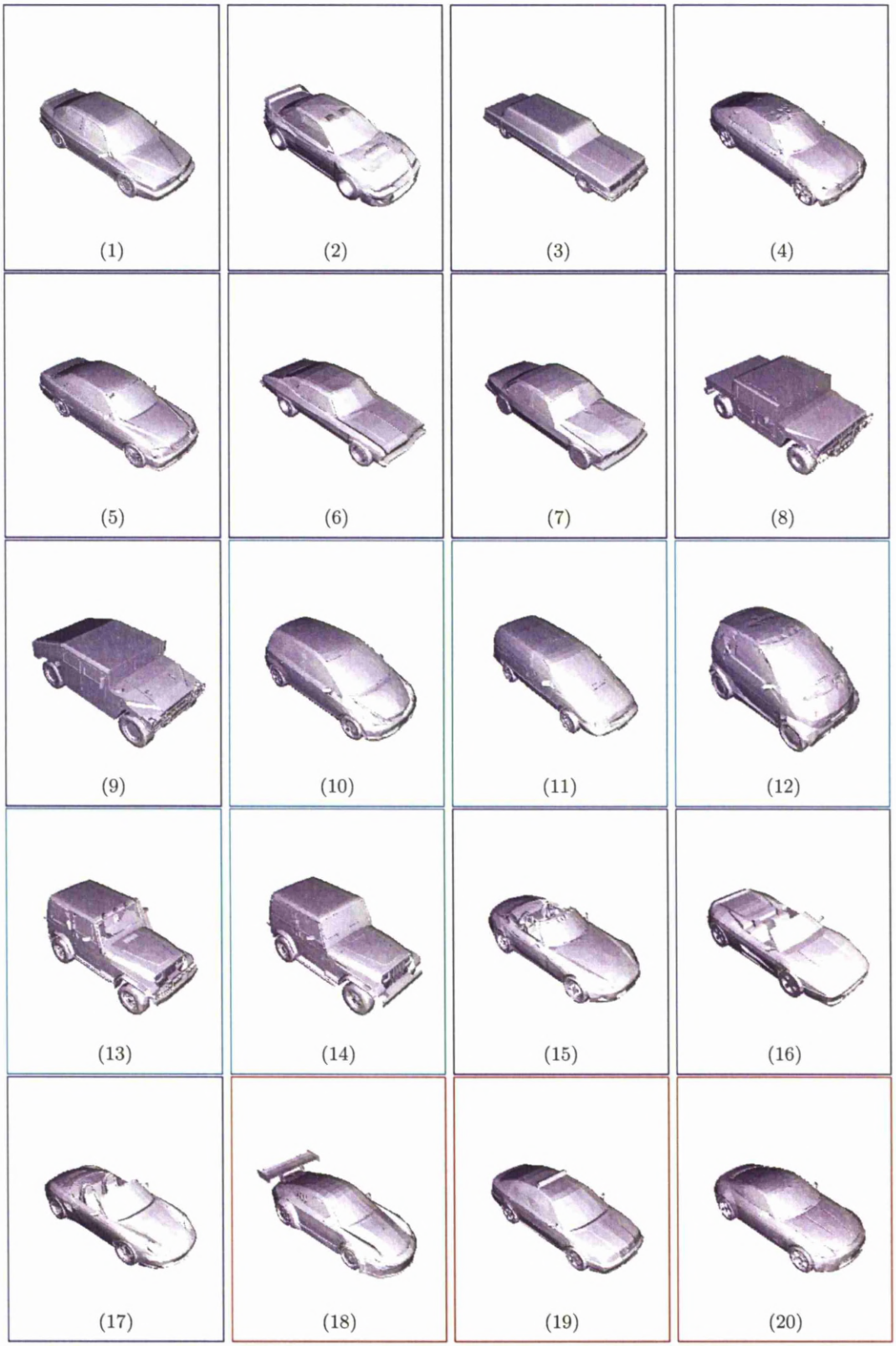

Figure 6.1: 3D CAD Models (1-20)

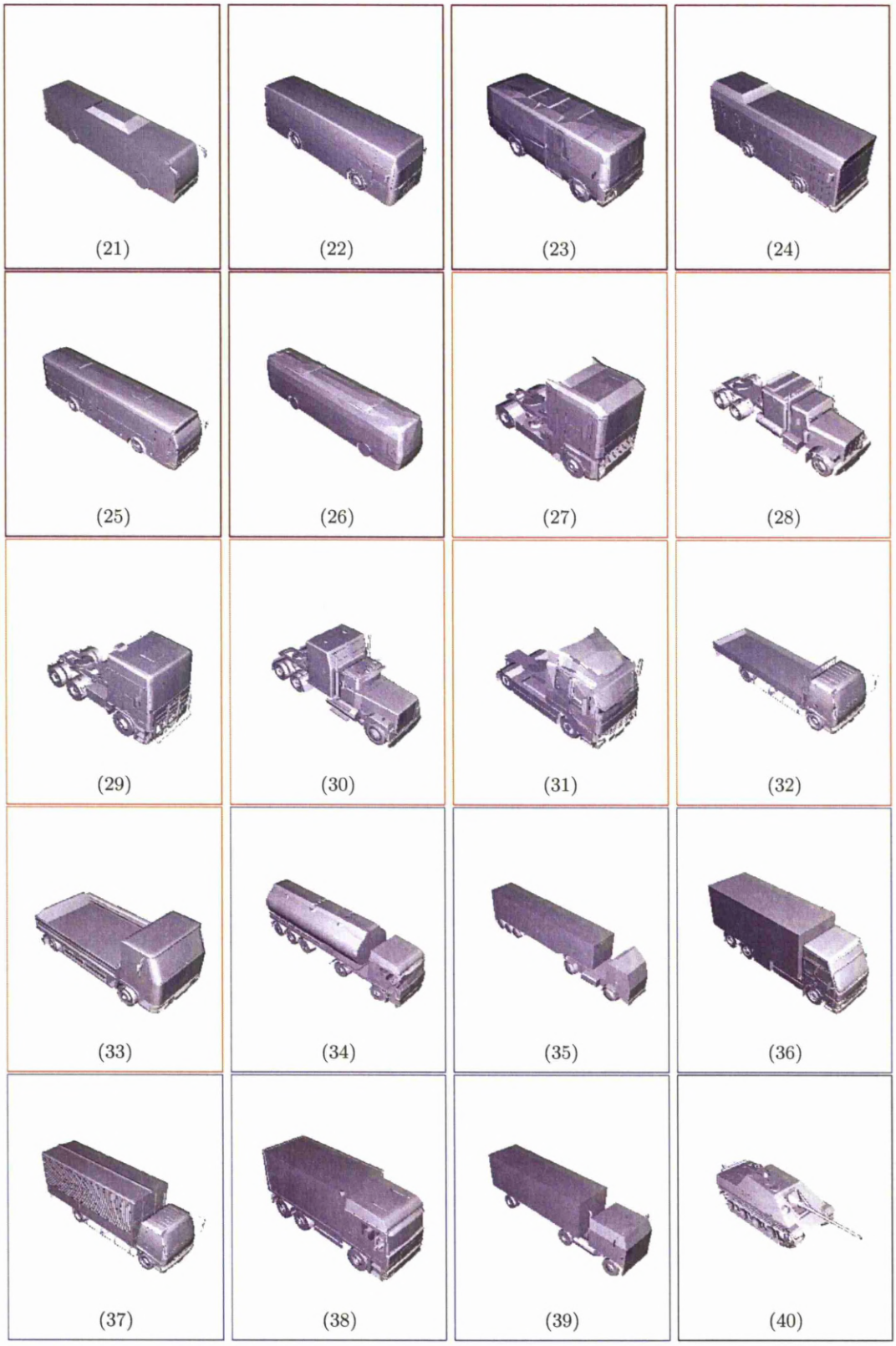

Figure 6.2: 3D CAD Models (21-40)

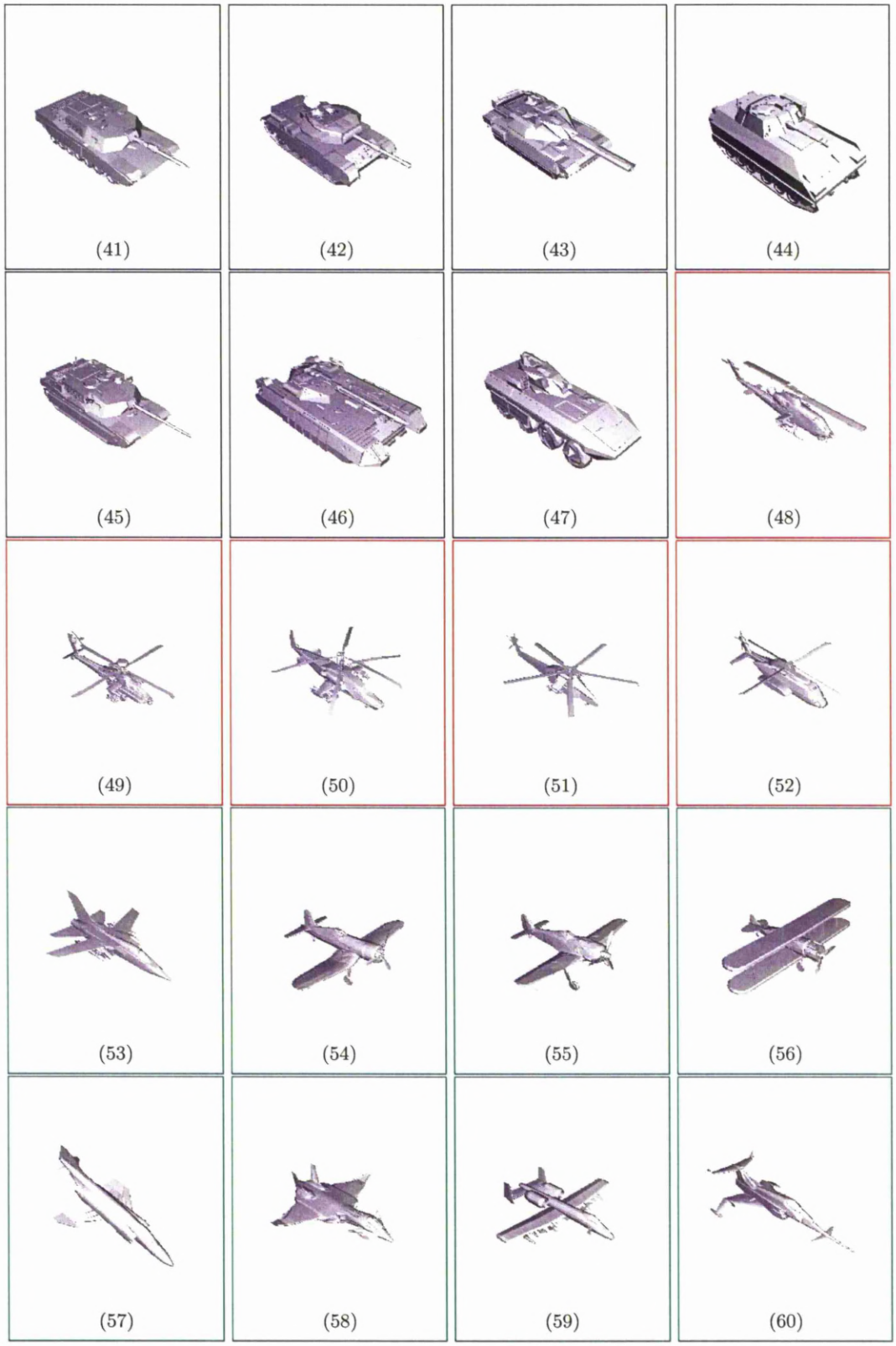

Figure 6.3: 3D CAD Models (41-60)

Table 6.1: Class and Models Labels

Class Label	Model Label	Models Number	Color
1	1-9	9	Blue
2	10-14	5	BlueGreen
3	15-17	3	BlueViolet
4	18-20	3	BrickRed
5	21-26	6	Brown
6	27-33	7	BurntOrange
7	34-39	6	CadetBlue
8	40-47	8	Black
9	48-52	5	Red
10	53-60	8	Green

6.1.1 Training Sets

There are two training sets are generated. The samples for the first set are taken by rotating each model around its vertical axis in 15^o angular intervals (0^o, 15^o, 30^o, 45^o, 60^o, 75^o, 90^o, 105^o, 120^o, 135^o, 150^o, 165^o, 180^o, 195^o, 210^o, 225^o, 240^o, 255^o, 270^o, 285^o, 300^o, 315^o, 330^o, and 345^o) at range equal to $600\,m$ from the sensor [54, 58, 111, 112]. This will generate 24 scans per model with a total of $1,440$ scans in the training set. Figure 6.4 shows some point clouds of Humvee model after applying the above procedure. The second training set is generated in a similar manner, except that the rotation will start at 5^o instead of 0^o, which will be used in testing the view effect.

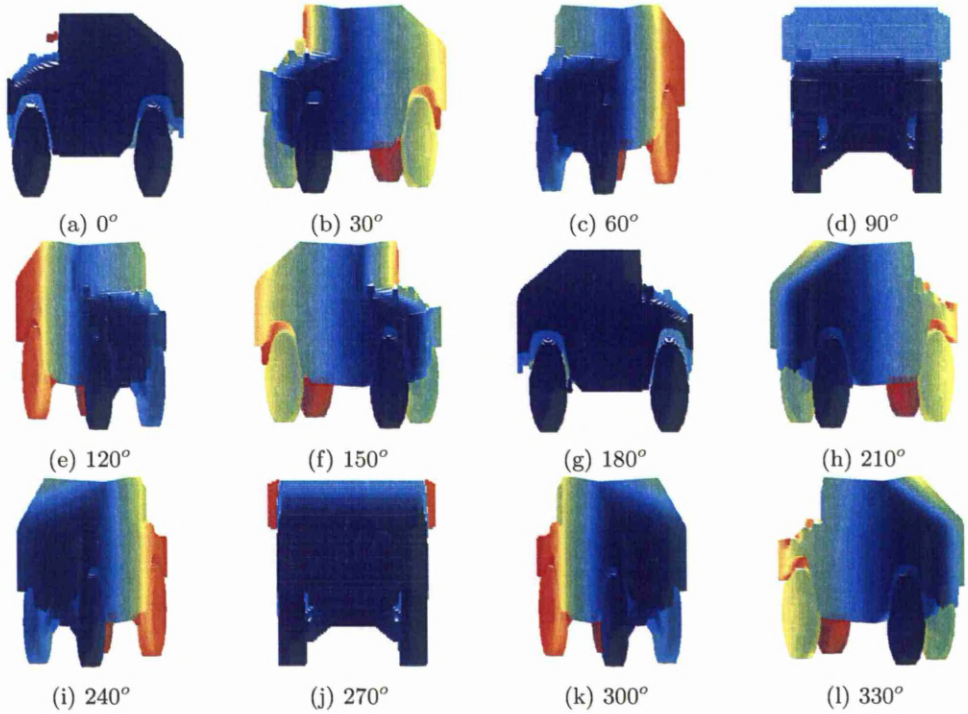

(a) 0^o (b) 30^o (c) 60^o (d) 90^o

(e) 120^o (f) 150^o (g) 180^o (h) 210^o

(i) 240^o (j) 270^o (k) 300^o (l) 330^o

Figure 6.4: Point Clouds of Scanning Humvee Model from Different Views (Near-Far).

6.1.2 Testing Sets

The testing sets are consist from 12 sets. Each set contains 5,760 scans, which they generated from scanning 60 models from 24 different views at four different ranges ($600\,m$, $800\,m$, $1000\,m$, and $1200\,m$) after applying specific effect [54, 58, 111, 112]. These effects include: noise, resolution, view, scaling, rotation, and translation. Thus for 12 testing sets the total number of scans that are generated is equal to 69,120 scans. The 24 view angles for all testing sets, are equal to these of the first training set except one testing set in which the rotation starts at 7.5^o instead of 0^o. This last set will be used with additional testing set in order to test the impact of the view effect on the descriptors performance (more explanation will be presented in subsection 6.3.3).

6.2 Testing Procedure

The testing procedure consists of two phases, which are the training phase and the testing phase. In the first phase the classifier is trained with the chromatic features that results from applying three different types of chromatic descriptors on the training sets after converting them to silhouette images. In each descriptor three projections are used at $\Theta = 0^o$, 45^o, and 90^o, which leads to produce a feature vector of six invariant features (two for each projection). These chromatic descriptors are:

- **Half Height Overlapping Gaussian Descriptor** (HHOGD): which is used Invariant Half Height Overlapping Gaussian Processors.
- **Half Height Overlapping Triangular Descriptor** (HHOTD): which is used Invariant Half Height Overlapping Triangular Processors.
- **Continuous Overlapping Triangular Descriptor** (COTD): which is used Invariant Continuous Overlapping Triangular Processors.

The classifier used is k-nearest neighbour classifier of two k values, which are equal to 1 and 3. This classifier is used with Euclidean distance metric and a Majority rule, in which the sample point is assigned to the class the majority of the k nearest neighbours are from [104]. In the testing phase the chromatic descriptors (six features per descriptor) are applied on the testing sets after converting them to silhouette images. In each testing set four types of confusion matrices are generated for each specific descriptor at each range (four ranges per testing set). These matrices represent a useful tool for evaluating the recognition performance [111–114]. The first type of these matrices is shown in Figure 6.5 and represents the recognition of the model that the enquiry scan belongs to using classifier of k=1. The second type that shown in Figure 6.6 is similar to the previous type except that the classifier is used with k=3. The third and the fourth types shown in Figure 6.7 represent the recognition of the class that the enquiry scan belongs to using classifier of k value equal to 1 and 3 respectively.

Referring to Figures 6.5, 6.6, and 6.7, the vertical axis of the confusion matrix is the model/class, the enquiry (test) scan belongs to, while on the horizontal axis is the model/class that the classifier decides the test scan most closely matches. Values in the confusion matrix represent the number of times the test scans on the left was recognised as the model/class at the top. Correct recognition occurs on the main diagonal where the test scan is associated with the correct model/class it belongs to [54, 58, 115].

After calculating these matrices, two performance metrics are calculated for each one to evaluate the descriptors, which are average recognition rate (recall) and average precision [115, 116]. The recognition rate for a certain model/class (which is shown at the right of confusion matrix) is defined as the percentage of correctly predicted records among all records in model/class [115, 116]. The precision for a certain model/class (which is shown on the bottom of confusion matrix) is defined as the percentage of correctly predicted records among all predicted records in model/class [115, 116].

The resultant values for these confusion matrices are then plotted with the distance value (i.e. Range) as shown in Figure 6.8. Therefore, if a specific effect is applied on the testing set, the impact of that effect will be evaluated at each range. In order to evaluate the overall impact of specific effect at all ranges, the previously mentioned confusion matrices types are recalculated but this time with all ranges as shown in Figures 6.9, 6.10, and 6.11. The resultant average recognition rate and precision for these matrices are very helpful when more than one effect is compared.

The testing procedure is also applied on the Invariant Moment descriptor to benchmark the results, where its feature vector is composed of seven invariant moments. These moments are considered as efficient features that can be used to describe images. This fact has been benefited in using invariant moment values as tools in LADAR target classification [60], synthetic aperture radar (SAR) target recognition [117], object detection [118], aircraft identification [119], 3D model retrieval [120] and other application [121–123]. Further information about this descriptor and its invariant moments is given in Appendix E on page 161.

Referring to Figure 6.8, which presents the model and class average recognition rates and precisions for the chromatic descriptors and the invariant moment at each range with using two k values (1,3). Generally all the graphs show that, both the average recognition rates and precisions decrease when the range increases. The results also show that, average class recognition rates and precisions are less effected by the range change comparing with the average model recognition rates and precisions. The results show, that the k value effects the recognition performance. Both class and model average recognition rates and precisions are slightly decrease when the number of k values increases from 1 to 3. As a comparison between the descriptors, the result show a comparable performance between the chromatic descriptors and the reduction in their performance with the range lower than for the invariant moment.

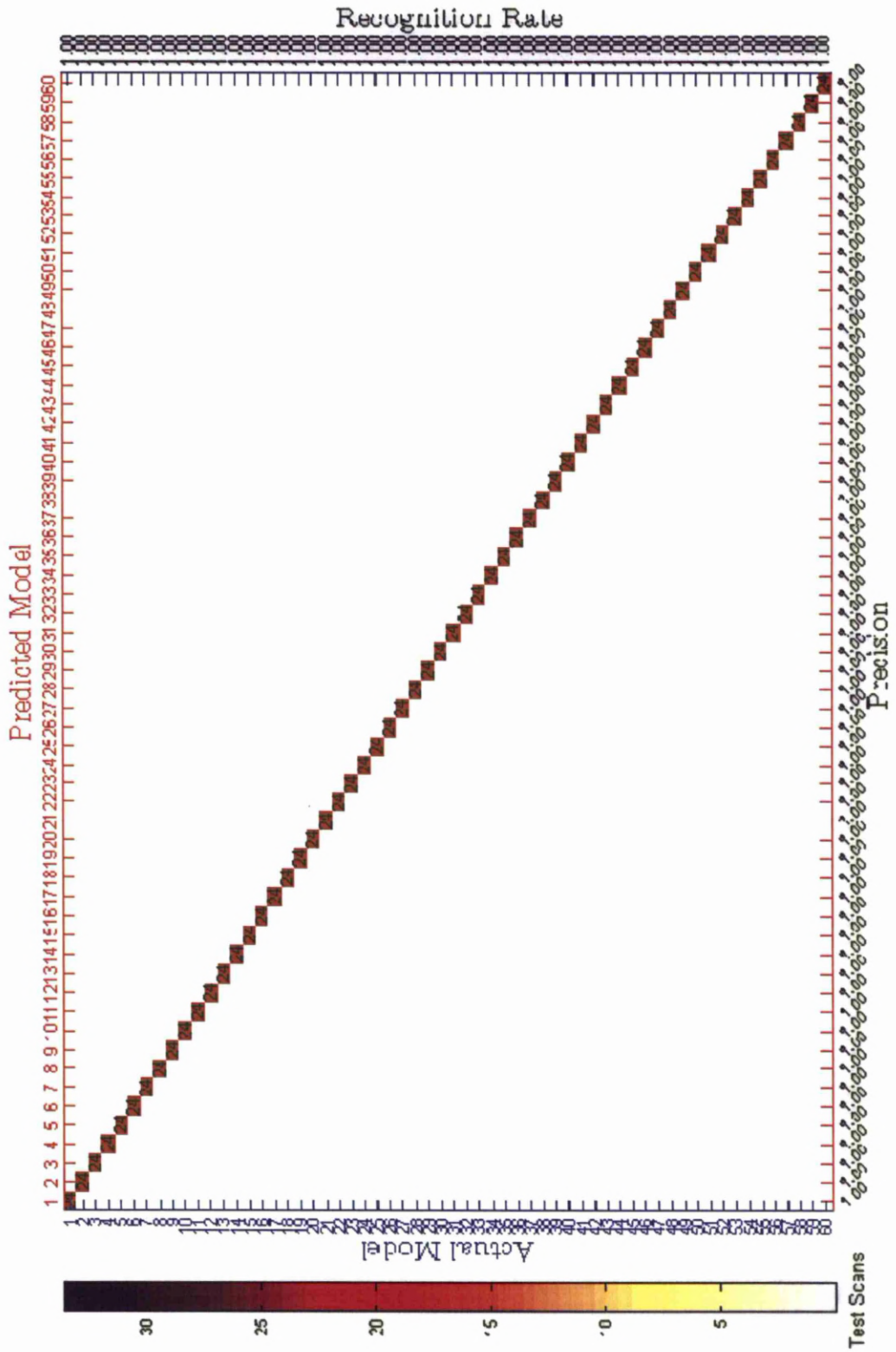

Figure 6.5: Model Confusion Matrix (k=1) with Recognition Rate and Precision for HHOGD (Range= 600 m).

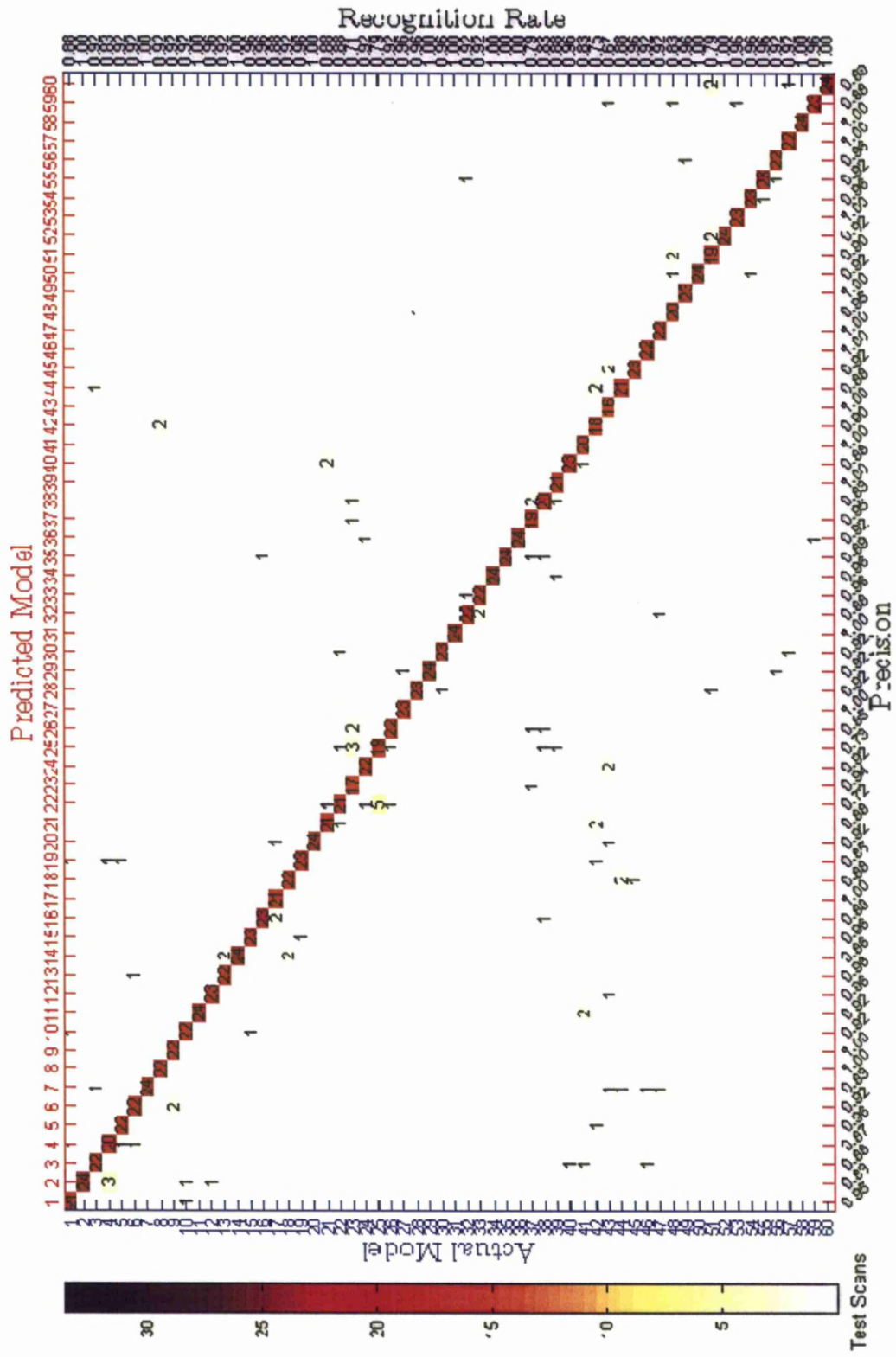

Figure 6.6: Model Confusion Matrix (k=3) with Recognition Rate and Precision for HHOGD (Range= 600 m).

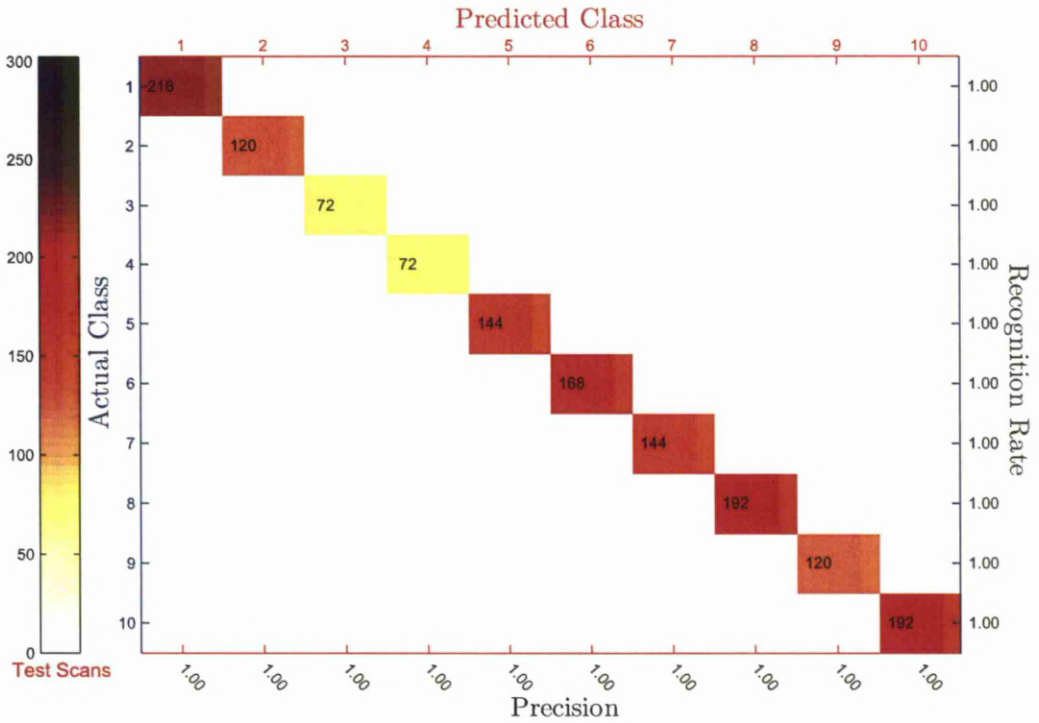

(a) Class Confusion Matrix (k=1).

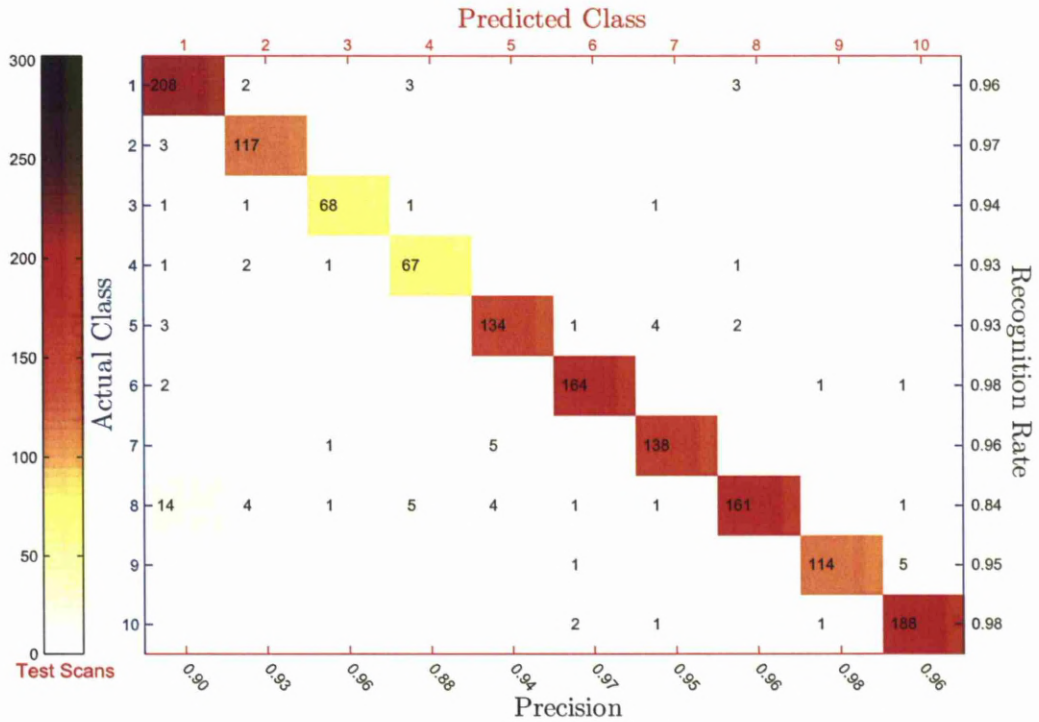

(b) Class Confusion Matrix (k=3).

Figure 6.7: Class Confusion Matrix with Recognition Rate and Precision for HHOGD (Range= 600 m).

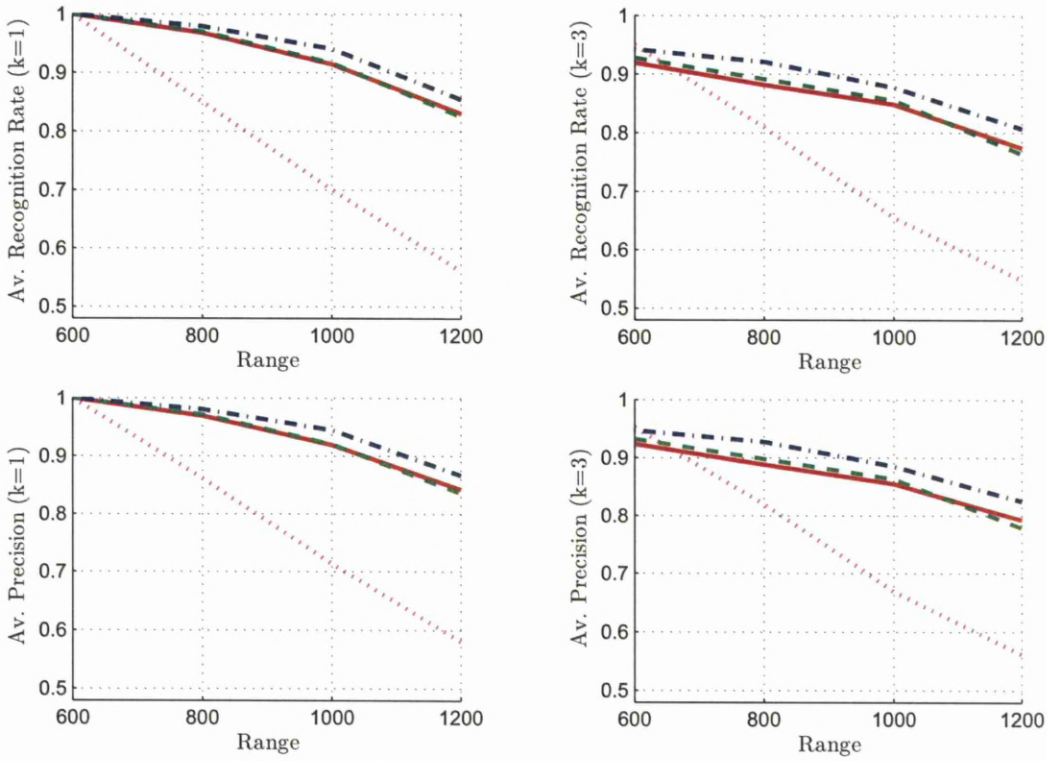

(a) Average Model Recognition Rate and Precision.

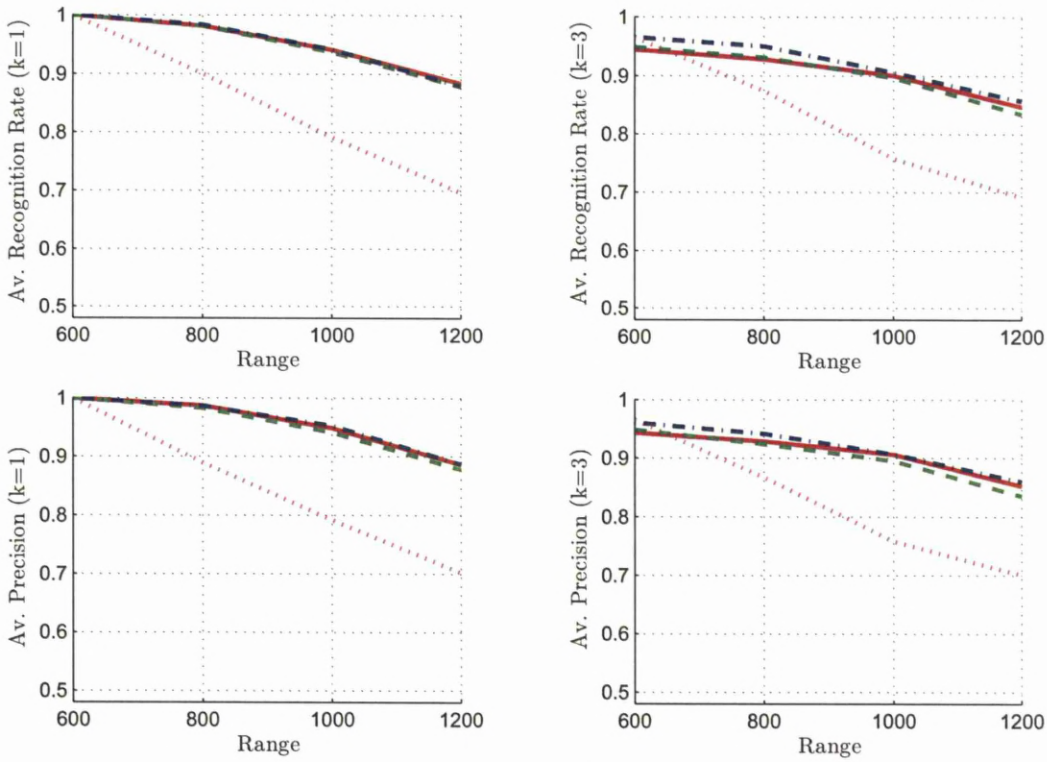

(b) Average Class Recognition Rate and Precision.

Figure 6.8: Average Recognition Rate and Precision with Range (without effect) for HHOGD "-", HHOTD "- -", COTD "-.-", and Invariant Moment "." Descriptors.

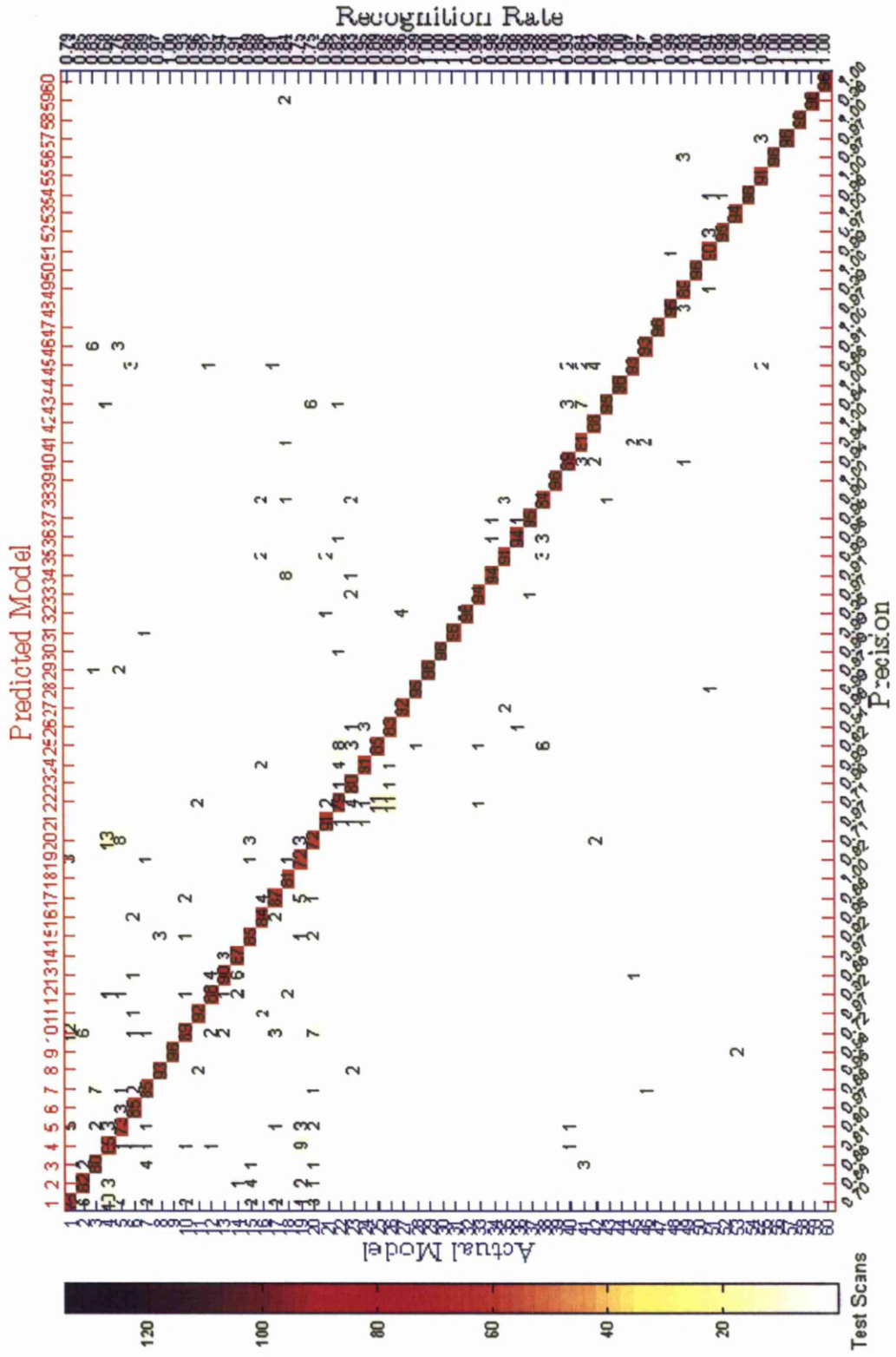

Figure 6.9: Model Confusion Matrix (k=1) with Recognition Rate and Precision for HHOGD (All Range Combined).

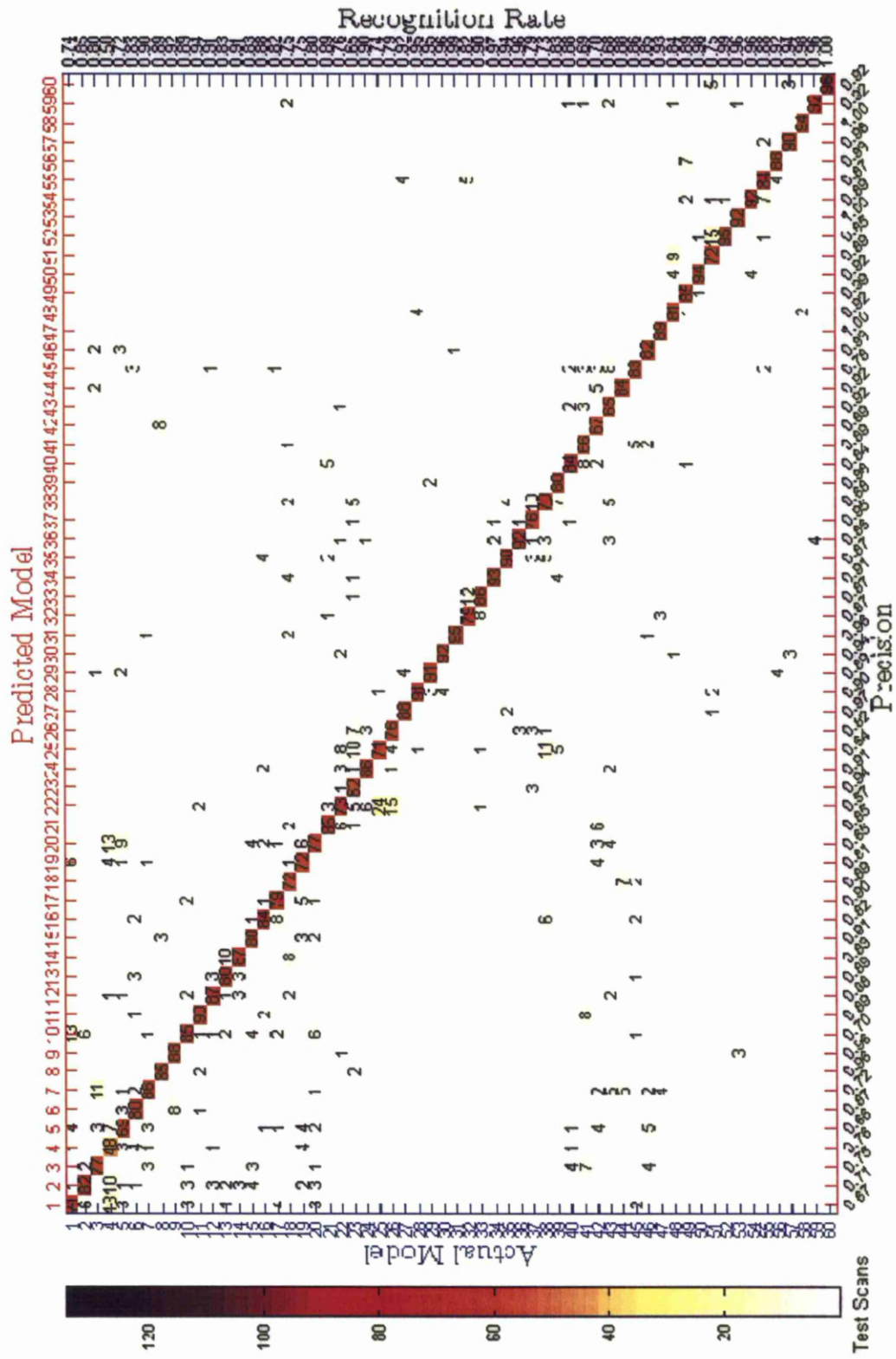

Figure 6.10: Model Confusion Matrix (k=3) with Recognition Rate and Precision for HHOGD (All Range Combined).

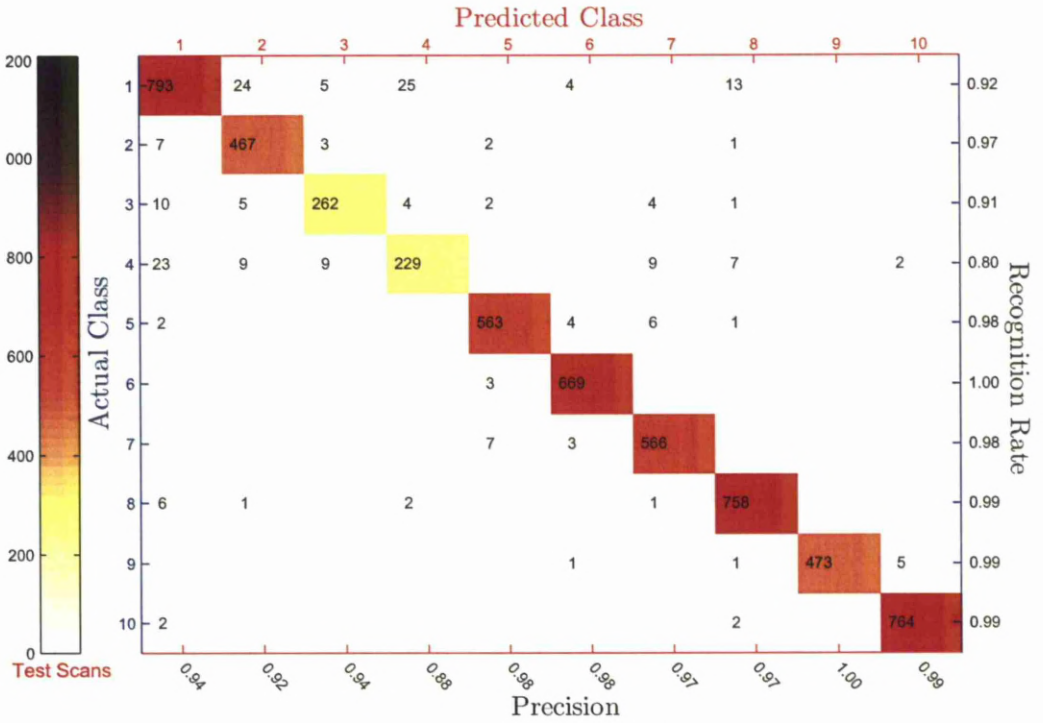

(a) Class Confusion Matrix (k=1).

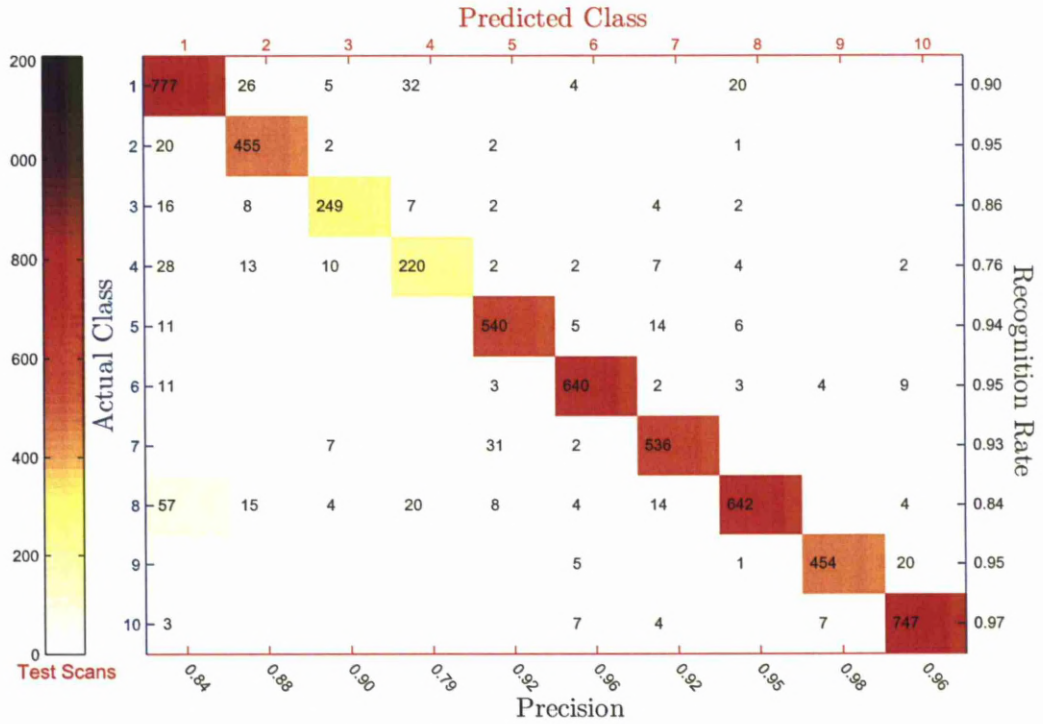

(b) Class Confusion Matrix (k=3).

Figure 6.11: Class Confusion Matrix with Recognition Rate and Precision for HHOGD (All Range Combined).

6.3 Simulation Results

This section presents the simulation results for noise, resolution, view, scaling, rotation, and translation effects.

6.3.1 Noise Effect

In order to evaluate the impact of the LADAR noise on the descriptors performance, all the 3D CAD models are scanned from 24 different views at four ranges after activating the effect of background, photo counting, and speckle noises with fully coherent laser light ($M_{CH} = 1$). Another two sets are then generated but with $M_{CH} = 50$ and 100 respectively. Figure 6.12 shows the effect of applying these noise types of different M_{CH} values on the resultant point clouds of Humvee car model. The simulation results for these testing sets at each range are shown in Appendix F.1. While the simulation results for these three sets at all ranges, are presented together in Figure 6.13. For all graphs in this figure, $M_{CH} = 150$ mean no noise were applied.

The simulation results in Figure 6.13 show that, both the average recognition rates and precisions are approximately constant for the chromatic descriptors with increasing noise level, but they decrease when the invariant moment used. The results also show that, the average class recognition rates and precisions are slightly higher than those of model recognition. The recognition performance is slightly higher with k=1. As a comparison between the descriptors, the result show lower performance for the moment comparing with the chromatic descriptors, which have a comparable performance in class recognition with slightly better performance for the COTD in model recognition.

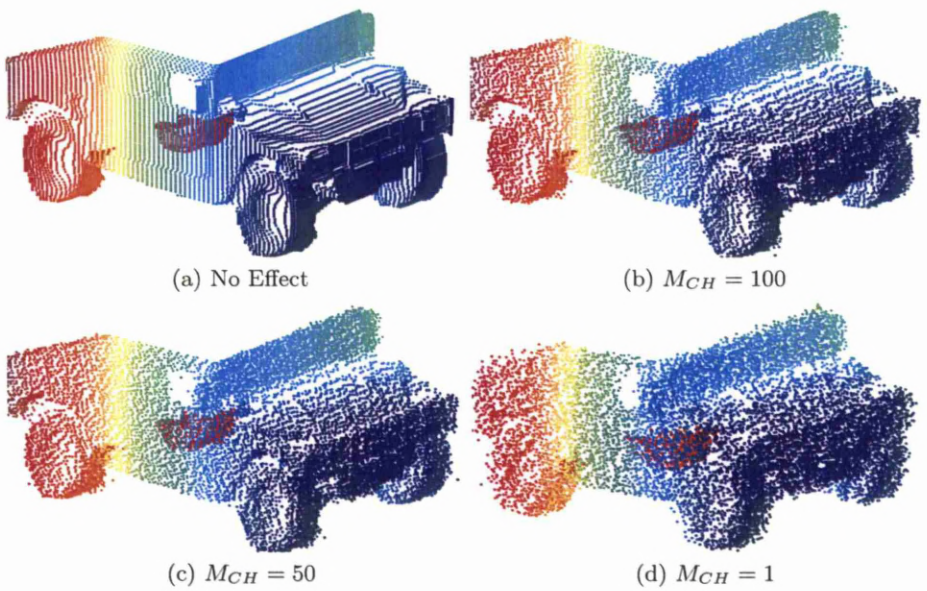

(a) No Effect (b) $M_{CH} = 100$

(c) $M_{CH} = 50$ (d) $M_{CH} = 1$

Figure 6.12: Point Clouds of Humvee Model at Different Noise Levels (Near-Far).

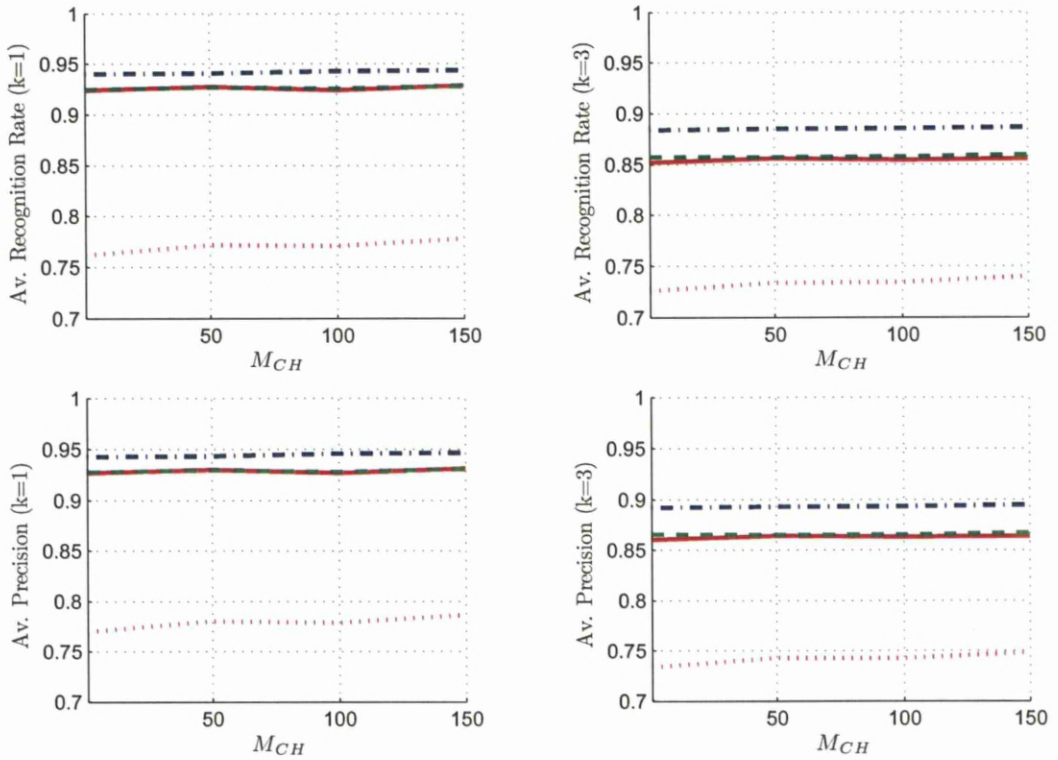

(a) Average Model Recognition Rate and Precision.

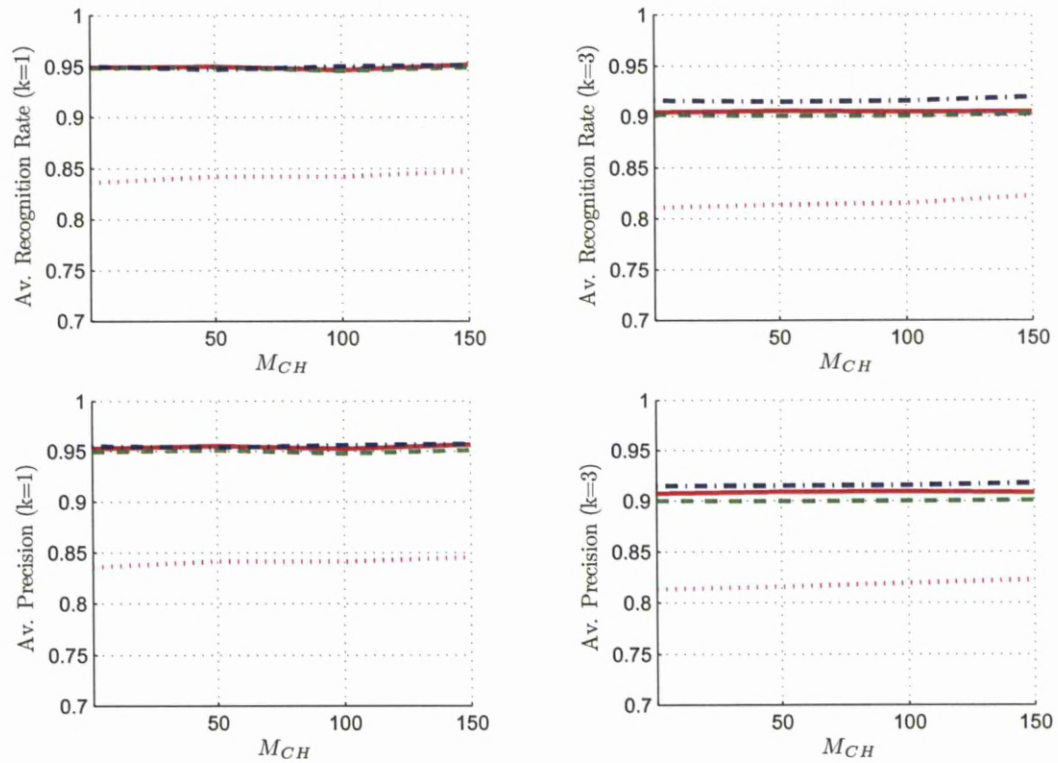

(b) Average Class Recognition Rate and Precision.

Figure 6.13: Average Recognition Rate and Precision During Noise Effect for HHOGD "-", HHOTD "- -", COTD "-.-", and Invariant Moment "." Descriptors.

6.3.2 Resolution Effect

Three testing sets are generated in the same manner as the previous sets of noise effect, but this time without applying noise. Each set is generated with different scanning resolutions, which are 0.006^o, 0.008^o, and 0.01^o. Figure 6.14 shows the effect of scanning the Humvee model with different resolutions on the resultant point clouds.

The simulation results for these testing sets at each range are shown in Appendix F.2. While the simulation results for these three sets (that represent three different scanning resolutions) at all ranges, are presented together in Figure 6.15.

In Figure 6.15, the simulation results show that, both the average recognition rates and precisions in all graphs decrease when the resolution value increase (i.e. decreasing resolution). The results also show that, average class recognition rates and precisions are less affected by the resolution change comparing with the average model recognition rates and precisions. Regarding the effects of the k value on the recognition performance the results show, that both class and model average recognition rates and precisions decrease slightly when the number of k values increase from 1 to 3. As a comparison between the descriptors, the result show lower performance for the moment compared to the chromatic descriptors, which have a comparable performance with slightly better performance for the COTD.

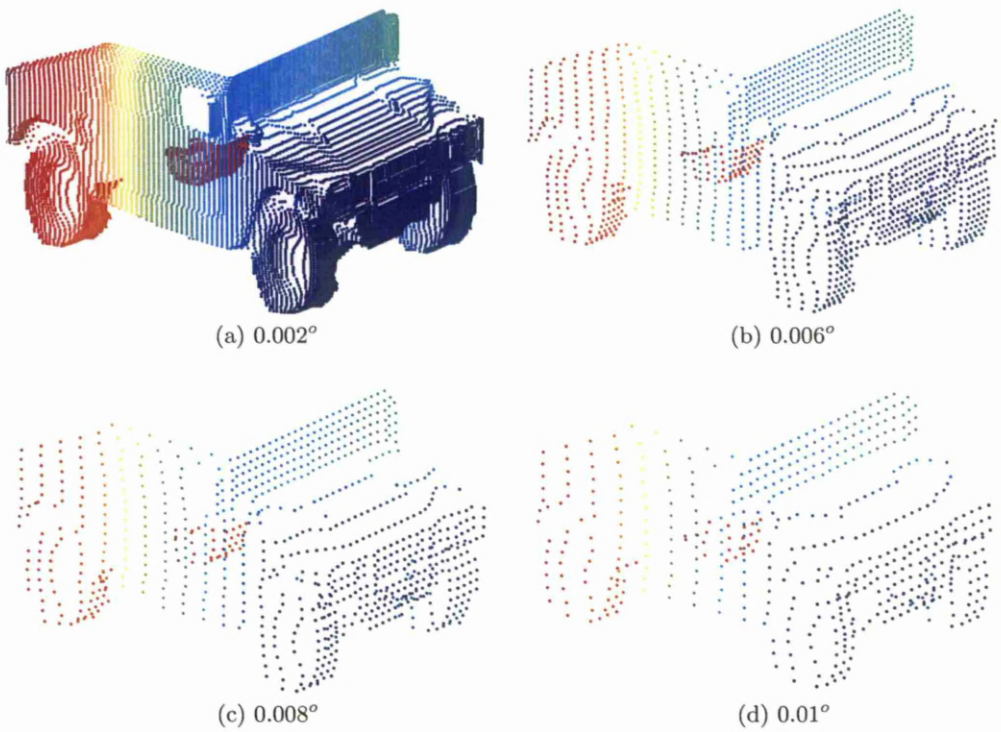

(a) 0.002^o (b) 0.006^o

(c) 0.008^o (d) 0.01^o

Figure 6.14: Point Clouds of Humvee Model at Different Scanning Resolutions (Near-Far).

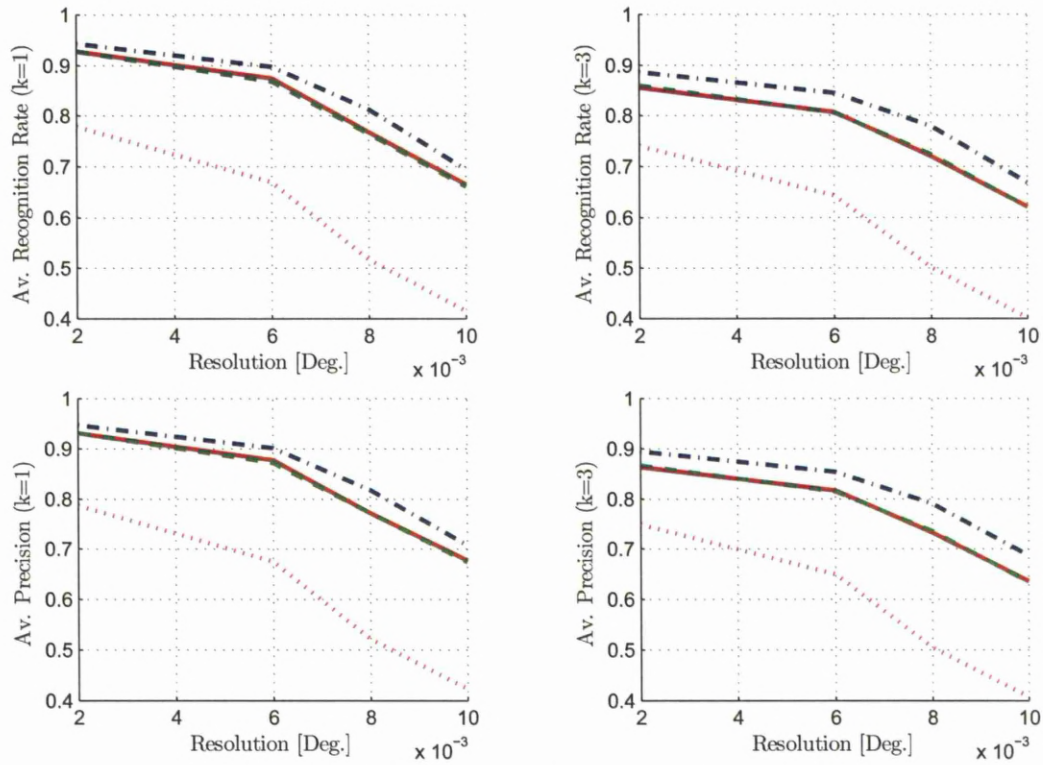

(a) Average Model Recognition Rate and Precision.

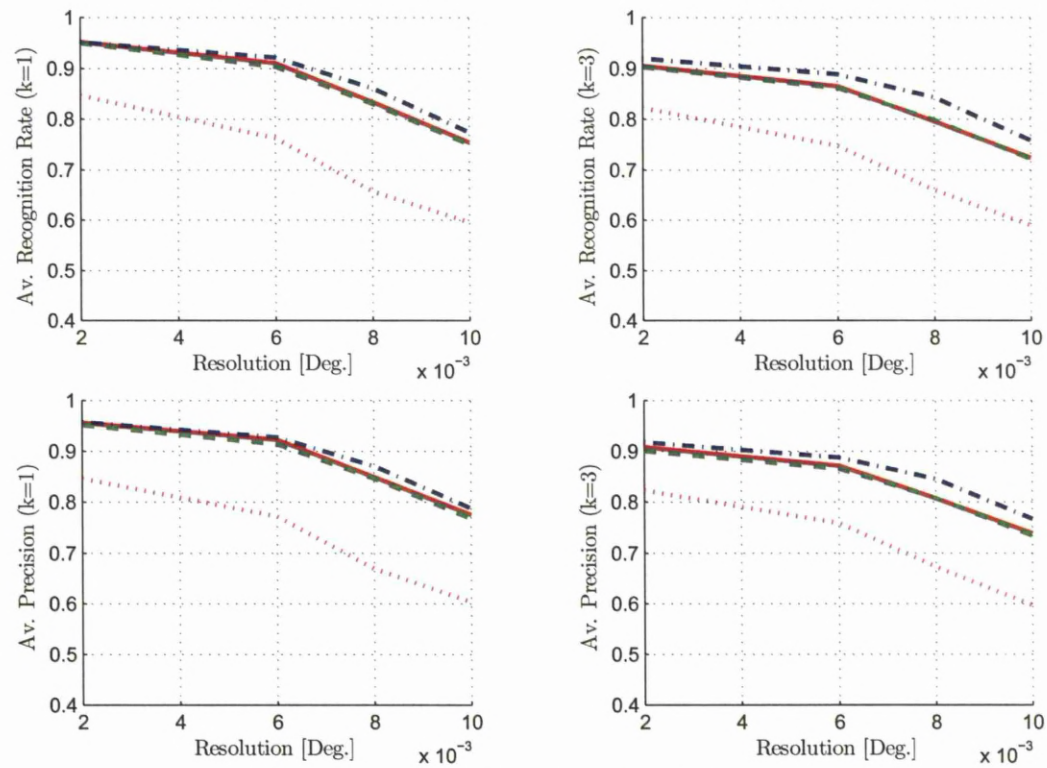

(b) Average Class Recognition Rate and Precision.

Figure 6.15: Average Recognition Rate and Precision During Resolution Effect for HHOGD "-", HHOTD "- -", COTD "-.-", and Invariant Moment "." Descriptors.

6.3.3 View Effect

In order to evaluate the impact of changing the scanning view on the descriptors performance. Two training sets and two testing sets are generated and used to create three differences in view angles, which are equal to 2.5^o, 5^o, and 7.5^o. The training sets are generated by scanning the models from 24 different views at $600\,m$ with angular interval equal to 15^o, where the first view angle for the first and second sets starts at 5^o and 0^o respectively.

The testing sets are generated by scanning models from 24 different views at four different ranges ($600\,m$, $800\,m$, $1000\,m$, and $1200\,m$). The angular interval for both sets is equal to 15^o, where the first view angle for the first and second sets is start from 0^o and 7.5^o respectively. Therefore by using the first training set with both testing sets, produce two differences in view angles (5^o and 2.5^o). And by using the second training set with second testing set, this produce a different in view angle equal to 7.5^o. Figure 6.16 shows the point clouds of the model with three differences in view angles.

The simulation results of the view angle tests at each range are shown in Appendix F.3. While the simulation results for these tests (that represent three differences in view angles) at all ranges, are presented together in Figure 6.17. The simulation results in Figure 6.17, show similar behaviour for the descriptors performance comparing with results of the previous test except that, all the chromatic descriptors have a comparable performance unlike the resolution test in which the COTD has slightly better performance over the other processors.

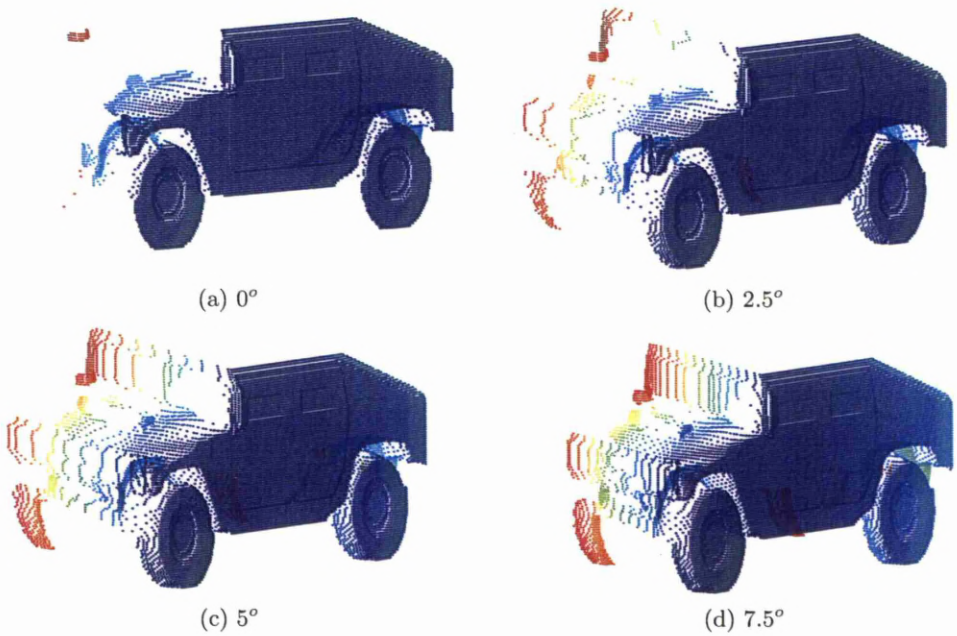

(a) 0^o (b) 2.5^o

(c) 5^o (d) 7.5^o

Figure 6.16: Point Clouds of Humvee Model at Three Diff. in View Angles (Near-Far).

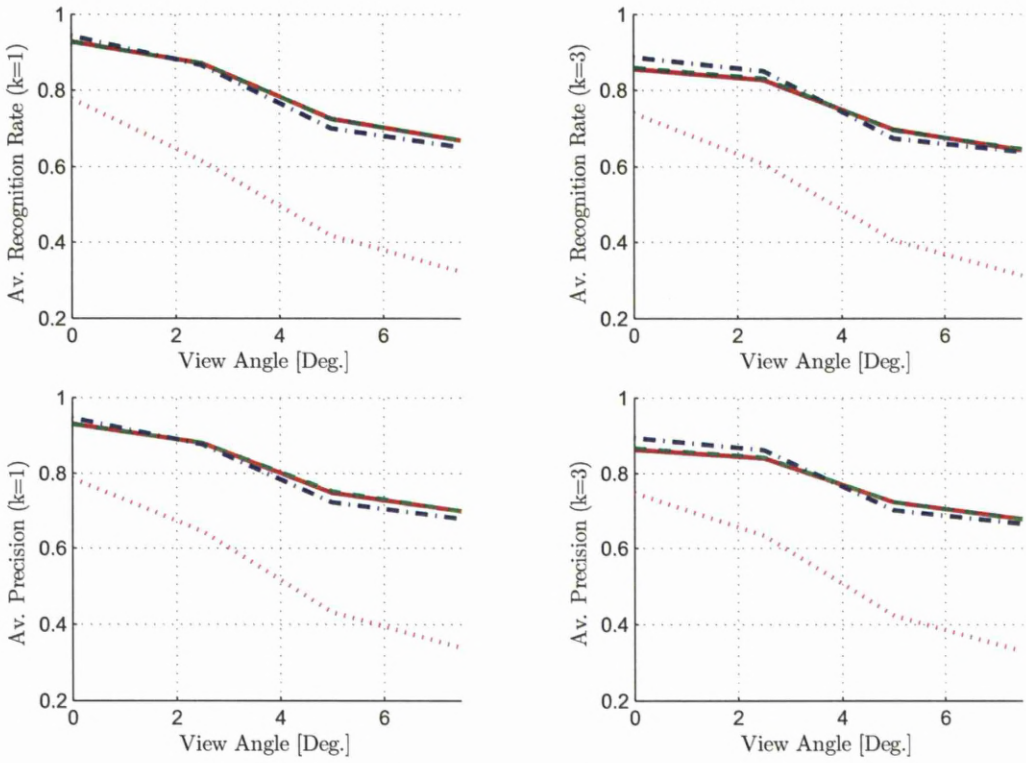

(a) Average Model Recognition Rate and Precision.

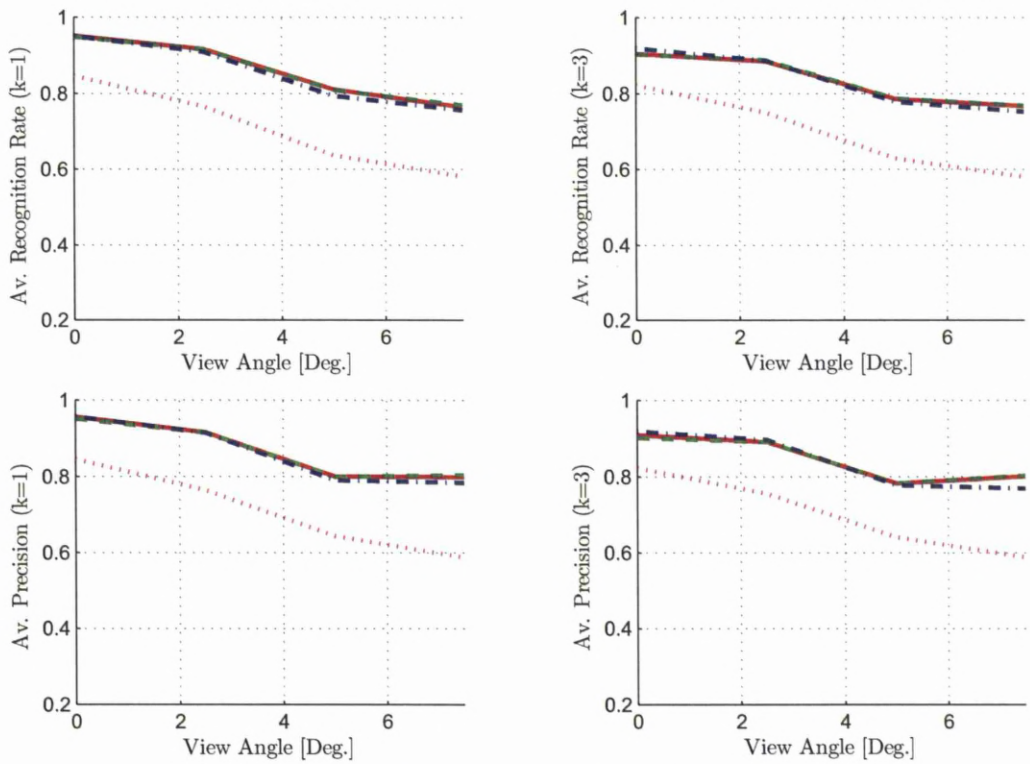

(b) Average Class Recognition Rate and Precision.

Figure 6.17: Average Recognition Rate and Precision During View Effect for HHOGD "-", HHOTD "- -", COTD "-.-", and Invariant Moment "." Descriptors.

6.3.4 Scale Effect

Changing the sampling grid resolution for the projected point clouds leads to change in the size or scale of their silhouette images. With size or scale effect, one of the pervious generated testing sets during view effect is used. This set is generated by scanning models from 24 different views at four different ranges (600m, 800m, 1000m, and 1200m) with angular interval equal to 15^o and rotation starts at 0^o. The point clouds for this set is converted to silhouette images with different scale factors (sampling grid resolutions), which are 10%, 20%, and 30% larger from the original images sizes. Figure 6.18 shows the effects of changing the scale factor on the resultant silhouette image. The simulation results for this testing set (that represent three different scale factors) at each range are shown in Appendix F.4. While the simulation results at all ranges, are presented together in Figure 6.19.

The simulation results in Figure 6.19 show that, both the average recognition rates and precisions for the descriptors are approximately constant with changing scale factors values, except these of the COTD which decrease slightly with increasing scale factor. The results also show that the average class recognition rates and precisions are slightly higher than the average model recognition rates and precisions. The recognition performance is slightly higher when k=1 is used. As a comparison between the descriptors, the result show lower performance for the moment comparing with the chromatic descriptors, which have a comparable performance, except COTD in which the recognition performance starts higher than the other chromatic descriptors or approximately equal in some cases (class recognition with k=1) and then decrease slightly with increasing scale factor.

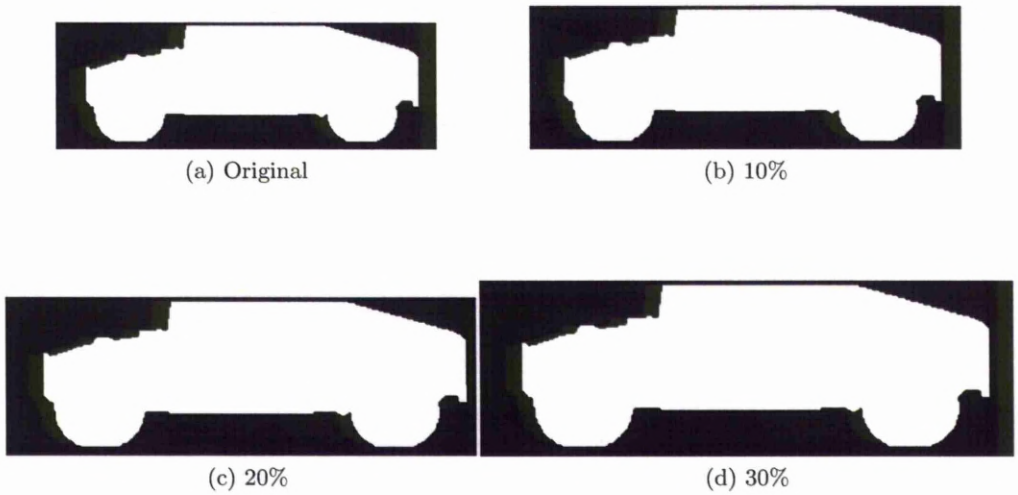

(a) Original (b) 10%

(c) 20% (d) 30%

Figure 6.18: Silhouette Images of Humvee Model at Different Scale Factors.

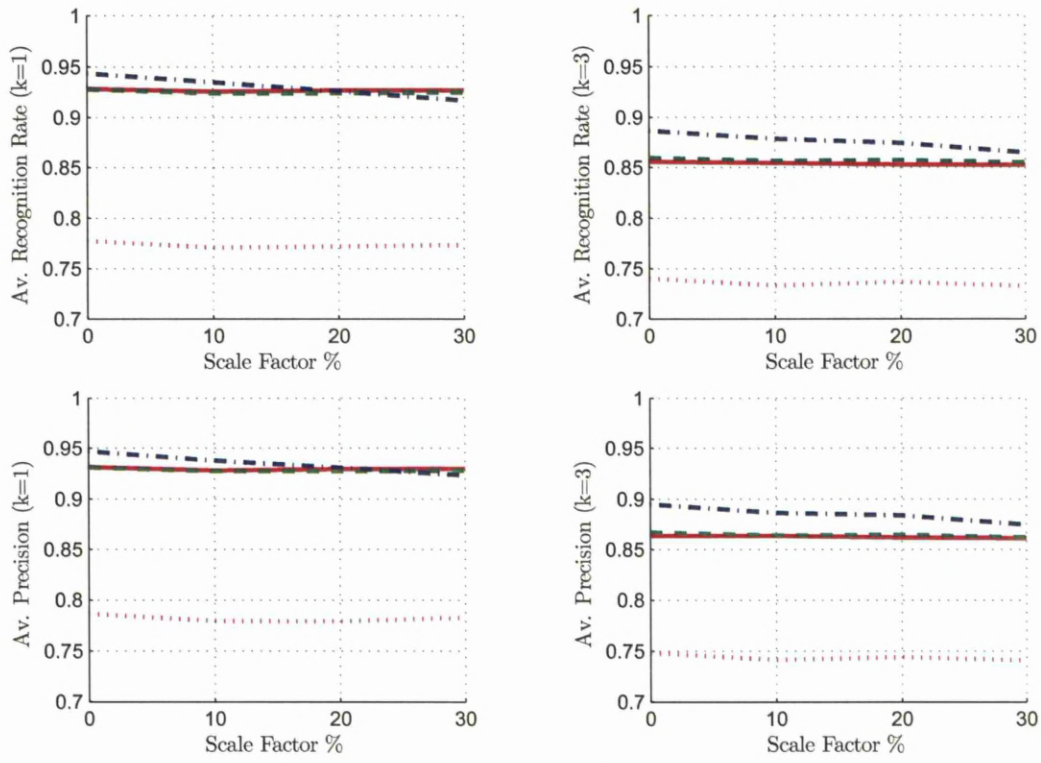

(a) Average Model Recognition Rate and Precision.

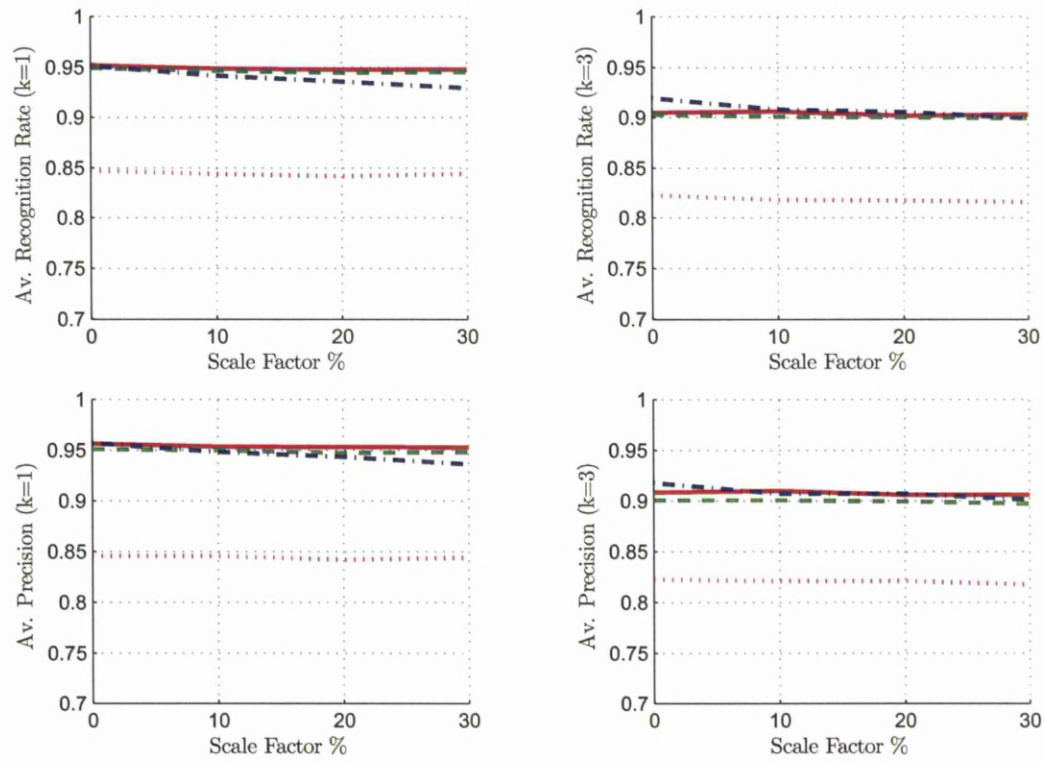

(b) Average Class Recognition Rate and Precision.

Figure 6.19: Average Recognition Rate and Precision During Scale Effect for HHOGD "-", HHOTD "- -", COTD "-.-", and Invariant Moment "." Descriptors.

6.3.5 Rotation Effect

The impact of the rotation effect on the descriptors performance is also evaluated. This effect arises from rotating either the model or the LADAR system or both around their horizontal axis, where in most practical cases this effect comes from rotating the LADAR system especially at high rotation angles.

For this effect three testing sets are generated, by scanning the models from 24 different views at four different ranges after rotating the LADAR around its horizontal axis with a specific rotation angle. The rotation angle for the first set is equal to 15^0, while the second and third sets angles are 30^0 and 45^0 respectively. Figure 6.20 shows the resultant point clouds of scanning Humvee model at different rotation angles.

The simulation results for these testing sets at each range are shown in Appendix F.5. While the simulation results for these three sets (that represent three different rotation angles) at all ranges, are presented together in Figure 6.21.

In Figure 6.21, the simulation results show that, both the average recognition rates and precisions in all graphs are approximately constant for the descriptors with changing rotation angle. The results also show that the average class recognition rates and precisions are slightly higher than the average model recognition rates and precisions. The recognition performance is slightly higher when k=1 is used. As a comparison between the descriptors, the results show lower performance for the moment comparing with the chromatic descriptors, which have a comparable performance, except COTD in which the model recognition performance are slightly higher than the other chromatic descriptors.

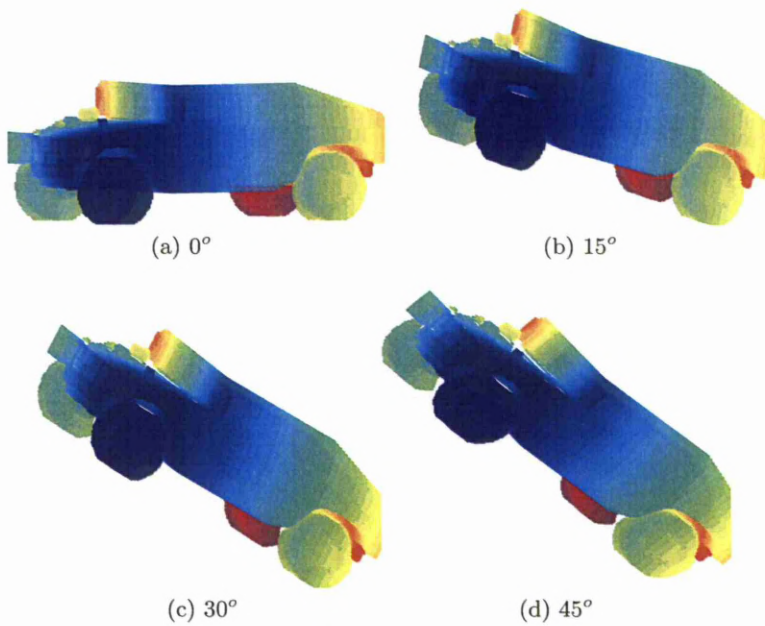

(a) 0^o (b) 15^o

(c) 30^o (d) 45^o

Figure 6.20: Point Clouds of Humvee Model at Different Rotation Angles (Near-Far).

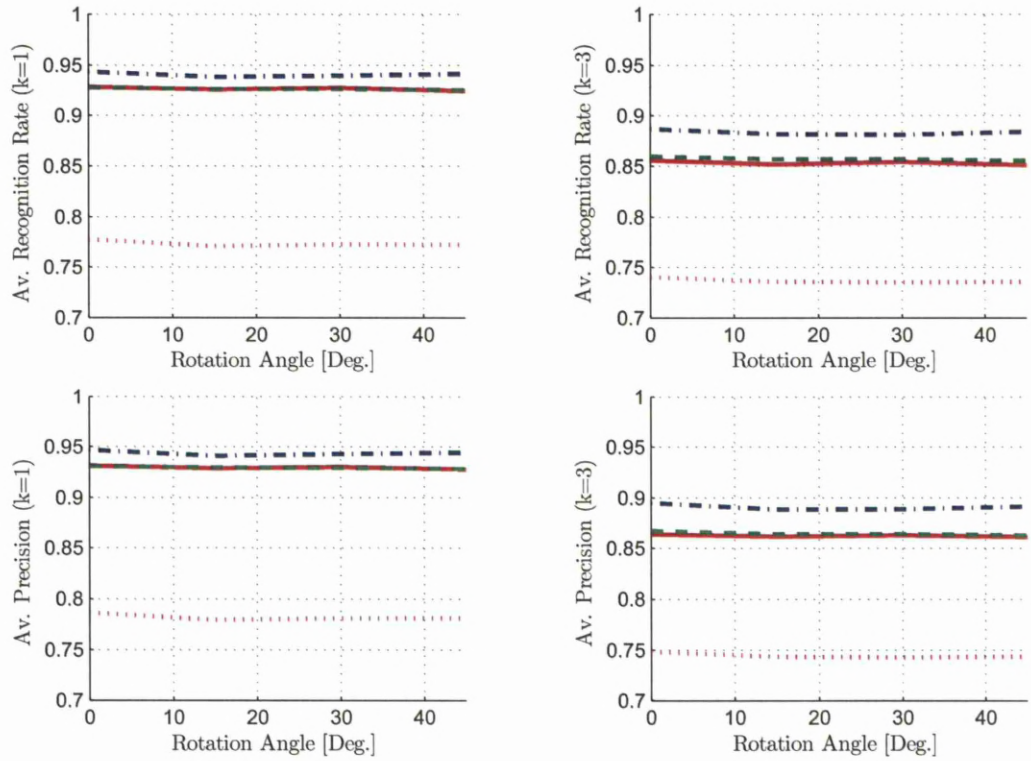

(a) Average Model Recognition Rate and Precision.

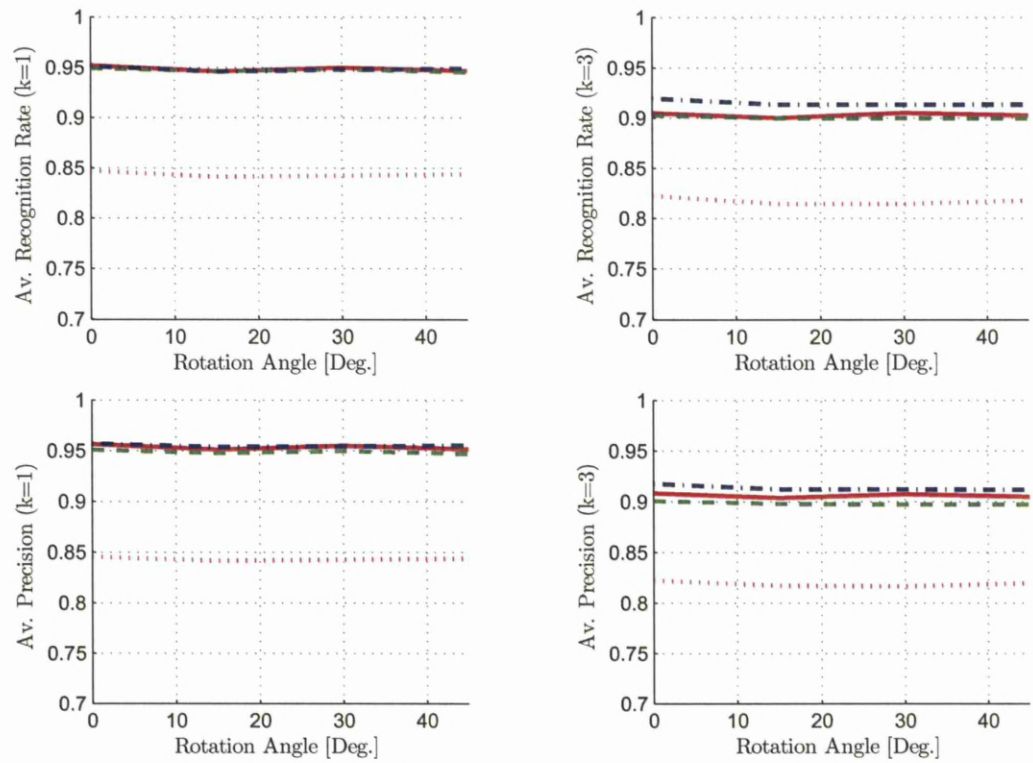

(b) Average Class Recognition Rate and Precision.

Figure 6.21: Average Recognition Rate and Precision During Rotation Effect for HHOGD "-", HHOTD "- -", COTD "-.-", and Invariant Moment "." Descriptors.

6.3.6 Translation Effect

Changing the models positions to the left or right of the central viewing axis of the LADAR system, translates or shifts their corresponding silhouette images. In additional to that, the scanning pattern in the LADAR system is not uniform. This leads to change the spatial distribution of the resultant point clouds, when the models positions changes. In order to test the descriptors with changing models positions, the testing set is generated by scanning the models from 24 different views at four different positions, which are $(X = 787.9\,m\,, Y = 138.9\,m)$, $(X = 787.9\,m\,, Y = 138.9\,m)$, $(X = 984.8\,m\,, Y = 173.6\,m)$, and $(X = 1181.8\,m\,, Y = 208.4\,m)$. These positions represent rotating the models centres 10^o around LADAR origin at ranges equal to $600\,m$, $800\,m$, $1000\,m$, and $1200\,m$ respectively, to guarantee scanning within LADAR limits.

Figure 6.22 shows the resultant point clouds arising from scanning Humvee model at four different positions, where the simulation results of these four positions are presented together in Figure 6.23. The average recognition rates and precisions decrease when the range (X and Y) increases. The results also show that, the average class recognition rates and precisions are less effected by the increasing range compared to those of model recognition. The k value effects on the recognition performance show, that both class and model average recognition rates and precisions decrease slightly when the number of k values increase from 1 to 3. As a comparison between the descriptors, the result show lower performance for the moment compared to the chromatic descriptors, which have a comparable performance with slightly better model recognition for the COTD.

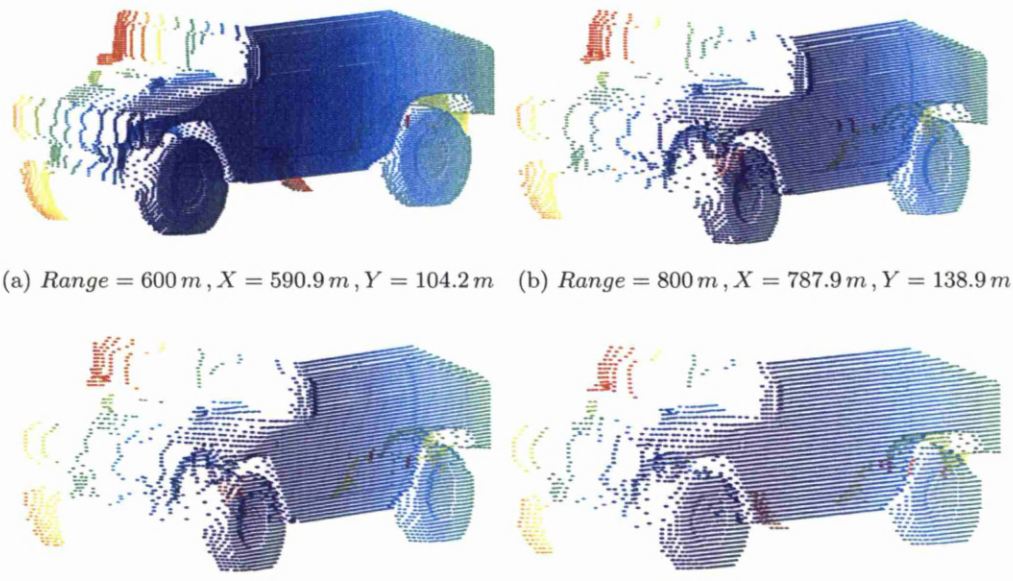

(a) $Range = 600\,m\,, X = 590.9\,m\,, Y = 104.2\,m$ (b) $Range = 800\,m\,, X = 787.9\,m\,, Y = 138.9\,m$

(c) $Range = 1000\,m\,, X = 984.8\,m\,, Y = 173.6\,m$ (d) $Range = 1200\,m\,, X = 1181.8\,m\,, Y = 208.4\,m$

Figure 6.22: Point Clouds of Humvee Model at Different Positions (Near-Far).

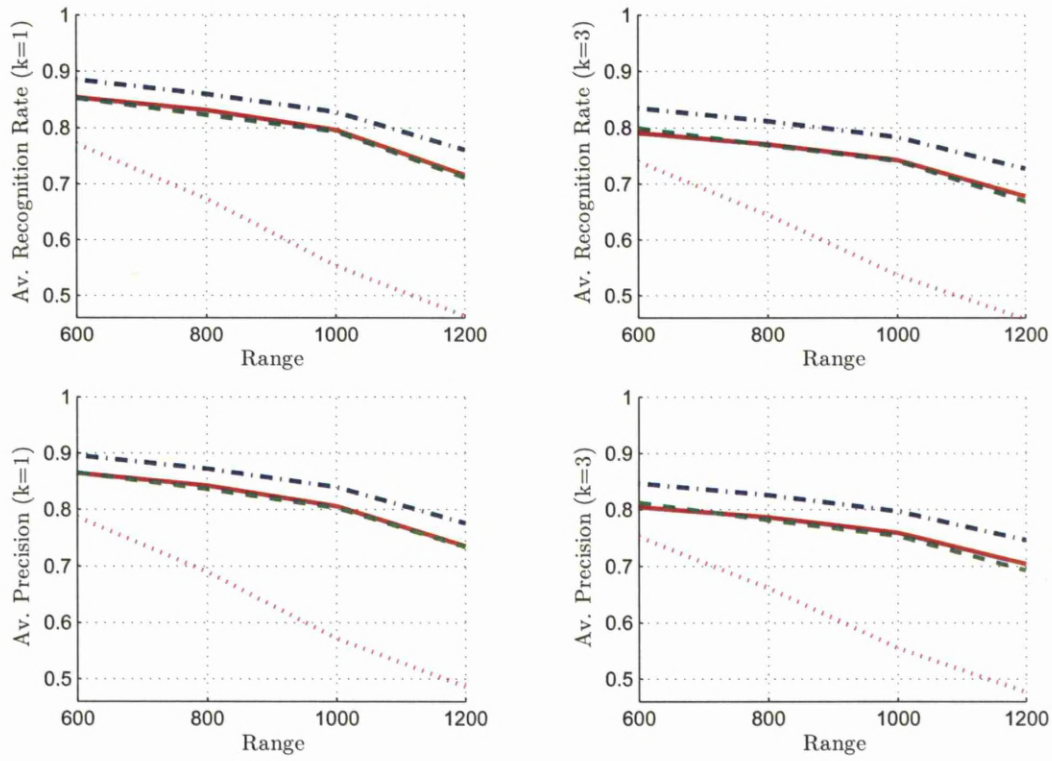

(a) Average Model Recognition Rate and Precision.

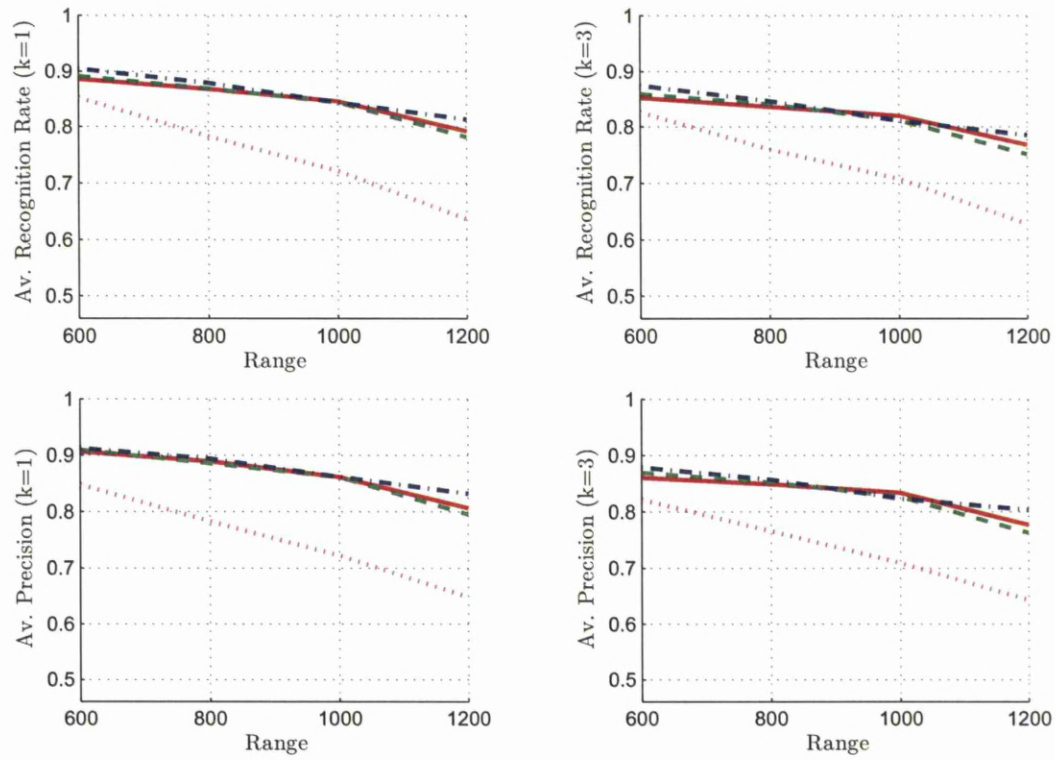

(b) Average Class Recognition Rate and Precision.

Figure 6.23: Average Recognition Rate and Precision During Translation Effect for HHOGD "-", HHOTD "- -", COTD "-.-", and Invariant Moment "." Descriptors.

6.4 Summary

The performance evaluation methodology for the chromatic descriptors with LADAR data processing is presented. This includes preparing the 3D CAD models and the principle used to divide them into ten classes. This also included how these models are then used to generate the training sets and several testing sets of noise, resolution, view, scaling, rotation, and translation effects.

The procedure of using these types of sets is also explained, which includes a description about the classifier type and the feature vectors that are used with this classifier for both the chromatic and invariant moment descriptors. This is followed by presenting the resultant confusion matrices and their performance metrics (average recognition rate and average precision). These were used to describe the descriptors performance with a specific type of effects.

The method of applying each one of these effects on the descriptors is also explained with describing the manner of presenting the resultant simulation results. Finally discussion about these simulation results is given for the chromatic descriptors and the invariant moment at each effect. Generally the simulation results show lower performance for the moment descriptor compared to the chromatic descriptors. The results also show, that both class and model average recognition rates and precisions decrease slightly when the number of k values increase from 1 to 3.

Chapter 7

Experimental Tests and Results for the LADAR System

Introduction

This chapter describes the experimental tests that have been undertaken on the new designed LADAR system in order to asses its recognition performance with the proposed chromatic descriptors and the invariant moment descriptor.

In this chapter, five sections are presented. The first section presents the experimental setup. While the second and the third sections describe the LADAR recognition program and the experimental procedure respectively. The experimental results are then presented in the fourth section and finally a summary of this chapter is given in the last section.

7.1 Experimental Setup

The experimental setup is shown in Figure 7.1 and it consists of the following:

- Testing Models: These models are selected to represent five different objects which are a car, a ATV, a train, a helicopter, and a plane as shown in Figure 7.2.
- Rotation Stage: This stage is used for mounting the testing models, where it can be rotated continuously through a full 360 degrees. The lower right side of Figure 7.1, shows the rotation stage mounting Train model at 0^o angle.
- Optical Bench: This bench is used for mounting the rotation stage at any distance within its length.
- Measuring Tape: This tape is used for measuring the distance between the rotation stage centre and the LADAR scanning system.
- LADAR Scanning System: As described in chapter 4, this system is used to scan the testing models and recognise them using different types of descriptors.

Figure 7.1: Experimental Setup for Testing LADAR Scanning System.

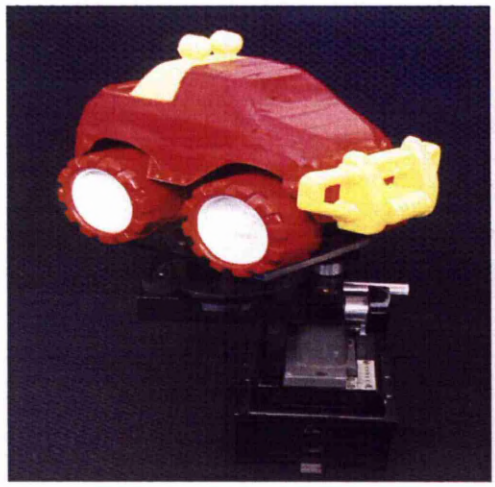

(a) Car Model.

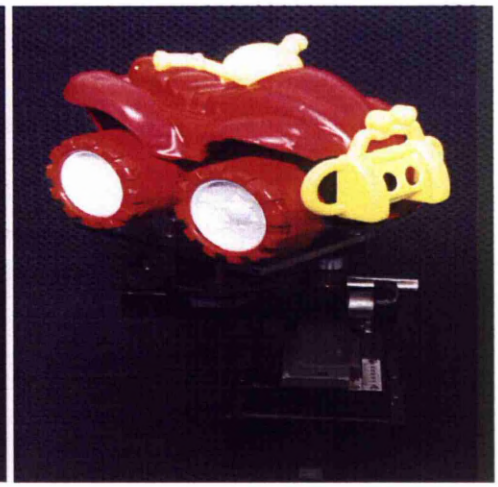

(b) ATV Model

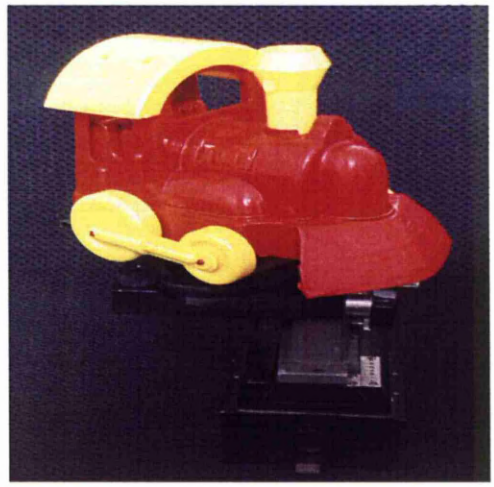

(c) Train Model.

(d) Helicopter Model.

(e) Plane Model.

Figure 7.2: Five Different Types of Testing Models.

7.2 LADAR Recognition Program

This program is written in order to enable the LADAR system to recognise different objects types after scanning them. The program performs the recognition in two stages, these are description stage and classification stage. In the first stage the program describes the resultant LADAR images after converting them to silhouette images, by applying one of four descriptors types, which are:

- **Half Height Overlapping Gaussian Descriptor** (HHOGD)
- **Half Height Overlapping Triangular Descriptor** (HHOTD)
- **Continuous Overlapping Triangular Descriptor** (COTD)
- **Invariant Moment** (Moment)

In each chromatic descriptor, three projections are used at $\Theta = 0^o$, 45^o, and 90^o, which produces a feature vector of six invariant features, while the feature vector for the moment descriptor, is composed of seven invariant moments.

For the classification stage, the program sents the resultant feature vector to the k-nearest neighbour classifier of two k values (which are equal to 1 and 3) after training it with the feature vectors of the training set, that were previously scanned and stored in a specific folder. This classifier is used with Euclidean distance metric and a Majority rule, in which the sample point is assigned to the class the majority of the k nearest neighbour are from [104].

Referring to Figure 7.3 the recognition program can be controlled by the recognition buttons ("**Training**" and "**Recognise**") and pop-up menu located in the Scanning Panel (previously mentioned in section 4.3.3). Pressing the "**Training**" button makes the recognition program load the training set and train the k-nearest neighbour classifier with the feature vectors, that results from applying each descriptor on this set. After training the classifier, the LADAR system is ready to recognise objects after scanning them. The recognition operation is then performed by pressing the "**Recognise**" button, which makes the program performs the description and classification stages with specific descriptor type and k value (where both can be selected by using the pop-up menu), and finally displayed the recognised object name in the corresponding text box.

7.3 Experimental Procedure

The testing procedure consists of two phases, which are the training phase and the testing phase. In the first phase the training set is generated using the LADAR system and it is then used to train the system. The samples for this set are taken by rotating

Figure 7.3: Recognition Buttons and Pop-Up Menu in LADAR GUI Control Window.

each model (shown in Figure 7.2) around its vertical axis in 45^o angular intervals (0^o, 45^o, 90^o, 135^o, 180^o, 225^o, 270^o, and 315^o) at range equal to $60\,cm$ from the sensor [54, 58, 111, 112]. This will generate eight scans per model with a total of 40 scans in the training set. Figure 7.4 shows point clouds of train model after applying the above procedure.

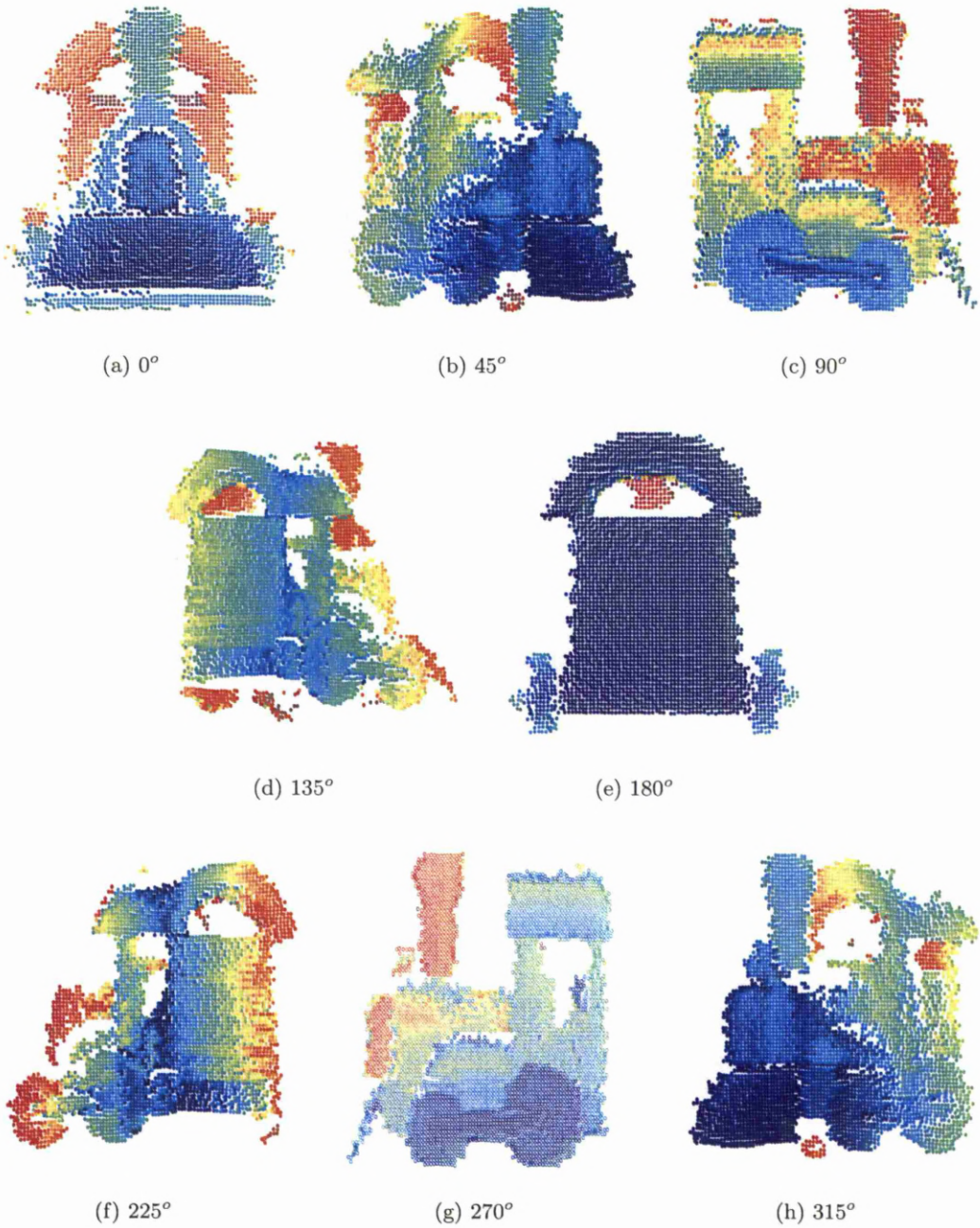

(a) 0^o (b) 45^o (c) 90^o

(d) 135^o (e) 180^o

(f) 225^o (g) 270^o (h) 315^o

Figure 7.4: Point Clouds of Scanning Train Model from Different Views (Near-Far).

In the testing phase, the LADAR system is used to scan and recognise the testing models from eight different views at six different ranges (60 cm, 100 cm, 150 cm, 200 cm, 250 cm, and 300 cm) after applying specific effect [54, 58, 111, 112]. These effects include: resolution, view, rotation, and translation. Thus the total number of scans that are generated is equal to 2640 scans. The eight view angles for all testing scans, are equal to those of the training scans except the angles of the view testing scans. The scanning resolution for all the training and testing scans is set to 0.1^o except the resolution testing scans (more explanation will be presented in the next sections).

In each effect, two types of confusion matrices are generated for each specific descriptor at each range (six ranges). The first type of these matrices is shown in Figure 7.5a and represents the recognition of the model that the enquiry scan belongs to using classifier of k=1. The second type that shown in Figure 7.5b is similar to the previous type except that the classifier is used with k=3. Table 7.1 presets the models types with their corresponding labels.

Table 7.1: Models Labels

Model Type	Model Label
Car	1
ATV	2
Helicopter	3
Plane	4
Train	5

After calculating these matrices, two performance metrics are calculated for each one to evaluate the descriptors, which are average recognition rate (recall) and average precision [115, 116]. The resultant values for these confusion matrices are then plotted with the distance value (i.e. Range) as shown in Figure 7.6. This is to evaluate the impact at each range for any applied effect. In order to evaluate the overall impact of a specific effect at all ranges, the previously mentioned confusion matrices types are recalculated with all ranges as shown in Figures 7.7. The resultant average recognition rate and precision for these matrices are then used to compare the effects.

Referring to the Figure 7.6, which presents the model average recognition rates and precisions for the chromatic descriptors and the invariant moment at each range with using two k values (1, 3). Generally all the graphs show that, both the average recognition rates and precisions decrease when the range increases. Regarding the effects of the k value on the recognition performance the results show, that the model average recognition rates and precisions decrease slightly when the number of k values increase from 1 to 3. As a comparison between the descriptors, the result show a comparable performance between the chromatic descriptors and the reduction in their performance with the range lower than for the invariant moment.

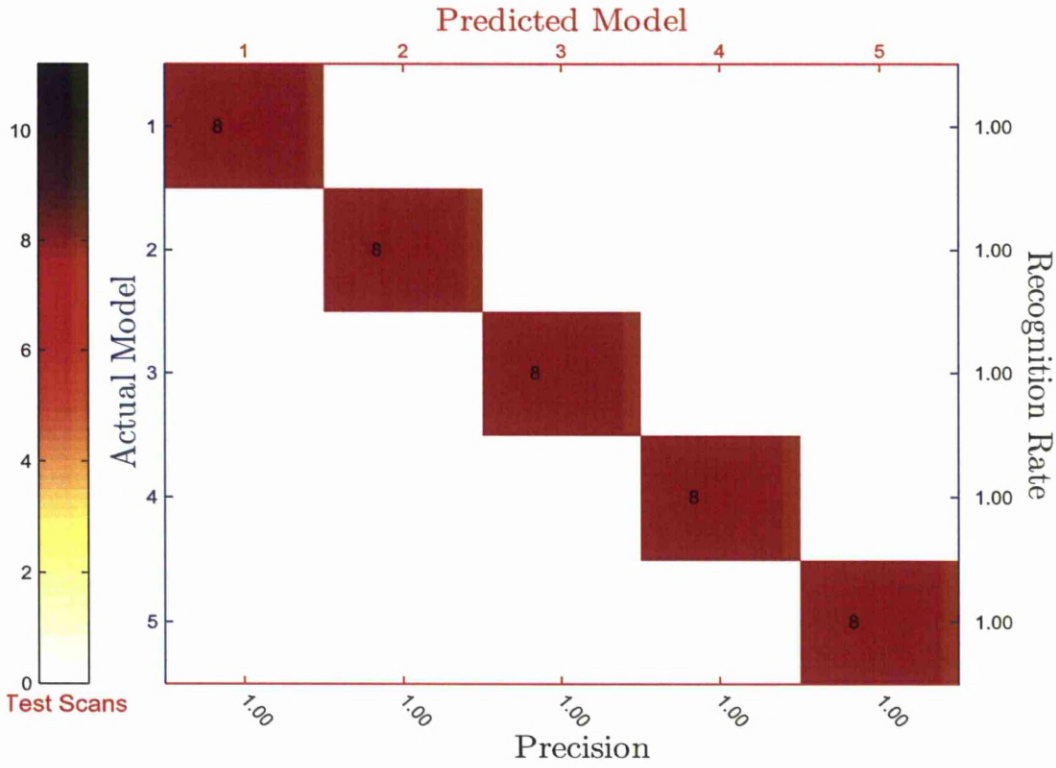

(a) Model Confusion Matrix (k=1).

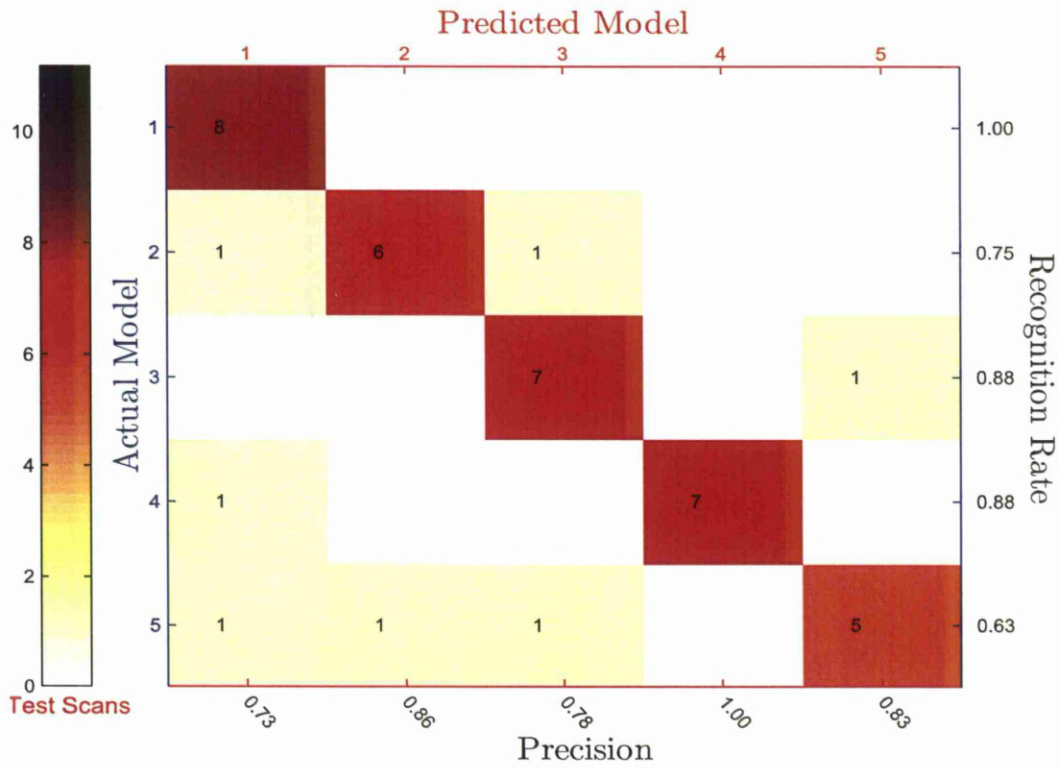

(b) Model Confusion Matrix (k=3).

Figure 7.5: Model Confusion Matrix with Recognition Rate and Precision for HHOGD (Range= 60 cm).

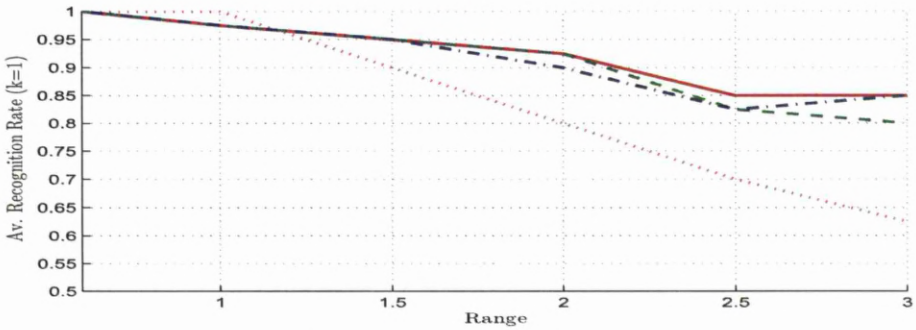

(a) Average Recognition Rate (k=1).

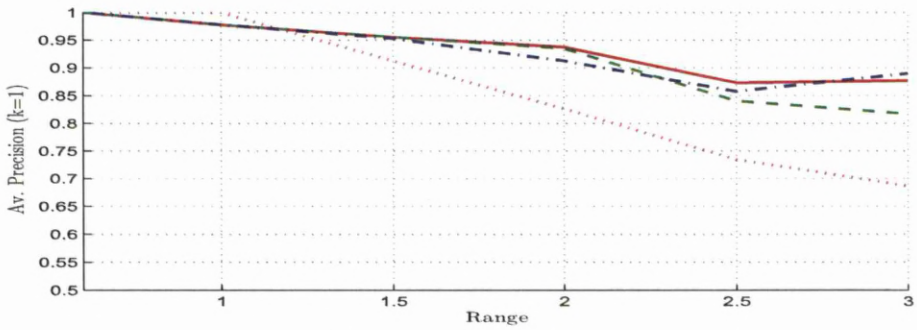

(b) Average Precision (k=1).

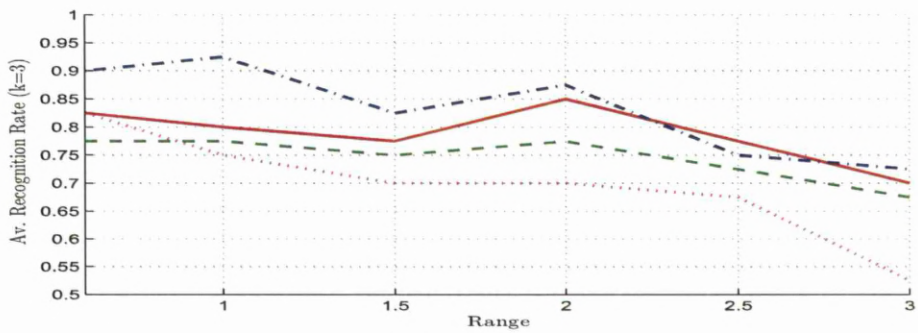

(c) Average Recognition Rate (k=3).

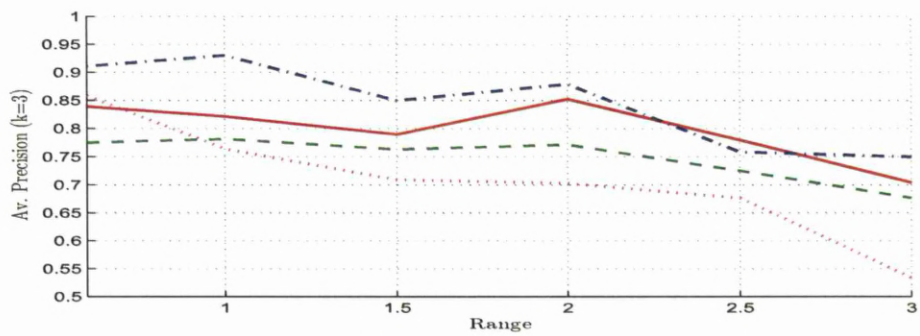

(d) Average Precision (k=3).

Figure 7.6: Average Model Recognition Rate and Precision with Range (without effect) for HHOGD "-", HHOTD "- -", COTD "-.-", and Invariant Moment "." Descriptors.

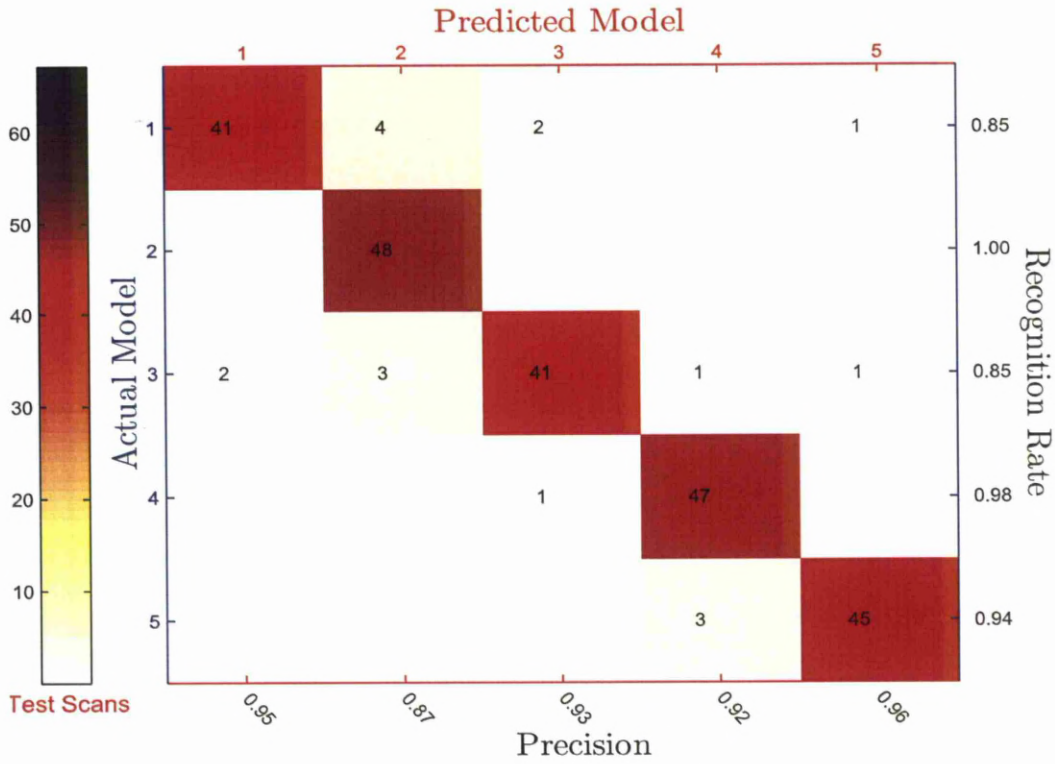

(a) Model Confusion Matrix (k=1).

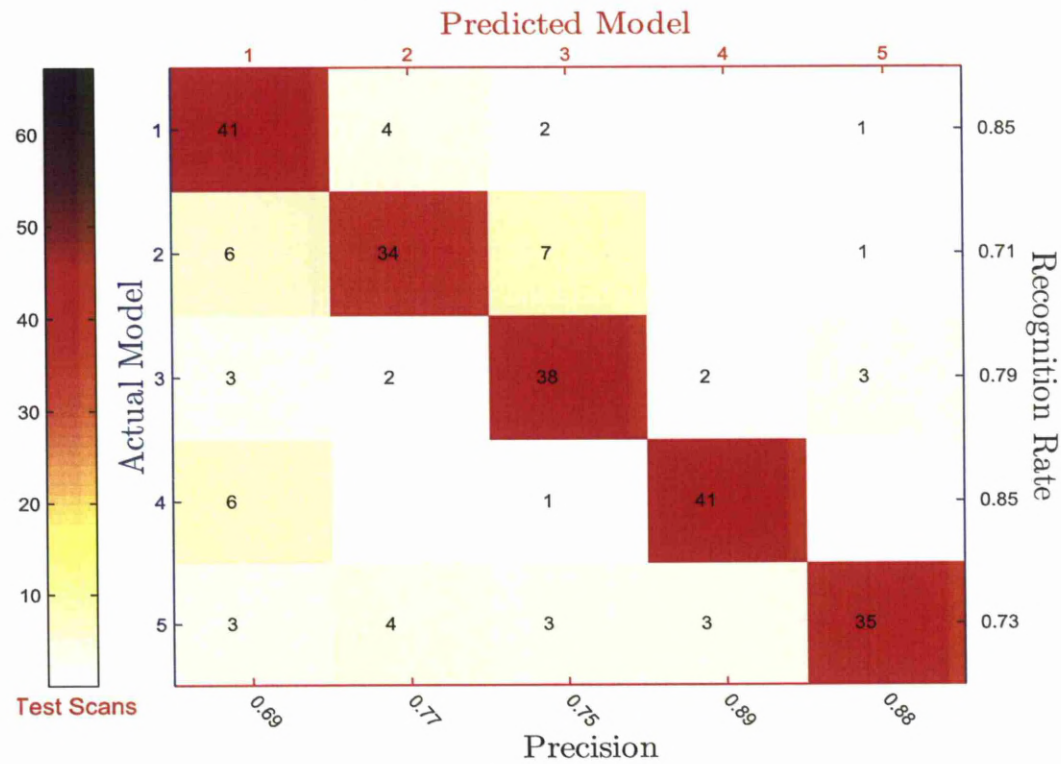

(b) Model Confusion Matrix (k=3).

Figure 7.7: Model Confusion Matrix with Recognition Rate and Precision for HHOGD (All Range Combined).

7.4 Experimental Results

This section presents the experimental results for resolution, view, rotation, and translation effects.

7.4.1 Resolution Effect

In order to evaluate the impact of the LADAR scanning resolution on the descriptors performance, the five testing models are scanned from 8 different views at six ranges with scanning resolution equal to 0.1^o. Another three sets are then generated but with resolution equal to 0.2^o, 0.3^o, and 0.4^o. Figure 7.8 shows the effect of scanning the train model with different resolutions on the resultant point clouds. The experimental results for these sets at each range are shown in Appendix G.1. While the experimental results at all ranges, are presented together in Figure 7.9.

In Figure 7.9, the experimental results show that, both the average recognition rates and precisions in all graphs decrease when the resolution value increase (i.e. decreasing resolution). The results also show that, the average recognition rates and precisions decrease slightly when the number of k values increase from 1 to 3. As a comparison between the descriptors, the result show lower performance for the moment compared to the chromatic descriptors, which have a comparable performance.

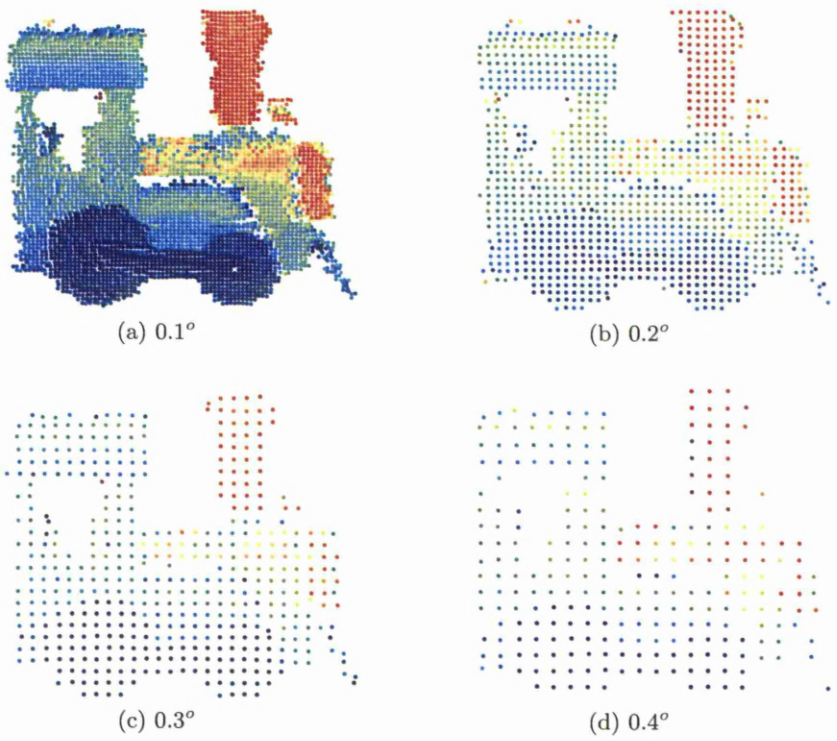

(a) 0.1^o (b) 0.2^o

(c) 0.3^o (d) 0.4^o

Figure 7.8: Point Clouds of Train Model at Different Scanning Resolutions (Near-Far).

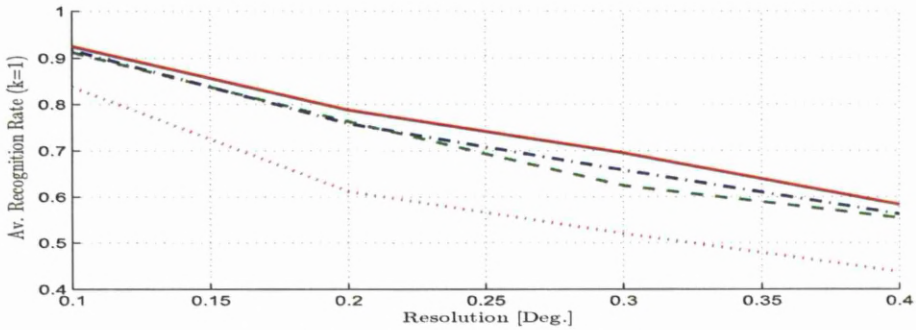

(a) Average Recognition Rate (k=1).

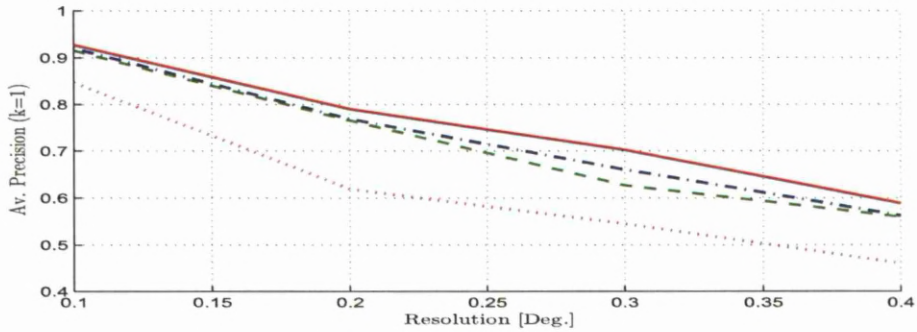

(b) Average Precision (k=1).

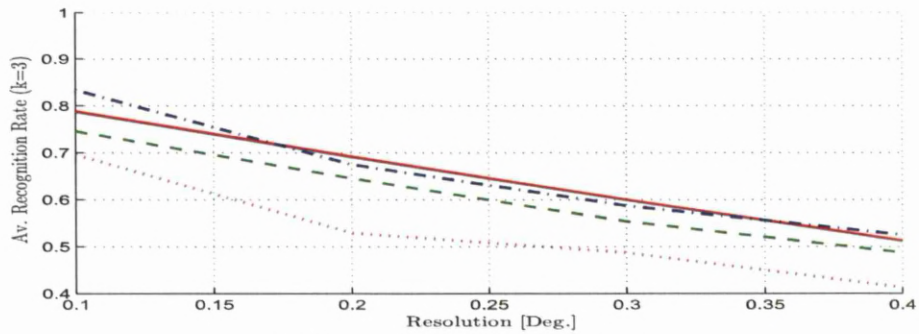

(c) Average Recognition Rate (k=3).

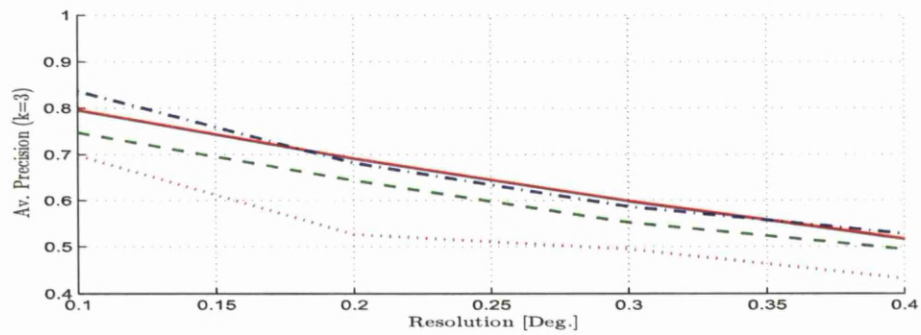

(d) Average Precision (k=3).

Figure 7.9: Average Model Recognition Rate and Precision During Resolution Effect for HHOGD "-", HHOTD "- -", COTD "-.-", and Invariant Moment "." Descriptors.

7.4.2 View Effect

The impact of changing the scanning view on the descriptors performance is evaluated by scanning the testing models from 8 different views at six different ranges (60 cm, 100 cm, 150 cm, 200 cm, 250 cm, and 300 cm) with an angular interval equal to 45^o and first view angle equal to 7.5^o. Another two sets are then generated but with setting the first view angle to 15^o, and 22.5^o respectively. Figure 7.10 shows the point clouds of train model with different view angles.

The experimental results of the view angle tests at each range are shown in Appendix G.2. While the experimental results for these tests (that represent three different view angles) at all ranges, are presented together in Figure 7.11. The experimental results in Figure 7.11 show that, both the average recognition rates and precisions in all graphs decrease when the value of the view angle increase. Regarding the effects of the k value on the recognition performance the results show, that the average recognition rates and precisions decrease slightly when the number of k values increase from 1 to 3. As a comparison between the descriptors, the result show lower performance for the moment compared to the chromatic descriptors, which have a comparable performance, when the classifier is used with k=1.

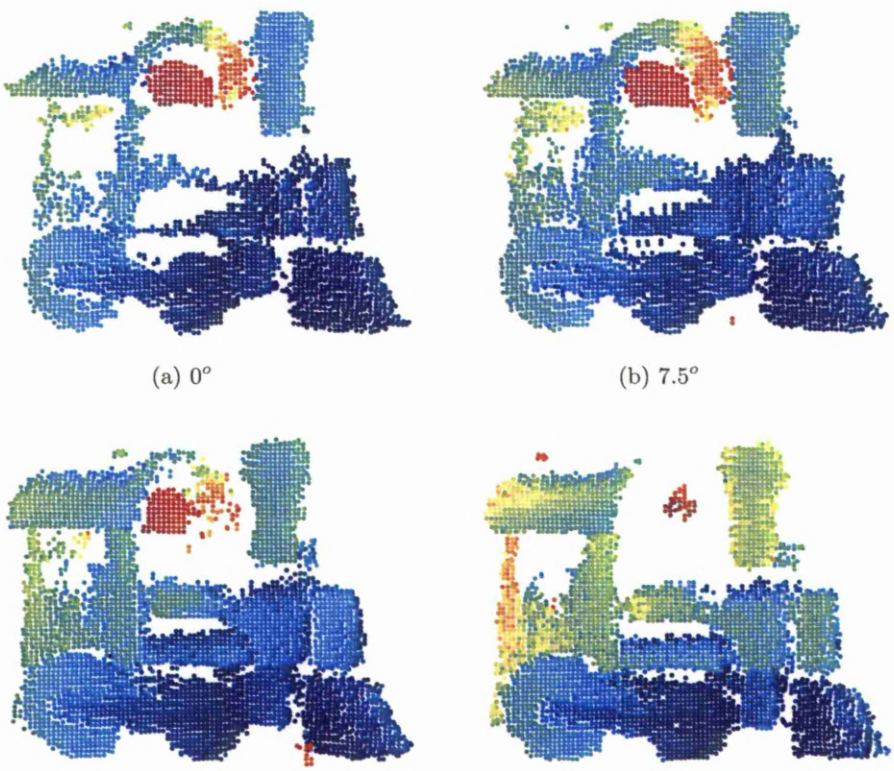

(a) 0^o (b) 7.5^o

(c) 15^o (d) 22.5^o

Figure 7.10: Point Clouds of Train Model with Different View Angles (Near-Far).

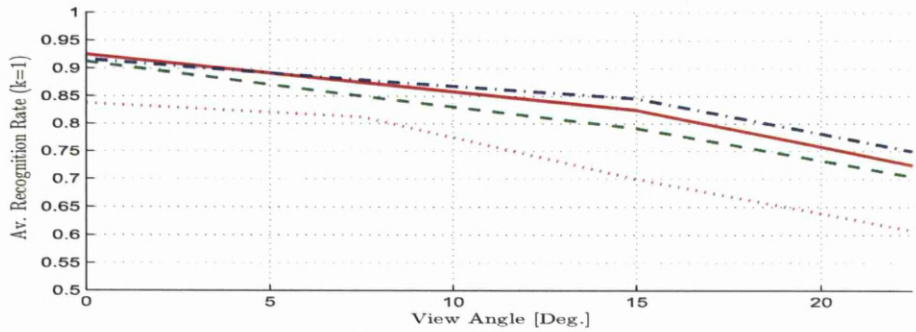

(a) Average Recognition Rate (k=1).

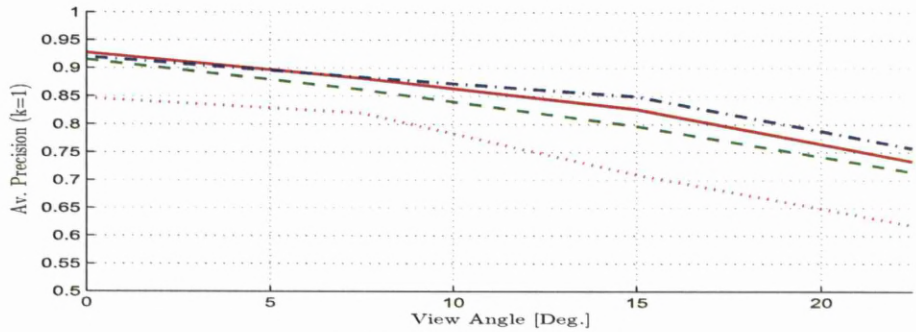

(b) Average Precision (k=1).

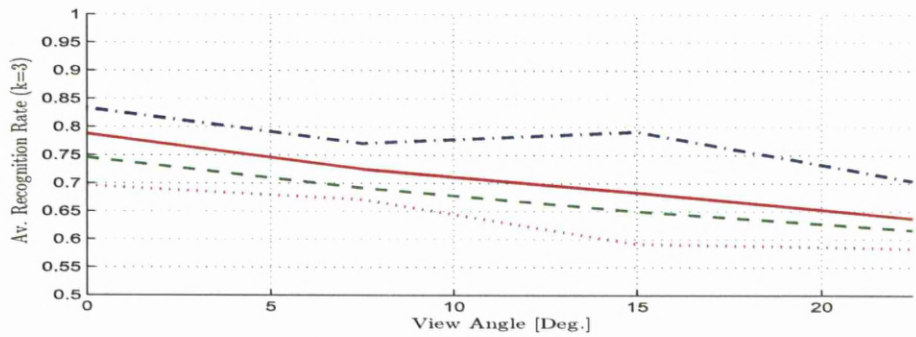

(c) Average Recognition Rate (k=3).

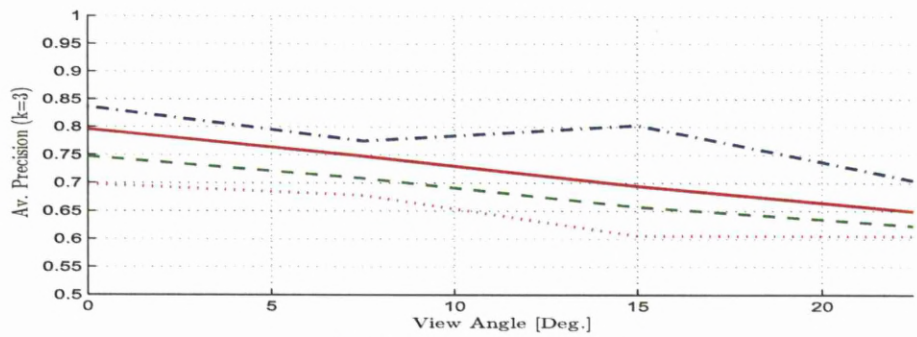

(d) Average Precision (k=3).

Figure 7.11: Average Model Recognition Rate and Precision During View Effect for HHOGD "-", HHOTD "- -", COTD "-.-", and Invariant Moment "." Descriptors.

7.4.3 Rotation Effect

The impact of the rotation effect on the descriptors performance is also evaluated. For this effect the testing models are scanned from 8 different views at six different ranges after rotating the resultant LADAR images around its horizontal axis with a specific rotation angle. The rotation angle for the first set is equal to 15^0, while the second and third sets angles are 30^0 and 45^0 respectively. Figure 7.12 shows the rotated point clouds of the train model at different rotation angles.

The experimental results for these sets at each range are shown in Appendix G.3. While the experimental results for these three sets (that represent three different rotation angles) at all ranges, are presented together in Figure 7.13.

In Figure 7.13, the experimental results show that, both the average recognition rates and precisions in all graphs are approximately constant for the chromatic descriptors with changing rotation angle. The recognition performance is slightly higher when k=1 is used. As a comparison between the descriptors, the results show lower performance for the moment comparing with the chromatic descriptors, which have a comparable performance, except HHOTD in which the recognition performance are slightly lower than the other chromatic descriptors when the classifier is used with k=3.

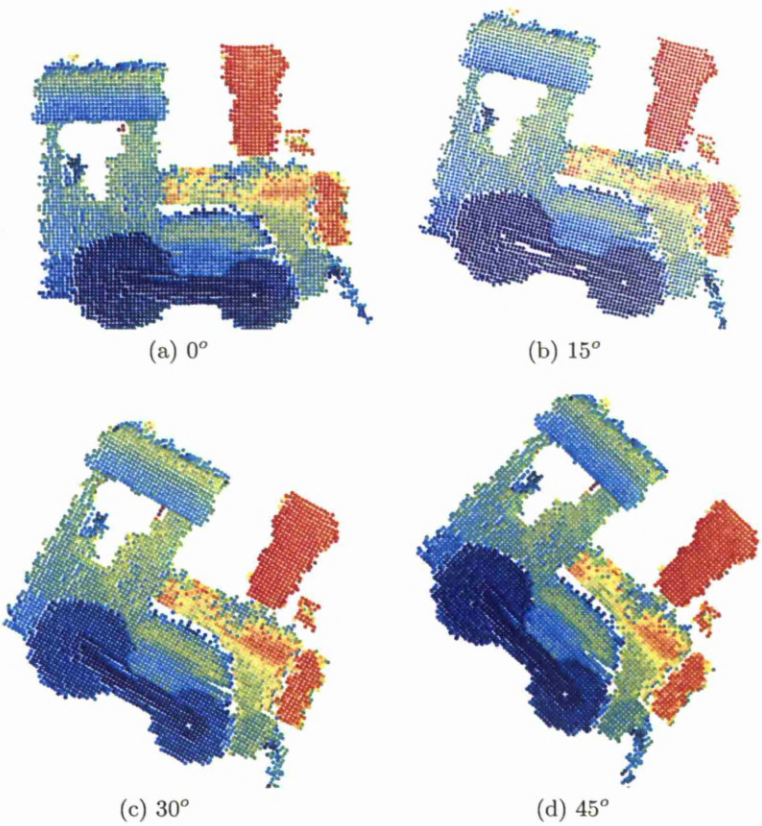

(a) 0^o (b) 15^o

(c) 30^o (d) 45^o

Figure 7.12: Point Clouds of Train Model at Different Rotation Angles (Near-Far).

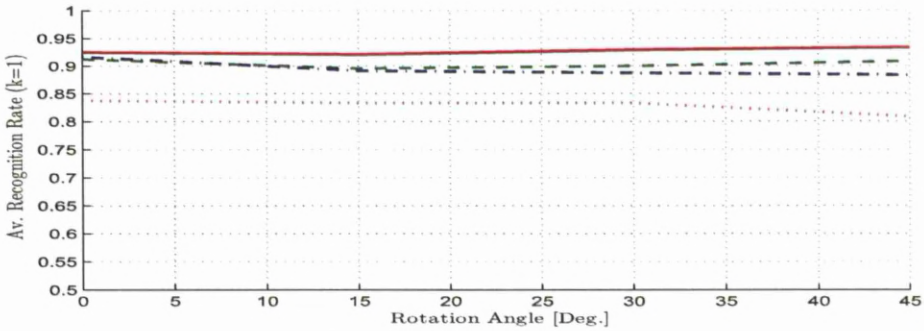

(a) Average Recognition Rate (k=1).

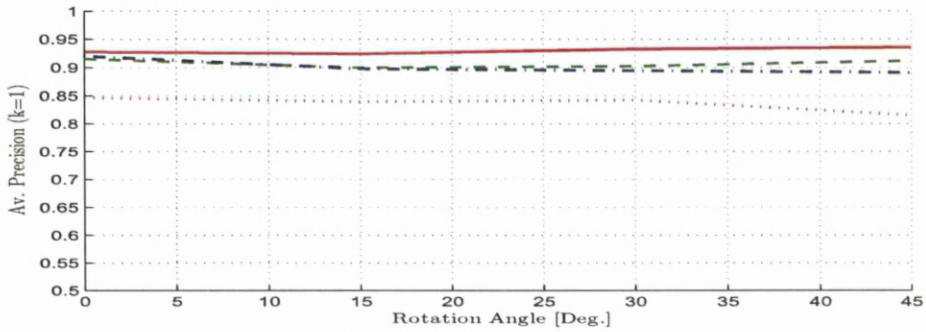

(b) Average Precision (k=1).

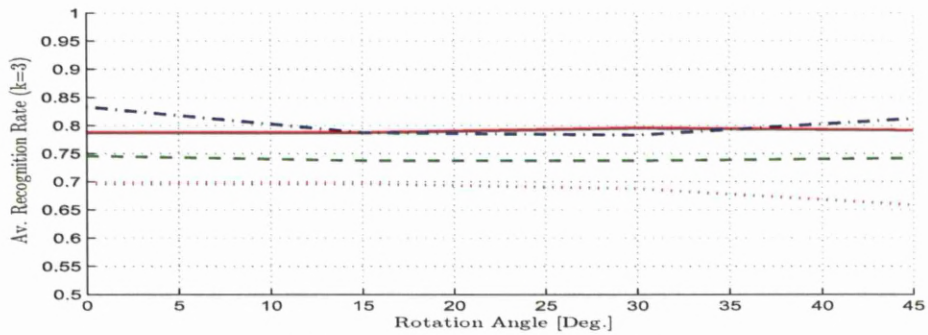

(c) Average Recognition Rate (k=3).

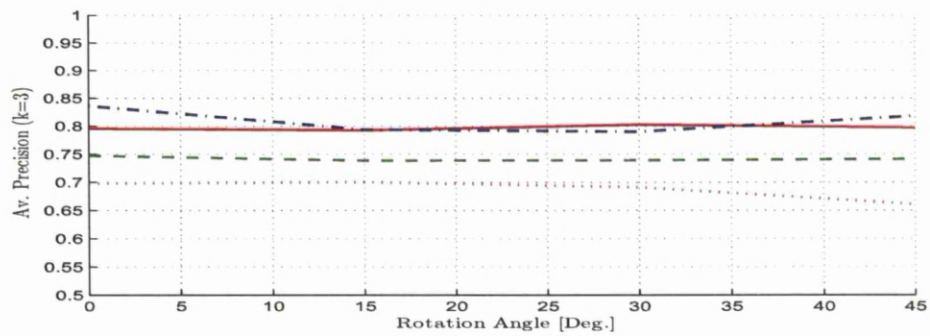

(d) Average Precision (k=3).

Figure 7.13: Average Model Recognition Rate and Precision During Rotation Effect for HHOGD "-", HHOTD "- -", COTD "-.-", and Invariant Moment "." Descriptors.

7.4.4 Translation Effect

As previously mentioned in section 6.3.6, changing the testing models positions to the left or right of the central viewing axis of the LADAR system, change the spatial distribution of the resultant point clouds and shift their corresponding silhouette images. In order to test the LADAR recognition performance with changing models positions, the five testing models are scanned from 8 different views at six different positions, which are ($X = 56.4\,cm\,, Y = 20.5\,cm$), ($X = 93.9\,cm\,, Y = 34.2\,cm$), ($X = 140.9\,cm\,, Y = 51.3\,cm$), ($X = 187.9\,cm\,, Y = 68.4\,cm$), ($X = 234.9\,cm\,, Y = 85.5\,cm$), and ($X = 281.9\,cm\,, Y = 102.6\,cm$). These positions represent rotating the models centres 20^o around LADAR origin at ranges equal to $60\,cm$, $100\,cm$, $150\,cm$, $200\,cm$, $250\,cm$, and $300\,cm$ respectively.

Figure 7.14 shows the resultant point clouds arising from scanning train model at four different positions, where the experimental results are presented together in Figure 7.15. The average recognition rates and precisions decrease when the range (X and Y) increases. The k value effects on the recognition performance show that, model average recognition rates and precisions decrease slightly when the number of k values increase from 1 to 3. As a comparison between the descriptors, the result show lower performance for the moment compared to the chromatic descriptors, which have a comparable performance. This difference between the chromatic and moment descriptors is decrease when the classifier is used with k=3.

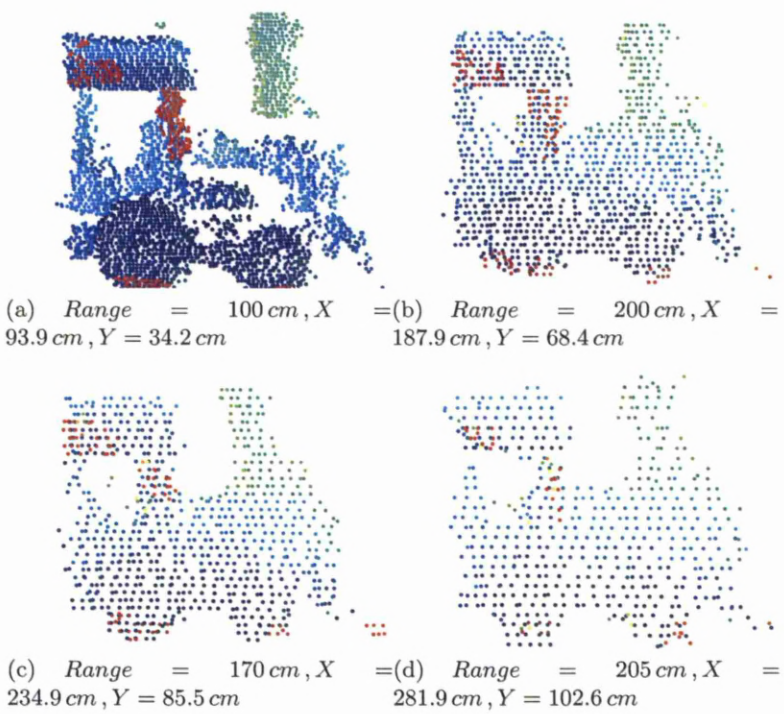

(a) *Range* = $100\,cm\,, X = 93.9\,cm\,, Y = 34.2\,cm$ (b) *Range* = $200\,cm\,, X = 187.9\,cm\,, Y = 68.4\,cm$

(c) *Range* = $170\,cm\,, X = 234.9\,cm\,, Y = 85.5\,cm$ (d) *Range* = $205\,cm\,, X = 281.9\,cm\,, Y = 102.6\,cm$

Figure 7.14: Point Clouds of Train Model at Different Positions (Near-Far).

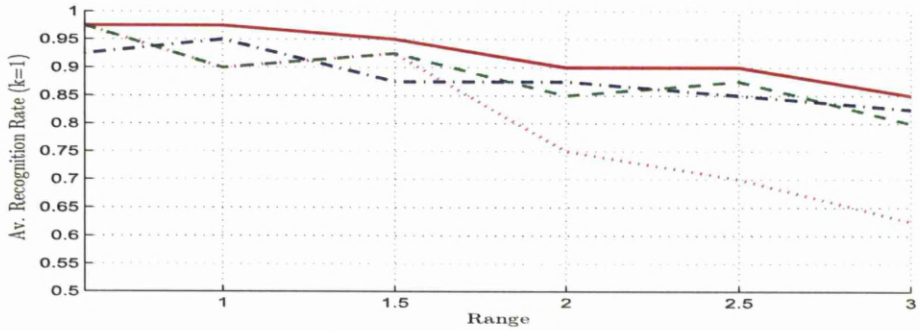

(a) Average Recognition Rate (k=1).

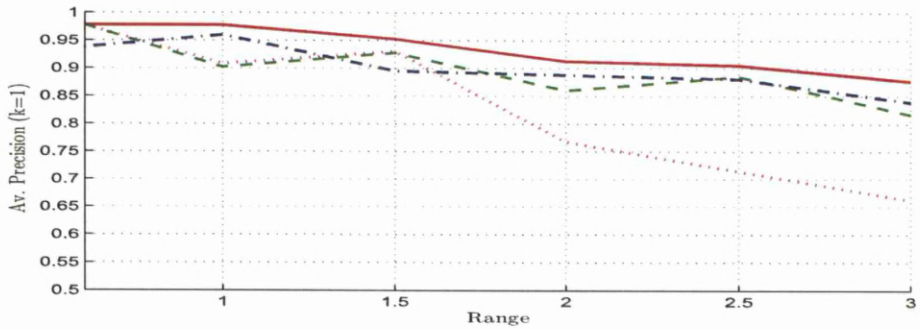

(b) Average Precision (k=1).

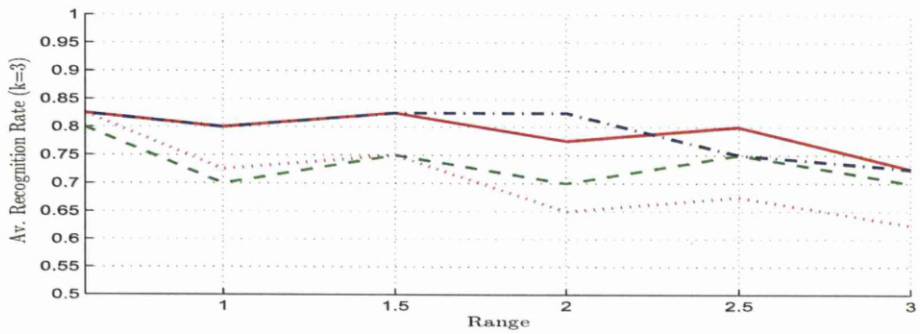

(c) Average Recognition Rate (k=3).

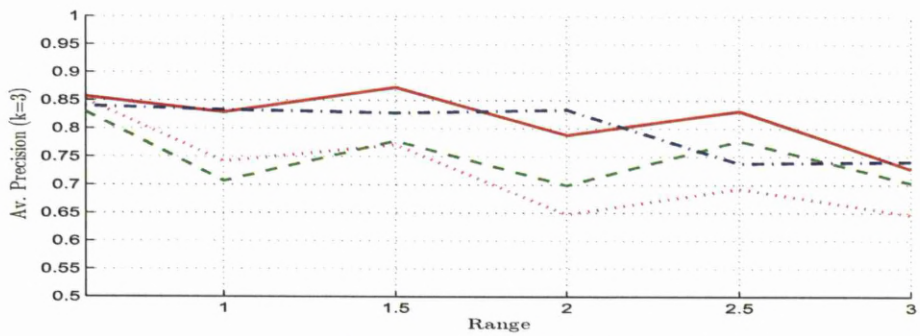

(d) Average Precision (k=3).

Figure 7.15: Average Model Recognition Rate and Precision During Translation Effect for HHOGD "-", HHOTD "- -", COTD "-.-", and Invariant Moment "." Descriptors.

7.5 Summary

The experimental tests for evaluating the recognition performance for the new designed LADAR system with the proposed chromatic descriptors and the invariant moment descriptor is presented. This includes describing the experimental setup and the procedure of using the testing models to train and test the LADAR system under several types of effects, which include resolution, view, rotation, and translation effects.

The LADAR recognition program that is written to enable the LADAR system to recognise different objects is also presented with the classifier type and the feature vectors that are used with this classifier for both the chromatic and invariant moment descriptors. This is followed by presenting the resultant confusion matrices and their performance metrics (average recognition rate and average precision).

The method of applying each one of these effects on the LADAR system is explained with describing the manner of presenting the experimental resultants. Finally discussion about these results is given for the chromatic descriptors and the invariant moment at each effect. Generally the experimental results show lower performance for the moment descriptor compared to the chromatic descriptors. The results also show, that model average recognition rates and precisions decrease slightly when the number of k values increase from 1 to 3.

Chapter 8

Conclusions and Future Work

Introduction

This chapter summaries this research work and its conclusions, and highlights areas that deserve further investigation.

8.1 Conclusions

New LADAR image descriptors are proposed, which are Half Height Overlapping Gaussian Descriptor, Half Height Overlapping Triangular Descriptor, and Continuous Overlapping Triangular Descriptor. These descriptors are able to extract invariant features from the LADAR silhouette images based on using proposed types of chromatic processors called 'invariant spatial chromatic processors'. Three types of chromatic processors are described with the proposed approach to making them invariant. These are Invariant Half Height Overlapping Gaussian Processors, Invariant Half Height Overlapping Triangular Processors, and Invariant Continuous Overlapping Triangular Processors.

The methods of using these new types of invariant processors to describe the images with invariant affine transformation (rotation, translation and scaling) features is also presented and tested with different objects at varies affine transformation and distortion effects, where its performance was compared with the Moment Invariant descriptor. The simulation results show, a comparable performance between them during affine effects with better performance for the chromatic descriptor during distortion effect.

The proposed approach of processing the LADAR data starting from generating the silhouette image and ending with extracting the chromatic features from it, is explained. The proposed descriptors are simple and their discrimination abilities can be easily extended by either increase the processors number or using additional image projections.

An efficient LADAR simulator software has been written to scan 3D CAD models and produce their simulated LADAR data. In order to allow the simulator to deal with more complex models and produces high resolution image with short execution

times, another approach for calculating the intersection points of the laser beam is proposed and described. The performance of this proposed approach is tested and the comparison of results shows that the proposed approach produces less execution time than the previous approach especially when the model consists of a large number of triangles, scanning with high resolution, or when a large number of laser footprint samples are required. The simulation steps for the LADAR simulator and its GUI are also presented with some selected results that show the effect of changing the scanning parameters (noise type and its strength, scanning resolution, and the laser beam width) on the resultant LADAR image. These simulation results also show the ability of the simulator to simulate the phenomena that related to the scanning process and produces LADAR images under a wide variety of conditions.

In order to evaluate the performance of the proposed LADAR descriptors with simulated data, the LADAR simulator is used to generate these data from scanning 60 3D CAD models with different artifacts such as noise, resolution, view, scaling, rotation, and translation.

With these artefacts the simulation results show that both the average recognition rates and precisions for the proposed descriptors are higher than those for the moment descriptor, where the later is used to benchmark the results. The constant recognition performance for the proposed descriptors during (rotation, scaling, and noise effects), show the effectiveness of both the invariant chromatic processors and the projection normalization approach to deal with the scaling and rotation effects respectively, and the robustness of the silhouette images with the noise effects. Regarding to the (resolution, view, and translation effects), the results show a decrement in the descriptors performance with increasing these effects. This reduction in the performance is lower for the proposed descriptors than the invariant moment descriptor. Finally the simulation results show that the recognition performance for all descriptors are slightly higher when the number of nearest neighbour used with the classifier is equal to one, which means a good separability for the descriptors features in the feature space. As a comparison between the proposed descriptors, the result show a comparable performance between them with slightly better performance for the COTD during noise, resolution, rotation, and translation effects.

A LADAR prototype system has been designed and implemented to be able to scan different objects and capture the 3D LADAR data from their surfaces. This system combines both the AccuRange 4000-LV laser distance sensor and the computer controlled Pan-Tilt Unit D46-17 with specific parameters, and produces a cost effective LADAR system of high sampling rate ($714\,sample/s$) and scanning resolution (0.0265^o). The hardware components and both the mathematical model and the controlling software that are required for reconstructing the resultant LADAR images from the scanning measurements are described. The resultant scanning images for the

LADAR system show the effectiveness of the mathematical model for producing these images in different formats (spherical and Cartesian). The results also show the ability of the controlling software to control the LADAR system and to filter the resultant LADAR images. The proposed LADAR descriptors are integrated with this system to enable it to recognise different objects after scanning them.

Experimental tests have been also undertaken on the new designed LADAR system in order to asses its recognition performance with the proposed descriptors and the invariant moment descriptor. The experimental results for these tests show similar general behaviour for the descriptors when they used with simulated data, which prove the ability of the new LADAR descriptors to process real LADAR data and provide recognition rates higher than the traditional techniques like the invariant moment descriptor.

8.2 Future Work

The generic nature for the chromatic methodology opens up the possibility for exploring additional chromatic processors (of new response shapes) with LADAR data processing. This is by applying on these new processors, the proposed approach of making the spatial chromatic processors works as invariant LADAR descriptors and then evaluate the performance of the resultant descriptors under the presence of noise and other effects that disturb the LADAR images.

In additional to that, it has been previously shown that the increase in the number of the spatial chromatic processors could enhance the signal discrimination but extending the number beyond six gives little advantage [95, 96]. Therefore a new research can be push towards investigating the impact of using more than three processors on the recognition performance under different conditions

Another interesting direction for future work is to extend the LADAR software ability by performing the full automatic target recognition. This is can be done by using one of the available segmentation techniques, that enable the software to automatically segment the target in the LADAR image from the background and pass it to the LADAR descriptors in order to identify it.

Appendices

Appendix A

AccuRange 4000-LV Laser Distance Measurement Sensor

A.1 General Description

The AccuRange 4000-LV is a laser diode-based distance measurement sensor for ranges up to 12.2 m. It is a Class IIIa laser product that emits visible light (red, $670\,nm$ wavelength) at a power level equal to $5\,mW$.

The sensor has two cables, which are RS-232 and the power/signal cables. The first cable transfers the commands and measurements values between the computer and the sensor. While the second one supplies power to the sensor and brings out other signals. These signals, include reflected signal strength, sensor temperature, background light level, and un-calibrated pulse-width modulated output (this output is enable if the sensor configured for use with the AccuRange 4000 High-Speed Interface and host-resident calibration software).

The sensor also has push-button switch and acknowledgment light-emitting diode (LED), which are used for entering the commands manually (an alternative to the RS-232 cable). Figure A.1 shows a photo of the sensor cables with push-button switch and the LED. More information about the sensor can be found in [75].

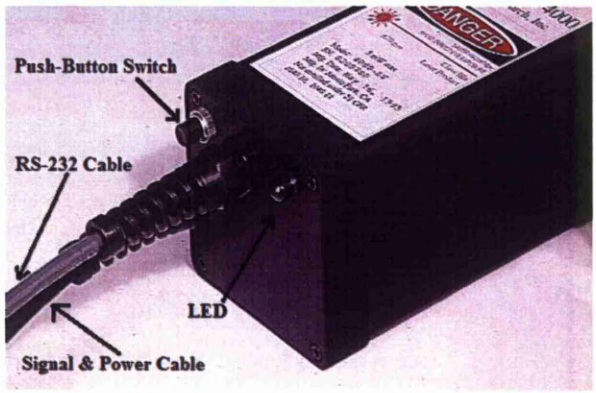

Figure A.1: AccuRange 4000-LV with its cables.

A.2 Mechanical Dimensions

The laser beam is emitted from the centre of the front panel, and the central 2.5 *inch* (63.5 *mm*) diameter of the front panel is a collector for return light. The bottom of the sensor has 4 blind holes which are used for mounting the sensor. The back of the sensor has a switch for configuration and reset, LED, and two 1.83 *m* cables. The outer case of the sensor is 3.2 *mm* aluminum, where the sensor weight is 0.625 *kg*. The acrylic front window and the back panel are sealed to the case, creating a watertight enclosure. Figure A.2 shows the mechanical dimensions for the AccuRange 4000-LV.

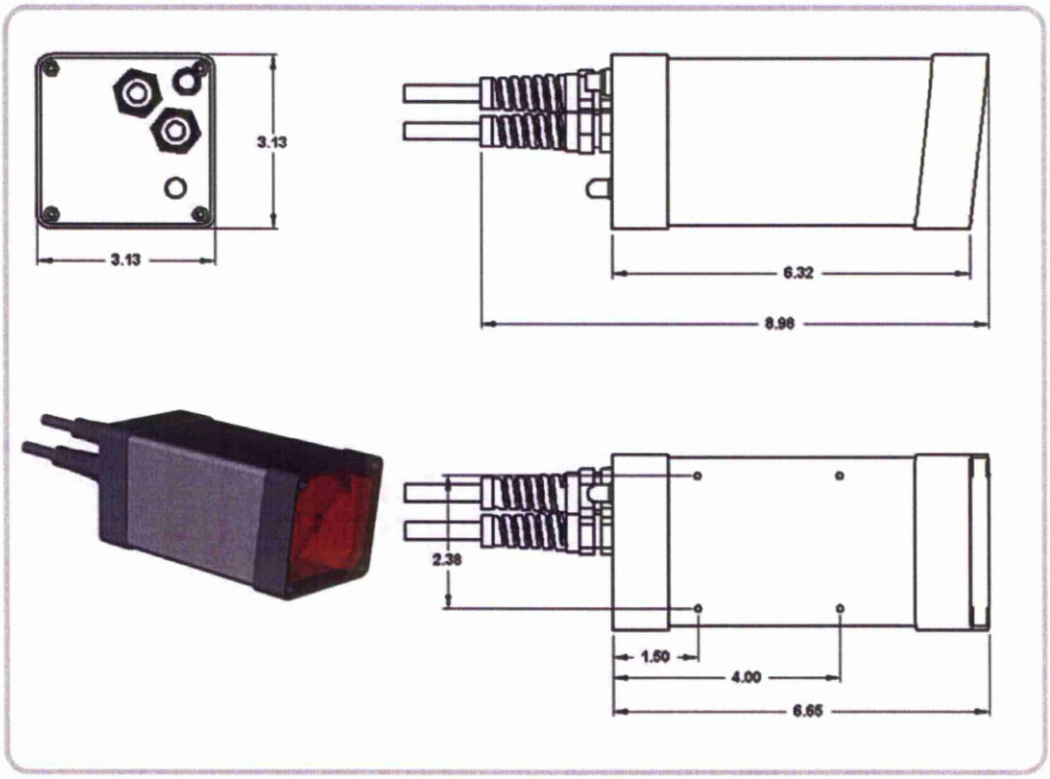

Figure A.2: Mechanical Dimension for Acuity AR4000-LV in inches [75].

A.3 Power Supply and Safety Interlock

The AccuRange 4000-LV AC to DC power supply is used to supply the sensor with the operating power and temperature stabilisation heater power. It is housed in NEMA-4 polycarbonate enclosures and it is permanently attached to the AccuRange 4000-LV with 1.83 *m* power/signal cable. The sensor's output signals are read through an additional 1.22 *m* cable, which extends beyond power supply as shown in Figure A.3.

In the AccuRange 4000-LV, the eight wires for the power/signal cable described in Table A.1 are all passed through the power supply to the extended cable except

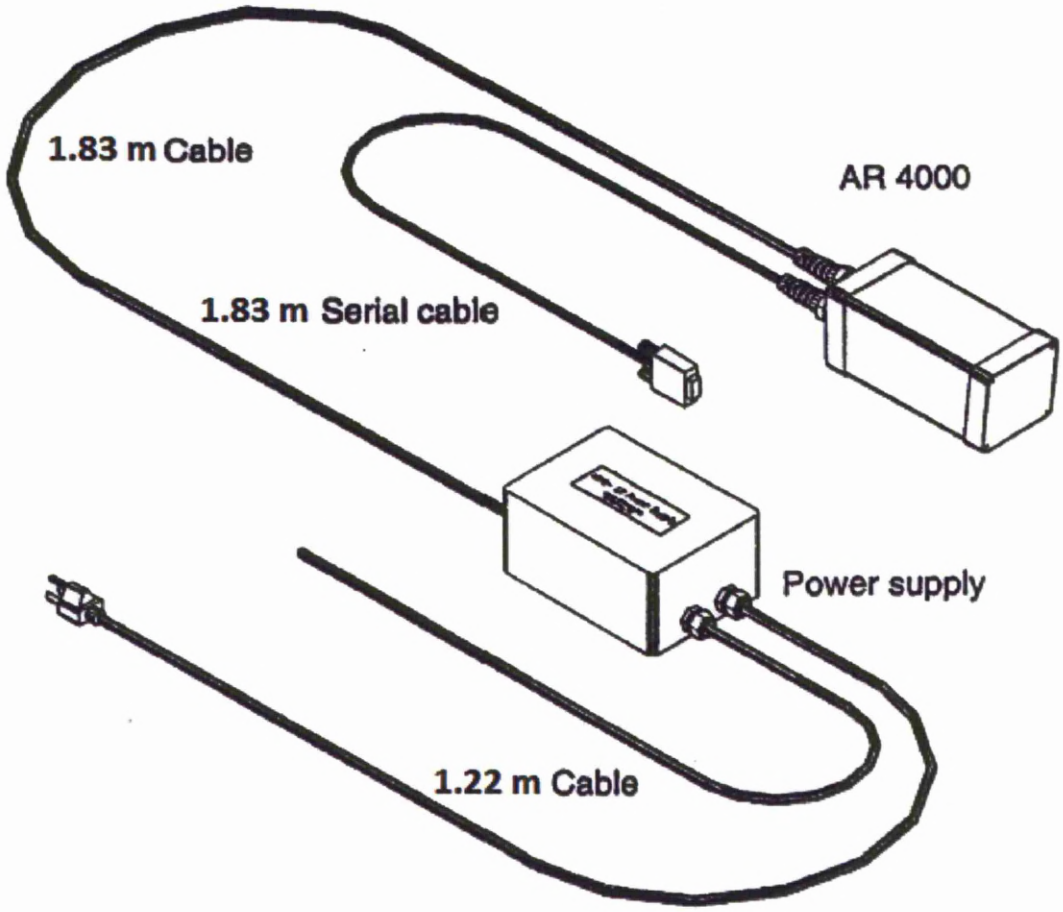

Figure A.3: AccuRange 4000-LV with Power Supply [75].

the 5-volt power and heater lines, and the heater return line which are connected only between the power supply and the sensor.

The power supply also includes a key switch and interlock jack inside its box, which must be turned and installed to complete the laser power supply circuit (access to these requires lifting the top half of the power supply case after removing the four screws from it). When the circuit is complete, the indicator lamp on the box will light, and power is applied to the sensor.

A.4 Performance and Measurement Accuracy

The AccuRange 4000-LV detects diffuse reflections from the objects with greatest sensitivity falling at distance about $2.44\,m$, although it is able to measure short distances right up to its front face. The sensor has no trouble picking up walls, floors, carpets, and even surfaces such as cathode ray tube (CRT) screens from almost any angle [75]. Shiny surfaces such as glossy plastic or paint can be more difficult to detect, depending on the angle at which the beam hits them.

Table A.1: Power and Signal Cable Wiring [75]

Wire	Function	Direction
Red	Power, $+5\,V$ $(5 - 6\,V)$	In
Black	Ground	
Orange	Heater Power, $+5\,V$ $(4.5 - 7\,V)$	In
Brown	Heater Power Return	
	Temperature, $0 - 5\,V$	Out
Blue	Pulse Width Range	Out
Green	Ambient Light Signal, $0 - 5\,V$	Out
Purple	Amplitude Signal, $0 - 5\,V$	Out
Shield	Ground at Supply End	

The following sub sections described the main factors that affect the performance of the AccuRange 4000-LV sensor.

A.4.1 Noise Factors

Three types of noise will affect the measurement accuracy in different ways, each one of these has a range of sample rates at which it is the predominant source of noise [75]. The first type is detector thermal noise, which originates in the signal detection photodiode, and is proportional to the square root of the sample rate. The second type is laser diode noise, and the third type of noise is the resolution limitation imposed by the sampling method (more information about these noise are found in [75]).

Figure A.4 shows the accuracy limit imposed by each type of noise for a given sample rate. The vertical scale is the attainable accuracy, while the horizontal scale is the sample rate. Each line represents a different constraint on the accuracy due to noise or sampling resolution. For any sample rate, the highest line at that rate represents the limiting factor and the attainable accuracy. At low sampling rates (below 10,000 samples per second) the limiting factor is the laser diode noise, shown as a horizontal line. At higher sampling rates the limiting factor becomes the detector thermal noise, shown as the curved line proportional to the square root of the sample rate. At the highest sampling rates, the sampling resolution becomes a factor, and the diagonal line represents the limitations of the AR4000 sampling resolution with a maximum range of 9.14 m [75].

A.4.2 Other Factors

In addition to noise, there are other factors that affect the indicated range output. The most significant of these is the amplitude of the return signal, or the reflectivity of the target. Indicated range can vary as much as $0.8\,cm$ between very weak signals and very strong ones. The sensor has a signal strength output, which is an analogue signal that ranges from 0 to 4 Volts and is approximately logarithmic with received light intensity.

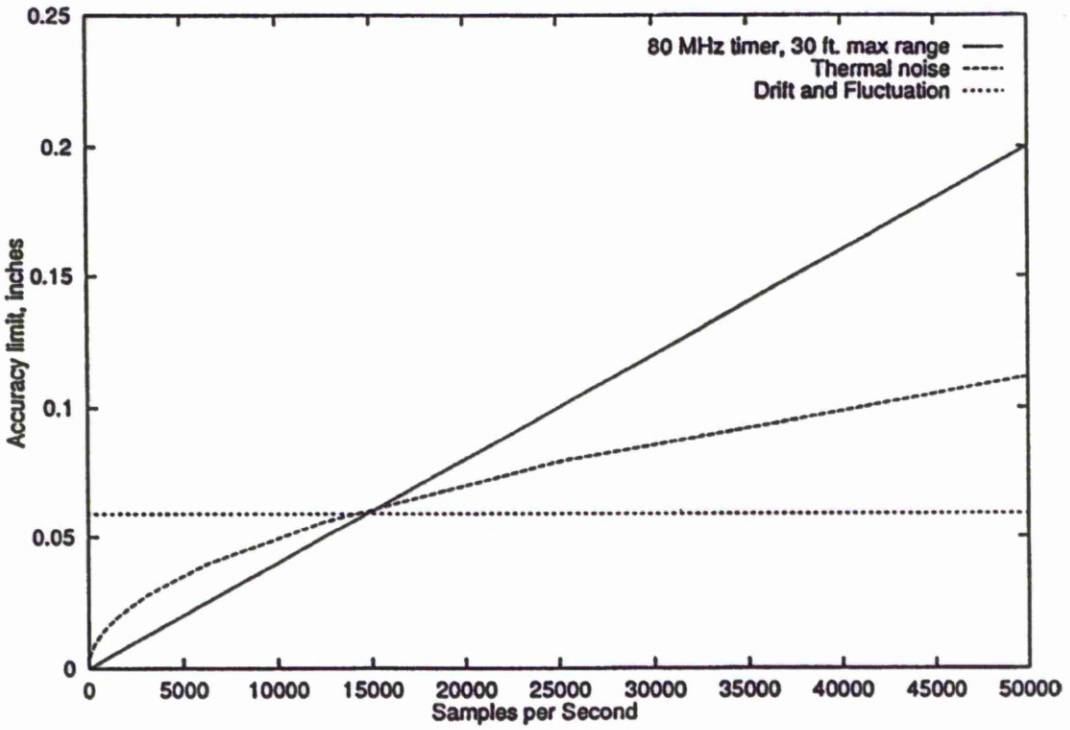

Figure A.4: Attainable Accuracy vs. Sampling Rate [75].

This output is used as an input to the sensor calibration software to compensates for variation in the reflectivity, it also can be used to create any scale images of objects over which the beam is scanned, and to determine whether a signal is valid or too weak to be reliable.

Temperature and the ambient light level also affect the measurement slightly. Analogue temperature and ambient light outputs allow these effects to be compensated for in the software, but typically they are not significant unless the sensor is used in an environment where they vary widely.

A.5 Serial Communications

Data is transmitted from the AccuRange 4000-LV as 8 data bits with no parity bit and 1 stop bit. The data sent may consist of calibrated distance readings, un-calibrated sensor data, or both together in each sample. Data may be sent in ASCII or binary format. Thus there are 6 data format combinations that can be transmitted by the 4000: ASCII calibrated only (the default), ASCII un-calibrated only, ASCII calibrated plus un-calibrated, binary calibrated only, binary un-calibrated only, and binary calibrated plus un-calibrated.

If calibrated output is enabled, the range information is the measured distance obtained by the sensors internal calibration process. This is then transmitted as ASCII

characters or binary bytes, depending on whether the ASCII or binary mode has been selected.

If un-calibrated mode is selected, the data transmitted by the sensor consists of a raw (uncorrected) range reading in sensor count units, the reflected signal strength, background light level, and sensor temperature. The size of the sensor count units in un-calibrated mode will depend on the maximum range and sample rate specified.

If both calibrated and un-calibrated outputs are enabled, the calibrated data is transmitted first, followed by the un-calibrated information. The location of the zero point may be changed for either calibrated or un-calibrated output with the Set Zero Point command. The direction of increasing output serial values from the zero point may be reversed by issuing the Set Span command with a distance closer than that used in a previously issued Set Zero Point command.

A.6 AccuRange 4000-LV Command Set

All configuration of the sensor may be done via commands sent over the serial port or by using the push-button switch and acknowledgment LED on the back panel. The serial port commands are ASCII commands that may be entered under computer control or from the keyboard of a terminal connected to the port.

Configuration information may be stored in nonvolatile Electrically Erasable Programmable Read-Only Memory (EEPROM)with the Write command, and is then retained through power cycling. Each ASCII command is one character, which for some commands must be followed by one or more parameter value characters. Table A.2 provides a quick reference of commands sent over the serial port, where one byte commands are shown as ASCII Code: < *Commandcharacter* > and multiple byte commands are shown as: ASCII Code: < *Commandcharacter* >< *Parametername* >>.

Table A.2: Commands for AccuRange Laser Scanner [75].

Command Name	Length	Command Code
Set Sample Interval	3 – 8 bytes	ASCII Code: S<Interval> (20<=Interval<=9999999)
Set Maximum Range	1 – 6 bytes	ASCII Code: F[<MaxRange>] (0<=MaxRange<=99999)
Set Zero Point (Calibrated)	1 – 6 bytes	ASCII Code:Z[<ZeroPoint>] (0<=ZeroPoint <= 99999)
Set Zero Point (Uncalibrated)	1 – 8 bytes	ASCII Code:Y[<ZeroPoint>] (0<=ZeroPoint <= 9999999)
Laser Power On	1 byte	ASCII Code: H
Laser Power Off	1 byte	ASCII Code: L
		Continued on next page

Table A.2 – continued from previous page

Command Name	Length	Command Code
Enable Serial Data Output	2 bytes	ASCII Code: A<Mode> (Mode: 1=English, 2=low level, 3=flowctl, 4=Metric(mm))
Disable Serial Data Output	2 bytes	ASCII Code: T<Mode> (Mode: 1=calibrated, 2=low level, 3=flowctl, 4=Metric(mm))
Set Baud Rate	2 bytes	ASCII Code: B<Baud Rate Code> 1=300, 2=600, 3=1200, 4=2400, 5=4800, 6=9600, 7=19200, 8=38400
Set Serial Output to ASCII	1 byte	ASCII Code: D
Set Serial Output to Binary	1 byte	ASCII Code: N
Set Span	1-8 bytes	ASCII Code: U[<Span] (0<=Span<=9999999)
Read Configuration Data From EEPROM	1 byte	ASCII Code: R
Write Configuration Data To EEPROM	1 byte	ASCII Code: W1234
Reset Configuration to Factory Defaults	1 byte	ASCII Code: I
Take Single Sample	2 byte	ASCII Code: E[<Cal/Uncal.] (1=calibrated, 2=uncalibrated, 3=both)
Set Minimum Valid Amplitude	1 – 4 byte	ASCII Code: P[Amplitude]
Set Maximum Valid Amplitude	1 – 4 byte	ASCII Code: M[Amplitude]
Show Version Number	4 bytes	ASCII Code: V1234

Appendix B

Computer Controlled Pan-Tilt Unit D46-17

B.1 General Description

The Computer-controlled pan-tilt unit is designed for high-speed, accurate positioning of camera, laser, antenna, or other payloads up to $2.72\,kg$ at speeds up to $300^o/s$. The pan-tilt controller is able to execute two different operation modes which are immediate and slaved modes. In the first mode the commands are executed as soon as they are received by the controller, while in the slaved mode all commands are stacked up until some specific command is sent to force all the commands to execute one by one. More information about the unit and its controller are found in [77].

B.2 Mechanical Dimensions

The pan-tilt unit has a weight equal to $1.361\,kg$ and its dimensions are $7.62\,cm$ wide $\times$ $13.03\,cm$ high $\times$ $10.8\,cm$ deep, while the controller dimensions are $8.3\,cm$ wide $\times$ $11.43\,cm$ long $\times$ $3.2\,cm$ high and its weight equal to $0.23\,kg$ [76]. The unit has one hole (for 1/4-20 screw standard) in the top for payload mounting and it can be mounting from the front or the bottom sides. Figure B.1 shows the mechanical dimensions (in inches) for the pan-tilt unit and its controller.

B.3 Power Supplies

The pan-tilt controller can be supplied with a DC power sources through a $2.1/5.5\,mm$ coaxial connector shown in Figure B.2. These power sources must be able to supply at least $17\,W$ continuous (e.g., battery power, vehicle power, or an AC/DC converter). The highest pan-tilt unit performance can be achieved by supply the motors with the highest motor voltage within the allowable range. For quietest pan-tilt operation, the lower motor voltage (e.g. 12 VDC) must be used.

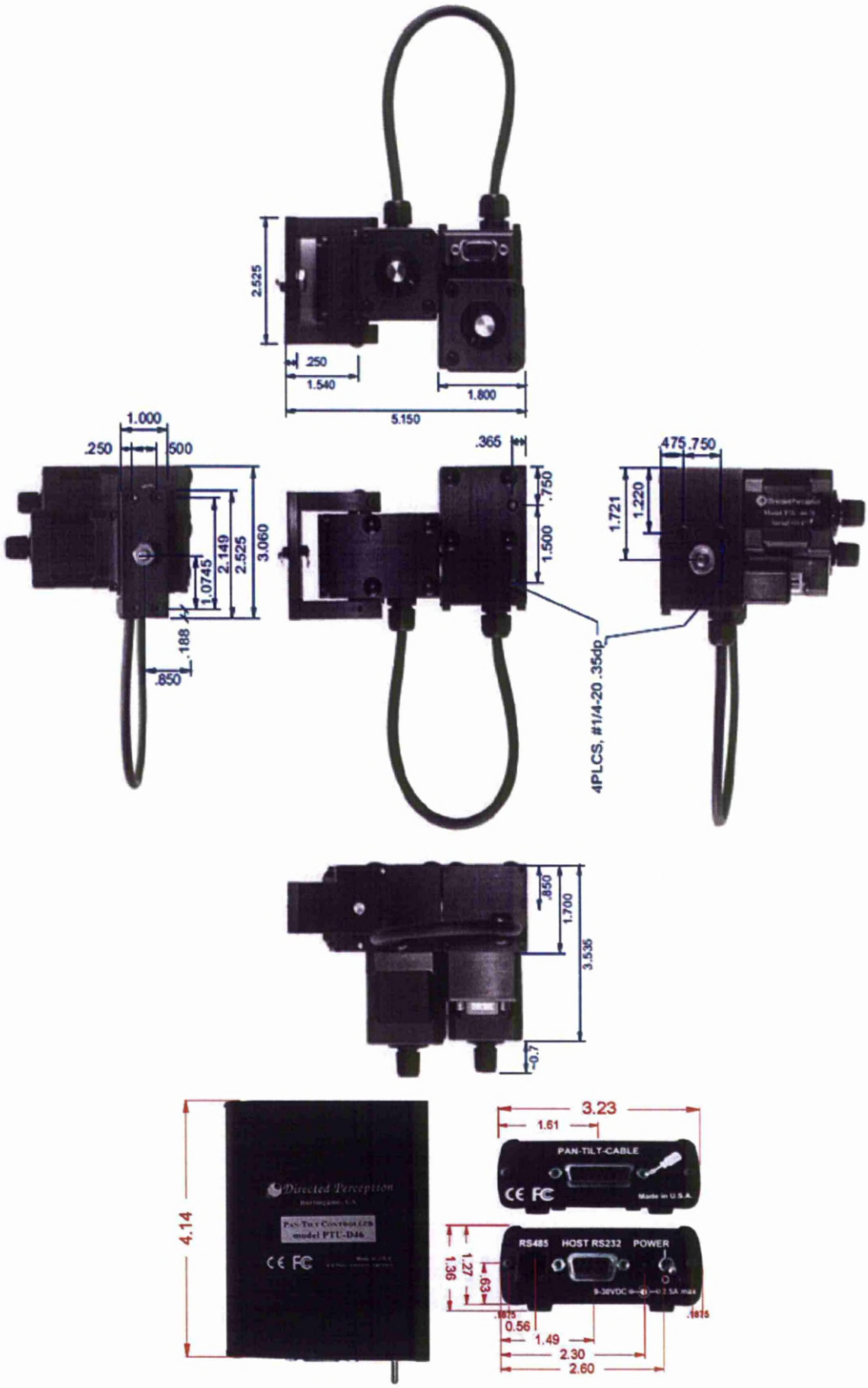

Figure B.1: Mechanical dimensions (in inches) for the pan-tilt unit (up) and its controller(down) [77].

Figure B.2: DC plug uses a $2.1/5.5\,mm$ connector [77].

B.4 RS-232 Cable and Host Settings

An RS-232 terminal or host computer are connects to the female DB-9 connector on the pan-tilt unit controller with the following connections: TxD (pin 2), RxD (pin 3), and GND (pin 5). Figure B.3 shows cable configurations for some common computer hosts, where both TxD and RxD assignments to pins 2 and 3 can vary on host computers. An RS-232 terminal or host computer should be set to 9600 baud, 1 start bit, 8 data bits, 1 stop bit, and no parity bit.

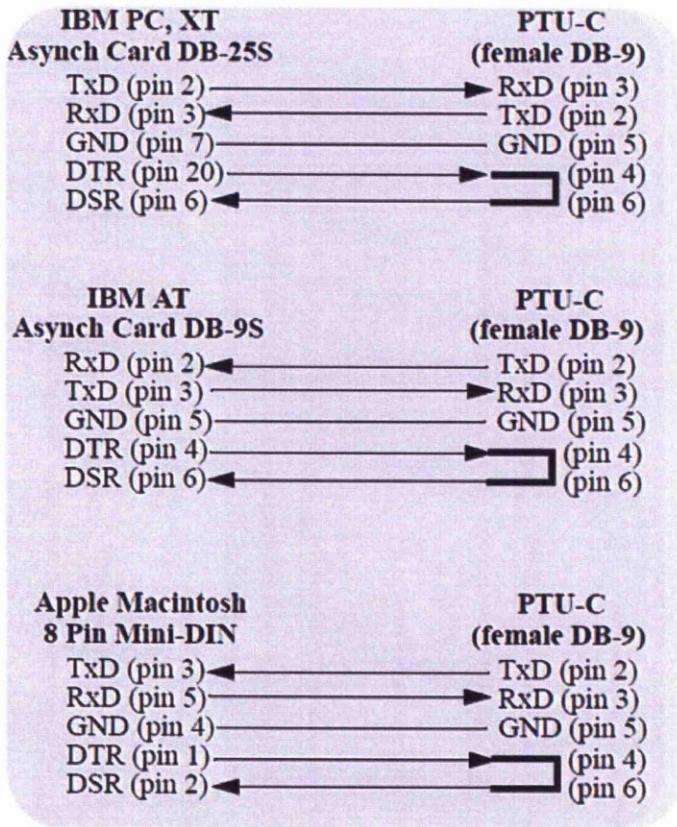

Figure B.3: RS-232 Pan-Tilt Controller (PTU-C) Connection to Common Hosts [77].

B.5 Command Sets

The pan-tilt unit can be controlled over the built-in serial port (RS-232 and RS-485) using ASCII commands. These commands can be divided in three sets, which are:

- Positional Control Commands & Queries Set: This set of commands are used to set and read the parameters that related to the unit's position such as offset, resolution, limits, etc.
- Speed Control Commands & Queries Set: This set of commands are used to set and read the speed and acceleration parameters.
- Unit Commands Set: This set of commands are deal with unit setting such as feedback format, commands save, etc.

If the unit is controlled from a terminal, a complete menu of these commands can be obtained by entering (?) character. Table B.1 provides a quick reference of commands for the above mentioned sets [124].

Table B.1: Command Sets for Pan-Tilt Unit [124].

Command Name	Command Code
Positional Control Commands & Queries	
Position (absolute)	
Query Current Absolute Pan Position	PP
Set Desired Absolute Pan Position	PP<Position>
Query Current Absolute Tilt Position	TP
Set Desired Absolute Tilt Position	TP<Position>
Offset Position (relative offset)	
Query Desired Pan Position	PO
Set Desired offset Pan Position	PO<Position>
Query Desired Tilt Position	TO
Set Desired offset Tilt Position	TO<Position>
Resolution per Position	
Query Pan Resolution	PR
Query Tilt Resolution	TR
Limit Position Queries	
Query Minimum Pan Position	PN
Query Maximum Pan Position	PX
Query Minimum Tilt Position	TN
Query Maximum Tilt Position	TX
Position Limit Enforcement	
Query Current Pan Position Limit Mode	L
Enable Pan Position Limits	LE
Disable Pan Position Limits	LD
Immediate Position Execution Mode	I

Continued on next page

Table B.1 – continued from previous page

Command Name	Command Code
Slaved Position Execution Mode	S
Await Position Command Completion	A
Halt Command	
Halt All Pan-Tilt Movement	H
Halt Pan Axis Movement	HP
Halt Tilt Axis Movement	HT
Speed Control Commands & Queries	
Speed (absolute)	
Query Desired Pan Speed	PS
Set Desired Pan Speed	PS<Positions/*Sec.* >
Query Desired Tilt Speed	TS
Set Desired Tilt Speed	TS<Positions/*Sec.* >
Delta Speed (relative offset)	
Query Current Pan Speed	PD
Set Desired Delta (Offset) Pan Speed	PD<Positions/*Sec.* >
Query Current Tilt Speed	TD
Set Desired Delta (Offset) Tilt Speed	TD<Positions/*Sec.* >
Acceleration	
Query Desired Pan Acceleration	PA
Set Desired Pan Acceleration	PA<Positions/$Sec.^2$ >
Query Desired Tilt Acceleration	TA
Set Desired Tilt Acceleration	TA<Positions/$Sec.^2$ >
Base (Start-Up) Speed	
Query Desired Pan Base Speed	PB
Set Desired Pan Base Speed	PB<Positions/*Sec.* >
Query Desired Tilt Base Speed	TB
Set Desired Tilt Base Speed	TB<Positions/*Sec.* >
Speed Bounds	
Query Upper Pan Speed Limit	PU
Set Upper Pan Speed Limit	PU<Positions/*Sec.* >
Query Lower Pan Speed Limit	PL
Set Lower Pan Speed Limit	PL<Positions/*Sec.* >
Query Upper Tilt Speed Limit	TU
Set Upper Tilt Speed Limit	TU<Positions/*Sec.* >
Query Lower Tilt Speed Limit	TL
Set Lower Tilt Speed Limit	TL<Positions/*Sec.* >
Unit Commands	
Reset Pan-Tilt Unit	
Performs Reset Calibration	R
Disable Reset Upon Power Up	RD
Reset Tilt Axis Only	RT
Reset Pan Axis Only	RP
Reset Both Pan and Tilt Axes Upon Power Up	RE
Default Save/Restore	
Save Current Settings as Defaults	DS

Continued on next page

Table B.1 – continued from previous page

Command Name	Command Code
Restore Stored Defaults	DR
Restore Factory Defaults	DF
Echo Query/Enable/Disable	
Query Current Echo Mode	E
Enable Host Command Echoing	EE
Disable Host Command Echoing	ED
Feedback Verbose/Terse/Off	
Enable Verbose ASCII Feedback	FV
Enable terse ASCII feedback	FT
Query ASCII Feedback Mode	F
Controller Firmware Version Query	V
Outside Supply Voltage and Controller Temperature Query	O

Appendix C

Object Rotation Angle

The rotation angle for the object Φ_o is the angle between the natural axis $x'_{\Re}$ for that object and the $x_{\Re}$-axis as shown in Figure C.1.

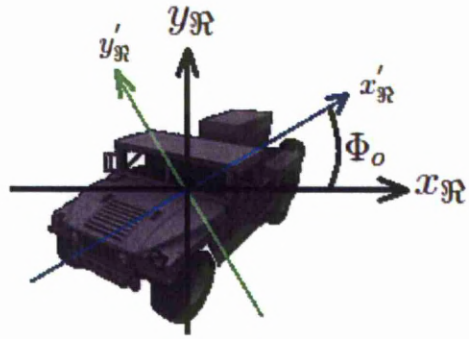

Figure C.1: Car Image Rotation Angle Φ_o and its Natural Axis ($x'_{\Re}$, $y'_{\Re}$).

The object natural axis ($x'_{\Re}$, $y'_{\Re}$) can be simply calculated by determining the eigenvalues of the image covariance matrix. This matrix is defined by [98]:

$$C_{\mathbf{sv}} = \frac{1}{K_s} \sum_{k_s=1}^{K_s} \mathbf{sv}_{k_s} \mathbf{sv}_{k_s}^T - \mathbf{m}_{\mathbf{SV}} \mathbf{m}_{\mathbf{SV}}^T \tag{C.1}$$

$$\mathbf{m}_{\mathbf{SV}} = \frac{1}{K_s} \sum_{k_s=1}^{Ks} \mathbf{sv}_{k_s} \tag{C.2}$$

where $\mathbf{sv}$ is the pixels distribution vector for the image and K_s is the number of the vector samples $\mathbf{sv}$. The matrix $C_{\mathbf{sv}}$ is a real and symmetric, therefore its eigenvalues are nonnegative real numbers [69]. These values are sorted in a non-increasing order in order to find the corresponding eigenvectors, which they represent the natural axis of the object. The eigenvectors have mirror symmetry problem which can be handled by making the positive axis direction towards the highest standard deviation (STD) of the vector's lengths (lengths between the pixel locations and the origin). More information about this procedure can be found in [125, 126]. If the STD are equal in both directions (positive and negative) then the natural axis of the second highest eigenvalues is used instead.

Appendix D

Silhouette Image Generation

The procedure steps for generating the silhouette image from the LADAR point cloud are presented as follows:

1. The point cloud are organized in a grid with storing their corresponding 3D Cartesian coordinates. The grid is then triangulated by connecting adjacent points in a square and then connecting one of the diagonals [79] as shown in Figure D.1a.

2. A sampling grid of defined size and resolution is created. This grid contains equal spaced points along the LADAR perspective view (see Figure D.1a).

3. The Barycentric local coordinates of these points are determined with respect to the projected triangles vertices (that connecting in step (1)). Figure D.1a (right side) shows the principle of calculating the Barycentric coordinates $(w_{I'}, w_{J'}, w_{K'})$ of point l' with respect to the projected triangle vertices ($\mathbf{I}'$, $\mathbf{J}'$, and $\mathbf{K}'$).

   These coordinates are defined by the following equations [127]:

$$w_{I'} = \left((J'_y - l'_y)(K'_z - l'_z) - (K'_y - l'_y)(J'_z - l'_z)\right)/Det \quad \text{(D.1)}$$

$$w_{J'} = \left((K'_y - l'_y)(I'_z - l'_z) - (I'_y - l'_y)(K'_z - l'_z)\right)/Det \quad \text{(D.2)}$$

$$w_{K'} = \left((I'_y - l'_y)(J'_z - l'_z) - (J'_y - l'_y)(I'_z - l'_z)\right)/Det \quad \text{(D.3)}$$

   where y and z are the Cartesian coordinates and

$$Det = \left((J'_y - I'_y)(K'_z - I'_z) - (K'_y - I'_y)(J'_z - I'_z)\right) \quad \text{(D.4)}$$

   The third dimension is also can be calculated for this point by [127]:

$$l'_x = I'_x w_{I'} + J'_x w_{J'} + K'_x w_{K'} \quad \text{(D.5)}$$

   Figure D.1b shows the resultant 3D interpolated points and their triangular connections, where these points have equal spaces along the y and z direction.

4. Finally the silhouette image is then generated by set the brightness at the points locations lies inside or in the projected triangles 1 ($0 \leq w_{I'}, w_{J'}, w_{K'} \leq 1$) to one and set the brightness for the other locations to zero as shown in Figure D.1c.

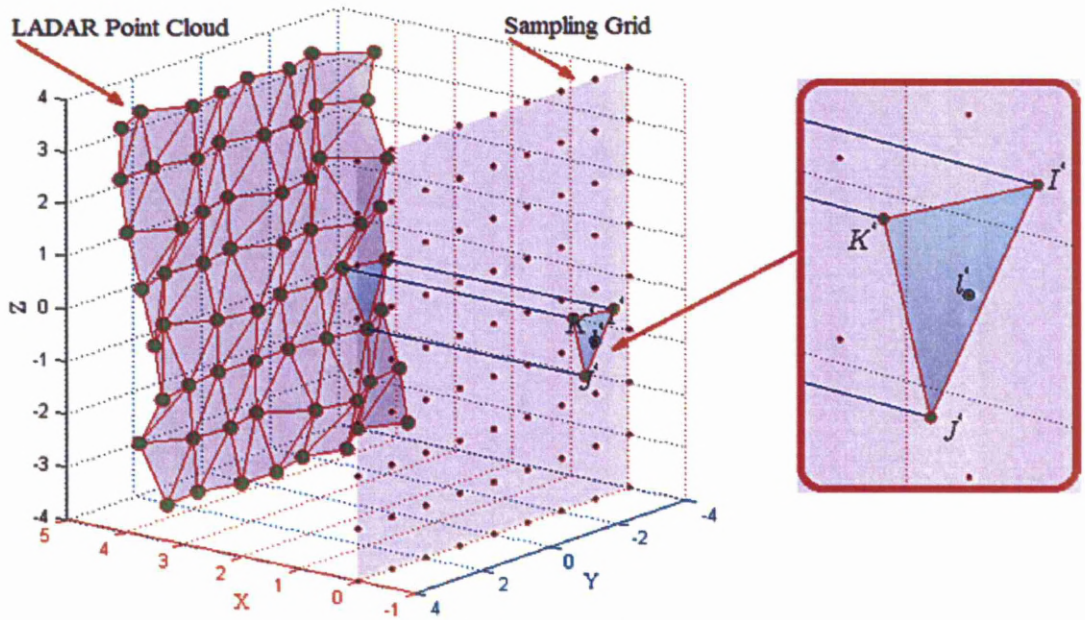

(a) Principle of Generating Silhouette Image.

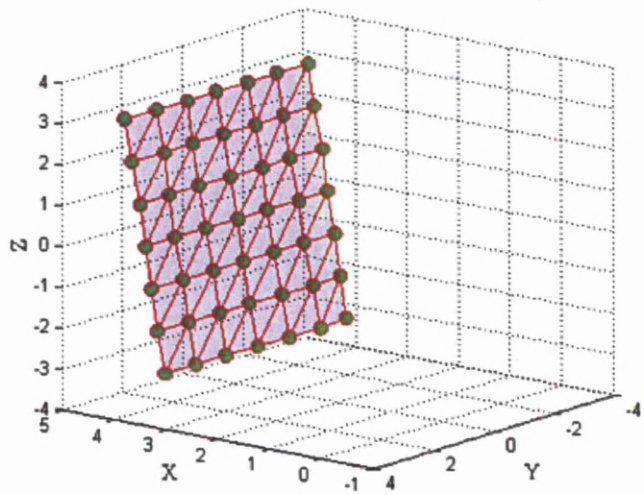

(b) Triangular Connection for the Neighbor Interpolated Points.

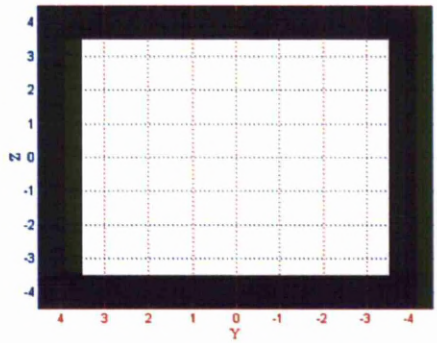

(c) Resultant Silhouette Image.

Figure D.1: Silhouette Image Generation Process.

Appendix E

Moments of Two-Dimensional Functions

For a 2-D continuous function $f(x_i, y_i)$, the moment of order (p_i, q_i) is defined as [105, 128]

$$m_{p_i q_i} = \int_{-\infty}^{\infty} \int_{-\infty}^{\infty} x_i^{p_i} y_i^{q_i} f(x_i, y_i) dx_i dy_i \tag{E.1}$$

for $p_i, q_i = 0, 1, 2, ...$ The *central moments* are defined as [105]

$$\mu_{p_i q_i} = \int_{-\infty}^{\infty} \int_{-\infty}^{\infty} (x_i - \overline{x}_i)^{p_i} (y_i - \overline{y}_i)^{q_i} f(x_i, y_i) dx_i dy_i \tag{E.2}$$

where

$$\overline{x}_i = \frac{m_{10}}{m_{00}}$$

and

$$\overline{y}_i = \frac{m_{01}}{m_{00}}$$

If $f(x_i, y_i)$ is a digital image, then E.1 becomes [129]

$$\mu_{p_i q_i} = \sum_{x_i} \sum_{y_i} x_i^{p_i} y_i^{q_i} f(x_i, y_i) \tag{E.3}$$

and E.2 becomes [105, 129]

$$\mu_{p_i q_i} = \sum_{x_i} \sum_{y_i} (x_i - \overline{x}_i)^{p_i} (y_i - \overline{y}_i)^{q_i} f(x_i, y_i) \tag{E.4}$$

The *central moments* of order up to 3 are [105]

$$\begin{aligned} \mu_{00} &= \sum_{x_i} \sum_{y_i} (x_i - \overline{x}_i)^0 (y_i - \overline{y}_i)^0 f(x_i, y_i) \qquad \text{(E.5)} \\ &= m_{00} \\ \mu_{10} &= \sum_{x_i} \sum_{y_i} (x_i - \overline{x}_i)^1 (y_i - \overline{y}_i)^0 f(x_i, y_i) \qquad \text{(E.6)} \\ &= 0 \end{aligned}$$

$$\mu_{01} = \sum_{x_i}\sum_{y_i}(x_i - \overline{x}_i)^0(y_i - \overline{y}_i)^1 f(x_i, y_i) \tag{E.7}$$
$$= 0$$
$$\mu_{11} = \sum_{x_i}\sum_{y_i}(x_i - \overline{x}_i)^1(y_i - \overline{y}_i)^1 f(x_i, y_i) \tag{E.8}$$
$$= m_{11} - \overline{y}_i m_{10}$$
$$\mu_{20} = \sum_{x_i}\sum_{y_i}(x_i - \overline{x}_i)^2(y_i - \overline{y}_i)^0 f(x_i, y_i) \tag{E.9}$$
$$= m_{20} - \overline{x}_i m_{10}$$
$$\mu_{02} = \sum_{x_i}\sum_{y_i}(x_i - \overline{x}_i)^0(y_i - \overline{y}_i)^2 f(x_i, y_i) \tag{E.10}$$
$$= m_{02} - \overline{y}_i m_{01}$$
$$\mu_{21} = \sum_{x_i}\sum_{y_i}(x_i - \overline{x}_i)^2(y_i - \overline{y}_i)^1 f(x_i, y_i) \tag{E.11}$$
$$= m_{21} - 2\overline{x}_i m_{11} - \overline{y}_i m_{20} + 2\overline{x}_i^2 m_{01}$$
$$\mu_{12} = \sum_{x_i}\sum_{y_i}(x_i - \overline{x}_i)^1(y_i - \overline{y}_i)^2 f(x_i, y_i) \tag{E.12}$$
$$= m_{12} - 2\overline{y}_i m_{11} - \overline{x}_i m_{02} + 2\overline{y}_i^2 m_{10}$$
$$\mu_{30} = \sum_{x_i}\sum_{y_i}(x_i - \overline{x}_i)^3(y_i - \overline{y}_i)^0 f(x_i, y_i) \tag{E.13}$$
$$= m_{30} - 3\overline{x}_i m_{20} + 2\overline{x}_i^2 m_{10}$$
$$\mu_{03} = \sum_{x_i}\sum_{y_i}(x_i - \overline{x}_i)^0(y_i - \overline{y}_i)^3 f(x_i, y_i) \tag{E.14}$$
$$= m_{03} - 3\overline{y}_i m_{02} + 2\overline{y}_i^2 m_{01}$$

In summary,

$$\mu_{00} = m_{00}$$
$$\mu_{10} = = 0$$
$$\mu_{01} = = 0$$
$$\mu_{11} = m_{11} - \overline{y}_i m_{10}$$
$$\mu_{20} = m_{20} - \overline{x}_i m_{10}$$
$$\mu_{02} = m_{02} - \overline{y}_i m_{01}$$
$$\mu_{21} = m_{21} - 2\overline{x}_i m_{11} - \overline{y}_i m_{20} + 2\overline{x}_i^2 m_{01}$$
$$\mu_{12} = m_{12} - 2\overline{y}_i m_{11} - \overline{x}_i m_{02} + 2\overline{y}_i^2 m_{10}$$
$$\mu_{30} = m_{30} - 3\overline{x}_i m_{20} + 2\overline{x}_i^2 m_{10}$$
$$\mu_{03} = m_{03} - 3\overline{y}_i m_{02} + 2\overline{y}_i^2 m_{01}$$

This set of central moments equations can be normalised under scaling by multiplying each of the above equations by $1/\mu_{00}^{\gamma}$, where $\gamma = \frac{p_i+q_i}{2} + 1$ for $(p_i + q_i = 2, 3, ...)$.

So the *normalised central moments* of order (p_i, q_i), are defined as [105, 129]

$$\partial_{p_i q_i} = \frac{\mu_{p_i q_i}}{\mu_{00}^{\gamma}} \tag{E.15}$$

for $p_i, q_i = 0, 1, 2, ...$

From the second and third moments, a set of seven *invariant moments* can be derived, which are [105, 129]

$$\vartheta_1 = \partial_{20} + \partial_{02} \tag{E.16}$$

$$\vartheta_2 = (\partial_{20} - \partial_{02})^2 + 4\partial_{11}^2 \tag{E.17}$$

$$\vartheta_3 = (\partial_{30} - 3\partial_{12})^2 + (3\partial_{21} - \partial_{03})^2 \tag{E.18}$$

$$\vartheta_4 = (\partial_{30} + \partial_{12})^2 + (\partial_{21} + \partial_{03})^2 \tag{E.19}$$

$$\begin{aligned}\vartheta_5 = {} & (\partial_{30} - 3\partial_{12})(\partial_{30} + \partial_{12})[(\partial_{30} + \partial_{12})^2 - 3(\partial_{21} + \partial_{03})^2] \\ & +(3\partial_{21} - \partial_{03})(\partial_{21} + \partial_{03})[3(\partial_{30} + \partial_{12})^2 - (\partial_{21} + \partial_{03})^2]\end{aligned} \tag{E.20}$$

$$\begin{aligned}\vartheta_6 = {} & (\partial_{20} - \partial_{02})[(\partial_{30} + \partial_{12})^2 - (\partial_{21} + \partial_{03})^2] \\ & +4\partial_{11}(\partial_{30} + \partial_{12})(\partial_{21} + \partial_{03})\end{aligned} \tag{E.21}$$

$$\begin{aligned}\vartheta_7 = {} & (3\partial_{21} - \partial_{03})(\partial_{30} + \gamma_{12})[(\partial_{30} + \partial_{12})^2 - 3(\partial_{21} + \partial_{03})^2] \\ & +(3\partial_{21} - \partial_{03})(\partial_{21} + \partial_{03})[3(\partial_{30} + \partial_{12})^2 - (\partial_{21} + \partial_{03})^2]\end{aligned} \tag{E.22}$$

This set of moments is invariant to translation, rotation, and scale change. The absolute value of the *log* was used instead of the *invariant moments* values themselves. Use of the *log* reduces the dynamic range, and the absolute value avoid having to deal with complex numbers that result when computing the *log* of negative *invariant moments*. Because interest generally lies on the invariance of the moments and not their sign [129]

Appendix F

Simulation Results with Range

This appendix presents the simulation results of evaluating the model/class recognition performance for the new chromatic descriptors and the invariant moment for each individual effect at each scanning range.

These effects are:

- Noise Effects.
- Resolution Effects.
- View Effects.
- Scaling Effects.
- Rotation Effects.

F.1 Noise Effect

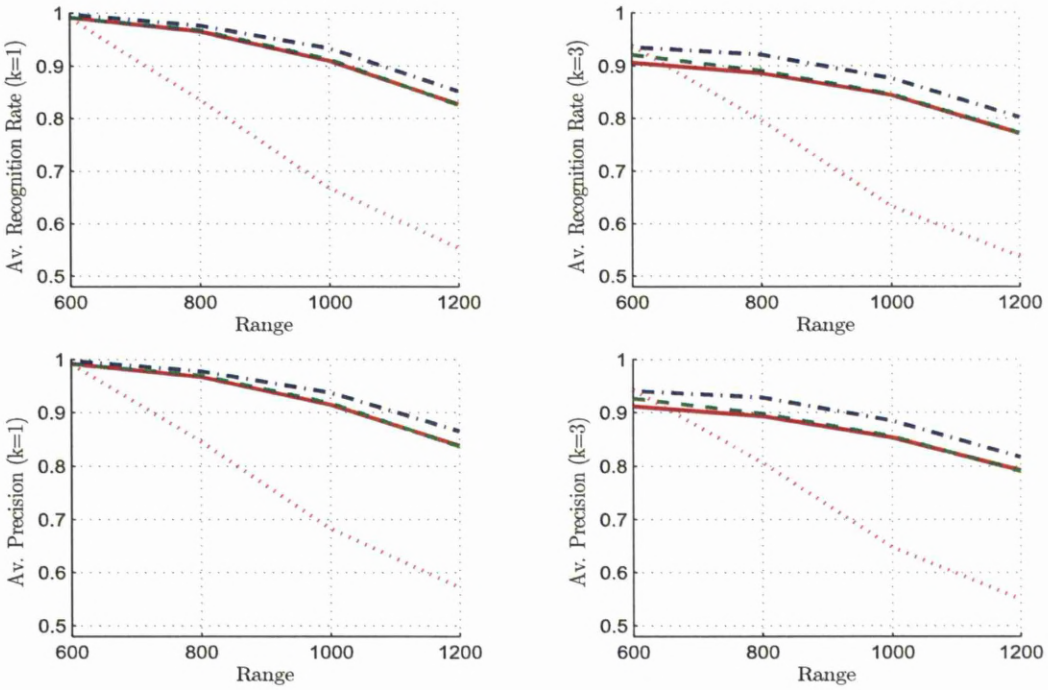

(a) Average Model Recognition Rate and Precision.

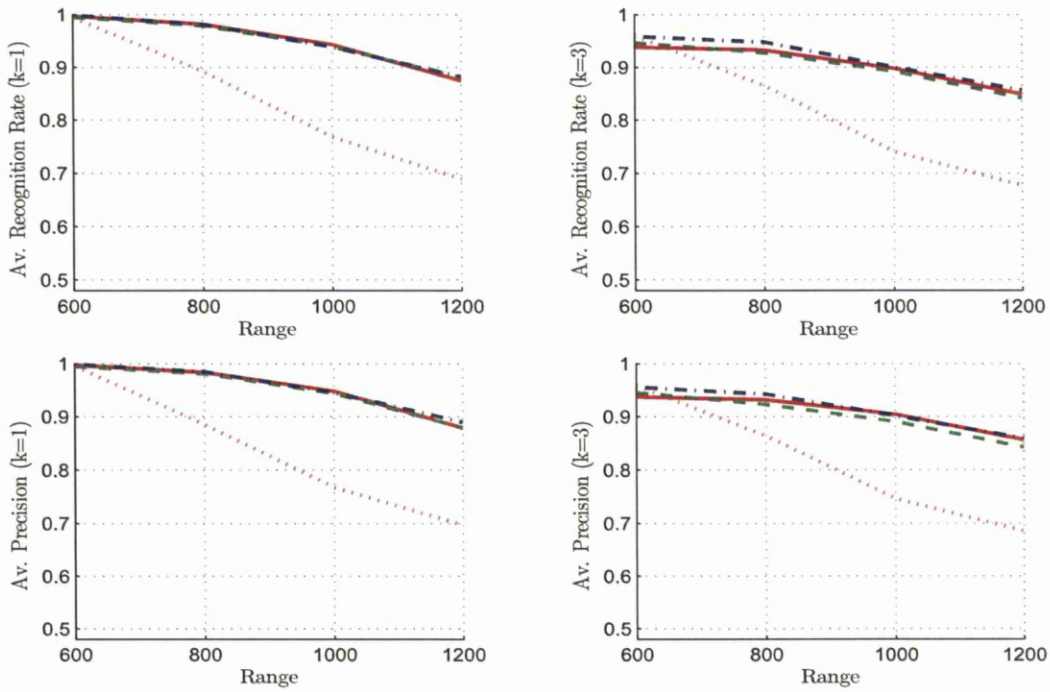

(b) Average Class Recognition Rate and Precision.

Figure F.1: Average Recognition Rate and Precision During Noise Effect ($M_{CH} = 1$) for HHOGD "-", HHOTD "- -", COTD "-.-", and Invariant Moment "." Descriptors.

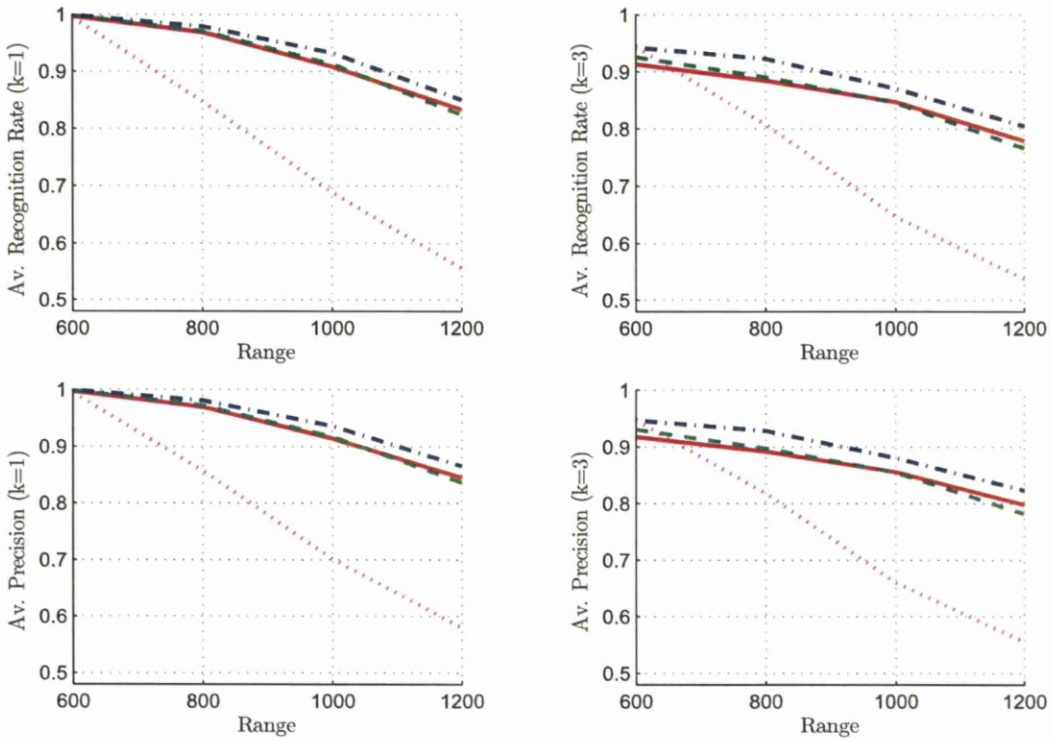

(a) Average Model Recognition Rate and Precision.

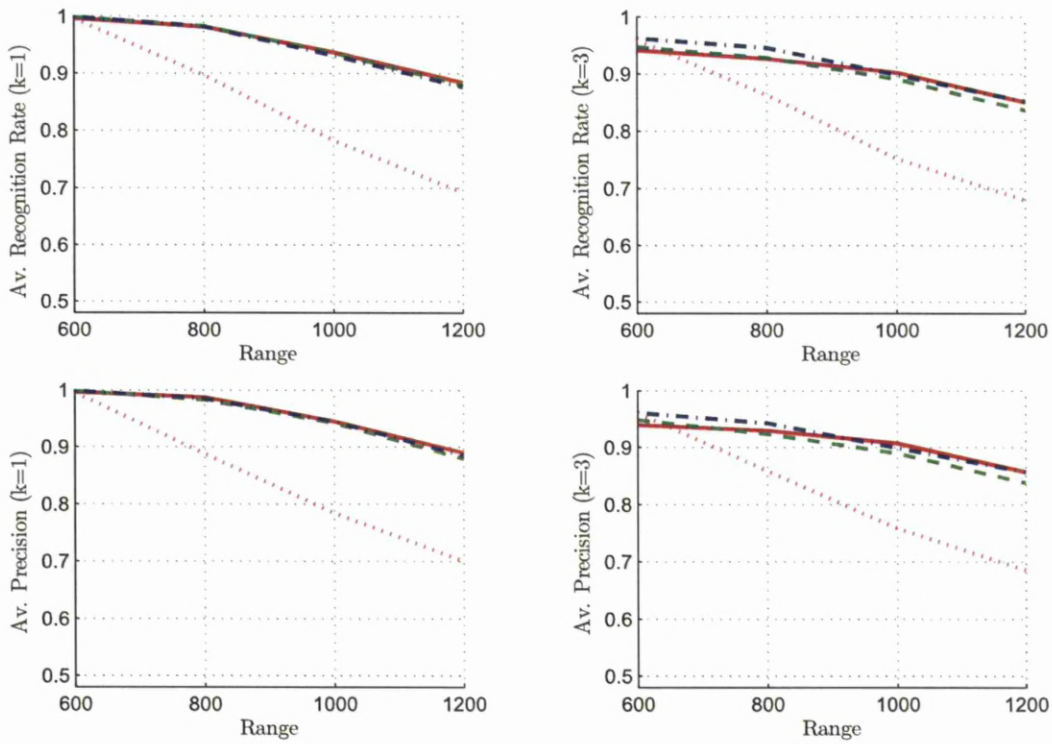

(b) Average Class Recognition Rate and Precision.

Figure F.2: Average Recognition Rate and Precision During Noise Effect ($M_{CH} = 50$) for HHOGD "-", HHOTD "- -", COTD "-.-", and Invariant Moment "." Descriptors.

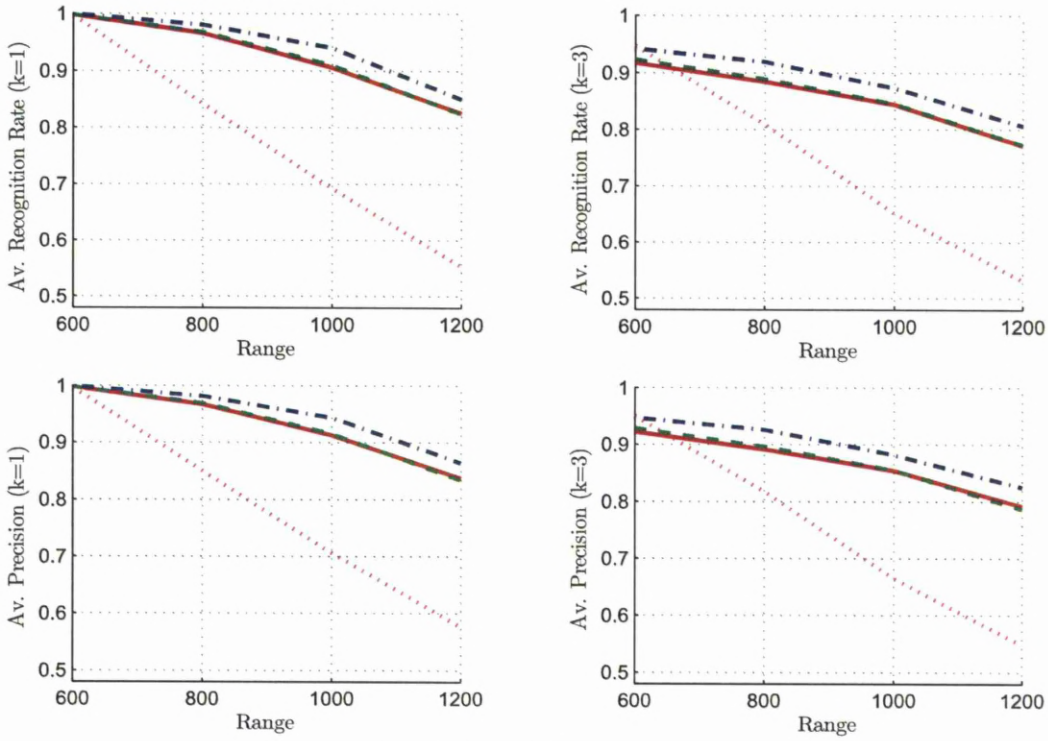

(a) Average Model Recognition Rate and Precision.

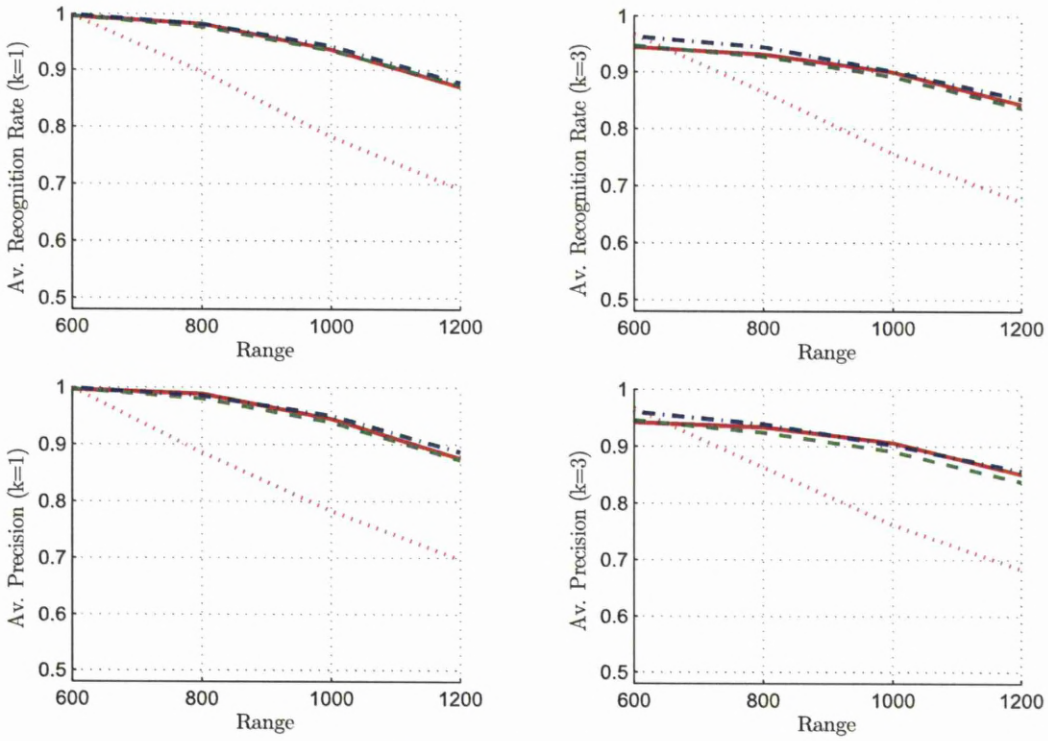

(b) Average Class Recognition Rate and Precision.

Figure F.3: Average Recognition Rate and Precision During Noise Effect ($M_{CH} = 100$) for HHOGD "-", HHOTD "- -", COTD "-.-", and Invariant Moment "." Descriptors.

F.2 Resolution Effect

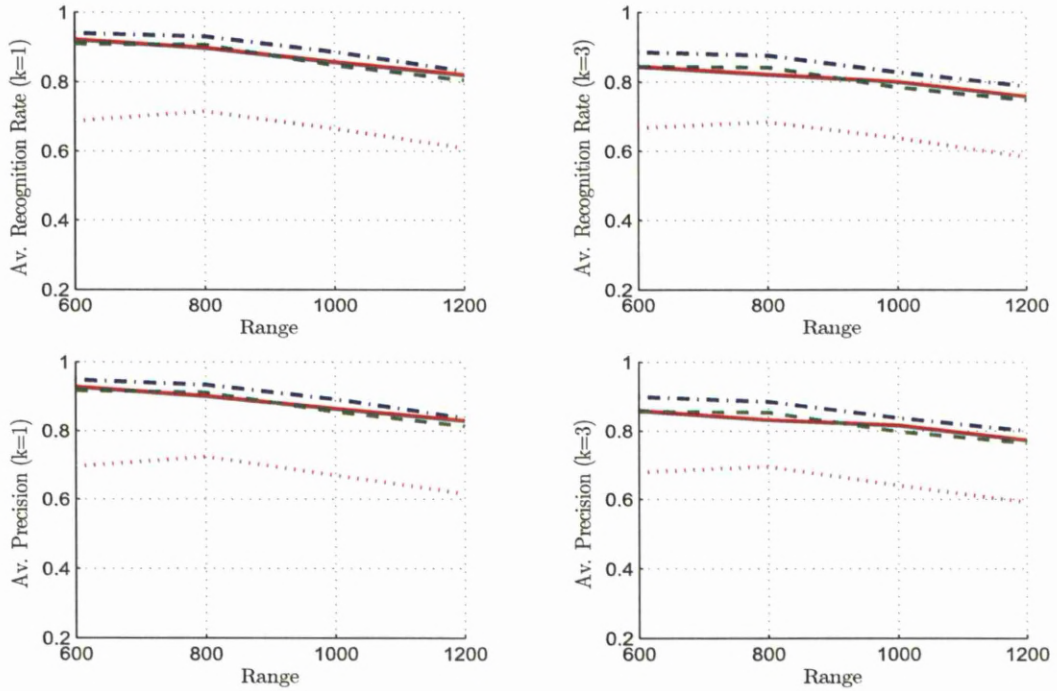

(a) Average Model Recognition Rate and Precision.

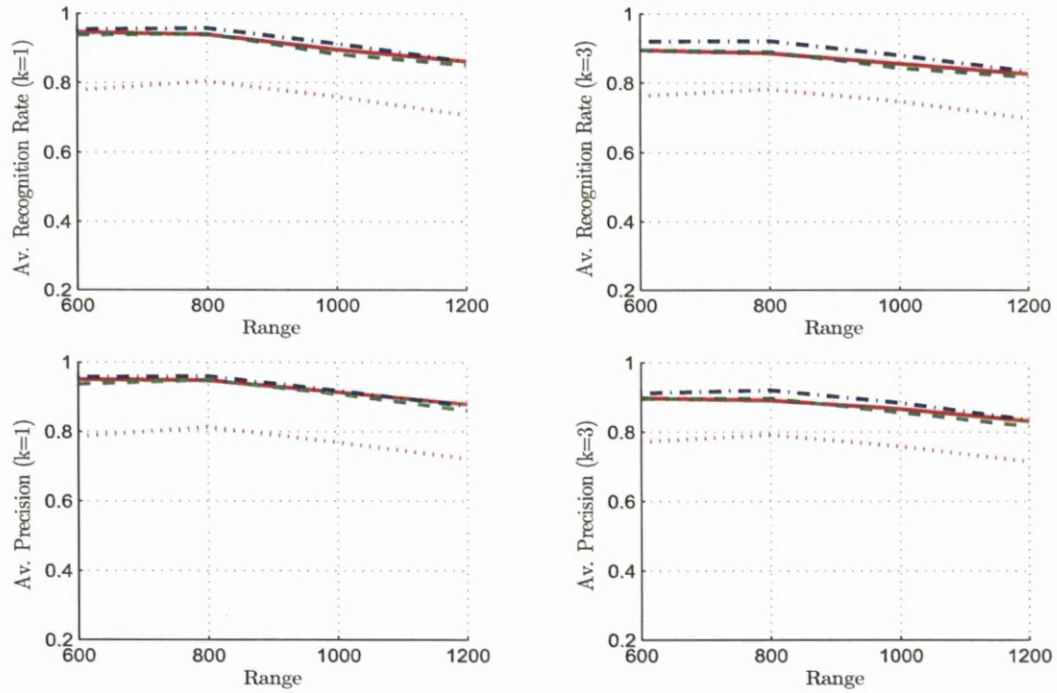

(b) Average Class Recognition Rate and Precision.

Figure F.4: Average Recognition Rate and Precision During Resolution Effect (0.006°) for HHOGD "-", HHOTD "- -", COTD "-.-", and Invariant Moment "." Descriptors.

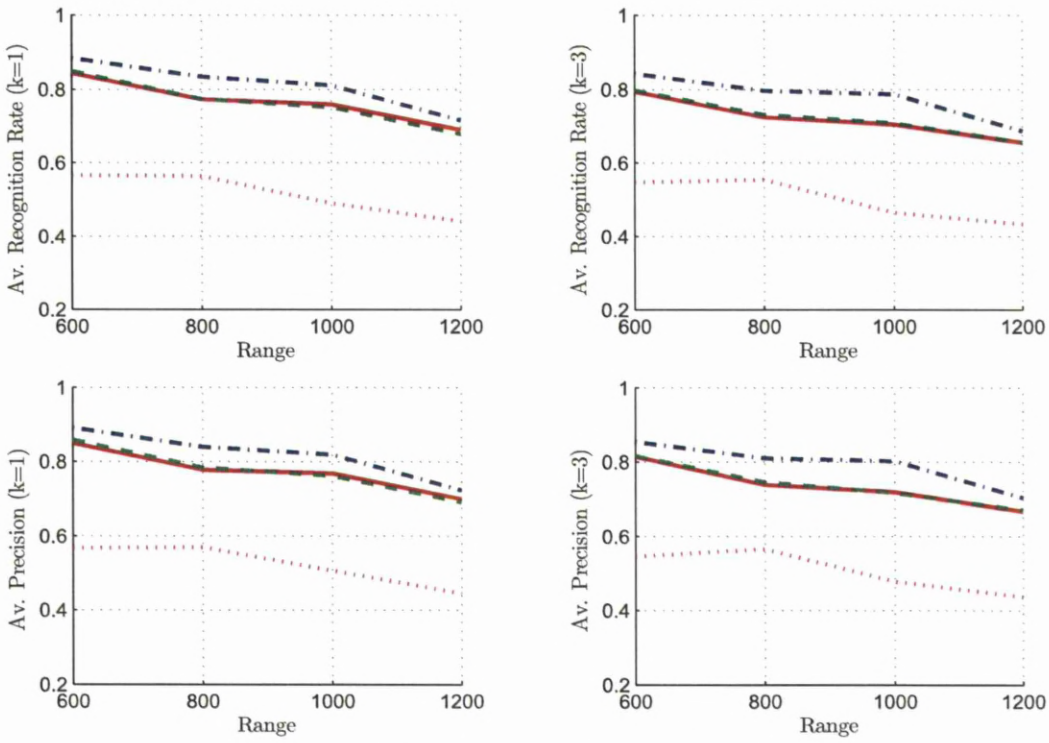

(a) Average Model Recognition Rate and Precision.

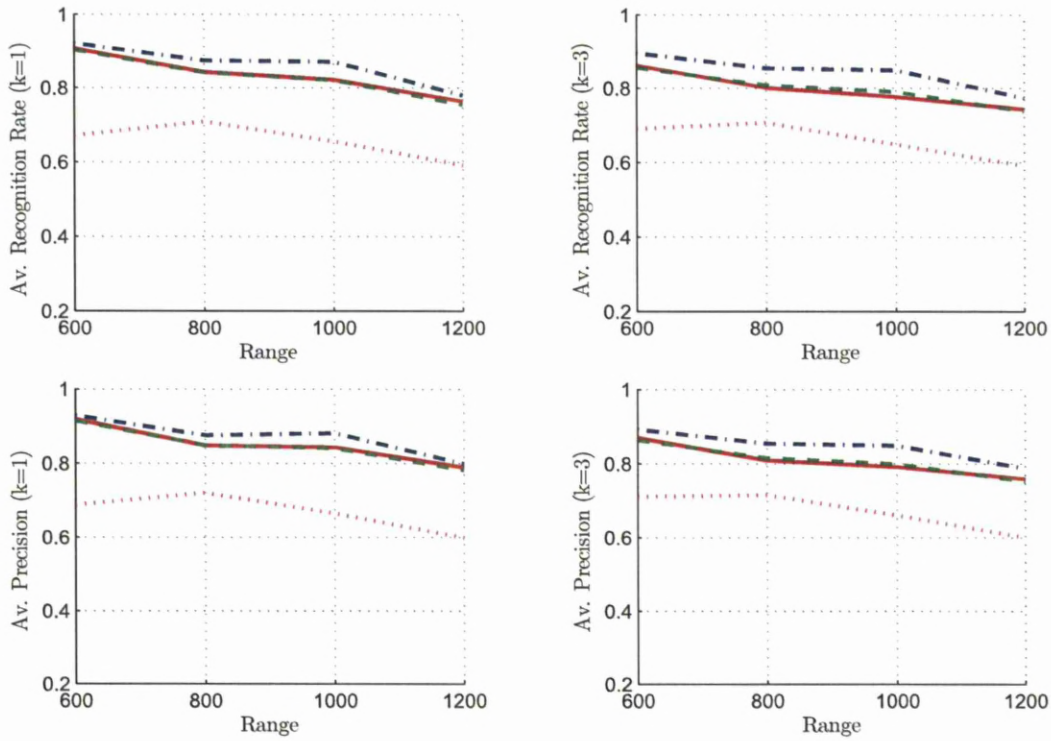

(b) Average Class Recognition Rate and Precision.

Figure F.5: Average Recognition Rate and Precision During Resolution Effect (0.008^o) for HHOGD "-", HHOTD "- -", COTD "-.-", and Invariant Moment "." Descriptors.

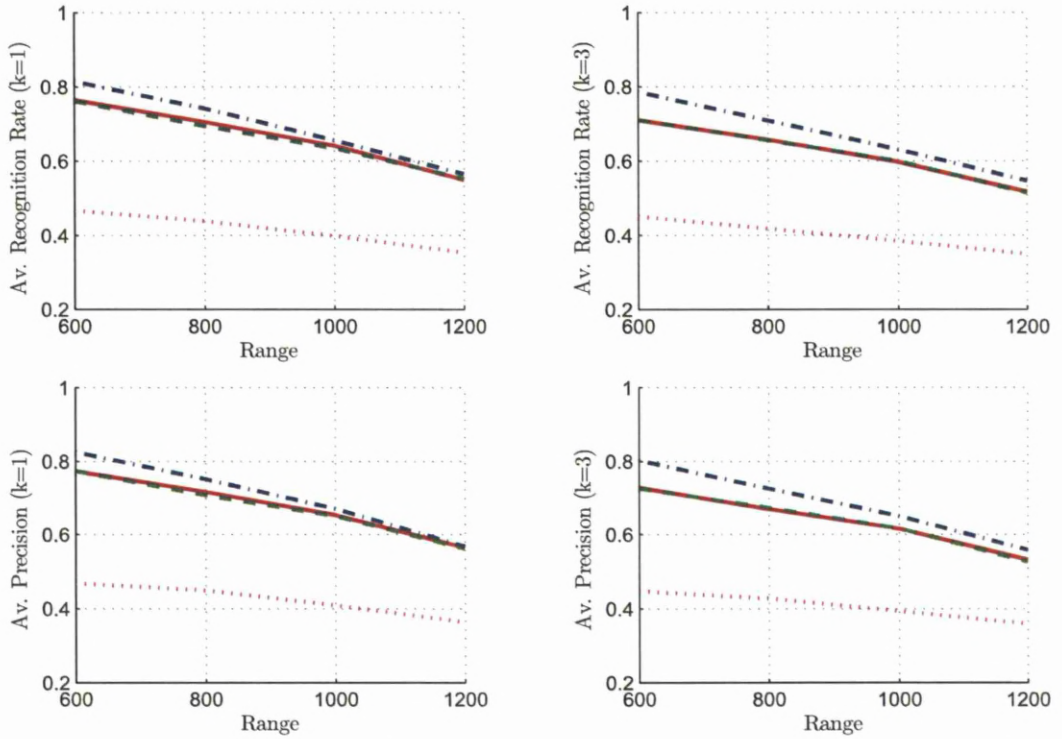

(a) Average Model Recognition Rate and Precision.

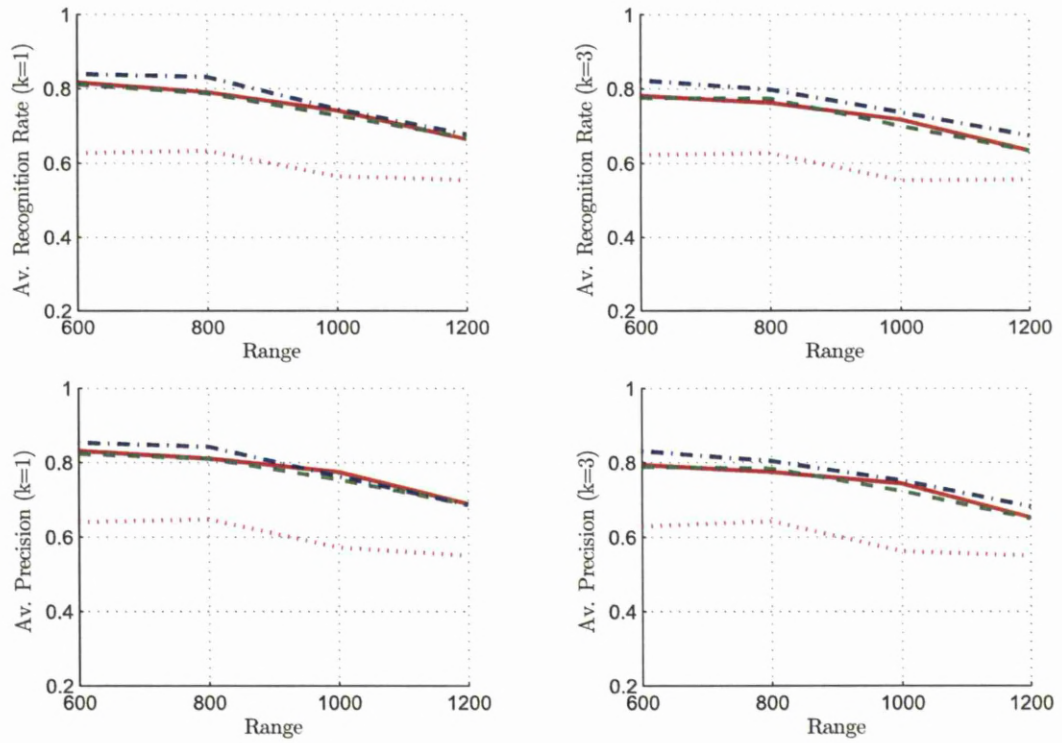

(b) Average Class Recognition Rate and Precision.

Figure F.6: Average Recognition Rate and Precision During Resolution Effect (0.01^o) for HHOGD "-", HHOTD "- -", COTD "-.-", and Invariant Moment "." Descriptors.

F.3 View Effect

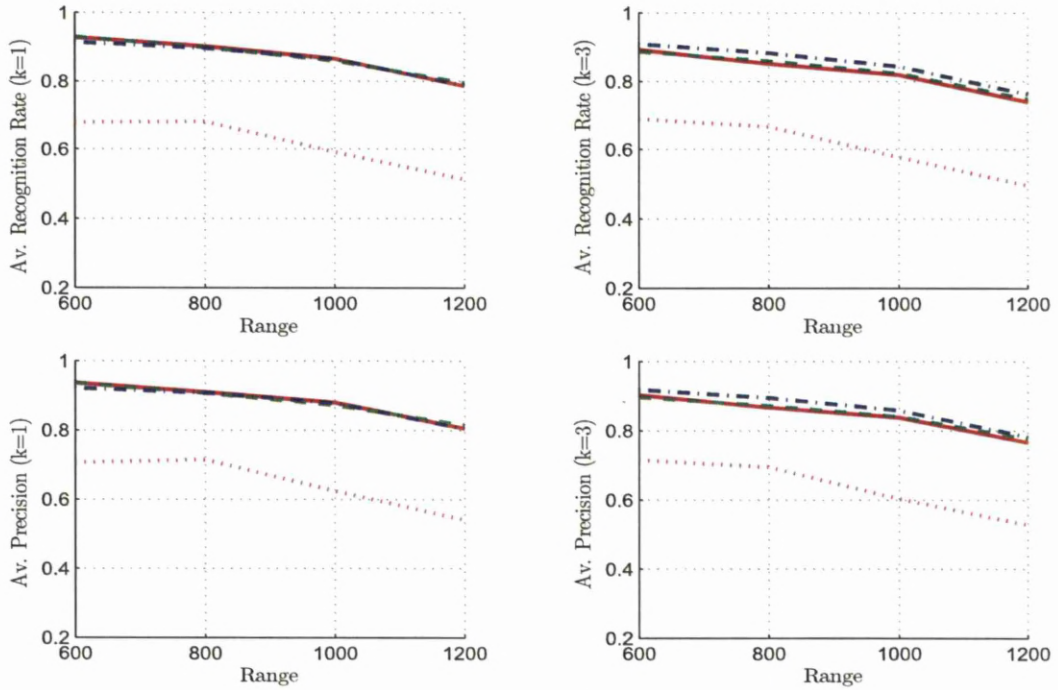

(a) Average Model Recognition Rate and Precision.

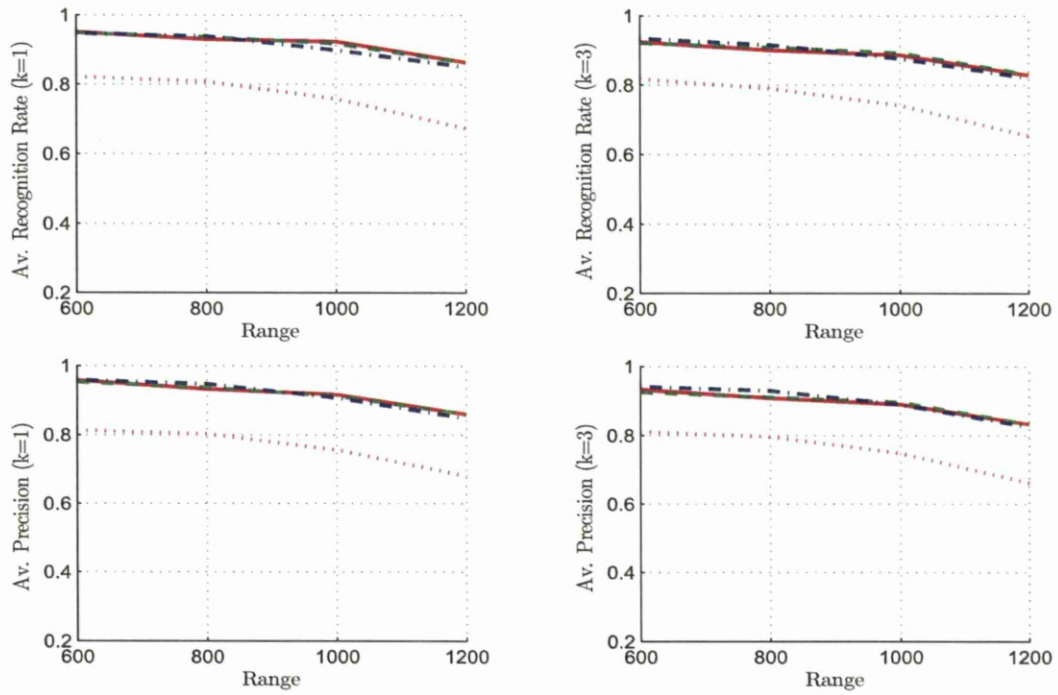

(b) Average Class Recognition Rate and Precision.

Figure F.7: Average Recognition Rate and Precision During View Effect (2.5°) for HHOGD "-", HHOTD "- -", COTD "-.-", and Invariant Moment "." Descriptors.

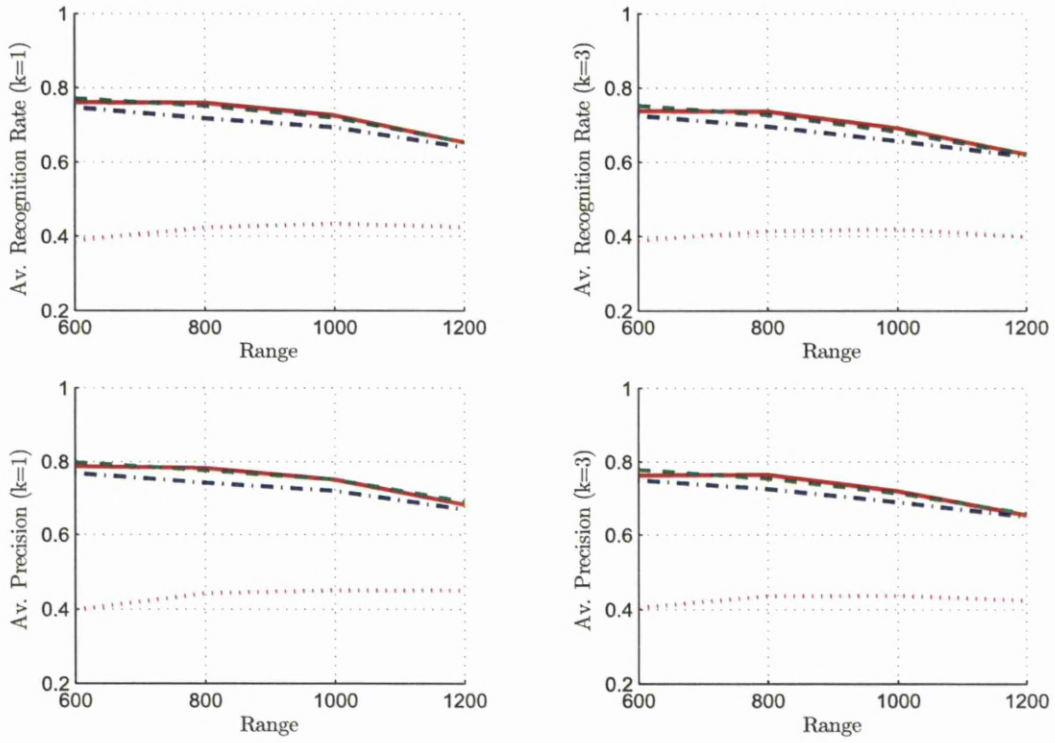

(a) Average Model Recognition Rate and Precision.

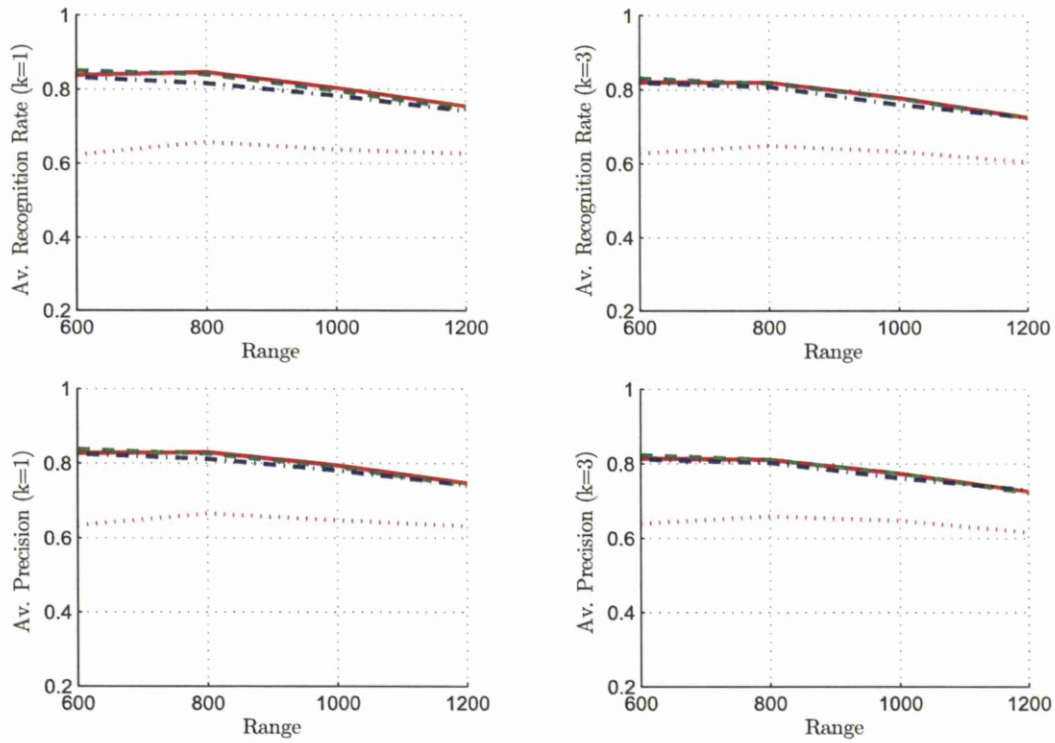

(b) Average Class Recognition Rate and Precision.

Figure F.8: Average Recognition Rate and Precision During View Effect (5^o) for HHOGD "-", HHOTD "- -", COTD "-.-", and Invariant Moment "." Descriptors.

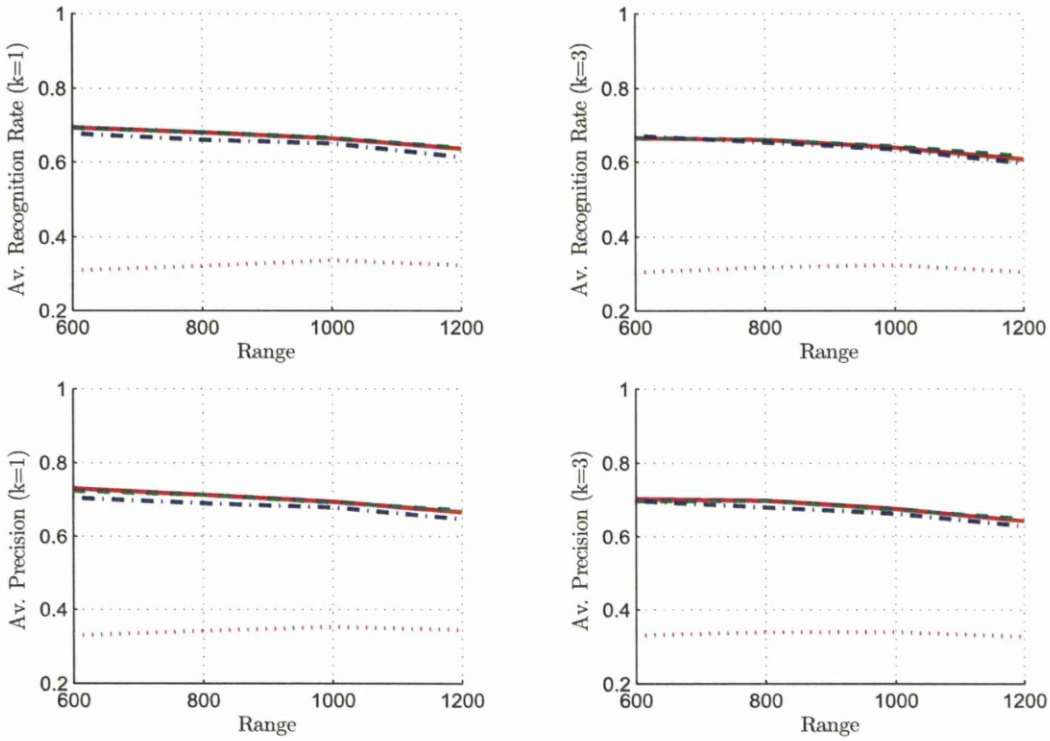

(a) Average Model Recognition Rate and Precision.

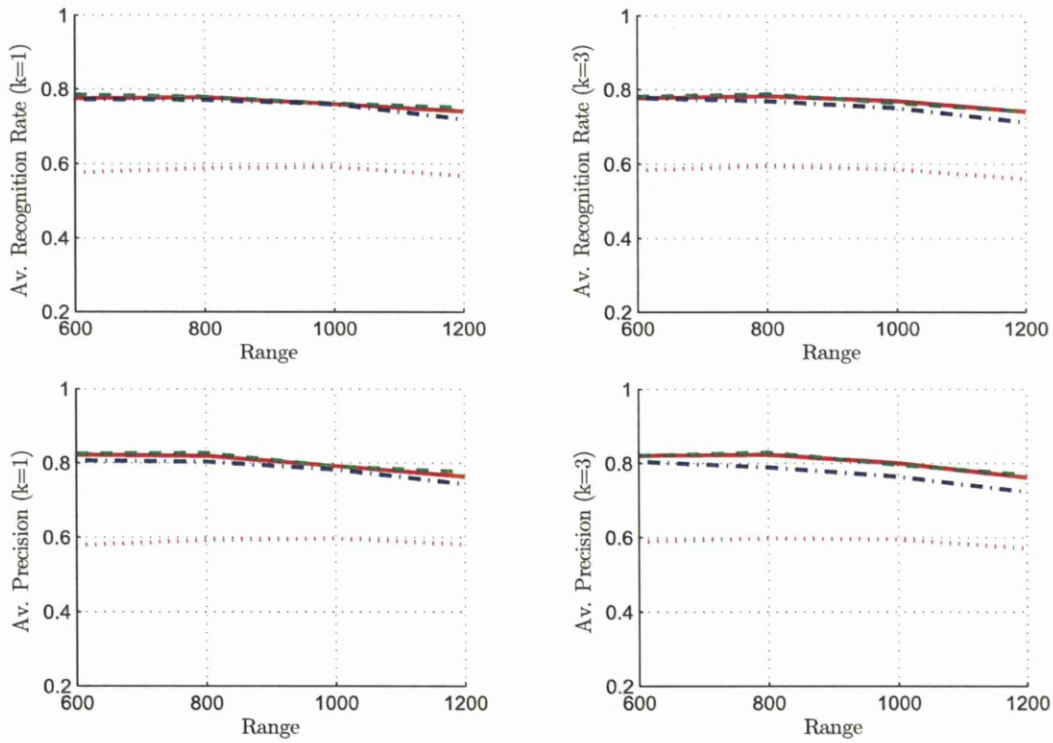

(b) Average Class Recognition Rate and Precision.

Figure F.9: Average Recognition Rate and Precision During View Effect (7.5°) for HHOGD "-", HHOTD "- -", COTD "-.-", and Invariant Moment "." Descriptors.

F.4 Scale Effect

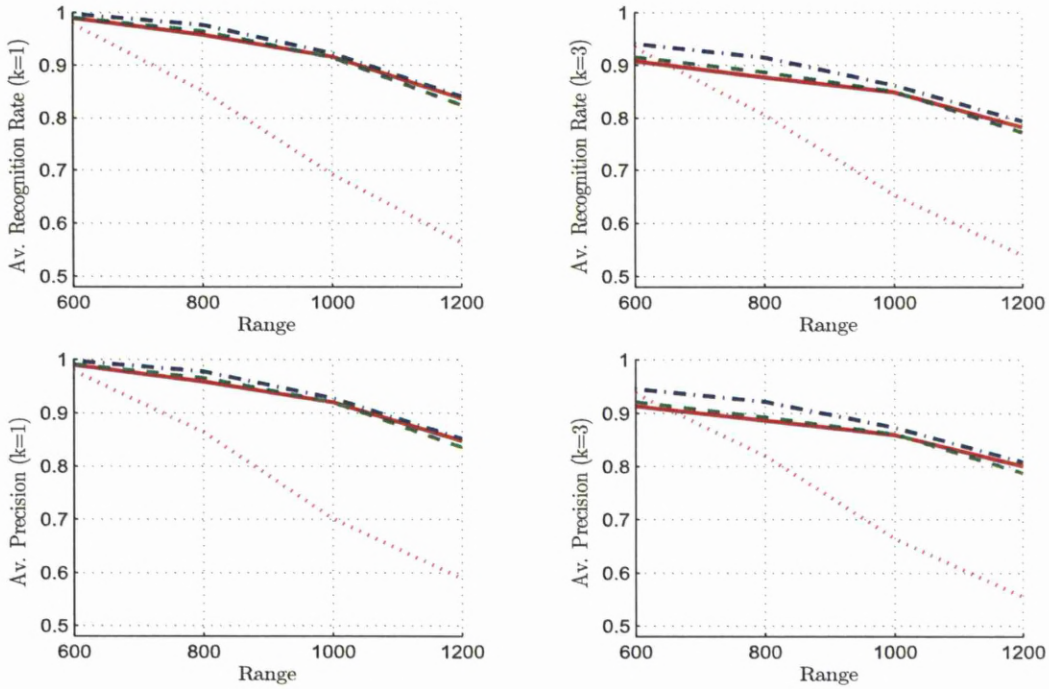

(a) Average Model Recognition Rate and Precision.

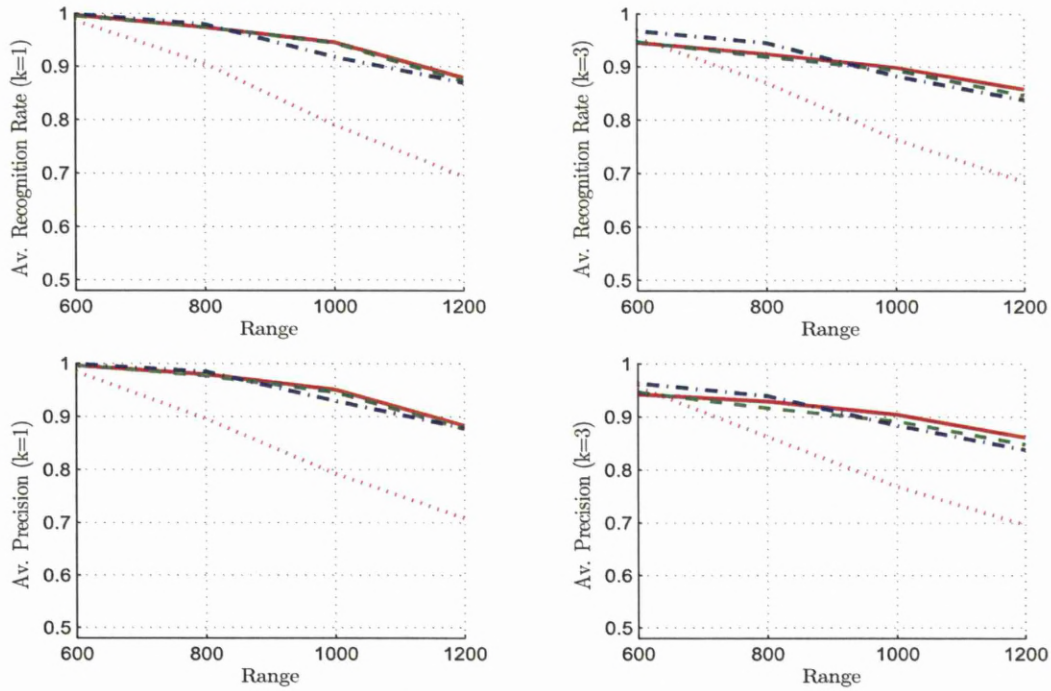

(b) Average Class Recognition Rate and Precision.

Figure F.10: Average Recognition Rate and Precision During Scale Effect (10%) for HHOGD "-", HHOTD "- -", COTD "-.-", and Invariant Moment "." Descriptors.

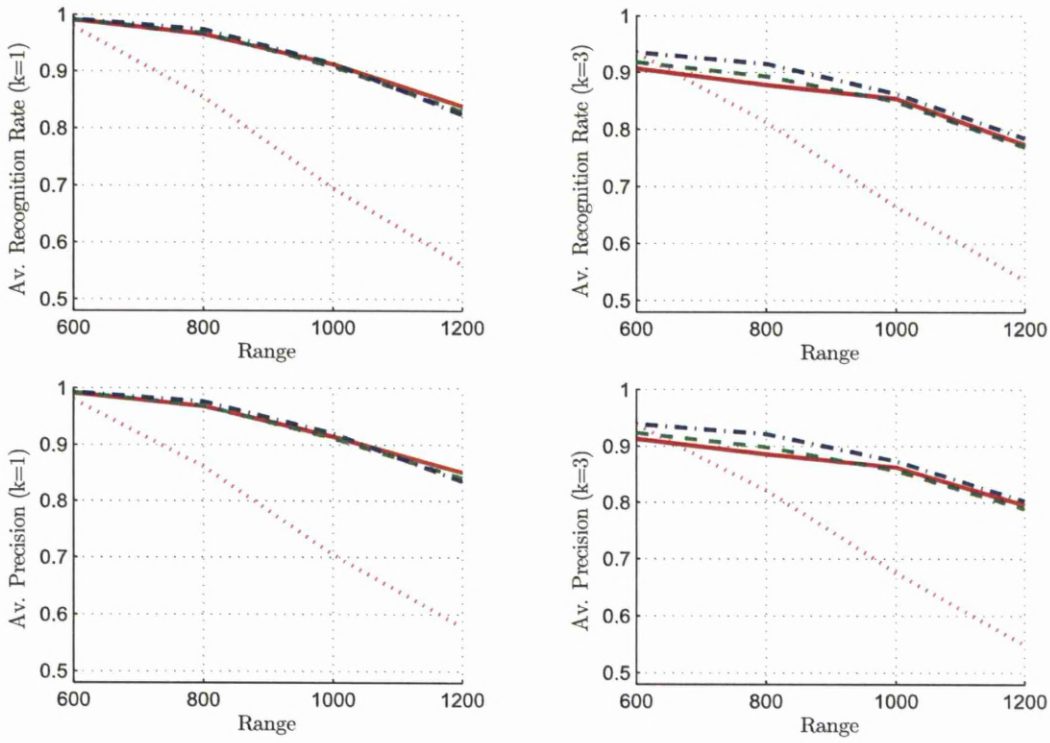

(a) Average Model Recognition Rate and Precision.

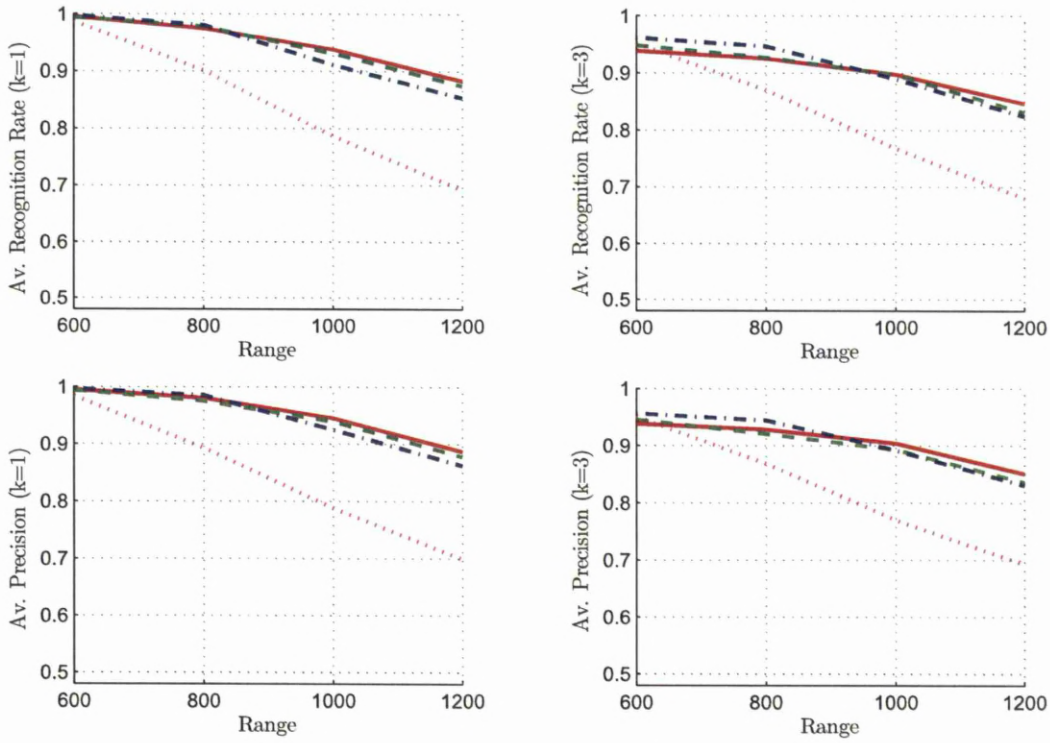

(b) Average Class Recognition Rate and Precision.

Figure F.11: Average Recognition Rate and Precision During Scale Effect (20%) for HHOGD "-", HHOTD "- -", COTD "-.-", and Invariant Moment "." Descriptors.

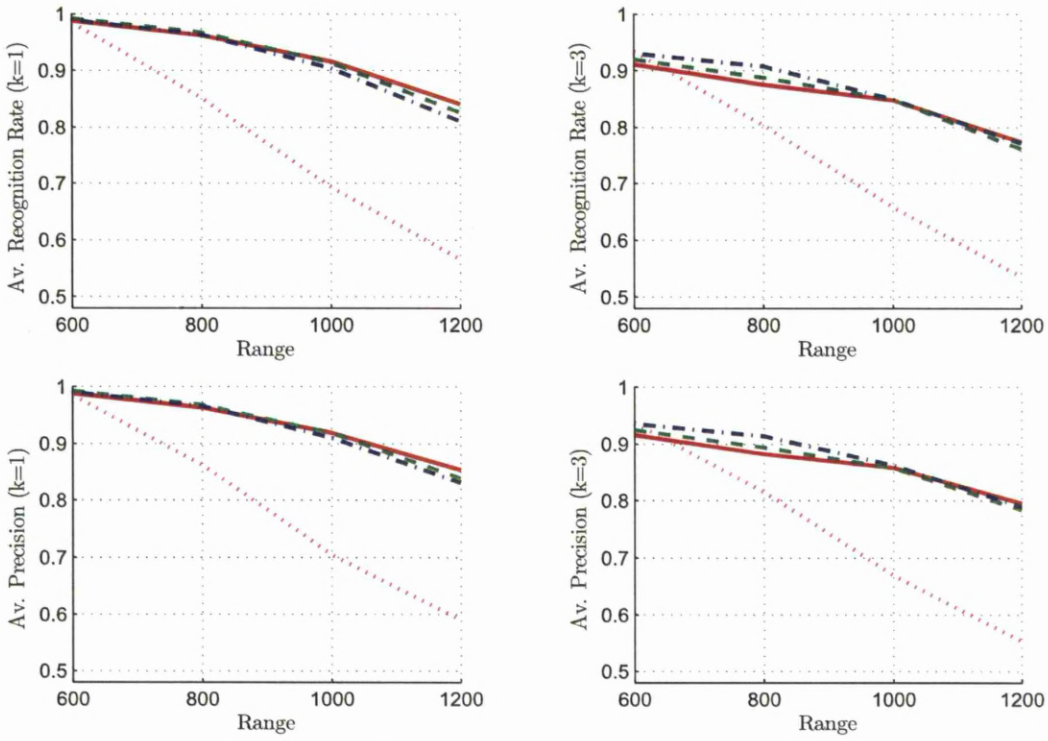

(a) Average Model Recognition Rate and Precision.

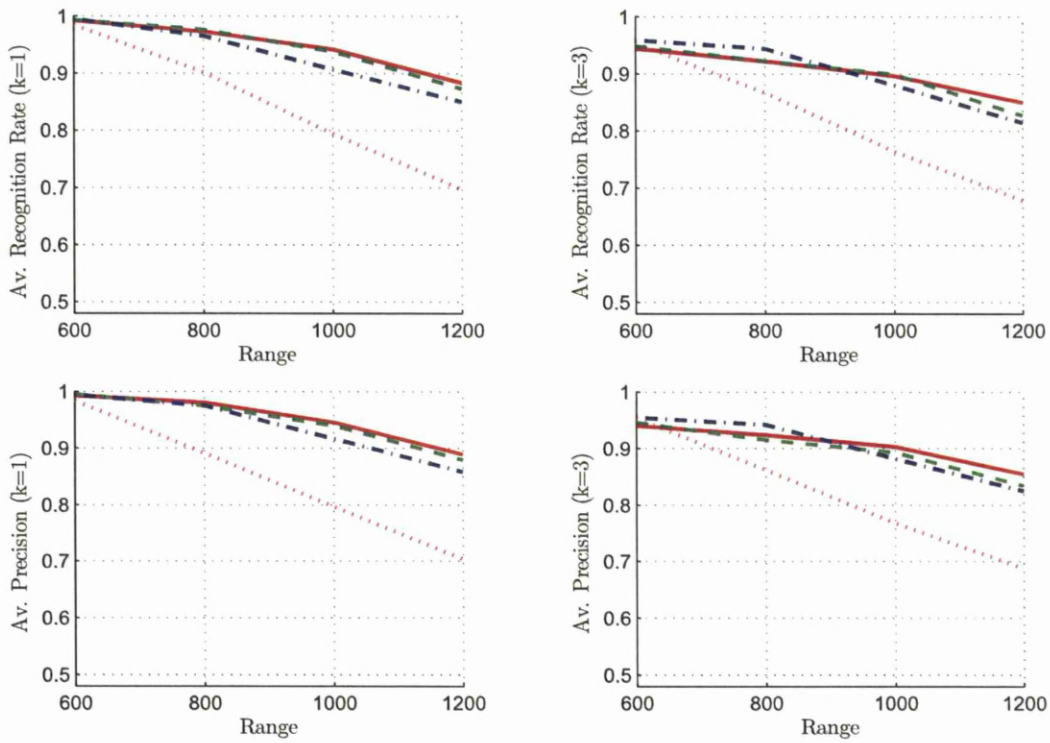

(b) Average Class Recognition Rate and Precision.

Figure F.12: Average Recognition Rate and Precision During Scale Effect (30%) for HHOGD "-", HHOTD "- -", COTD "-.-", and Invariant Moment "." Descriptors.

F.5 Rotation Effect

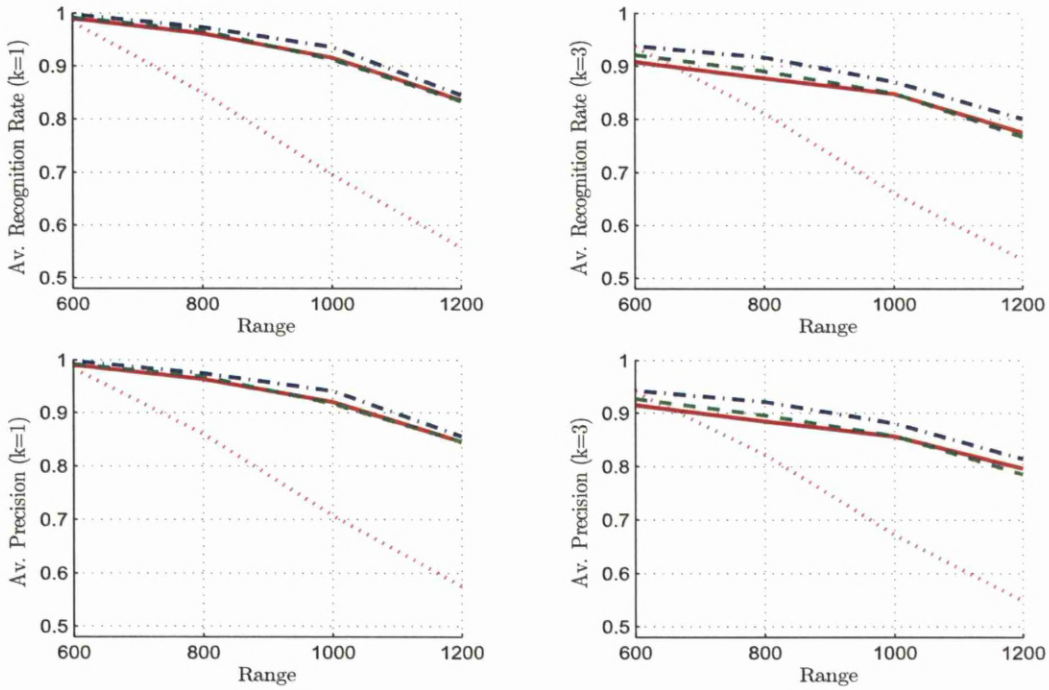

(a) Average Model Recognition Rate and Precision.

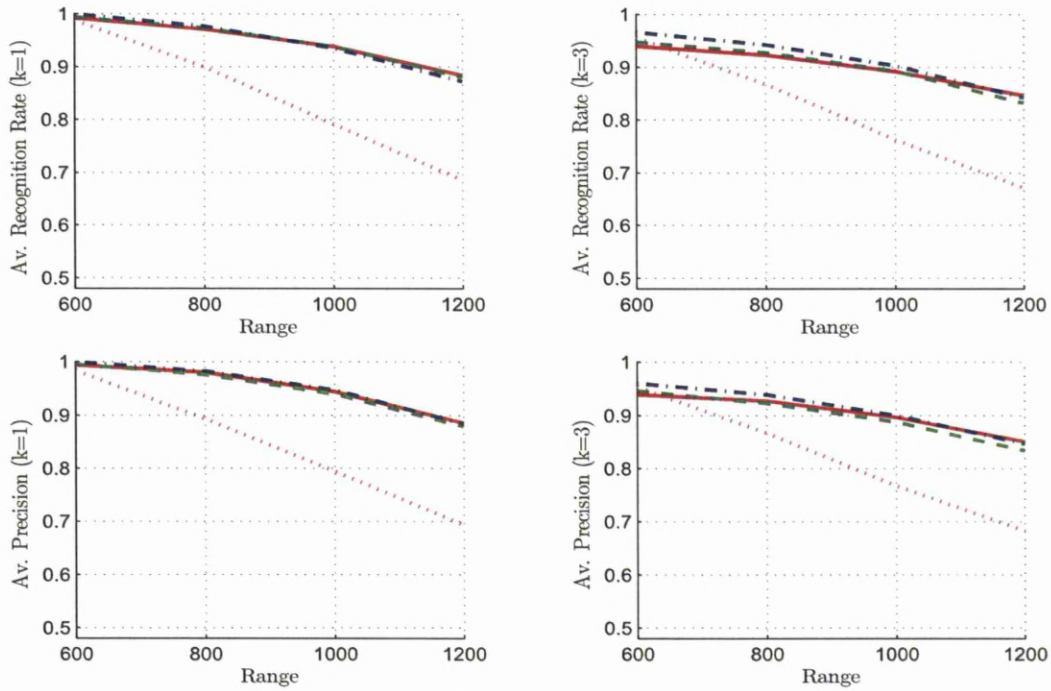

(b) Average Class Recognition Rate and Precision.

Figure F.13: Average Recognition Rate and Precision During Rotation Effect (15°) for HHOGD "-", HHOTD "- -", COTD "-.-", and Invariant Moment "." Descriptors.

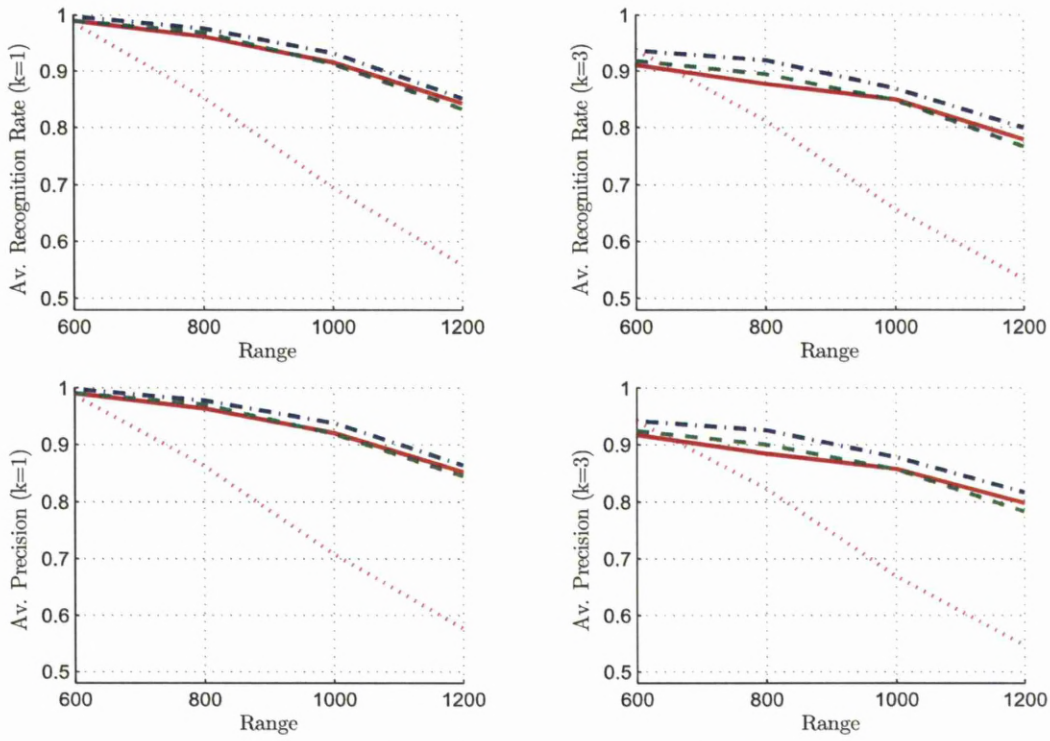

(a) Average Model Recognition Rate and Precision.

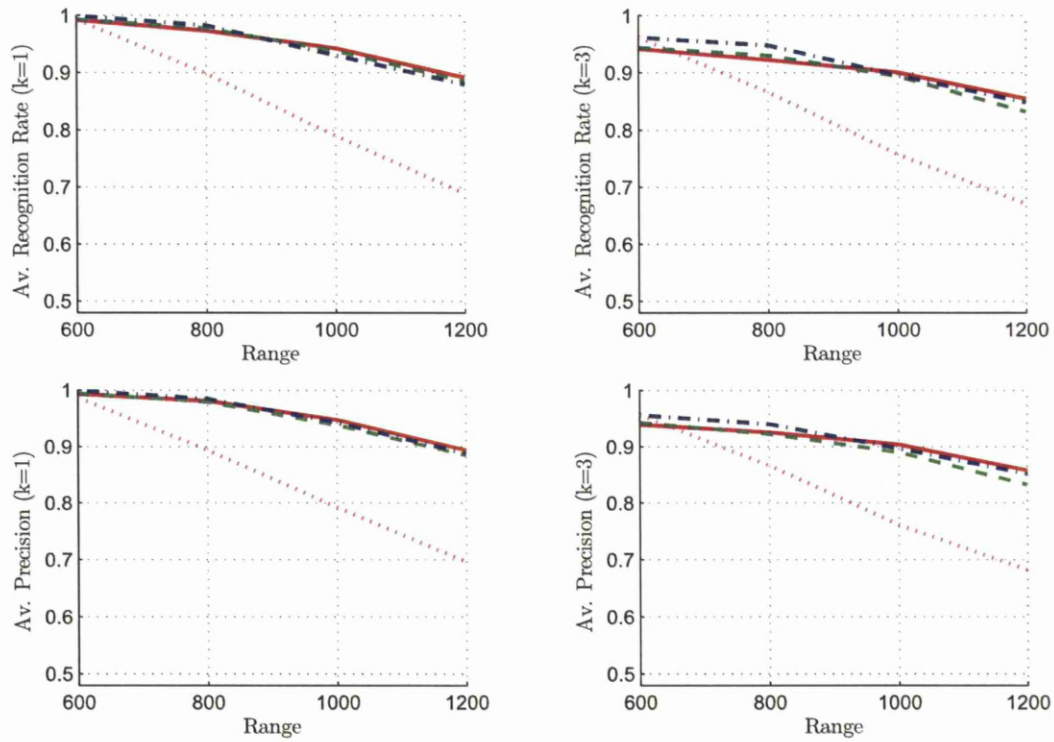

(b) Average Class Recognition Rate and Precision.

Figure F.14: Average Recognition Rate and Precision During Rotation Effect (30^o) for HHOGD "-", HHOTD "- -", COTD "-.-", and Invariant Moment "." Descriptors.

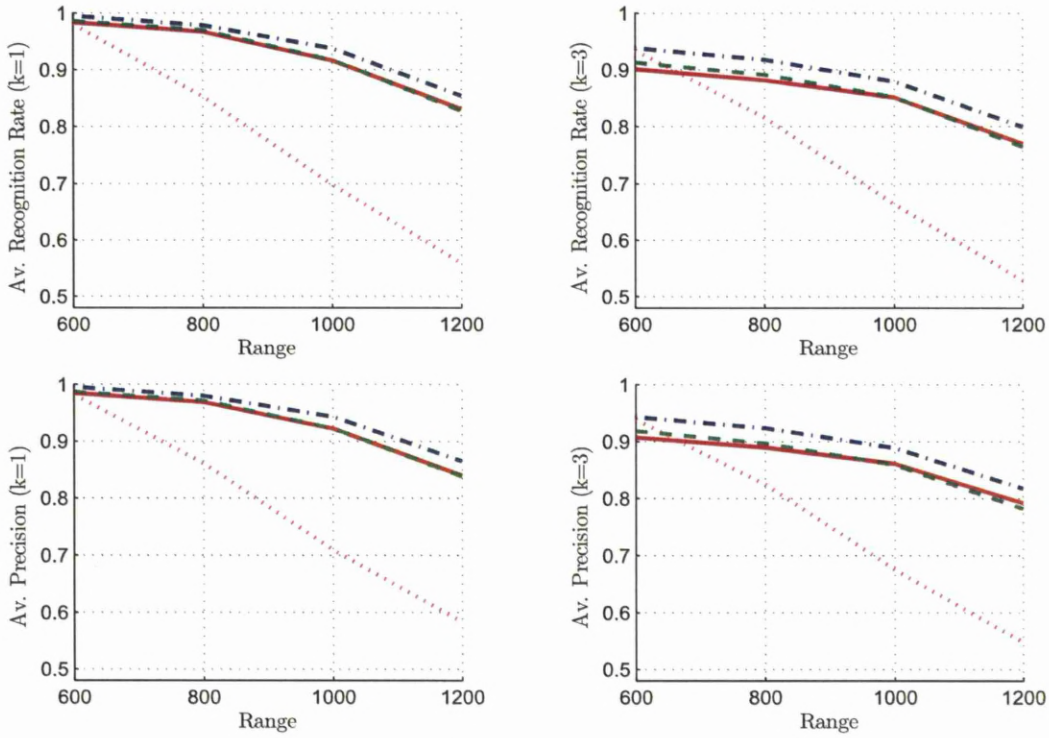

(a) Average Model Recognition Rate and Precision.

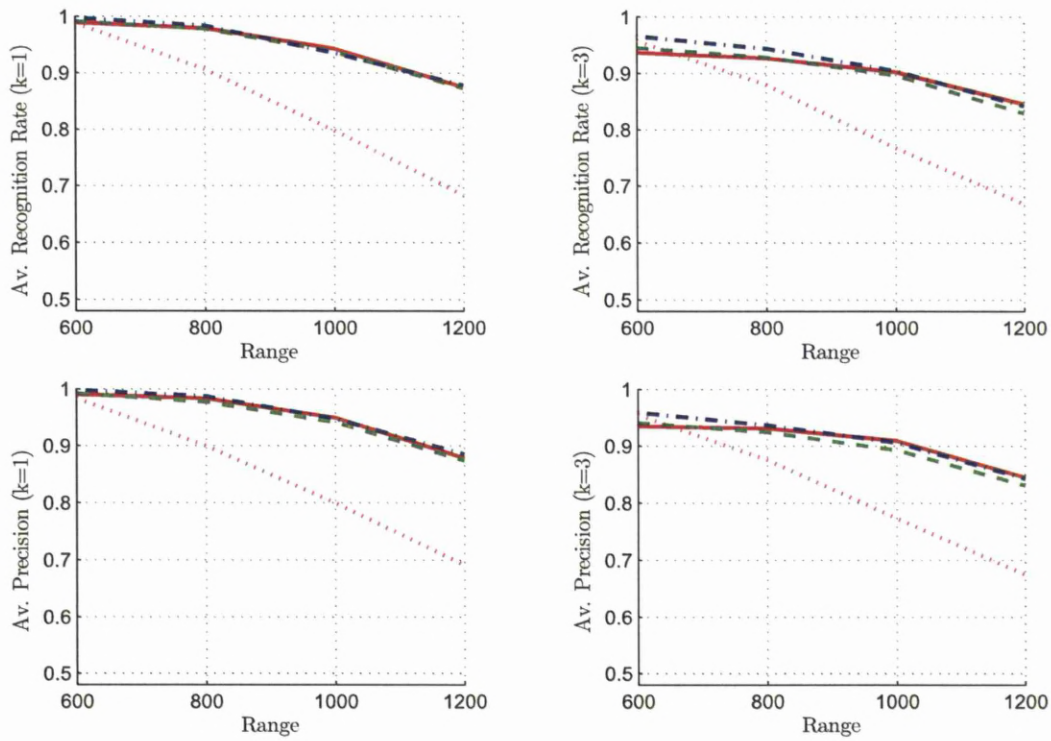

(b) Average Class Recognition Rate and Precision.

Figure F.15: Average Recognition Rate and Precision During Rotation Effect (45°) for HHOGD "-", HHOTD "- -", COTD "-.-", and Invariant Moment "." Descriptors.

Appendix G

Experimental Results with Range

This appendix presents the experimental results of evaluating the model recognition performance for the new designed LADAR system for each individual effect at each scanning range.

These effects are:

- Resolution Effects.
- View Effects.
- Rotation Effects.

G.1 Resolution Effect

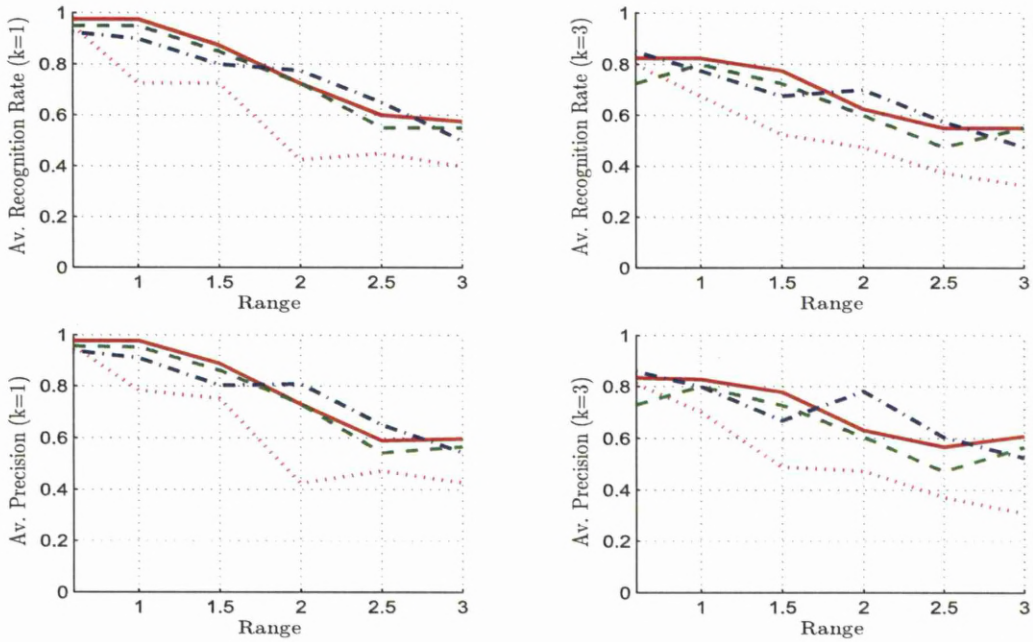

Figure G.1: Average Model Recognition Rate and Precision During Res. Effect (0.2^o) for HHOGD "-", HHOTD "- -", COTD "-.-", and Invariant Moment "." Descriptors.

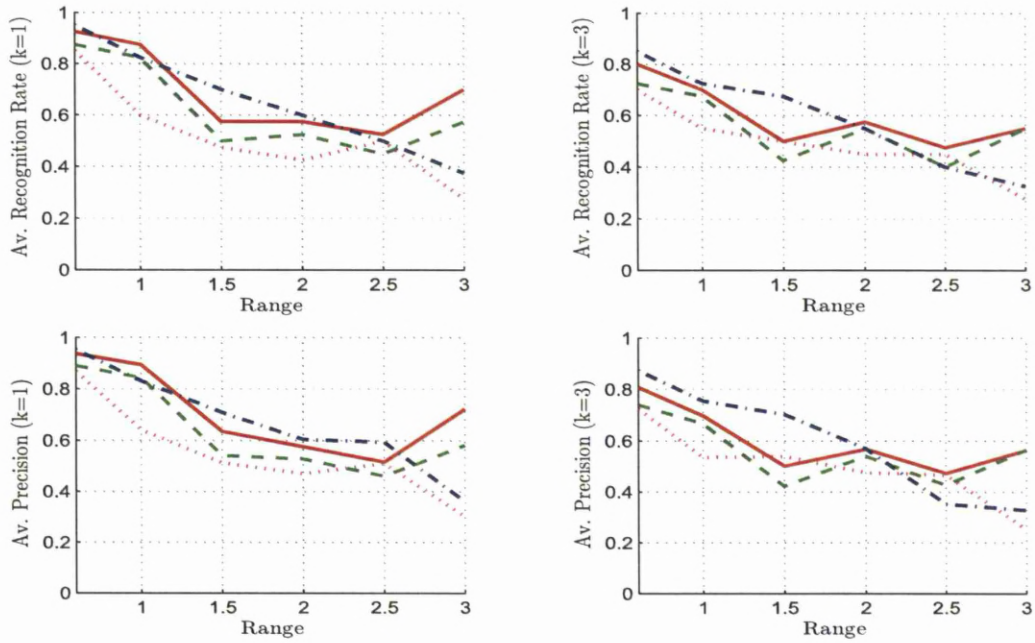

Figure G.2: Average Model Recognition Rate and Precision During Res. Effect (0.4^o) for HHOGD "-", HHOTD "- -", COTD "-.-", and Invariant Moment "." Descriptors.

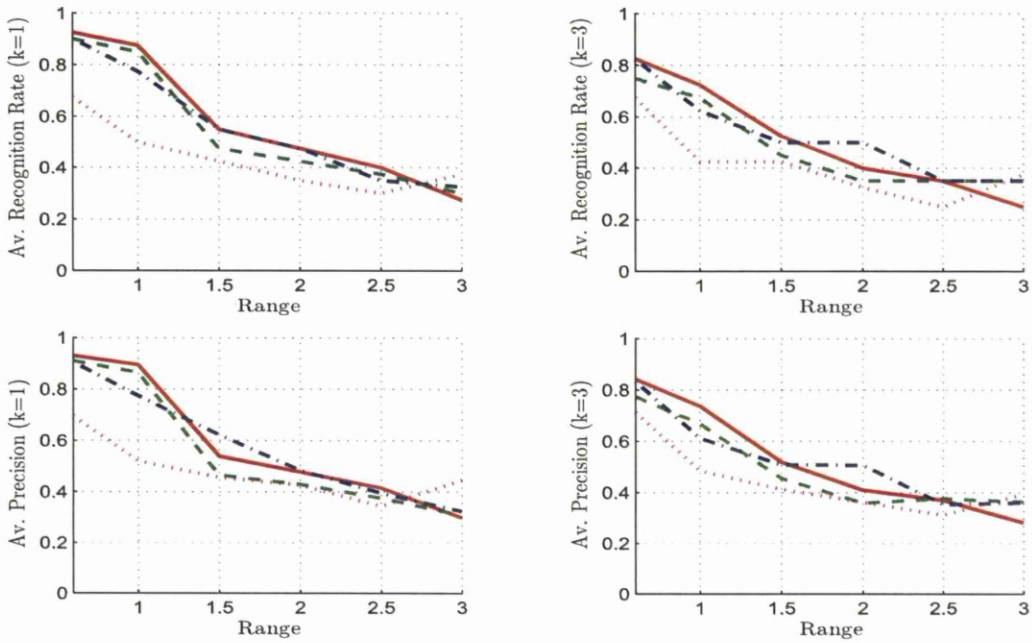

Figure G.3: Average Model Recognition Rate and Precision During Res. Effect (0.6^o) for HHOGD "-", HHOTD "- -", COTD "-.-", and Invariant Moment "." Descriptors.

G.2 View Effect

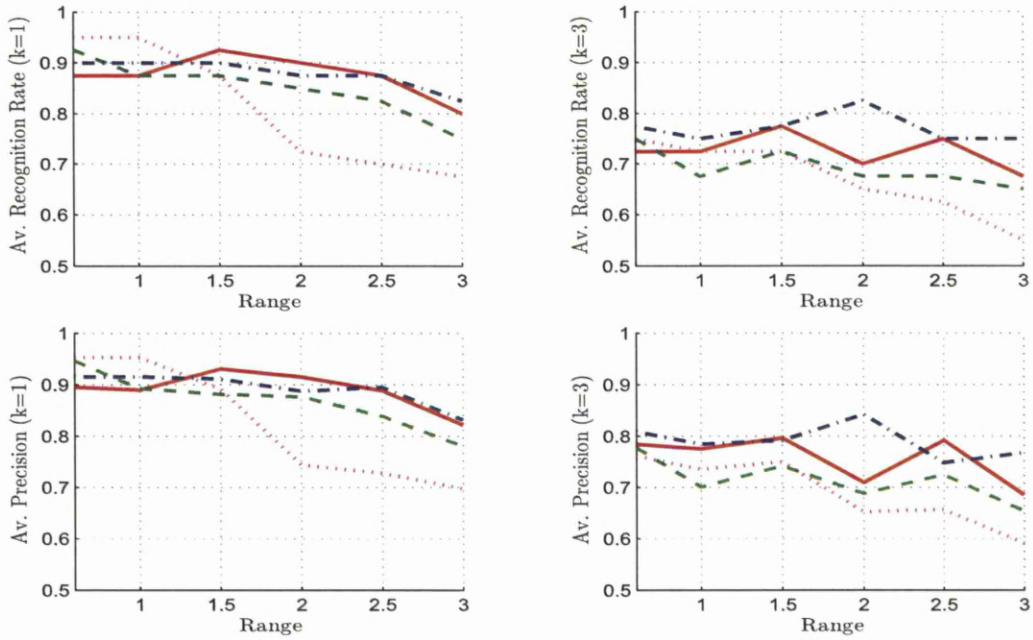

Figure G.4: Average Model Recognition Rate and Precision During View Effect (7.5^o) for HHOGD "-", HHOTD "- -", COTD "-.-", and Invariant Moment "." Descriptors.

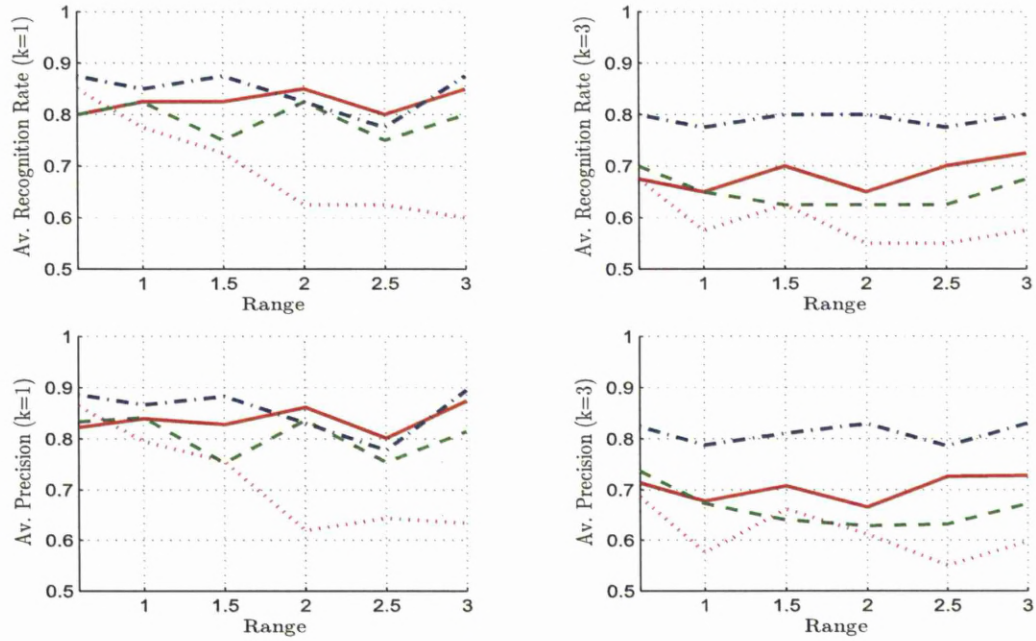

Figure G.5: Average Model Recognition Rate and Precision During View Effect (15^o) for HHOGD "-", HHOTD "- -", COTD "-.-", and Invariant Moment "." Descriptors.

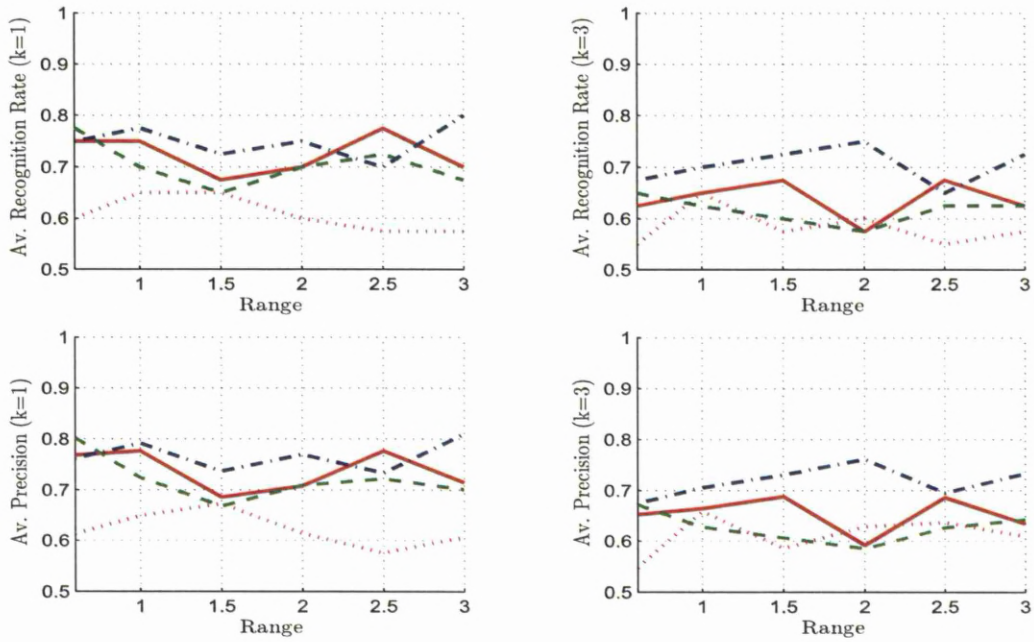

Figure G.6: Average Model Recognition Rate and Precision During View Effect (22.5^o) for HHOGD "-", HHOTD "- -", COTD "-.-", and Invariant Moment "." Descriptors.

G.3 Rotation Effect

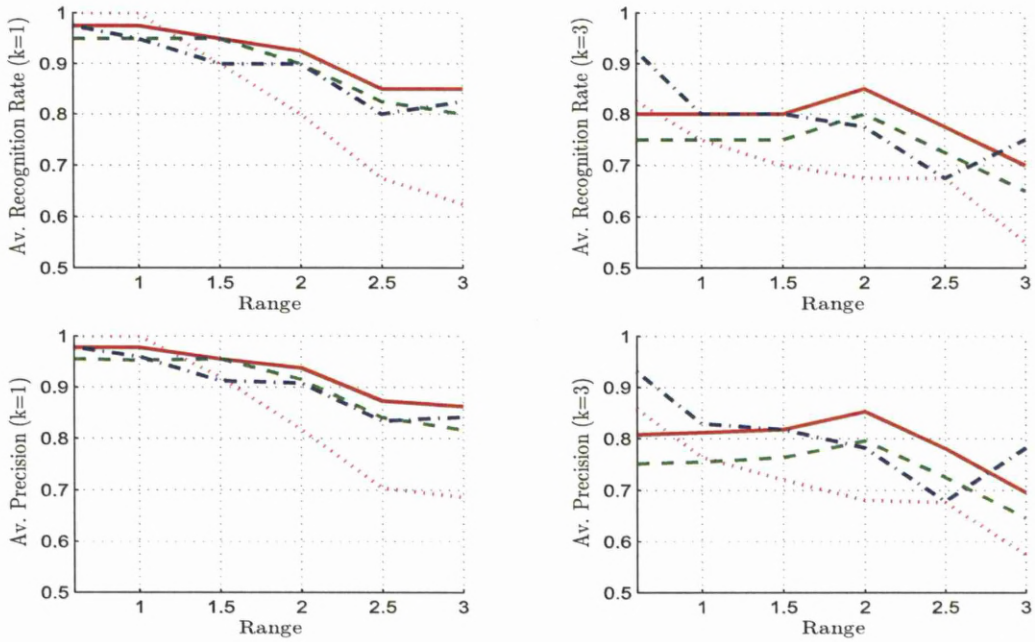

Figure G.7: Average Model Recognition Rate and Precision During Rot. Effect (15^o) for HHOGD "-", HHOTD "- -", COTD "-.-", and Invariant Moment "." Descriptors.

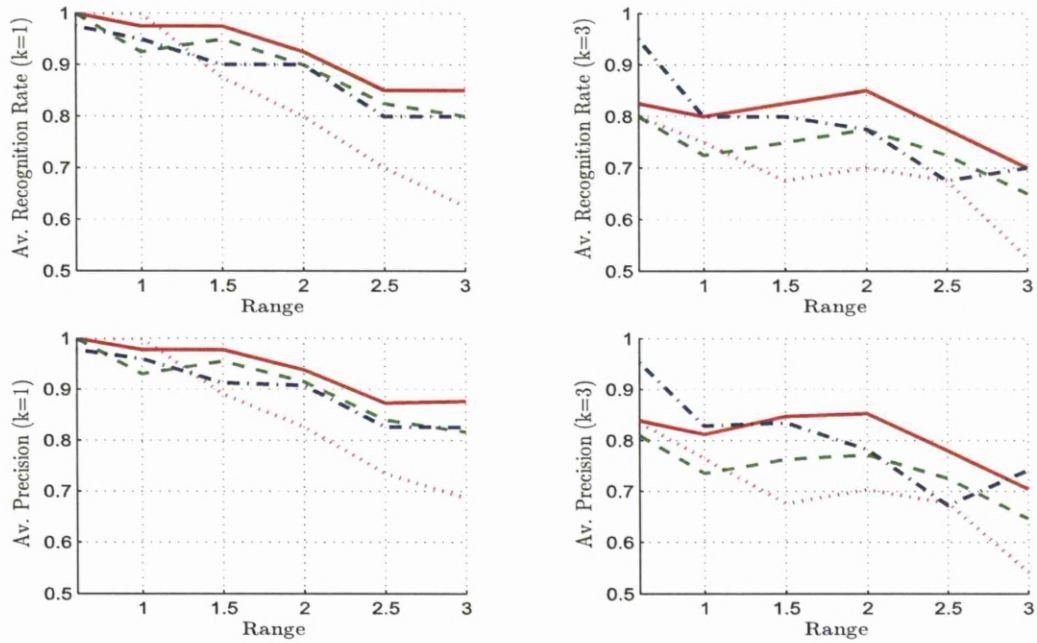

Figure G.8: Average Model Recognition Rate and Precision During Rot. Effect (30^o) for HHOGD "-", HHOTD "- -", COTD "-.-", and Invariant Moment "." Descriptors.

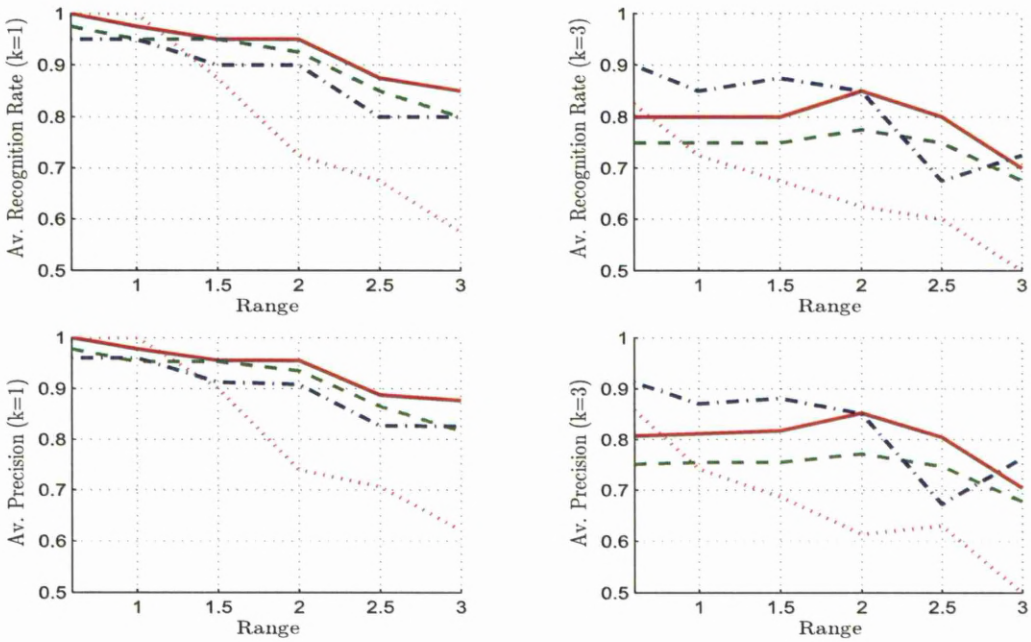

Figure G.9: Average Model Recognition Rate and Precision During Rot. Effect (45^o) for HHOGD "-", HHOTD "- -", COTD "-.-", and Invariant Moment "." Descriptors.

Appendix H

Publications

Invariant Spatial Chromatic Processors for Region Image Description

Ali Adnan Al-Temeemy
Department of Electrical Engineering and Electronics
University of Liverpool
Liverpool UK
ali.al-temeemy@liv.ac.uk

J. W. Spencer
Department of Electrical Engineering and Electronics
University of Liverpool
Liverpool UK
joe@liv.ac.uk

***Abstract*— A new region image descriptor is proposed. This descriptor arises from the chromatic methodology to extract the features from the images by applying new type of processors called 'Invariant spatial chromatic processors'. The properties of the spatial chromatic processors and the proposed approach of making them invariant are presented. A database of more than one thousand gray scale images is used to test the proposed descriptor with rotation, translation, scaling, and noise effects, where the Moment Invariant is also used to benchmark the results. The simulation results show, a comparable performance between the proposed descriptor and the Moments Invariant during affine effects with better performance during noise effect.**

Keywords-component; Chromaticity; feature extraction; moment invariant;

I. INTRODUCTION

The chromatic methodology has evolved from a number of origins, some based upon human perceptions and the others on scientific and analytical approaches. It provides a means of processing a signal that avoids some of the difficulties associated with the Fourier approach at the expense of depressing some minor signal details relative to major ones. These difficulties include complexity of the Fourier transformed signal and the transformation instability in the presence of noise [1]. The method derived initially from the photic field concepts described by Moon and Spencer [2]. But its generic nature has recently enabled it to be extended far beyond the visible part of spectrum to other domains of information extraction. These domains include ultrasonic domain for tracking system [3], time domain for processing continuous signal [4], and acoustic domain for Rail track monitoring [5] and identifying optoacoustical signals from high voltage circuit breakers [6].

In this paper the feasibility of extending the chromatic methodology to be a region image descriptor is explained. This represents the first step toward using this methodology for processing images. The proposed descriptor characterizes the normalized projections of the image through the use of proposed type of processors called 'invariant spatial chromatic processors'. A database of more than one thousand images is used to study the rotation, translation, scaling, and noise effects on the descriptor performance. The Moment Invariant descriptor was also used in this study to benchmark the performance of the proposed descriptor.

In the following sections, an overview of the spatial chromatic processors and their discrimination ability. Then an explanation of the proposed approach for making theses processors invariant to translation and scaling effects and how these invariant processors can be use as region image descriptor. Simulation results from testing the proposed descriptor with affine transformation (rotation, translation, and scaling) and distortion (Gaussian and Salt pepper noises) effects are presented. This is followed by discussion and conclusion.

II. SPATIAL CHROMATIC PROCESSORS

Chromatic processing often involves three non-orthogonal (overlapping) processors. The outputs from these processors are used to form cross correlations between the signal and the different processors responses [7]. Normally each processor response may have a Gaussian shape aligning with the Gabor transform [8], a triangle or other shapes may be preferred for some cases when a special type of responsivity is required. Whatever the processor shape, the non-orthogonality is significant in cross correlating the subdivided signal on each channel and in providing a means of selective tuning in the regions of overlap. It has been shown that although three spatial chromatic processors provide a high level of signal discrimination, additional processors could enhance signal discrimination even further but that extending the number beyond six gives little advantage [8], [9]. For this reason and for computing simplicity three half height overlapping Gaussian processors 'HHOGPs' are used in this paper.

The approach is to evaluate combinations of these cross correlations to yield coordinates which define the signal in one of several chromatic modes (e.g. x:y, Lab, HLS, etc.) depending on the nature of the information sought. The Hue-Lightness-Saturation (HLS) scheme is used in this work, where L represents the strength of the signal, S its spread in the measured domain and H is the dominant measured value [10]. In this paper the H and S values are only used, because of their robustness to the noise effect and their built-in ability to have a fixed range of values, while L required normalization and it's more sensitive to noise effect.

978-1-4244-6494-4/10/$26.00 ©2010 IEEE

In the half height overlapping Gaussian processors type, two Gaussian processors R (left) and B (right) are overlapped at their half-height points with another processor G (middle) as shown in Fig.1 (a). The response profiles for these processors make the Hue value varies between 0 and 0.67 when a monochromatic signal swept under them as shown in Fig.1 (b). This variation is nonlinear with low sensitivity between 0 and 50, and between 250 and 300, because there is no overlapping in these regions.

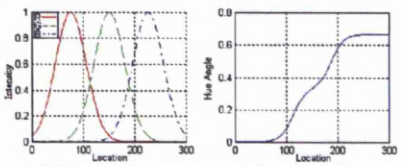

(a) RGB Chromatic Processors. (b) Monochromatic Response.

Figure 1. Half height overlapping Gaussian processors and their monochromatic response.

The spatial distributions of the chromatic processors make them variant to the shift and scale effects. If the signal is moved from its original location, or enlarged the H and S values will change. Table.1 shows the change in the processors output values when the original signal shown in Fig.2 was moved from its original location to the right and enlarges in the horizontal direction.

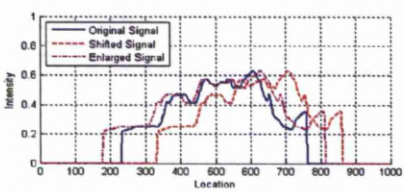

Figure 2. Signal before and after applying shifting effect by 100 units, and scaling effect by 1.2.

TABLE I. HUE AND SATURATION VALUES FOR THE SIGNALS OF FIG.2

Signal Type	Hue	Saturation
Original signal	0.3621	0.4732
Shifted signal	0.4962	0.7601
Enlarged signal	0.3808	0.3586

III. INVARIANT SPATIAL CHROMATIC PROCESSORS

To make these processors invariant, a new approach is proposed. This approach is to make the centers of the processors and widths adaptable to the input signal type. The approach starts by calculating the centroid of the (discrete) input signal $f(x)$ of l length that shown in Fig.3 by

$$c = \sum_{x=1}^{l} xf(x) \Big/ \sum_{x=1}^{l} f(x) \quad (1)$$

This centroid is then used as a boundary condition for calculating two processors centers C_R and C_B as follow:

$$C_R = \sum_{x=1}^{c} xf(x) \Big/ \sum_{x=1}^{c} f(x) \quad (2)$$

$$C_B = \sum_{x=c}^{l} xf(x) \Big/ \sum_{x=c}^{l} f(x) \quad (3)$$

The third processor center C_G can be determined from the following equation:

$$C_G = (C_R + C_B)/2 \quad (4)$$

The widths for the three chromatic processors w_{RGB} are all equal and they define as

$$w_{RGB} = \frac{(C_B - C_R)}{AO} \quad (5)$$

Where AO : is the overlapping regions constant, which equal to 5 for half height overlapping Gaussian processors.

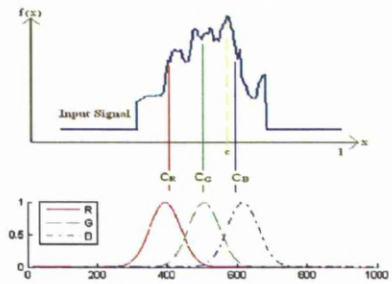

Figure 3. Chromatic processors centers calculated by the proposed approach.

The processors (of adapted centers and widths), are then applied on the input signal to extract the features from it. The outputs for R, G, and B processors are calculated by applying the following equations respectively:

$$R_o = \sum_{x=1}^{l} \exp\left(\frac{-(x-C_R)^2}{2w_{RGB}^2}\right) \times f(x) \quad (6)$$

$$G_o = \sum_{x=1}^{l} \exp\left(\frac{-(x-C_G)^2}{2w_{RGB}^2}\right) \times f(x) \quad (7)$$

$$B_o = \sum_{x=1}^{l} \exp\left(\frac{-(x-C_B)^2}{2w_{RGB}^2}\right) \times f(x) \quad (8)$$

Applying this approach, make the processors deployments change their locations and widths with respect to shift and scale effects. Fig. 4 shows the processors deployments changes, when the signal (a) is shifted to the right (b) and enlarged horizontally by 20% (c).

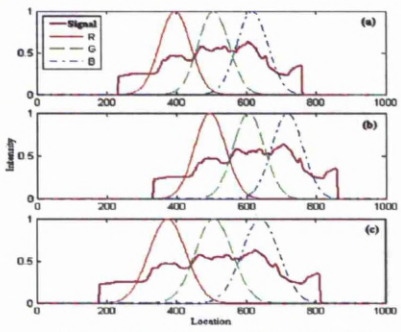

Figure 4. Processors before (a) and after shift (b), and scale (c) effects.

Table below shows the robustness of the processors outputs when they process the signals of Fig. 4. (see Appendix).

TABLE II. HUE AND SATURATION VALUES FOR THE SIGNALS OF FIG.3

Signal Type	Hue	Saturation
Original signal	0.4763	0.1168
Shifted signal	0.4763	0.1168
Enlarged signal	0.4762	0.1169

IV. REGION IMAGE DESCRIPTOR

The proposed descriptor utilizes the discrimination ability of the "invariant spatial chromatic processors" to describe the images with rotational, translational, and scaling invariant features, by applying two sets of these processors on the horizontal and vertical normalized image projections (Note the R, G, B processors are applied to characterize the intensity profiles of the image projections and not the color information). These projections are calculated by applying Radon transform to the image $I(x, y)$ at two normalizing angles θ and $\theta + \pi/2$ respectively.

Radon transform [11] of the image is the line integral parallel to the y'-axis and it's define as

$$R_\theta(x') = \int_{-\infty}^{\infty} I(x'\cos\theta - y'\sin\theta, x'\sin\theta + y'\cos\theta)dy' \quad (9)$$

$$\text{Where } \begin{bmatrix} x' \\ y' \end{bmatrix} = \begin{bmatrix} \cos\theta & \sin\theta \\ -\sin\theta & \cos\theta \end{bmatrix} \begin{bmatrix} x \\ y \end{bmatrix} \quad (10)$$

Figure below illustrates the geometry of the Radon transform.

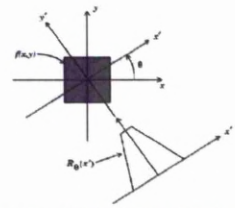

Figure 5. Geometry of the Radon Transform [11].

Normalized angle has been widely used in the pattern recognition applications and it's calculated according to [12]. Define the two dimensional moment of order $(p+q)$ of a (discrete) image $I(x, y)$ as

$$m_{pq} = \sum_x \sum_y x^p y^q I(x, y) \quad (11)$$

The corresponding central moment μ_{pq} is

$$\mu_{pq} = \sum_x \sum_y (x - \bar{x})^p (y - \bar{y})^q I(x, y) \quad (12)$$

Where $\bar{x} = m_{10}/m_{00}$ and $\bar{y} = m_{01}/m_{00}$

Define the two tensors t_1 and t_2:

$$t_1 = \mu_{12} + \mu_{30} \text{ and } t_2 = \mu_{21} + \mu_{03} \quad (13)$$

The normalizing angle θ is then define as

$$\theta = -\delta - \pi/2 \quad (14)$$

Where $\delta = \arctan(-t_1/t_2)$

If $-t_1 \sin\delta + t_2 \cos\delta < 0$ then $\theta = \theta - \pi$ [13].

The calculations of the projections from the normalized angles of the object make them invariant to object rotation. While object translation and scaling effects, make the projections locations and size changed respectively, without changing in the patterns. Fig.6 shows the similarity between the normalized projections of the original image (a) and the rotated image (b).

Therefore applying the translation and scale invariant chromatic processors on these normalized projections make the descriptor features invariant to rotation, translation and scaling (equal scaling factors) effects. These features described as H_H, S_H for horizontal projection at θ and H_V, S_V for vertical projection at $\theta + \pi/2$.

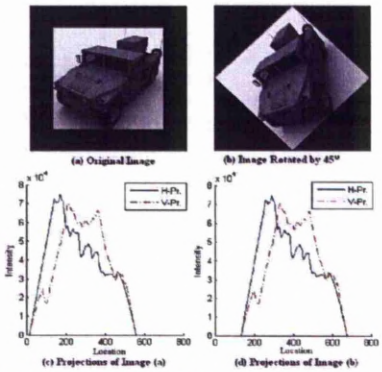

Figure 6. Horizontal "H-Pr." and vertical "V-Pr." Normalizing Projections during Rotation effect.

V. Simulation Results

To evaluate the performance of the proposed descriptor, a database of more than one thousand gray scale images was used. These images depict one hundred objects of different shapes, each one representing a different class and are subject to different translation, scale, rotation transformations and noise effects to create training and testing sets [14] (see Fig.7).

Figure 7. Example of some training images from the database (www.the3dstudio.com).

The classifier used in all the tests was K-nearest neighbor classifier of two K values, which are (K=1 and K=3). This classifier is used with Euclidean distance metric and Majority rule, in which the sample point is assigned to the class the majority of the k nearest neighbors are from [15].

These tests were also applied on the Moment Invariant descriptor to benchmark the results, where its feature vector is composed of normalized central moments:

$$h_{GM} = [\varphi_1 \ldots\ldots \varphi_7] \tag{15}$$

This set of moments has been shown to be invariant to translation, rotation, and scale changes [16].

They can be derived from normalizing the central moment equation (12) under scaling by

$$\vartheta_{p,q} = \frac{\mu_{pq}}{\mu_{00}^{\gamma}} \text{ Where } \gamma = \frac{p+q}{2} + 1 \,,\; p+q = 2,3 \cdots \tag{16}$$

Therefore from the second and third moments, a set of seven invariant moments can be derived [16]:

$$\varphi_1 = \vartheta_{20} + \vartheta_{02} \tag{17}$$

$$\varphi_2 = (\vartheta_{20} - \vartheta_{02})^2 + 4\vartheta_{11}^2 \tag{18}$$

$$\varphi_3 = (\vartheta_{30} - 3\vartheta_{12})^2 + (3\vartheta_{21} - \vartheta_{03})^2 \tag{19}$$

$$\varphi_4 = (\vartheta_{30} + \vartheta_{12})^2 + (\vartheta_{21} + \vartheta_{03})^2 \tag{20}$$

$$\varphi_5 = (\vartheta_{30} - 3\vartheta_{12})(\vartheta_{30} + \vartheta_{12})((\vartheta_{30} + \vartheta_{12})^2 - 3(\vartheta_{21} + \vartheta_{03})^2) + (3\vartheta_{21} - \vartheta_{03})(\vartheta_{21} + \vartheta_{03})(3(\vartheta_{30} + \vartheta_{12})^2 - (\vartheta_{21} + \vartheta_{03})^2) \tag{21}$$

$$\varphi_6 = (\vartheta_{20} - \vartheta_{02})((\vartheta_{30} + \vartheta_{12})^2 - (\vartheta_{21} + \vartheta_{03})^2) + 4\vartheta_{11}(\vartheta_{30} + \vartheta_{12})(\vartheta_{21} + \vartheta_{03}) \tag{22}$$

$$\varphi_7 = (3\vartheta_{21} - \vartheta_{03})(\vartheta_{30} + \vartheta_{12})((\vartheta_{30} + \vartheta_{12})^2 - 3(\vartheta_{21} + \vartheta_{03})^2) - (3\vartheta_{12} - \vartheta_{30})(\vartheta_{21} + \vartheta_{03})(3(\vartheta_{30} + \vartheta_{12})^2 - (\vartheta_{21} + \vartheta_{03})^2) \tag{23}$$

The recognition rates for the proposed descriptors with the Moment Invariant are shown in Table 3.

TABLE III. Recognition Rate For The Proposed Descriptor With The Moments

Effect Type	Proposed Descriptor		Moments Invariant	
	K=1	*K=3*	*K=1*	*K=3*
Affine Effects				
Translation by [40 20]	100%	98%	100%	89%
Scaling by 0.4	99%	95%	95%	85%
Scaling by 1.2	100%	98%	100%	91%
Rotation by 45°	100%	98%	99%	88%
Rotation by 230°	100%	98%	100%	89%
Gaussian Noise Effects				
Variance equal to 1%	76%	74%	49%	52%
Variance equal to 5%	41%	37%	16%	15%
Salt Pepper noise Effects				
Density equal to 1%	98%	96%	91%	84%
Density equal to 5%	82%	82%	47%	50%
Average Performance	**88.4%**	**86.2%**	**77.4%**	**71.4%**

VI. Discussion

The simulation results show that for K equal to one, the recognition rate between the Moments Invariant and the proposed chromatic descriptor are comparable when subjected to affine effects. When the K value is equal to three, the performance for both descriptors decreased, but with better performance for the proposed descriptor over the Moments.

During noise effect test, two types of noise were applied. Each noise was applied at two different levels. With Gaussian noise, the performances for descriptors decreased with increase variance level for both K values. And for Salt Pepper noise the recognition rate also decreased with increase density level for both K values. For both types of these noises the chromatic descriptor shows higher performance than the Moment Invariant. The reason behind that is related to the nature of the chromatic processors and the RGB to HLS conversion algorithm. This algorithm make one of the three processors (that has the minimum output) works as noise or offset level estimator and subtract its value from the other two values before calculating the Hue [10].

VII. Conclusion

We proposed a region image descriptor based on using invariant chromatic processors. A descriptor was tested with different objects at varies affine transformation and distortion effects. The simulation results show, a comparable performance between the chromatic processors and the Moments during affine effects with better performance than the last mentioned during distortion effect. The proposed descriptor is simple and its discrimination ability can be easily extended by either increase the processors number or using additional image projections.

Appendix

The equations relating the processors outputs (R, G, B) to the chromatic parameters H and S are [10]:

$$r = R_o - \min(R_o, G_o, B_o) \quad (1)$$

$$g = G_o - \min(R_o, G_o, B_o) \quad (2)$$

$$b = B_o - \min(R_o, G_o, B_o) \quad (3)$$

$$If \quad r = 0, \quad H = 0.667 - 0.333 \times \frac{g}{g+b} \quad (4)$$

$$If \quad g = 0, \quad H = 1.000 - 0.333 \times \frac{b}{b+r} \quad (5)$$

$$If \quad b = 0, \quad H = 0.333 - 0.333 \times \frac{r}{r+g} \quad (6)$$

$$S = \frac{\max(R_o, G_o, B_o) - \min(R_o, G_o, B_o)}{\max(R_o, G_o, B_o) + \min(R_o, G_o, B_o)} \quad (7)$$

If R_o & G_o & $B_o = 0$ then S = 0 and H is undefined.

References

[1] G. R. Jones, P. C. Russell, and other, " Chromatic processing of optoacoustic signals for identifying incipient faults on electric power equipment," *The Institution of Electrical Engineers*, 1996.

[2] M. P. and S. D. E., "The Photic Field," MA: MIT Press, Cambridge, 1981.

[3] C. Lappas, "Chromatic Ultrasonic Tracking," Ph.D. dissertation, Elect. Eng. Dept. Electron., Liverpool Univ., Liverpool, UK, 2007.

[4] G. R. Jones, P. C. Russell, and A. Vourdas, "Chromatic Compression of Sensor Signals in the Wavelength, Time and Parameter Domains," *IEE Colloquium Intell. Self-Validating Sensor*, pp. 9/1-9/4, Jun. 1999.

[5] A.G. Deakin, I. Rallis, J. Zhang, J.W. Spencer and G.R. Jones, "Towards holistic chromatic intelligent monitoring of complex systems," *Sensor Review J.*, vol. 26, no. 1, pp. 11-17, 2006.

[6] Cosgrave J. A., Russell P. C., Hall B. S. B. and Jones G. R., "Optoacoustic monitoring of electric arcs in high voltage circuit breakers," *Int. Conf. on Switching Arcs, Xian Jiaotong University, People's Republic of China*, pp 598–605.

[7] G. R. Jones, A. G. Deakin, and J. W. Spencer, "Chromatic Monitoring of Complex Conditions," pp. 13-14, 2008.

[8] G. R. Jones, P. C. Russell, A. Vourdas, J. Cosgrave, L. Stergioulas and R. Huber, "The Gabor Transform Basis of Chromatic Monitoring," *Meas. Sci. Technol.*, vol. 11, pp. 489-498, Jan. 2000.

[9] L. Stergioulas, A., Vourdas, and G. R. Jones "Gabor Representation of Optical Signals using a Truncated Von Neumann Lattice and its Practical Implementation," *Society of Photo-Optical Instrumentation Engineers*, vol. 39, pp. 1965-1971, July 2000.

[10] S. Xu and G. R Jones, "Event and Movement Monitoring using Chromatic," *Meas. Sci. Technol.*, pp.3204–3211, 2006.

[11] Bracewell, and Ronald N., "Two-Dimensional Imaging," *Englewood Cliffs, NJ, Prentice Hall*, pp. 505-537, 1995.

[12] M. Al ghoniemy and A. H. Tewfik, "Geometric Invariance in Image Watermarking," *Fellow, IEEE Trans. on Image processing*, vol. 13, no. 2, pp. 145-153, Feb. 2004.

[13] L. Lei-da, G. Bao-long, and G. Lei, "Rotation, scaling and translation invariant image watermarking using feature points," *The Journal of China Universities of Posts and Telecommunications*, vol. 15, Issue 2, pp. 82-87, June 2008.

[14] S. Paschalakis, and P. Lee., "Pattern Recognition in Gray Level Images using Moment based Invariant Features," *IEE Conf. on Image Processing and its Applications*, no. 465, pp. 245-249, 1999.

[15] Tom M. Mitchell," Machine Learning, " *McGraw-Hill series in computer science*, 1997.

[16] R. Gonzalez and R.Woods, "Digital Image Processing," prentice -hall, 2002.

Simulation of 3D LADAR Imaging System using Fast Target Response Generation Approach

Al-Temeemy Ali A.[a] and Spencer J. W. [a]

[a]Department of Electrical Engineering and Electronics, University of Liverpool, Brownlow Hill, L69 3GJ, Liverpool, United Kingdom;

ABSTRACT

A new approach has been used to generate the target response for the Laser Detection and Ranging or laser radar (LADAR) simulator. This approach is fast and able to deal with high scanning requirements and complex target models. This leads to a more efficient LADAR simulator and opens up the possibility for simulating more complex scenes LADAR images. The approach is to derived the target angular ranges algorithms in order to directly select the target's parts that lie in the laser field (parts required for target response generation) instead of checking the whole target as it's done by the normal approach. The performances of these two approaches are compared for a variety of conditions. The simulation results show an enhanced performance when using the proposed approach.

Keywords: LADAR Simulator, 3D Laser Imaging, Laser Beam Propagation

1. INTRODUCTION

LADAR systems have unique capability to give intensity and full 3-D images of an object. These systems have many civilian and military applications such as terrain modeling, object detection and classification as well as object positioning.[1] Consequently, simulations for these systems have become a valuable tool for developing LADAR systems and their recognition algorithms.[2] In order to simulate these systems, it's required to generate the target response for each laser pulse transmitted towards its parts. In this paper, a new approach for generating the target response is presented. This approach is based on deriving the algorithms that required to calculate the target angular ranges. It then used these ranges to directly select the target's parts that interact with the laser beam and calculate the target response from them, instead of checking the whole object's parts as its done by the normal approach.[3] This leads to reduce the computational time and speed up the process of simulating the LADAR images. In the following sections, an overview about the Laser beam propagation and the target response generation approach. Then an explanation about the proposed approach of speeding up the calculation process. The testing program and the comparison results of testing both approaches are then presented, followed by the conclusion.

2. LASER BEAM PROPAGATION THEORY

The propagation of the laser beam from the transmitter to the target, and back to the receiver is described in this section. The process of simulating the propagation of a beam has been divided into four parts which are:

2.1 Laser Beam Energy Distribution

In order to simulate the effects of the target shape, the laser pulse has to be modelled in time (temporal distribution) as well as in space (spatial distribution) which leads to a four dimensional model. So the outgoing pulse intensity is decomposed as:[4]

$$G(t, H_{ls}, V_{ls}, R_{ls}) = p(t) \times I(H_{ls}, V_{ls}, R_{ls}) \tag{1}$$

Further author information: (Send correspondence to Al-Temeemy A. A.)
Al-Temeemy A. A.: E-mail: ali.al-temeemy@liv.ac.uk, Telephone: +44 (0)7881448495

Optical Design and Engineering IV, edited by Laurent Mazuray, Rolf Wartmann, Andrew Wood, Jean-Luc M. Tissot, Jeffrey M. Raynor, Proc. of SPIE Vol. 8167, 816720 · © 2011 SPIE · CCC code: 0277-786X/11/$18 · doi: 10.1117/12.902309

where $p(t)$ is the discrete pulse shape in time domain; $I(H_{ls}, V_{ls}, R_{ls})$ is the proportion of energy contained within a component located at a location of H_{ls}, V_{ls}, R_{ls} dimensions, where $t, H_{ls}, V_{ls}, R_{ls}$ take on discrete values. Figure 1 shows these two distributions for the laser pulse traveling from the LADAR system to the target, where H_{ls} and V_{ls} are the horizontal and vertical cross-range dimensions and R_{ls} is range dimension (in the direction of the pulse traveling).

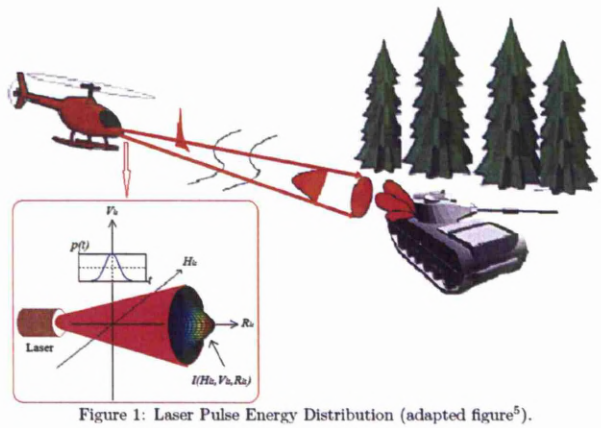

Figure 1: Laser Pulse Energy Distribution (adapted figure[5]).

2.1.1 Temporal Distribution

The amount of laser power $p(t)$ that is produced by the LADAR source and transmitted toward the target area is assumed to have a Gaussian distribution with time. This distribution is defined by the laser pulse energy E_t in unit of joules and pulse width τ (full-width at half-max power in unit of seconds). The following equation[2,4] is used to model this distribution as:

$$p(t) = \frac{2E_t}{\tau}\sqrt{\frac{\ln 2}{\pi}}\exp\frac{-4t^2 ln2}{\tau^2} \tag{2}$$

2.1.2 Spatial Distribution

The laser intensity profile produced by laser source cavity is not constant across the beam diameter at all ranges. Generally this profile is modeled as a spatial Gaussian function in horizontal H_{ls}, vertical V_{ls}, and range R_{ls} dimensions:[6,7]

$$I(H_{ls}, V_{ls}, R_{ls}) = \frac{2}{\pi W^2(R_{ls})}\exp\frac{-2(H_{ls}^2 + V_{ls}^2)}{W^2(R_{ls})} \tag{3}$$

$$W(R_{ls}) = W_o\sqrt{1 + (\frac{\lambda R_{ls}}{\pi W_o^2})^2}$$

Where W_o is the beam waist at $(R_{ls} = 0)$ and λ is the laser wavelength.

2.2 Atmospheric Effects

When the transmitted laser beam propagates through the atmosphere, some of the energy is absorbed and scattered by atmospheric molecules, suspended dust, and aerosols.[4] This can be modeled using Beer's law as shown in equation 4:[4,8]

$$T_a = \exp\left(-\sigma_s(\lambda) \times R_{ls}\right) \tag{4}$$

where T_a is the one way atmospheric transmission value and $\sigma_s(\lambda)$ is the atmospheric coefficient in m^{-1} for the wavelength λ.

2.3 Target Interaction

The interaction between the transmitted laser beam and the target surface produces a reflected signal. The characteristics for this signal are depend on the surface reflectance parameter ρ_{tr}, angle of dispersion Ω_{tr} (*Lambertian targets* are assumed i.e. $\Omega_{tr} = \pi$[4,8,9]), surface area A_{tr} (*extended targets* are assumed), and finally the surface shape.

2.4 LADAR Receiver

The process of determining the range to the target from the reflected signal is accomplished by the LADAR receiver. This process is depends on the detection technique (direct or coherent), optical transmission T_o (the fraction of energy that arrives at the detector from the total energy captured by the receiver aperture), quantum efficiency η (the fraction of the signal that is converted into photoelectrons) of the detector, and pulse detection technique. The direct detection technique is used with Constant Fraction Discrimination pulse peak detector, as this is insensitive to the amplitude fluctuation that cause jitter in the time of arrival.[10]

With the previous assumptions, the received signal power at the receiver aperture P_r can be calculated using the modified LADAR range equation:[4,10,11]

$$P_r = \frac{P_t \rho_{tr} T_a^2 T_o D_R^2}{4 R_{ls}^2} \tag{5}$$

where P_t is the transmitter pulse power and D_r is the diameter of circular receiver aperture. In order to simulate the reflected signal for each individual pulse shot by the LADAR towards the target. The target response for that pulse must be generated and then convolved with the pulse temporal distribution modeled in equation 2. Figure 2 shows the simulated shapes for the reflected signals that result from interaction the laser beam at different incident angles with the step target.

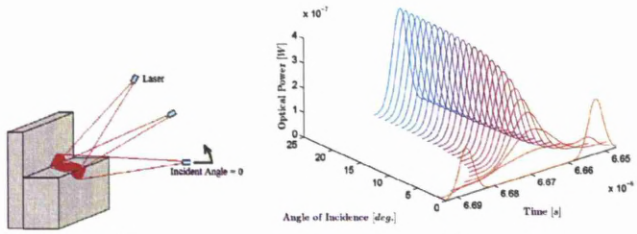

(a) (b)

Figure 2: Illustration of Return Pulse Shaping (b) by Step Target Geometry (a).

3. GENERATION OF TARGET RESPONSE

Target response can be generated by summing the reflected powers reaching the receiver from each sample in laser footprint with the same round time indices. Calculating these powers can be done by obtaining the intersection points of the laser rays vectors that represent the laser beam footprint samples with the triangles faces that represent the model surface (see figure 3). The distances from these points to the LADAR location are used to calculate the round trip time (twice distance / speed of light) for each sample, while the reflected power at each sample location is calculated from the LADAR range equation.

To obtain the intersection points of the laser rays vectors with the triangles faces, each vector is defined by the following equation:[12]

$$\mathbf{P} = \mathbf{S} + l\mathbf{V} \tag{6}$$

where $\mathbf{S}$ represents the ray's starting position, $\mathbf{V}$ represents the direction in which the ray points, and l corresponding to the point $\mathbf{P}$ where the ray intersects the plane of the triangle. The l value is given by :

$$l = \frac{\mathbf{N} \cdot (\mathbf{P}_0 - \mathbf{S})}{\mathbf{N} \cdot \mathbf{V}} \tag{7}$$

$$\mathbf{N} = (\mathbf{P}_1 - \mathbf{P}_0) \times (\mathbf{P}_2 - \mathbf{P}_0)/|(\mathbf{P}_1 - \mathbf{P}_0) \times (\mathbf{P}_2 - \mathbf{P}_0)|$$

where $\mathbf{N}$ is the plane normal and $\mathbf{P}_0$, $\mathbf{P}_1$, and, $\mathbf{P}_2$ are the triangle vertices. If the denominator is equal to zero, then no intersection occurs. Otherwise, plugging this value of l back into equation 6 produces the point $\mathbf{P}$ where the ray intersects the plane of the triangle.

To determined whether the point $\mathbf{P}$ lies inside the triangle's edges, the *Barycentric coordinates*[13] for this point with respect to the triangle's vertices must be calculated. These coordinates represent a weighted average of the triangle's vertices and are expressed as the scalars w_0, w_1, and w_2 such that

$$\begin{aligned} \mathbf{P} &= w_0\mathbf{P}_0 + w_1\mathbf{P}_1 + w_2\mathbf{P}_2 \\ \text{where } 1 &= w_0 + w_1 + w_2 \end{aligned} \tag{8}$$

In general, a point is inside (or on) the triangle if and only if $0 \leq w_1 \leq 1{,}0 \leq w_2 \leq 1$, and $w_1 + w_2 \leq 1$.

By defining the following vectors:

$$\mathbf{v}_0 = \mathbf{P}_1 - \mathbf{P}_0 \ , \ \mathbf{v}_1 = \mathbf{P}_2 - \mathbf{P}_0 \ , \ \mathbf{v}_2 = \mathbf{P} - \mathbf{P}_0 \tag{9}$$

The Cramer's rule is used to obtain the values for w_1, and w_2 by the following equations:

$$w_1 = \frac{(\mathbf{v}_2 \cdot \mathbf{v}_0)(\mathbf{v}_1 \cdot \mathbf{v}_1) - (\mathbf{v}_1 \cdot \mathbf{v}_0)(\mathbf{v}_2 \cdot \mathbf{v}_1)}{(\mathbf{v}_0 \cdot \mathbf{v}_0)(\mathbf{v}_1 \cdot \mathbf{v}_1) - (\mathbf{v}_1 \cdot \mathbf{v}_0)(\mathbf{v}_0 \cdot \mathbf{v}_1)} \tag{10}$$

$$w_2 = \frac{(\mathbf{v}_0 \cdot \mathbf{v}_0)(\mathbf{v}_2 \cdot \mathbf{v}_1) - (\mathbf{v}_2 \cdot \mathbf{v}_0)(\mathbf{v}_0 \cdot \mathbf{v}_1)}{(\mathbf{v}_0 \cdot \mathbf{v}_0)(\mathbf{v}_1 \cdot \mathbf{v}_1) - (\mathbf{v}_1 \cdot \mathbf{v}_0)(\mathbf{v}_0 \cdot \mathbf{v}_1)} \tag{11}$$

Therefore by applying intersection point algorithms between every laser ray vector and all model's triangles, the total laser footprint samples on the target model can be generated.[3] But in spite of the fact that this normal approach is simple and straightforward, extensive calculations are required to do it, make it very slow, especially when the model consists of a large number of triangles or when a large number of laser footprint samples are required.

4. PROPOSED APPROACH

To overcome on the limitation of the normal approach, another approach was proposed. This approach is to evaluate the intersection points only between the vectors and triangles that lie in the same angular range, which leads to reduction in the calculations and speed up the process. Figure 3 gives a view of the principles used, where the steps in the procedure are presented in the following:

1. The angular extant in terms of azimuth and elevation angular ranges for each triangle is calculated and stored. These calculation are required ones per scanning setup.
2. The laser rays vectors (right side of figure 3) are generated. These vectors are depend on the LADAR viewing direction, laser footprint size, and the number of the laser footprint samples.
3. The triangles whose angular extents lie within the laser beam illumination direction are selected (the blue edges triangles in figure 3) .
4. For every selected triangle, the laser rays vectors that lie in the field of that triangle are selected and the intersection points between them are calculated. The up-right side of the figure 3, shows the selected rays that lie in the field of the green edges triangle. It also shows the intersection points on the triangle plane (green & yellow points) and inside the triangle itself (green points).
5. If the laser ray vector lie in the field of more than one triangle, and have intersection point with each one of them, then the point that has the smaller distance to the laser are selected and stored.

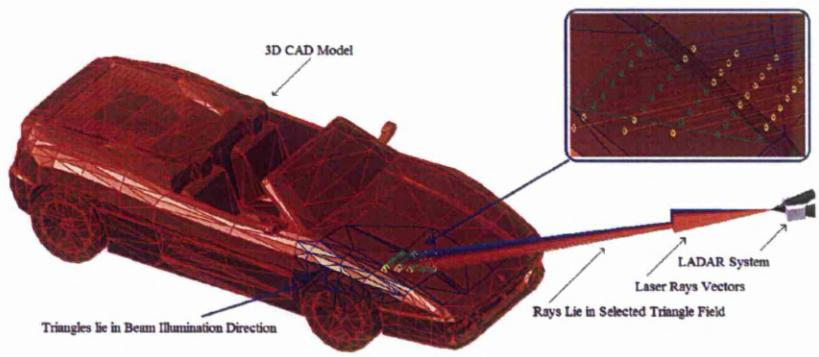

Figure 3: LADAR System Scan Car Model with the Proposed Approach.

The azimuth and elevation angular ranges mentioned in previously in (step 1) are calculated as following:

- Azimuth Angular Range: This angular range can be computed by calculated the azimuth angle for each triangle vertices, and comparing these angles with each other to find the minimum and the maximum values, that represent the azimuth angular range.
- Elevation Angular Range: The method of calculating this range is similar to the above method, but the calculated elevation angles for the triangles vertices are not always represent the range. Therefore, additional three edge angles (one per triangle edge) are calculated and added to the comparison. Figure 4a

shows the calculation principle for the edge angle ϕ_l. It starts by finding the line equation for the triangle edge of points $\mathbf{P}_0$ & $\mathbf{P}_1$ (see red line in figure 4a) by:

$$\begin{aligned} \mathbf{P}_l &= \mathbf{P}_0 + l_l(\mathbf{P}_1 - \mathbf{P}_0) \\ \langle x, y, z\rangle &= \langle x_0, y_0, z_0\rangle + l_l(\langle x_1, y_1, z_1\rangle - \langle x_0, y_0, z_0\rangle) \\ \langle x, y, z\rangle &= \langle x_0 + l_l(x_1 - x_0), y_0 + l_l(y_1 - y_0), z_0 + l_l(z_1 - z_0)\rangle \end{aligned} \tag{12}$$

where $\mathbf{P}_l$ is any point in the line of parameter l_l and its elevation angle ϕ_l can be calculated by:

$$\begin{aligned} \phi_l &= \arctan \frac{z}{\sqrt{x^2 + y^2}} \\ &= \arctan \frac{z_0 + l_l(z_1 - z_0)}{\sqrt{(l_l(x_1 - x_0))^2 + (y_0 + l_l(y_1 - y_0))^2}} \end{aligned} \tag{13}$$

The first derivative for equation 13 is then taken and solved for zero, in order to find the parameter value l_{rp} at which there is a round point $\mathbf{P}_{rp}$. After the derivation and simplification of the equation 13 it becomes:

$$l_{rp} = \frac{(-z_0 x_0 x_1) - (z_0 y_0 y_1) + (z_1 x_0^2) + (z_1 y_0^2)}{U1 + U2} \tag{14}$$

where

$U1 = (z_0 x_1^2) + (z_0 y_1^2) + (z_1 x_0^2) + (z_1 y_0^2)$
$U2 = (z_0 x_0 x_1) - (z_0 y_0 y_1) - (z_1 x_0 x_1) - (z_1 y_0 y_1)$

If l_{rp} is between 0 and 1 then an additional elevation angle is required and its value can be calculated by substituting l_{rp} value into equation 13. Figure 4b shows the vertices elevation angles (at the start and at the end of curve) and the additional edge angle at the round point $\mathbf{P}_{rp}$ (middle red circle).

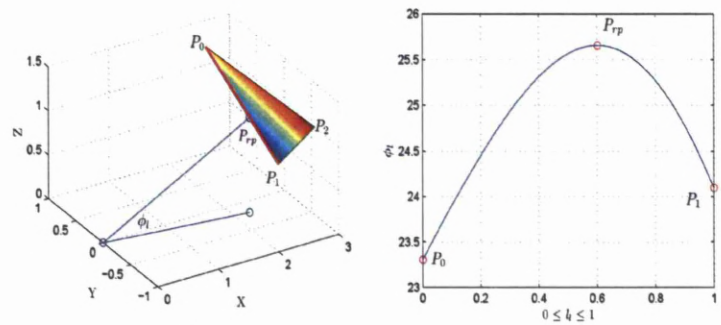

(a) (b)

Figure 4: This figure shows: (a) the additional elevation angle ϕ_l for triangle edge (red line) of vertices $\mathbf{P}_0$ & $\mathbf{P}_1$ and (b) the elevation angles values from $\mathbf{P}_0$ to $\mathbf{P}_1$.

Figure 5 shows the resultant LADAR image after scanning the car model shown in figure 3 with a train of pulses, where the target response for each pulse is generated by using the proposed approach.

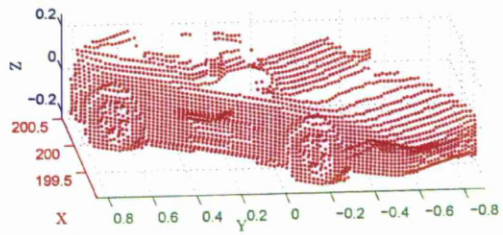

Figure 5: The Simulation Results of Scanning the Car Model shown in figure 3.

5. TESTING PROGRAM

Two tests were applied to evaluate the performance of the proposed approach. The first test starts by scanning different plane targets with a laser beam (consists from 49 vectors or samples) using both approaches (normal and proposed) and calculates the required time to get the intersection points for each individual scan. These plane targets have the same size but they are consist from different triangles number. This test is then repeated with another two laser beams of vectors number (Vc. No.) 169, and 441 respectively. Figure 6 shows the effect of changing the triangles number on the execution time for these three beams.

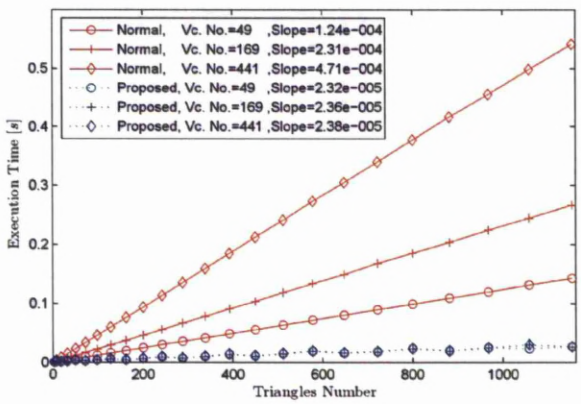

Figure 6: Execution Time for Both Approaches Versus the Triangles Number for Specific Vectors Numbers.

The second test starts by scanning a plane target (consists from 50 triangles) with different laser beams using both approaches and calculates the required time to get the intersection points for each individual scan. These laser beams have the same width but they are different with the samples (vectors) number that represent them. This test is then repeated with another two planes of triangles number (Tr. No.) 288 and 800 respectively. Figure 7 shows the effect of changing the vectors number on the execution time for these three planes.

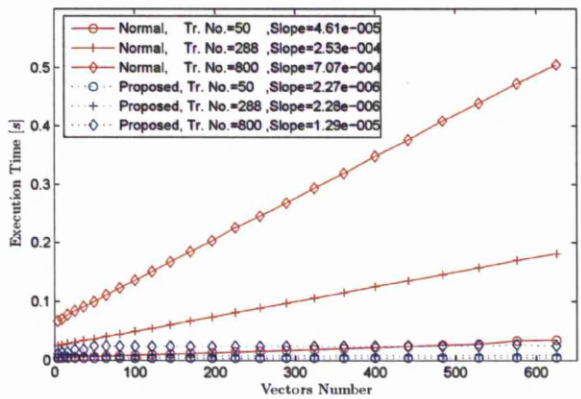

Figure 7: Execution Time for Both Approaches Versus the Vectors Number for Specific Triangles Numbers.

6. COMPARISON OF RESULTS

In order to compare between the results the execution time slope for each case is calculated using least square method. The results in figure 6 show increment in slopes for both approaches, when the vectors number increase from 49 to 441. The same situation in figure 7 but this time when the triangles number increase from 50 to 800. The results also show that the normal approach slopes are very large comparing with these of the proposed approach, which reached in figure 7 at (Tr. No.=800) to 55 times larger.

7. CONCLUSION

This paper presents a new and fast approach to enhance the LADAR simulator performance. It shows that generating the target response by direct selection for the target's parts that interact with the laser beam, significantly speed up the process. The performance of this approach is tested and compared with the normal approach under the effects of changing both the triangles and vectors numbers. The comparison of results shows that the proposed approach is faster (less slope) than the normal especially when the model consist of a large number of triangles or when the laser footprint contains large number of samples.

REFERENCES

[1] Al-Temeemy, A. A., Spencer, J. W., and Ralph, J. F., "Levy flights for improved ladar scanning," in [*2010 IEEE International Conference on Imaging Systems and Techniques, IST 2010 - Proceedings*], 225–228 (july 2010).

[2] Budge, S., Leishman, B., and Pack, R., "Simulation and modeling of return waveforms from a ladar beam footprint in usu ladarsim," 263 – 268, Pro. of SPIE (2006).

[3] Song, Z., "2d laser ray tracing for the simulation of laser perception," tech. rep., College of Engineering, Utah State University, 4160 Old Main Hill, Logan Utah 84322-4160, USA (2004).

[4] Richmond, R. D. and Cain, S. C., [*Direct-Detection LADAR Systems*], SPIE Press (2010).

[5] Steinvall, O. and Carlsson, T., "Three-dimensional laser radar modelling," **4377**, 23–34, SPIE Press (2001).

[6] Koechner, W., [*Solid-State Laser Engineering (Springer Series in Optical Sciences)*], Springer, 6th, rev. and updated ed. ed. (2006).
[7] Saleh, B. E. A. and Teich, M. C., [*Fundamentals of Photonics*], Wiley-Interscience, 2nd. ed. (2007).
[8] Jelalian, A. V., [*Laser Radar Systems*], Artech House (1992).
[9] Bachman, C. G., [*Laser Radar Systems and Techniques*], Artech House (1979).
[10] Accetta, J. S. and Shumaker, D. L., [*The Infrared and Electro-Optical Systems Handbook.*], vol. 6 of *Active Electro-Optical Systems*, SPIE Press (1993).
[11] Der, S., Redman, B., and Chellappa, R., "Simulation of error in optical radar range measurements," *Applied Optics* **36**(27), 6869 – 6874 (1997).
[12] Lengyel, E., [*Mathematics for 3D Game Programming and Computer Graphics*], Charles River Media, 2nd ed. (2004).
[13] Ericson, C., ed., [*Real Time Collision Detection*], Morgan Kaufmann (2005).

Three Dimensional LADAR Imaging System using AR-4000LV Laser Rangefinder

Al-Temeemy Ali A.[a] and Spencer J. W. [a]

[a]Department of Electrical Engineering and Electronics, University of Liverpool, Brownlow Hill, L69 3GJ, Liverpool, United Kingdom;

ABSTRACT

A new Laser Detection and Ranging or laser radar (LADAR) prototype system has been designed and implemented to be able to capture the 3D LADAR data from the surfaces of various objects. This system is designed to have a high technical specification (sampling rate and resolution) at a minimum cost. This opens up the possibility for further research in the LADAR field, which is currently limited because of the high cost of traditional LADAR systems. This paper describes the technical aspects of the LADAR design which include hardware components and both the mathematical model and the controlling software that are required for reconstructing the resultant LADAR images from the scanning measurements.

Keywords: LADAR, 3D Laser Imaging, Laser Rangefinder

1. INTRODUCTION

LADAR is a three-dimensional (3-D) spatial measurement tool that used in many applications,[1] including precision distance measurements, target detection, precise aircraft navigation, and medical applications. The high prices for these devices make their use very limited in the research field. Therefore a new design is required in order to make LADAR systems more affordable and usable in this field. In this paper a new LADAR prototype system is designed and implemented to satisfy the above requirements. The cost for this system is approximately equal to $5K\,(GBP)$ and it is designed to have a high sampling rate and scanning resolution, where both the scanning field of view and the resolution are selectable by the user. In the following sections, an explanation of both the LADAR system architecture and the mathematical model derivation that is required for the data generating process. The hardware implementation is then presented, including details about the main hardware used and the design parameters. The LADAR software implementation is described and its possibilities are presented by showing a collection of the selected results. This is followed by the conclusion.

2. SYSTEM ARCHITECTURE

The LADAR system is designed to have a large field of view. It can reach up to $+/-159^o$ in the pan direction and -47^o to $+31^o$ in the tilt direction, and it is able to scan objects with an angular resolution of 0.0265^o at a scanning speed equal to 714 angular positions per second (in both pan and tilt directions).

The hardware architecture for the LADAR system is shown in figure 1, consisting of:

- AccuRange 4000-LV Laser Distance Measurement Sensor: This sensor responsible for measures the distance values of the object surface from its location and sends these values to the computer via a serial port. This sensor provides only one dimension for the scanned object, because it measures the distance to a single point on the surface of that object.
- Computer Controlled Pan-Tilt Unit D46-17 with its controller: The pan-tilt unit is responsible for acquiring the other two object dimensions, by positioning the laser sensor in both pan and tilt directions. The controller is used to handle the precise motion control for this unit according to computer commands.

Further author information: (Send correspondence to Al-Temeemy A. A.)
Al-Temeemy A. A.: E-mail: ali.al-temeemy@liv.ac.uk, Telephone: +44 (0)7881448495

Optical Design and Engineering IV, edited by Laurent Mazuray, Rolf Wartmann, Andrew Wood, Jean-Luc M. Tissot, Jeffrey M. Raynor, Proc. of SPIE Vol. 8167, 816721 · © 2011 SPIE · CCC code: 0277-786X/11/$18 · doi: 10.1117/12.902310

- Two Power Supplies: One for the laser sensor and the other for the pan-tilt unit and its controller, where these power supplies are different in their output power.
- Microsoft LifeCam VX-1000: This color camera is used to provide the images for the scene on the computer screen.
- Computer System **SONY** ***VAIO*** EB2MOE: The last part in the LADAR system, which provides a platform for the LADAR control software which is written to generate resultant 3D object image.

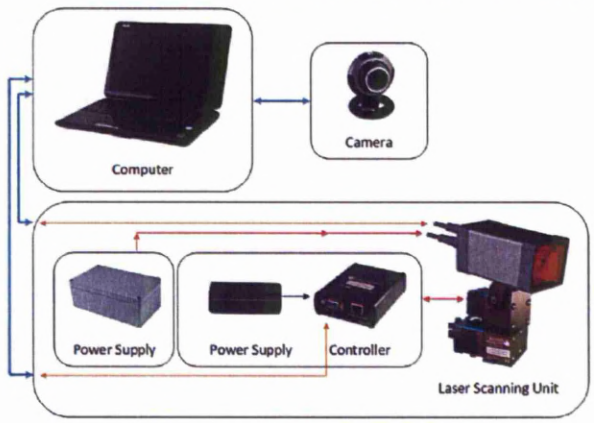

Figure 1: Schematic of the LADAR Hardware Architecture.

3. LADAR MATHEMATICAL MODEL

In this particular LADAR system, the sensing head is mounted with pan and tilt motors to varies its angular position with specific pan θ_M and tilt ϕ_M angles. This type of mounting required a special mathematical model to reconstruct the LADAR images from the distance measurements that generated by the laser sensor.

This model starts by defining a spherical coordinate system whose origin is the point O shown in figure 2. It is then models the object as a spherical range image (ρ, θ, ϕ) with respect to this point, where ρ is the distance to point $\mathbf{P} = \langle x, y, z \rangle$ on the object surface at azimuth angle θ and elevation angle ϕ. For each (θ, ϕ) position, the sensor emits a pulse of visible-red laser light that either reflects off a scene surface and generates a range measurement or there is no reflection therefore no measurement generated.

The mathematical model then defines a relation between the parameters at which the point $\mathbf{P}$ is measured (distance from the sensor lens c_s, pan angle θ_M, and tilt ϕ_M) and the spherical coordinate (ρ, θ, ϕ) parameters that represents this point. This is necessary because of the offset introduced by the sensing head mounting. The implication is that the sensing head is no longer at the origin O, which makes the measured distance value c_s and the tilt motor angle ϕ_M not related directly to the ρ and ϕ respectively in spherical coordinate system. Referring to figure 2, the relationships are given by the following equations:

$$\rho = \sqrt[2]{(b_s + c_s)^2 + a_s^2} \quad (1)$$

$$\theta = \theta_M \quad (2)$$

$$\phi = \phi_M + \arctan[a_s/(b_s + c_s)] \quad (3)$$

where

a_s: Distance between O and the sensing head center point M.
b_s: Distance between M and the start location for the measured value c_s.

In this system, a_s and b_s are equal to $90\,mm$ and $95\,mm$ respectively. The conversion from the spherical to Cartesian coordinates is defined by the following equations:

$$x = \rho\cos\phi\cos\theta \quad (4)$$
$$y = \rho\cos\phi\sin\theta \quad (5)$$
$$z = \rho\sin\phi \quad (6)$$

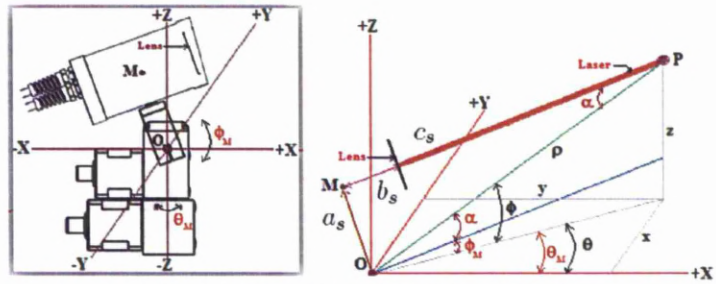

Figure 2: Parameters of the LADAR Mathematical Model.

4. HARDWARE IMPLEMENTATION

This section describes the detail of the hardware used in the LADAR system shown in figure 3, including the AccuRange 4000-LV laser distance measurement sensor and the computer controlled pan-tilt unit D46-17 with its controller. The section also presents the design parameters that used with these units in order to generate the LADAR images.

4.1 AccuRange 4000-LV

4.1.1 General Description

AccuRange 4000-LV is a unique laser distance measurement sensor. It uses a modified time-of-flight measurement principle (patented in 1994[2]) that leads to ultra fast (up to $200,000\,sample/s$)[3] and accurate distance measurements. The sensor has a working range of zero to $12.2\,m$ on 85% diffuse reflectance surfaces with a resolution equal to $0.32\,mm$,[3,4]

The AccuRange 4000-LV is a Class IIIa laser product. It uses a laser diode as an optical source, which emits a visible laser beam at a wavelength equal to $670\,nm$ and $5\,mW$ optical power. The beam leave the aperture with a spot of $2.5\,mm$ and a divergence equal to $0.5\,mrad$.[3]

4.1.2 Principle of Operation

AccuRange 4000-LV sensor uses a patented rangefinding technique to measure the distance to the target.[2] This technique generates a frequency based on range by creating an oscillator with a laser source and the photodetector after the light has traveled to a certain distance. The schematic diagram of the sensor and the light paths through its optical components and detection and triggering circuits is shown in figure 4.

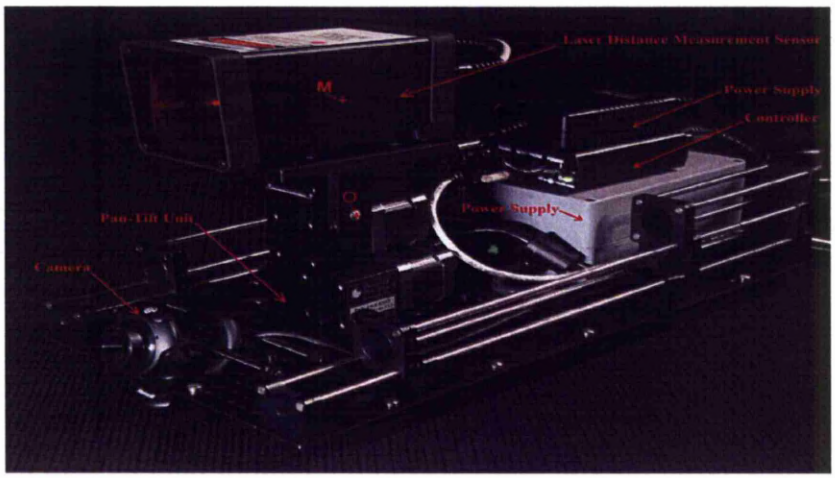

Figure 3: LADAR Scanning System.

Referring to figure 4, the laser diode is controlled by a modulator to produce a laser light at two different intensities. This light is collimated into a beam by collimating optics and emitted from the center of the front face of the sensor to the target. The reflected light from that target is collected by a Fresnel lens and focused onto an avalanche photodiode. The photodiode signal is amplified up to a limited level by the amplifier and inverted by the inverter.

The resultant signal is a logic level 1 or 0 and is input to the modulator to drives the laser diode. This configuration forms an oscillator, with the laser switching itself on and off using its own signal. The time that the light takes to travel to the target and return plus the propagation time through the electronics t_e from the photodiode to the laser diode determines the period of oscillation t_o (1 / rate at which the laser is switched on and off). This period can be expressed as:[2]

$$t_o = 2t_e + 4c_s/c \tag{7}$$

where c_s is the distance from the sensor to the target, and c is the speed of light value.

The oscillation period is measured by frequency measurement circuitry, which counts a fixed number of oscillation cycles and times the interval taken. The measurement is somewhat nonlinear and dependent on signal strength (which is measured by amplitude measurement electronics) and temperature, so a calibration process is performed in the sensor to remove these effects.

The advantages of using this techniques to measure the distance are:[2]

- Higher resolution than the phase measurement method, due to the timers being more accurate than phase detectors.
- Range ambiguity problem that plague phase comparison methods is absent in this technique, where the maximum range is only limited by the power of the light source and the reflectivity of the target.

- By measuring the time required for multiple oscillations the distance can be measured more accurately than if a single pulse of energy is timed.
- The binary switching used in this technique makes it less sensitive to the noise and more immune to errors induced by low intensity return signals from for example dust particles in the beam path. This is due to the small fluctuations in the incoming signal will not cause a transition of the output state.

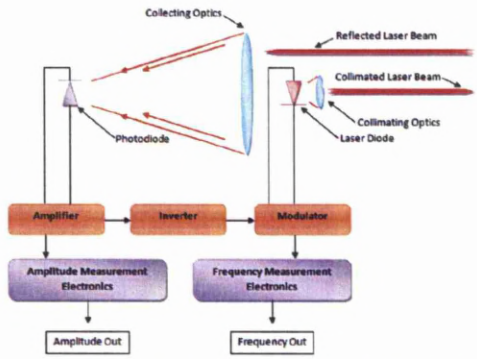

Figure 4: The schematic diagram of the Laser Distance Measurement Sensor.[2]

4.1.3 Sensor Output

The sensor output can be selected to either calibrated distance readings, un-calibrated sensor data, or both together in each sample. Data is transmitted as 8 bits with no parity bit and 1 stop bit and sent in ASCII or binary format. The sensor configuration is done via commands sent over the serial port, which are ASCII commands entered under computer control. The sensor is able to produce calibrated range readings at a sample rate of up to 714 samples per second through the RS-232 serial port.[5] If higher rates are required (up to $200,000\,Hz$) then, the un-calibrated sensor output must be used with the PCI interface card.

The AccuRange 4000-LV is set to transmit data via the RS-232 serial port as calibrated range measurements and with a sampling rate equal to $714\,sample/s$. This rate is limited by the time required to transmit each sample at the specified baud rate. Therefore to allow the sensor to transmit the data at this rate, the sensor transmission baud rate is set to the maximum, which is equal to $38400\,bit/s$ and the data format is set to binary. The reason behind selecting the binary over ASCII format is that, the binary format requires only three bytes to represent the measurement (two distance bytes representing the range in mm followed by one byte with a value FF Hex for framing). This makes the time required to transmit each sample at maximum baud rate smaller than the sample time, while the ASCII format requires from six to eight bytes and more transmission time (larger than the sample time).

4.2 Computer Controlled Pan-Tilt Unit D46-17

This unit is fully computer controlled and has programmable speed, acceleration, and other parameters. It is used to position the laser distance measurement sensor in both pan and tilt directions. The load capacity for this unit is $2.72\,kg$ and it's capable of moving in both pan and tilt directions at a speed reached to $300^o/s$, with a maximum angular resolution of 0.013^o.[6] The unit is connected to the pan-tilt controller, which accepts ASCII and binary command formats via RS-232 from a host computer, and drives the pan-tilt unit to a new position

with a certain speed and acceleration. The data is transmitted as 8 bit with 1 stop bit and no parity bit at a baud rate equal to 38400 bit/s.

The pan-tilt unit is programmed to position the laser beam over the object surface using a raster scanning pattern (row by row) and with a scanning speed equal to 714 $positions/s$ in both pan and tilt directions. Selecting this value to be the same as the laser sensor sampling rate (714 $sample/s$), makes the LADAR system capable of producing range measurement for each new position. To guaranty regular (equal) time intervals between each position, the base speeds (in pan and tilt directions) are set to be equal to the scanning speeds. The motion resolution for the controller is set to 0.0265°. This available resolution produces fast and smooth positioning for the laser sensor (i.e. moving from one position to another without losing synchronisation).

5. SOFTWARE DESCRIPTION

This section describes the software that has been written for the LADAR hardware setup in order to control its operation and produce the LADAR data. A Graphical User Interface (GUI) is also designed into this software. This GUI contains the panels that required for setting the scanning parameters and displaying the resultant data. Figure 5 shows the GUI window's panels that are used for scanning the train model, where these panels are:

Figure 5: LADAR GUI Control Window.

5.1 Visualization Panels

Two visualization panels were designed in this window. The first panel (right-side) displays the results, while the second panel (left-side) displays the scanned scene image and laser spot marker. This marker is displayed over the scene image as a red shape (see figure 5) and used to guide the user to the location of the laser spot by finding the maximum intensity on the red channel of the scene image.

5.2 LADAR Parameters Panel

This panel is used for adjusting the LADAR scanning resolutions and its scanning limits. Estimating the exact LADAR scanning limits for a specific object is not easy task in most cases. Therefore the panel is designed to aid the user to specify these limits easily, by positioning the laser beam directly towards the object border points (by using "Up","Down", "Left", and "Right" buttons) and then select and set the pan / tilt values for each point (by using "Select Points" and "Set Angles" respectively) to determine the scanning limits. These values can also be deleted by using the "Clear Points" button.

5.3 Scanning Panel

Pressing the "Scan Start/Stop" button in this panel, starts the LADAR scanning operation, which can be also stopped at any time by pressing this button again. During this operation, the resultant LADAR data are displayed directly on the visual panel screen (row by row) until the end of that operation. The panel also has a button which allow the laser to be switched *on* and *off*.

5.4 Output Panel

The software is designed to display and save the resultant LADAR data in four different formats, one in spherical coordinates (spherical image) and the other three in Cartesian coordinates (Mesh, Surfaces, and point cloud). These formats are selecting by using the corresponding buttons in this panel. Figure 6 shows the resultant LADAR formats of scanning the train model with the scanning parameters shown in figure 5.

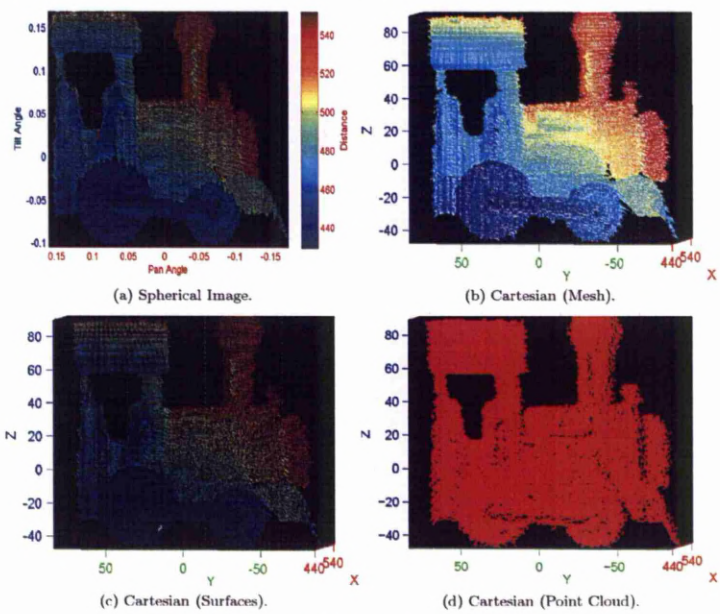

(a) Spherical Image.

(b) Cartesian (Mesh).

(c) Cartesian (Surfaces).

(d) Cartesian (Point Cloud).

Figure 6: Four types of Scanning Results for Train Model

5.5 Data Filtering Panel

This panel consists from two filters, which are the objects and the mixed pixel filters:

5.5.1 Objects Filter

This filter works in conjunction with the output panel to remove unwanted objects from the resultant data manually. The filter is designed to be able to filter the data in three dimensions with one of two different coordinates, which are spherical and Cartesian coordinates. The type of coordinates that will be used during the filtering process will depend on which data format has been selected via the output panel. Therefore if the data is displayed as a spherical image the spherical coordinates will be selected, while the Cartesian coordinates will be selected if the data are displayed with one of the other three formats (Mesh, Surfaces, Point Cloud).

The data filtering is performed by defining the range limits of the desired measurement values in each dimension. This will allows the filter to remove all the unwanted values that lay outside this range in that dimension.

In each dimension, the range limit values R_1 and R_2 are calculated by applying the following equation:

$$\begin{aligned} Range &= [R_1, R_2] \\ &= [(F_c - F_w/2), (F_c + F_w/2)] \end{aligned} \tag{8}$$

where F_c and F_w are the filter centre and filter width respectively. These can be set either by typing their values directly in the corresponding edit text boxes or by using the corresponding sliding bars. If the sliding bars are used then F_c and F_w values are calculated using the following equations:

$$F_c = R_{min.} + slv_{center} \times (R_{max.} - R_{min.}) \tag{9}$$

$$F_w = slv_{width} \times (R_{max.} - R_{min.}) \tag{10}$$

where

$R_{min.}$: Minimum measure range values.
$R_{max.}$: Maximum measure range values.
slv_{center} : Location values for the "**Centre**" sliding bar.
slv_{width} : Location values for the "**Width**" sliding bar.

Both slv_{center} and slv_{width} values are adjusted by moving the corresponding slider bars to the left or to the right, where their values are varied between 0 and 1. During the slider bars movement, both the centre and width edit texts values are set to the new calculated F_c and F_w (to allow re-adjustment using edit text boxes) and the filtered data are directly displayed on the visual panel screen. Figures 7a and 7b show respectively the train before and after filtering the wall that lies behind it. The "Save" button in the output panel is then used to save the resultant filtered data with a specific name.

5.5.2 Mixed Pixel Filter

LADAR system measurements are corrupted by noise and artifacts that can undermine the performance of registration, segmentation, surface reconstruction, recognition, and other algorithms operating on the data.[7] Laser data artifacts can be divided into two categories: intrinsic sensor errors (range drift due to temperature variations , systematic errors and random noise, etc), and errors due to the interaction of the laser beam with the environment. Most common spurious range measurements occur when the laser beam hits simultaneously two objects at different distances. Such errors are known in the literature as mixed pixels, or discontinuous points,[8–11] and several method have been developed in order to identified, filtered, and restored these mixed pixels.[7–10,12–15] Figure 7a shows the mixed pixels between the train and the wall, while figure 7b shows these pixels on the train edges.

In this software, the edge-length algorithm is used to remove these pixels.[7] Referring to figure 7, this algorithm starts by triangulated the point cloud data shown in figure 7b by organizing these points in a grid with storing their corresponding 3D Cartesian coordinates. The grid is then triangulated by connecting adjacent points in a square and then connecting one of the diagonals as shown in figure 7c.

The edge-length algorithm relies on the observation that triangles spanning a depth discontinuity often have long edge lengths (see figure 7c). Any triangle with an edge longer than a specified threshold is marked as a depth discontinuity triangle, where the summation of the mean and standard deviation values for the triangles edge lengths is used as a threshold value. After eliminating depth discontinuity triangles, any isolated 3D points (i.e., points not connected to any remaining triangles) are considered mixed pixel points.

Once a mixed pixel is identified the general approach is to remove it outright. This deals with the problem of the mixed pixel, but has potential to introduce other errors, such as distorting object edges and creating holes in surfaces.[12] For this reasons, the first and second mixed pixel neighbors points (that are not marked as mixed pixels) are used to restored that pixel. This is by replacing the mixed pixel Cartesian coordinates with the mean values of the neighbors Cartesian coordinates. The procedure then is to checked if the resultant restored pixel is still produces long edge triangle in order to remove it from the point cloud. Figures 7d shows the resultant filtered point cloud data, which is more clearer than the original point cloud shown in figure 7b.

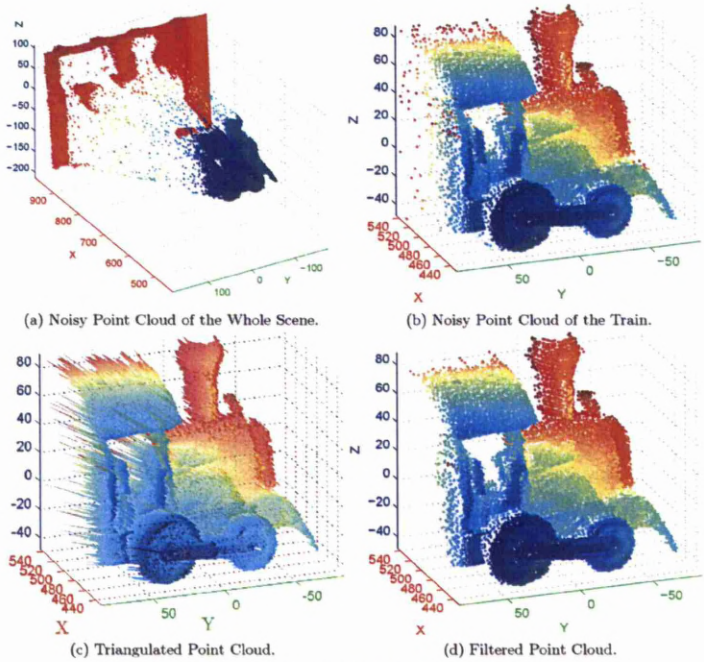

(a) Noisy Point Cloud of the Whole Scene.

(b) Noisy Point Cloud of the Train.

(c) Triangulated Point Cloud.

(d) Filtered Point Cloud.

Figure 7: Wall and Mixed Pixel Filtering using Data Filtering Panel.

Proc. of SPIE Vol. 8167 816721-9

6. CONCLUSION

This paper presents a new LADAR prototype system. It shows that combining both the AccuRange 4000-LV laser distance sensor and the computer controlled Pan-Tilt Unit D46-17 with specific parameters, produces a cost effective LADAR system of high sampling rate and scanning resolution.

The resultant scanning images for the LADAR system show the effectiveness of the mathematical model for producing these images in different formats (spherical and Cartesian). The results also show the ability of the controlling software to control the LADAR system and to filter the resultant LADAR images.

REFERENCES

[1] Al-Temeemy, A. A., Spencer, J. W., and Ralph, J. F., "Levy flights for improved ladar scanning," in [*2010 IEEE International Conference on Imaging Systems and Techniques, IST 2010 - Proceedings*], 225–228 (july 2010).

[2] Clark, R. R., "Scanning rangefinder with range to frequency conversion," (May 1994).

[3] "Accurange 4000 sensor datasheet." `http://www.acuitylaser.com/pdf/ar4000-data-sheet.pdf` (2008).

[4] "Acuity laser measurement sensors homepage." `http://www.acuitylaser.com/acuity.shtml`.

[5] "Accurange 4000 sensor user's manual." `http://www.acuitylaser.com/pdf/ar4000-users-manual.pdf` (2008).

[6] "Pan-tilt unit-d46 specifications." `http://www.dperception.com/pdf/specs-ptu-d46.pdf`.

[7] Tang, P., Huber, D., and Akinci, B., "A comparative analysis of depth-discontinuity and mixed-pixel detection algorithms," in [*3DIM 2007 - Proceedings 6th International Conference on 3-D Digital Imaging and Modeling*], 29 – 36 (2007).

[8] Tuley, J., Vandapel, N., and Hebert, M., "Analysis and removal of artifacts in 3-d ladar data," in [*Proceedings - IEEE International Conference on Robotics and Automation*], 2203 – 2210 (april 2005).

[9] Skrzypczynski, P., "How to recognize and remove qualitative errors in time-of-flight laser range measurements," in [*International Conference on Intelligent Robots and Systems*], 2958 – 2963 (sept. 2008).

[10] Ye, C., "Mixed pixels removal of a laser rangefinder for mobile robot 3-d terrain mapping," in [*International Conference on Information and Automation*], 1153 –1158 (june 2008).

[11] Hebert, M. and Krotkov, E., "3-d measurements from imaging laser radars: how good are they?," in [*IEEE/RSJ - Intelligent Robots and Systems*], 359 –364 vol.1 (nov 1991).

[12] Larkins, R., Cree, M., Dorrington, A., and Godbaz, J., "Surface projection for mixed pixel restoration," in [*24th International Conference Image and Vision Computing New Zealand (IVCNZ 2009)*], 431 – 436 (nov. 2009).

[13] Godbaz, J. P., Cree, M. J., and Dorrington, A. A., "Multiple return separation for a full-field ranger via continuous waveform modelling," in [*Proceedings of SPIE - The International Society for Optical Engineering*], **7251**(1), 72510T, SPIE (2009).

[14] Godbaz, J., Cree, M., and Dorrington, A., "Mixed pixel return separation for a full-field ranger," in [*23rd International Conference Image and Vision Computing New Zealand (IVCNZ 2008)*], 1 – 6 (nov. 2008).

[15] Wang, Q., Li, Q., Chen, Z., Sun, J., and Yao, R., "Range image noise suppression in laser imaging system," *Optics and Laser Technology* **41**(2), 140 – 147 (2009).

Levy Flights for Improved Ladar Scanning

Ali Adnan Al-Temeemy
Department of Electrical Engineering and Electronics
University of Liverpool
Liverpool UK
ali.al-temeemy@liv.ac.uk

J. W. Spencer
Department of Electrical Engineering and Electronics
University of Liverpool
Liverpool UK
joe@liv.ac.uk

J. F. Ralph
Department of Electrical Engineering and Electronics
University of Liverpool
Liverpool UK
jfralph@liv.ac.uk

Abstract—**A new approach has been used to improve Ladar performance in real time applications based on the use of Levy statistics. This approach speeds up target detection and does not require a full scan of the field of view and the subsequent data processing. This leads to a more efficient Ladar system and opens up the possibility for more real time applications. The approach is to use "Levy flights" instead of traditional techniques, such as Raster and Lissajous scanning, to detect the target in the scene. The performances of these latter techniques and this new approach are compared for a variety of conditions. The simulation results show an enhanced performance when using Levy flights as a scanning technique.**

Keywords-levy flights; stable random variable; ladar system

I. INTRODUCTION

Laser Detection and Ranging (Ladar) is poised to become the ubiquitous three-dimensional (3-D) spatial measurement tool in many applications. These include precision distance measurements, target detection, robotic applications, precise aircraft navigation, and medical applications (see reference 1 for example applications). The power of Ladar lies in the inherent 3-D nature of the data it produces. These data are created by scanning a scene with a laser beam. The return time and beam strength are recorded. The return strength produces intensity data and the time of return leads to range data. The format of the range data is (azimuth angle, elevation angle, range) – that is, spherical coordinates whose origin is at the sensor. The intensity data are gray scale values associated with each spatial location in the range [2]. A number of problems arise with existing Ladar systems, typically, these systems scan a large area and collect enormous amount of data which must be processed in order to determine potential objects. The response time is important factor for locating, recognizing, and classifying objects.

To overcome these limitations, previous investigators [3] proposed to reduce the amount of data by scanning a portion of the scene at low resolution principally to locate the region of interest, and then scan that region at high resolution in order to segment the target (locate its border). The segmented region is then scanned at resolution higher than used with segmentation to identify the object. Other researchers like Lanterman, Miller, and Snyder [4], attempt to speed up the process by using a low-resolution wide field-of-view radar to detect the object, and high resolution narrow field-of-view Ladar to identify it. Mamanakis and other [5] have applied a visual saliency algorithm on the scene images to guide the Ladar to the area of interest. This algorithm decreases the saliency by scanning the most salient area and saccading to the next most salient area until the object-of-interest is recognized

In this paper, a new approach for object detection is presented. This approach is based on using Levy flights as a scanning technique. This technique enables the Ladar to detect the object in the scene with small number of angular steps and without the need to scan the whole field of view. Raster and Lissajous scanning techniques are also used in this study to benchmark the performance of the proposed technique. In the following sections, an overview of Levy statistics and how they can be used to generate Ladar scan patterns are given – followed by a brief review of Raster and Lissajous scanning techniques. The object detection method is then explained. The simulation procedure and a comparison of the results of tests on each of the scan techniques are presented, followed by conclusions and a discussion of potential future improvements.

II. LEVY SCAN TECHNIQUE

A Levy flight is a category of random walk first devised by Paul Levy in 1937 by generalizing Brownian motion to include non-Gaussian randomly distributed step sizes for the distance moved. Levy flights have distributions that are characterized by long tails, an infinite second order moment and the fact that they converge to a non-Gaussian stable distribution. Levy flights have been applied in a diverse range of fields [6, 7], including the analysis of natural hunting behavior in biological systems.

A Levy-stable distribution requires four parameters to describe [8]: an index of stability (tail exponent) $\alpha \in [0,2)$, a skewness parameter $\beta \in [-1,1]$, a scale parameter $\sigma > 0$, and a location parameter $\mu \in R$. The tail exponent α determines the rate at which the tails of the distribution taper off as shown in Fig. 1. For the case $\alpha = 2$ the behavior is Gaussian, but for lower values of α, the behavior becomes dominated by the large jumps in allowed by the long tails of the distribution. The sign of the skewness parameter β indicates the skew direction, positive to the right, and negative to the left. When $\beta = 0$, the distribution is symmetric. The last two parameters are the width σ and the shift μ of the distribution peaks.

978-1-4244-6494-4/10/$26.00 ©2010 IEEE

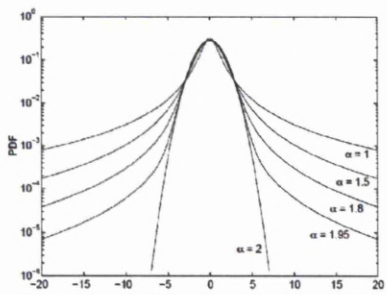

Figure 1. A semilog plot of symmetric ($\beta = \mu = 0$) Levy-stable probability density functions for α = 2, 1.95, 1.8, 1.5 and 1. The Gaussian (α=2) density forms a parabola and is the only Levy-stable density with exponential tails [8].

To adapt a Ladar system to scan the scene with a Levy flights pattern, the Chambers-Mallows-Stuck method [9] is used to generate random locations for the laser beam by applying the following procedure:

- A uniform random variable V that varies between $-\pi/2$ and $\pi/2$ is generated with an independent exponential random variable W with a mean equal to one;
- For $\alpha \neq 1$ compute:

$$X = S_{\alpha,\beta}\frac{\sin(\alpha(V+B_{\alpha,\beta}))}{(\cos(V))^{\frac{1}{\alpha}}}\left(\frac{\cos(V-\alpha(V+B_{\alpha,\beta}))}{W}\right)^{\frac{(1-\alpha)}{\alpha}} \quad (1)$$

where $B_{\alpha,\beta} = \frac{1}{\alpha}\arctan\left(\beta\tan\frac{\pi\alpha}{2}\right)$,

$$S_{\alpha,\beta} = \left[1+\beta^2\tan^2\frac{\pi\alpha}{2}\right]^{1/(2\alpha)}$$

- For $\alpha = 1$ compute:

$$X = \frac{2}{\pi}\left[\left(\frac{\pi}{2}+\beta V\right)\tan V - \beta\log\left(\frac{W\cos V}{\frac{\pi}{2}+\beta V}\right)\right] \quad (2)$$

- The Levy-stable random variable is calculated for the user defined parameter α, β, σ and μ, by using the following property:

$$Y = \begin{cases} \sigma X + \mu, & \alpha \neq 1, \\ \sigma X + \frac{2}{\pi}\beta\sigma\log\sigma + \mu, & \alpha = 1, \end{cases} \quad (3)$$

- The azimuth θ and elevation ϕ Ladar angles are then generated depending on the resultant Levy variable by using the following equations:

$$\theta = \omega(Y\cos(2\pi\varphi)) \quad (4)$$

$$\phi = \omega(Y\sin(2\pi\varphi)) \quad (5)$$

where φ is uniform random variable between [0, 1] and ω is the angular resolution. The periodic boundary conditions were used for the generated angles values that exceed the field of view limits.

III. Raster and Lissajous Scan Techniques

In a Raster scan technique, the beam sweeps horizontally from left-to-right at a steady rate, when it reaches the right edge of the field of view it moves down by an amount Ω and then it moves back to the left to scan the next line and so on. When the beam reaches the bottom edge of the field of view, it goes back to the top left and repeats the procedure [10].

In a Lissajous scan, the pattern is defined by:

$$\theta = \omega(M\sin(m\psi)) \quad (6)$$

$$\phi = \omega(N\sin(n\psi+\tau)) \quad (7)$$

where M and N are the peak amplitudes of θ and ϕ angles respectively, $\psi \in [0,2\pi]$, m and n are the number of cycles per scan, and τ is their relative phase adjustment [11].

This type of pattern is used to detect objects by decreasing the peak amplitudes by a specific amount δ until an object is found. The figure below shows the patterns for these scanning techniques.

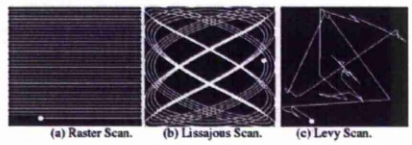

(a) Raster Scan. (b) Lissajous Scan. (c) Levy Scan.

Figure 2. Raster, Lissajous, and Levy flights scanning patterns.

IV. Object Detection

The approach described in this paper consists of two modes: a "pre-scanning" mode and a "detection" mode. In the first mode the Ladar scans the scene using a Raster pattern to generate a background image, as shown in Fig.3a. When it completes the initial scan, it stores the data (see Fig.3b) and switches to the next mode.

In the detection mode the Ladar system searches for the object by scanning the scene using a Levy pattern. It measures the distance values continuously and compares them with the values that were previously stored as shown in Fig.3c. If the difference exceeds a scene-dependent threshold value, the Ladar records the location at which the difference is detected. This location can then be explored to identify the target. After this operation, the Ladar system updates the background data by re-scanning the scene (see Fig.3d) and moves back to the detection mode, and so on.

V. SIMULATION PROCEDURE

The performance of the scanning techniques during the "detection" mode was simulated with objects of different sizes and locations. The simulation program starts by generating a scene containing a circular object at a random location with an area equal to 1/1000 of the field of view. The program then applies each of the three scanning techniques (Raster, Lissajous, and Levy) to detect the object. The total number of steps required to detect the object for each scanning technique is measured and stored.

The same procedure was repeated one thousand times, each time with the same object area but with a new random location. A uniform probability density function PDF is used to generate the locations for these objects. After generating one thousand different object locations, the program computes the mean and the median of the stored values (one thousand values) for each technique and stores the resultant values. The program then increases the object area by 0.1% and repeats the same test, and so on until the ratio R between the object's area and the field of vie equals 10%. This procedure generates one hundred mean and median values for each technique (see the flowchart shown in Fig. 4).

In this study Ω and δ were set to 7 angular steps to cover the minimum object size, where the angular resolution ω was set to 0.1. The small difference between the Spherical and Cartesian coordinates were neglected, because most Ladar systems use a small field of view [12]. Table 1 summarizes the scanning parameters techniques used in this study.

TABLE I. SCANNING PARAMETERS

Scanning Techniques											
Levy					*Lissajous*					*Raster*	
ω	α	β	σ	μ	ω	τ	m	n	δ	ω	Ω
0.1	1.1	1	20	0	0.1	90	3	5	7	0.1	7

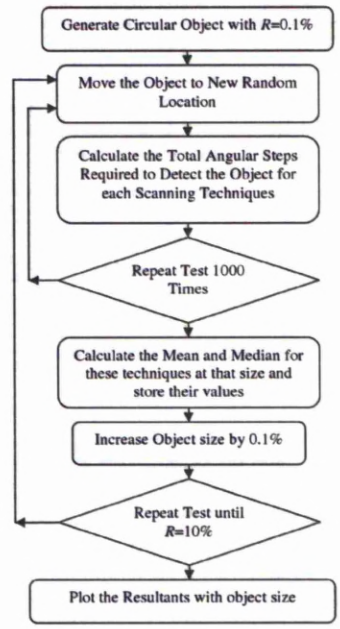

Figure 4. Testing Procedure Flowchart.

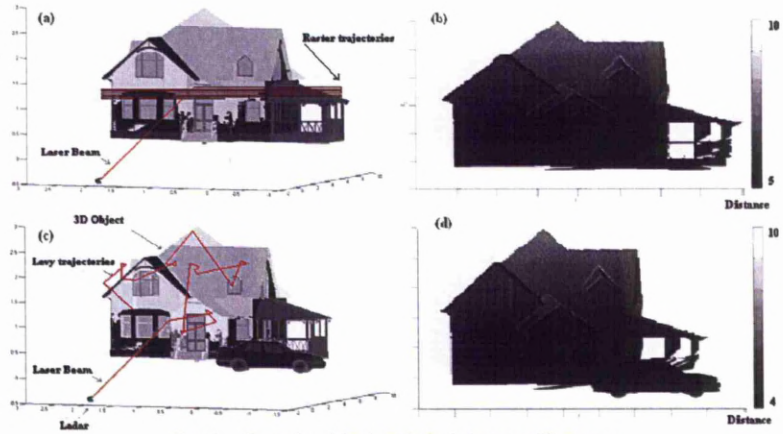

Figure 3. Pre-scanning and detection modes for a Ladar scan two different scenes.

VI. Comparison of Results

The figures below show the mean and the median for the total number of angular steps, when the Raster, Lissajous, and Levy scans are used in the object detection mode. The results show an inverse relation between the total angular steps and the object's area, because the chance of detecting the small object with small angular steps is less than that for the large object. The mean and the median for the Lissajous and Levy techniques decrease rapidly as the size of the object is increased, while they decrease much more slowly for the Raster scan. When the ratio R is equal to or larger than 0.4%, the Levy technique performs better than either of the other two techniques.

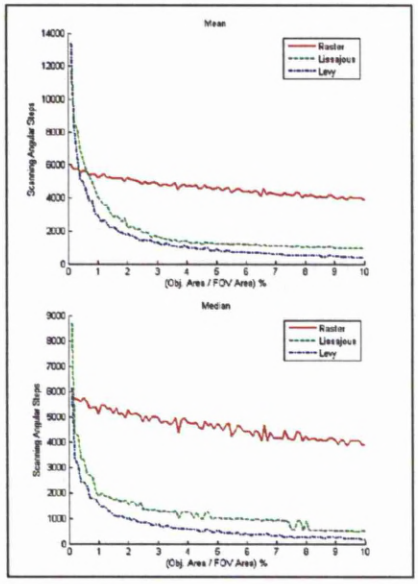

Figure 5. Mean (above) and median (below) of the total angular steps for Raster, Lissajous, and Levy techniques.

VII. Conclusions

This paper represents a new step towards using Levy statistics in the Ladar systems field. It shows that using Levy flights to steer the laser beam during the object detection mode improves detection speed. The performance of this scan technique is tested and compared with Raster and Lissajous scans by calculating the mean and the median for the total number of angular steps for a wide variety of scenes. The comparison of results shows that Levy flights are efficient when the target's area is equal to or larger than 4/1000 of the field of view.

Extensions of this work include dealing with dynamic targets and testing the scanning techniques experimentally with real scenes, where noise is taken into account and the regions that produce unstable measurements, such as edges and trees.

References

[1] W. C. Stone, and M. Juberts, "Towards the Ultimate Construction Site Sensor." 19th International Symposium on Automation and Robotics in Construction: NIST Special Publication 989, pp. 393–402, 2002.

[2] D. DeKruger, J. Hodge, J. C. Bezdek, J. M. Keller, and P. Gader, "Detecting Mobile Land Targets in LADAR Imagery with Fuzzy Algorithms", *Journal of Intelligent and Fuzzy Systems*, vol. 10, pp. 197-213. 2001.

[3] U. Landau, and K. Shluchot, "Apparatus and Method for Laser Imaging," *United State Patent*, no.5638164, 1997.

[4] A. D. Lanterman, M. I. Miller, and D. L. Snyder, "The unification of detection, tracking, and recognition for millimeter wave and infrared sensors," *Proc. SPIE*, vol. 2562, pp. 150-161, July 1995.

[5] M. T. Mamanakis, R. R. Fullmer, R. T. Pack, and S. Budge, "Active and Attentive LADAR Scanning for Automatic Target Recognition." *Proc. of SPIE*, vol. 6971, pp. 69710I-1 - 69710I-12, Jan. 2008.

[6] N. Chakravarti, "Beyond Brownian motion: A Levy flight in magic boots," *RESONANCE*, pp. 50-63, 2004.

[7] P. Barthelemy, J. Bertolotti, and D. S. Wiersma, "A levy flight for light," *Nature*, vol. 453, pp. 495-498, May 2008.

[8] R. Weron,"Levy-stable distributions revisited: Tail index >2 does not exclude the Levy-stable regime," *International Journal of Modern Physics C 12*, pp. 209-223, 2001.

[9] R. Weron, "On the Chambers–Mallows–Stuck method for simulating skewed stable random variables," *Statist. Probab. Lett.* 28, pp. 165–171, 1996.

[10] S. George and S. May, "Early Television: A Bibliographic Guide to 1940," Taylor & Francis, pp. 47, 1997.

[11] F. Blais, M. Rioux, and S.G. Mclean, "Intelligent, Variable Resolution Laser Scanner for the Space Vision System," *SPIE*, vol. 1482, pp. 473-479, 1991.

[12] P. J. Besl, "Surfaces in Range Image Understanding.", pp. 311-316, 1988.

References

[1] C. W. Trussell. 3d imaging for army applications. In *Proceedings of SPIE - The International Society for Optical Engineering*, volume 4377, pages 126 – 131, 2001.

[2] R. M. Marino and W. R. Davis. Jigsaw: A foliage-penetrating 3d imaging laser radar system. *Lincoln Laboratory Journal*, 15(1):23 – 36, 2005.

[3] Ultra high speed laser scanner (leica hds6000) specifications. `http://www.pacificsurvey.com/pdf/HDS6000.pdf`.

[4] Swiss ranger sr-2 datasheet. `http://www8.cs.umu.se/research/ifor/dl/Productnfo/SR-2_DataSheet.pdf`.

[5] Z+f imager 5010 specifications. `http://www.zf-laser.com/Broschuere_5010_E.pdf`.

[6] Ultra-high speed laser scanning with extended range (hds7000) datasheet. `http://www.leica-geosystems.com/en/HDS7000_90337.htm`.

[7] P. Cho, H. Anderson, R. Hatch, and P. Ramaswami. Real-time 3d ladar imaging. *Lincoln Laboratory Journal*, 16(1):147 – 164, 2006.

[8] G. Powell, D. Marshall, R. Milliken, and K. Markham. Data fusion of flir and ladar in autonomous weapons systems. In *Proceedings of Information Fusion*, 2003.

[9] S. Petitjean. A survey of methods for recovering quadrics in triangle meshes. *ACM Comput. Surv.*, 34(2):2110–0262, 2002.

[10] A. Johnson. *Spin-Images: A Representation for 3-D Surface Matching.* PhD thesis, Robotics Institute, Carnegie Mellon University, 1997.

[11] R. D. Richmond and S. C. Cain. *Direct-Detection LADAR Systems.* SPIE Press, 2010.

[12] C. G. Bachman. *Laser Radar Systems and Techniques.* Artech House, 1979.

[13] A. Soloviev and M. U. De Haag. Three-dimensional navigation with scanning ladars: concept & initial verification. *IEEE Transactions on Aerospace and Electronic Systems*, 46(1):14 – 31, 2010.

[14] J. T. Sackos, B. D. Bradley, B. Nellums, and C. Diegert. Emerging versatility of a scannerless range imager. In *Proceedings of SPIE - The International Society for Optical Engineering*, volume 2748, pages 47 – 60, 1996.

[15] T. C. Monson, J. W. Grantham, S. W. Childress, J. T. Sackos, R. O. Nellums, and S. M. Lebien. Characterization of scannerless ladar. volume 3707, pages 409 – 420. SPIE, 1999.

[16] C. L. Smithpeter, R. O. Nellums, S. M. Lebien, and G. Studor. Miniature, high-resolution laser radar operating at video rates. In *Proceedings of SPIE - The International Society for Optical Engineering*, volume 4035, pages 279 – 286, 2000.

[17] B. Stann, A. Abou-Auf, S. Frankel, M. Giza, W. Potter, W. Ruff, P. Shen, D. Simon, M. Stead, Z. Sztankay, and L. Lester. Research progress on scannerless ladar systems using a laser diode transmitter and fm/cw radar principles. In *Proceedings of SPIE - The International Society for Optical Engineering*, volume 4377, pages 12 – 22, 2001.

[18] M. J. Halmos, M. Jack, J. Asbrock, C. Anderson, S. Bailey, G. Chapman, E. Gordon, P. Herning, M. Kalisher, L. Klaras, K. Kosai, V. Liquori, M. Pines, V. Randall, R. Reeder, J. Rosbeck, S. Sen, P. Trotta, P. Wetzel, A. Hunter, J. Jensen, T. DeLyon, W. Trussell, A. Hutchinson, and R. Balcerak. 3-d flash ladar at raytheon. In *Proceedings of SPIE - The International Society for Optical Engineering*, volume 4377, pages 84 – 97, 2001.

[19] M. Vaidyanathan, A. Joshi, S. Xue, B. Hanyaloglu, M. Thomas, M. Zandian, D. Edwall, G. Williams, J. Blackwell, W. Tennant, and G. Hughes. High performance ladar focal plane arrays for 3d range imaging. In *IEEE Aerospace Conference Proceedings*, volume 3, pages 1776 – 1781, 2004.

[20] K. Johnson, M. Vaidyanathan, S. Xue, W. Tennant, L. Kozlowski, G. Hughes, and D. Smith. Adaptive ladar receiver for multispectral imaging. In *Proceedings of SPIE - The International Society for Optical Engineering*, volume 4377, pages 98 – 105, 2001.

[21] U. Schael and H. Rothe. Field measurements with 1574-nm imaging and scannerless eye-safe laser radar. In *SPIE*, volume 4377, pages 1 – 11, 2001.

[22] R. Burnham. Three-dimensional laser radar for long-range applications. In *Proceedings of SPIE - The International Society for Optical Engineering*, volume 4377, pages 35 – 45, 2001.

[23] W. Ruff, K. Aliberti, J. Dammann, M. Giza, P. Shen, and B. Stann. Performance of an fm/cw prototype ladar using a 32-element linear self-mixing detector array. In *Proceedings of SPIE - The International Society for Optical Engineering*, volume 5086, pages 58 – 69, 2003.

[24] B. Krause, P. Gatt, C. Embry, and J. Buck. High-resolution 3d coherent laser radar imaging. In *Proceedings of SPIE - The International Society for Optical Engineering*, volume 6214, pages 62140V (1–11), 2006.

[25] K. W. Holman, D. G. Kocher, and S. Kaushik. Mit/ll development of broadband linear frequency chirp for high-resolution ladar. In *Proceedings of SPIE - The International Society for Optical Engineering*, volume 6572, 2007.

[26] F. Blais. Review of 20 years of range sensor development. *Journal of Electronic Imaging*, 13(1):231 – 243, 2004.

[27] D. Langer, M. Mettenleiter, F. Hartl, and C. Frohlich. Imaging ladar for 3-d surveying and cad modeling of real-world environments. *International Journal of Robotics Research*, 19(11):1075 – 1088, 2000.

[28] G. S. Cheok, W. C. Stone, and A. Lytle. Standards requirements for ladars? In *Proceedings of SPIE - The International Society for Optical Engineering*, volume 5791, pages 250 – 261, 2005.

[29] A. Ewald and V. Willhoeft. Laser scanners for obstacle detection in automotive applications. In *IEEE Intelligent Vehicles Symposium, Proceedings*, pages 682 – 687, 2000.

[30] R. Bostelman, T. Hong, and R. Madhavan. Obstacle detection using a time-of-flight range camera for automated guided vehicle safety and navigation. *Integrated Computer-Aided Engineering*, 12(3):237 – 249, 2005.

[31] H. C. Moon, H. C. Lee, and J. H. Kim. Obstacle detecting system of unmanned ground vehicle. In *2006 SICE-ICASE International Joint Conference*, pages 1295 – 1299, 2006.

[32] C. H. Caldas, C. T. Haas, K. A. Liapi, and J. Teizer. Modeling job sites in real time to improve safety during equipment operation. In *Proceedings of SPIE - The International Society for Optical Engineering*, volume 6174 II, pages 61743K (1–8), 2006.

[33] T. C. Ng, J. I. Guzmn, and J. C. Tan. Development of a 3d ladar system for autonomous navigation. In *2004 IEEE Conference on Robotics, Automation and Mechatronics*, pages 792 – 797, 2004.

[34] R. Madhavan and T. Hong. Robust detection and recognition of buildings in urban environments from ladar data. In *Proceedings - Applied Imagery Pattern Recognition Workshop*, pages 39 – 44, 2005.

[35] C. Ye. Toward safe navigation in urban environments. In *Proceedings of SPIE - The International Society for Optical Engineering*, volume 6561, pages 1 – 12, 2007.

[36] W. S. Wijesoma, K. R. S. Kodagoda, and A. P. Balasuriya. Road-boundary detection and tracking using ladar sensing. *IEEE Transactions on Robotics and Automation*, 20(3):456 – 464, 2004.

[37] M. Jabbour and P. Bonnifait. Global localization robust to gps outages using a vertical ladar. In *9th International Conference on Control, Automation, Robotics and Vision, 2006, ICARCV '06*, 2006.

[38] M. U. De Haag, D. Venable, and M. Smearcheck. Use of 3d laser radar for navigation of unmanned aerial and ground vehicles in urban and indoor environments. In *Proceedings of SPIE - The International Society for Optical Engineering*, volume 6550, pages 65500C (1–12), 2007.

[39] K. Bers, K. R. Schulz, and W. Armbruster. Laser radar system for obstacle avoidance. In *Proceedings of SPIE - The International Society for Optical Engineering*, volume 5958, pages 1 – 10, 2005.

[40] A. K. Vadlamani and M. U. De Haag. Aerial vehicle navigation over unknown terrain environments using inertial measurements and dual airborne laser scanners or flash ladar. In *Proceedings of SPIE - The International Society for Optical Engineering*, volume 6550, pages 65500B (1–12), 2007.

[41] A. R. Jimnez, R. Ceres, and F. Seco. A laser range-finder scanner system for precise maneouver and obstacle avoidance in maritime and inland navigation. In *Proceedings Elmar - International Symposium Electronics in Marine*, pages 101 – 106, 2004.

[42] J. Barenz, R. Baumann, F. Imkenberg, D. Krogmann, and H. D Tholl. All solid state imaging infrared / imaging ladar sensor system. In *Proceedings of SPIE - The International Society for Optical Engineering*, volume 5459, pages 171 – 179, 2004.

[43] B. C. Redman, B. Stann, W. Lawler, M. Giza, J. Dammann, W. Ruff, W. Potter, R. G. Driggers, J. Garcia, J. Wilson, and K. Krapels. Chirped am ladar for anti-ship missile tracking and force protection 3d imaging: Update. In *Proceedings of SPIE - The International Society for Optical Engineering*, volume 6214, pages 62140O (1–15), 2006.

[44] A. M. Wallace, G. S. Buller, R. C. W. Sung, R. D. Harkins, A. McCarthy, S. Hernandez-Marin, G. J. Gibson, and R. Lamb. Multi-spectral laser detection and ranging for range profiling and surface characterization. *Journal of Optics A: Pure and Applied Optics*, 7(6):S438 – S444, 2005.

[45] A. M. Wallace, R. C. W. Sung, G. S. Buller, R. D. Harkins, R. E. Warburton, and R. A. Lamb. Detecting and characterising returns in a pulsed ladar system. *IEE Proceedings: Vision, Image and Signal Processing*, 153(2):160 – 172, 2006.

[46] V. Jolivet, J. Fournier, X. Normandin, and J. . Cariou. Feasibility of air target identification using laser radar vibrometry. In *Proceedings of SPIE - The International Society for Optical Engineering*, volume 5807, pages 222 – 232, 2005.

[47] R. M. Marino, W. R. Davis, G. C. Rich, J. L. McLaughlin, E. I. Lee, B. M. Stanley, J. W. Burnside, G. S. Rowe, R. E. Hatch, T. E. Square, L. J. Skelly, M. O'Brien, A. Vasile, and R. M. Heinrichs. High-resolution 3d imaging laser radar flight test experiments. In *Proceedings of SPIE - The International Society for Optical Engineering*, volume 5791, pages 138 – 151, 2005.

[48] R. O. Nellums, R. D. Habbit, M. R. Heying, T. A. Pitts, and J. V. Sandusky. 3d scannerless ladar for orbiter inspection. In *Proceedings of SPIE - The International Society for Optical Engineering*, volume 6220, pages 62200G (1–17), 2006.

[49] S. Ruel, C. English, M. Anctil, J. Daly, C. Smith, and S. Zhu. Real-time 3d vision solution for on-orbit autonomous rendezvous & docking. In *Proceedings of SPIE - The International Society for Optical Engineering*, volume 6220, pages 622009 (1–11), 2006.

[50] D. C. Woffinden and D. K. Geller. Navigating the road to autonomous orbital rendezvous. *Journal of Spacecraft and Rockets*, 44(4):898 – 909, 2004.

[51] J. M. Trenkle, P. Tchoryk Jr., G. A. Ritter, J. C. Pavlich, and A. S. Hickerson. 3-d sensor algorithms for spacecraft pose determination. In *Proceedings of SPIE - The International Society for Optical Engineering*, volume 6220, pages 62200D (1–14), 2006.

[52] Q.A. Holmes, X. Zhang, and D. Zhao. Multiresolution surface feature analysis for automatic target identification based on laser radar images. In *International Conference on Image Processing*, volume 3, pages 468 – 471, 1997.

[53] J. Dufour and V. Martin. Active/passive cooperative image segmentation for automatic target recognition. *Proceedings of SPIE - The International Society for Optical Engineering*, 2298:552 – 560, 1994.

[54] C. English, S. Ruel, L. Melo, P. Church, and J. Maheux. Development of a practical 3d automatic target recognition and pose estimation algorithm. In *Proceedings of SPIE - The International Society for Optical Engineering*, volume 5426, pages 112 – 123, 2004.

[55] H. Delingette, M. Hebert, and K. Ikeuchi. A spherical representation for the recognition of curved objects. In *Fourth International Conference on Computer Vision, 1993. Proceedings*, pages 103 – 112, 1993.

[56] A. S. Mian, M. Bennamoun, and R. A. Owens. Automatic correspondence for 3d modeling: An extensive review. *International Journal of Shape Modeling*, 11(2):253 – 291, 2005.

[57] M. Ankerst, G. Kastenmuller, H. P. Kriegel, and T. Seidl. 3d shape histograms for similarity search and classification in spatial databases. In *Advances in Spatial Databases*, volume 1651, pages 207 – 228. Springer, 1999.

[58] Greg J. Meyer and James R. Weber. The effects of different shape-based metrics on identification of military targets from 3d ladar data. volume 6056, pages 60560H (1–11). SPIE, 2006.

[59] M.T. Suzuki, T. Kato, and N. Otsu. A similarity retrieval of 3d polygonal models using rotation invariant shape descriptors. In *IEEE International Conference on Systems, Man, and Cybernetics*, volume 4, pages 2946 – 2952, 2000.

[60] M. R. Stevens, M. Snorrason, H. Ruda, and S. Amphay. Feature based target classification in laser radar. In *Proceedings of SPIE - The International Society for Optical Engineering*, volume 4726, pages 46 – 57, 2002.

[61] H. Maas. Closed solutions for the determination of parametric building models from invariant moments of airborne laserscanner data. *Transformation Journal*, 32:193 – 199, 1999.

[62] O. Steinvall and T. Carlsson. Three-dimensional laser radar modelling. volume 4377, pages 23 – 34. SPIE Press, 2001.

[63] S. Budge, B. Leishman, and R. Pack. Simulation and modeling of return waveforms from a ladar beam footprint in usu ladarsim. pages 263 – 268. Pro. of SPIE, 2006.

[64] W. Koechner. *Solid-State Laser Engineering (Springer Series in Optical Sciences)*. Springer, 6th, rev. and updated ed. edition, 2006.

[65] B. E. A. Saleh and M. C. Teich. *Fundamentals of Photonics*. Wiley-Interscience, 2nd. edition, 2007.

[66] A. V. Jelalian. *Laser Radar Systems*. Artech House, 1992.

[67] J. S. Accetta and D. L. Shumaker. *The Infrared and Electro-Optical Systems Handbook.*, volume 6 of *Active Electro-Optical Systems*. SPIE Press, 1993.

[68] S. Der, B. Redman, and R. Chellappa. Simulation of error in optical radar range measurements. *Applied Optics*, 36(27):6869 – 6874, 1997.

[69] E. Lengyel. *Mathematics for 3D Game Programming and Computer Graphics*. Charles River Media, 2nd edition, 2004.

[70] C. Ericson, editor. *Real Time Collision Detection*. Morgan Kaufmann, 2005.

[71] Z. Song. 2d laser ray tracing for the simulation of laser perception. Technical report, College of Engineering, Utah State University.

[72] R. R. Clark. Scanning rangefinder with range to frequency conversion, 1994.

[73] Accurange 4000 sensor datasheet. `http://www.acuitylaser.com/pdf/ar4000-data-sheet.pdf`, 2008.

[74] Acuity laser measurement sensors homepage. `http://www.acuitylaser.com/acuity.shtml`.

[75] Accurange 4000 sensor user's manual. `http://www.acuitylaser.com/pdf/ar4000-users-manual.pdf`, 2008.

[76] Pan-tilt unit-d46 specifications. `http://www.dperception.com/pdf/specs-ptu-d46.pdf`.

[77] Pan-tilt unit-d46-17 user's manual. `http://www.dperception.com/pdf/products/PTU-D46/PTU-manual-d46.pdf`, 2006.

[78] Pan-tilt unit-d46 quick configuration guide. `http://www.dperception.com/pdf/products/PTU-D46/PTU-D46-Config.pdf`.

[79] P. Tang, D. Huber, and B. Akinci. A comparative analysis of depth-discontinuity and mixed-pixel detection algorithms. In *3DIM 2007 - Proceedings 6th International Conference on 3-D Digital Imaging and Modeling*, pages 29 – 36, 2007.

[80] J. Tuley, N. Vandapel, and M. Hebert. Analysis and removal of artifacts in 3-d ladar data. In *Proceedings - IEEE International Conference on Robotics and Automation*, pages 2203 – 2210, 2005.

[81] P. Skrzypczynski. How to recognize and remove qualitative errors in time-of-flight laser range measurements. In *International Conference on Intelligent Robots and Systems*, pages 2958 – 2963, 2008.

[82] Cang Ye. Mixed pixels removal of a laser rangefinder for mobile robot 3-d terrain mapping. In *International Conference on Information and Automation*, pages 1153 – 1158, june 2008.

[83] M. Hebert and E. Krotkov. 3-d measurements from imaging laser radars: how good are they? In *IEEE/RSJ - Intelligent Robots and Systems*, volume 1, 1991.

[84] R.L. Larkins, M.J. Cree, A.A. Dorrington, and J.P. Godbaz. Surface projection for mixed pixel restoration. In *24th International Conference Image and Vision Computing New Zealand (IVCNZ 2009)*, pages 431 – 436, 2009.

[85] J. P. Godbaz, M. J. Cree, and A. A. Dorrington. Multiple return separation for a full-field ranger via continuous waveform modelling. In *Proceedings of SPIE - The International Society for Optical Engineering*, volume 7251, pages 72510T (1–12). SPIE, 2009.

[86] J.P. Godbaz, M.J. Cree, and A.A. Dorrington. Mixed pixel return separation for a full-field ranger. In *23rd International Conference Image and Vision Computing New Zealand (IVCNZ 2008)*, pages 1 – 6, 2008.

[87] Q. Wang, Q. Li, Z. Chen, J. Sun, and R. Yao. Range image noise suppression in laser imaging system. *Optics and Laser Technology*, 41(2):140 – 147, 2009.

[88] G. R. Jones, A. G. Deakin, and J. W. Spencer. *Chromatic Monitoring of Complex Conditions.* CRC Press, 2008.

[89] G.R. Jones, P.C. Russell, J. Cosgrave, J.W. Spencer, A. Vourdas, W. Hall, and A. Wilson. Chromatic processing of optoacoustic signals for identifying incipient faults on electric power equipment. pages 3/1 – 3/5. The Institution of Electrical Engineers, 1996.

[90] P. H. Moon and D. E. Spencer. *The photic field.* MIT Press, 1981.

[91] C. Lappas. *Chromatic Ultrasonic Tracking.* PhD thesis, University of Liverpool, 2007.

[92] G. R. Jones, P. C. Russell, and A. Vourdas. Chromatic compression of sensor signals in the wavelength, time and parameter domains. pages 9/1 – 9/4. IEE Intelligent and Self-Validating Sensors, 1999.

[93] A.G. Deakin, I. Rallis, J. Zhang, J.W. Spencer, and G.R. Jones. Towards holistic chromatic intelligent monitoring of complex systems. *Sensor Review*, 26(1):11 – 17, 2006.

[94] J. A. Cosgrave, P. C. Russell, B. S. B. Hall, and G. R. Jones. Optoacoustic monitoring of electric arcs in high voltage circuit breakers. pages 598 – 605, Man Jiaotong University, 1997. Int. Conf. on Switching Arcs.

[95] G. R. Jones, P. C. Russell, A. Vourdas, J. Cosgrave, L. Stergioulas, and R Haber. The gabor transform basis of chromatic monitoring. *Measurement Science and Technology*, 11(5):489 – 498, 2000.

[96] L.K. Stergioulas, A. Vourdas, and G.R. Jones. Gabor representation of optical signals using a truncated von neumann lattice and its practical implementation. *Optical Engineering*, 39(7):1965 – 1971, 2000.

[97] S. Xu and G. R. Jones. Event and movement monitoring using chromatic. *Measurement Science and Technology*, 17(12):3204 – 3211, 2006.

[98] R. C. Gonzalez and R. E. Woods. *Digital Image Processing.* Pearson/Prentice Hall, 3th edition, 2008.

[99] C. Tang and H. Hang. A feature-based robust digital image watermarking scheme. *IEEE Transactions on Signal Processing*, 51(4):950 – 959, 2003.

[100] L. LI, B. GUO, and L. GUO. Rotation, scaling and translation invariant image watermarking using feature points. *Journal of China Universities of Posts and Telecommunications*, 15(2):82 – 87, 2008.

[101] M. Alghoniemy and A. H. Tewfik. Geometric invariance in image watermarking. *IEEE Transactions on Image Processing*, 13(2):145 – 153, 2004.

[102] The 3d studio. `http://www.the3dstudio.com`.

[103] S. Paschalakis and P. Lee. Pattern recognition in grey level images using moment based invariant features. In *IEE Conference Publication*, pages 245 – 249, 1999.

[104] T. M. Mitchell. *Machine Learning*, volume 6 of *computer science.* McGraw-Hill, 1997.

[105] R. C. Gonzalez and R. E. Woods. *Digital Image Processing.* Prentice Hall, 2nd edition, 2002.

[106] P. J. Besl. *Surfaces in Range Image Understanding.* Springer, 1988.

[107] S. Li and D. Zhao. Three-dimensional range data interpolation using b-spline surface fitting. *Journal of Electronic Imaging*, 10(1):268 – 273, 2001.

[108] 3dvia model library. `http://www.3dvia.com/products/3dvia-shape/`.

[109] Artist-3d model library. `http://artist-3d.com/`.

[110] Meshlab software. `http://meshlab.sourceforge.net/`.

[111] S. Ruel, C. E. English, L. Melo, A. Berube, D. Aikman, A. M. Deslauriers, P. M. Church, and J. Maheux. Field testing of a 3d automatic target recognition and pose estimation algorithm. volume 5426, pages 102 – 111. SPIE, 2004.

[112] G. Bouchette, P. Iles, C. English, M. Labrie, B. Powaschuk, P. Church, and J. Maheux. Rapid automatic target recognition using generic 3d sensor and shape-from-motion data. volume 6566, pages 656619 (1–12). SPIE, 2007.

[113] M. T. Perona, A. Mahalanobis, and K. N. Zachery. Ladar automatic target recognition using correlation filters. *Proceedings of SPIE - The International Society for Optical Engineering*, 3718:388 – 396, 1999.

[114] N. ZHANG and T. WATANABE. Image representation and classification based on data compression. In *SAC 10 Proceedings of the 2010 ACM Symposium on Applied Computing*, pages 981 – 982, 2010.

[115] J. Han and M. Kamber. *Data Mining Concepts and Techniques.* Morgan Kaufmann, 2nd. edition, 2006.

[116] Dan Li, J.S. Deogun, and Kefei Wang. Gene function classification using fuzzy k-nearest neighbor approach. In *2007 IEEE International Conference on Granular Computing*, pages 644 – 647, 2007.

[117] F. Yan, W. Mei, and Z. Chunqin. Sar image target recognition based on hu invariant moments and svm. In *5th International Conference on Information Assurance and Security, IAS 2009*, volume 1, pages 585 – 588, 2009.

[118] M. Rizon, H. Yazid, P. Saad, A. Y. M. Shakaff, A. R. Saad, M. R. Mamat, S. Yaacob, H. Desa, and M. Karthigayan. Object detection using geometric invariant moment. *American Journal of Applied Sciences*, 2(6):1876 – 1878, 2006.

[119] S. A. Dudani, K. J. Breeding, and R. B. McGhee. Aircraft identification by moment invariants. *IEEE Transactions on Computers*, C-26(1):39 – 46, 1977.

[120] W. Liu and Y. He. 3d model retrieval based on orthogonal projections. In *Proceedings - Ninth International Conference on Computer Aided Design and Computer Graphics, CAD/CG 2005*, volume 2005, pages 157 – 162, 2005.

[121] G. . Zhang, B. Cheng, R. . Feng, and J. . Li. Real-time driver eye detection method using support vector machine with hu invariant moments. In *Proceedings of the 7th International Conference on Machine Learning and Cybernetics, ICMLC*, volume 5, pages 2999 – 3004, 2008.

[122] M. S. Al-Batah, N. A. Mat Isa, K. Z. Zamli, Z. M. Sani, and K. A. Azizli. A novel aggregate classification technique using moment invariants and cascaded multilayered perceptron network. *International Journal of Mineral Processing*, 92(1-2):92 – 102, 2009.

[123] K. R. Radhika, M. K. Venkatesha, and G. N. Sekhar. Off-line signature authentication based on moment invariants using support vector machine. *Journal of Computer Science*, 6(3):305 – 311, 2010.

[124] Pan-tilt unit-d46-17 command reference manual. `http://www.dperception.com/pdf/products/other/Pan-Tilt-Command-Reference-Manual.pdf`, 2008.

[125] E. Paquet and M. Rioux. Content-based search engine for vrml databases. In *Proceedings of the IEEE Computer Society Conference on Computer Vision and Pattern Recognition*, pages 541 – 546, 1998.

[126] E. Paquet, K. M. Robinette, and M. Rioux. Management of three-dimensional and anthropometric databases: Alexandria and cleopatra. *Journal of Electronic Imaging*, 9(4):421 – 431, 2000.

[127] D. F. WATSON. *CONTOURING : A Guide To The Analysis and Display of Spatial Data.* Pergamon Press, 1992.

[128] M. S. Nixon and A. S. Aguado. *Feature extraction and image processing.* Newnes, 1st edition, 2002.

[129] R. C. Gonzalez, R. E. Woods, and S. L. Eddins. *Digital Image Processing using MATLAB.* Pearson/Prentice Hall, 3th edition, 2004.